INFORMATION TO USERS

This manuscript has been reproduced from the microfilm master. UMI films the text directly from the original or copy submitted. Thus, some thesis and dissertation copies are in typewriter face, while others may be from any type of computer printer.

The quality of this reproduction is dependent upon the quality of the copy submitted. Broken or indistinct print, colored or poor quality illustrations and photographs, print bleedthrough, substandard margins, and improper alignment can adversely affect reproduction.

In the unlikely event that the author did not send UMI a complete manuscript and there are missing pages, these will be noted. Also, if unauthorized copyright material had to be removed, a note will indicate the deletion.

Oversize materials (e.g., maps, drawings, charts) are reproduced by sectioning the original, beginning at the upper left-hand corner and continuing from left to right in equal sections with small overlaps.

ProQuest Information and Learning
300 North Zeeb Road, Ann Arbor, MI 48106-1346 USA
800-521-0600

COMPUTER SIMULATION STUDIES OF HETEROGENEOUS CRYSTAL GROWTH

by

Mohamed Shajahan Gulam Razul

Submitted in partial fulfillment of the requirements
for the degree of Doctor of Philosophy

at

Dalhousie University
Halifax, Nova Scotia
July 2005

DALHOUSIE UNIVERSITY

To comply with the Canadian Privacy Act the National Library of Canada has requested that the following pages be removed from this copy of the thesis:

Preliminary Pages

Examiners Signature Page (pii)

Dalhousie Library Copyright Agreement (piii)

Appendices

Copyright Releases (if applicable)

Dedicated to my Parents for all the years of love and sacrifice

TABLE OF CONTENTS

LIST OF TABLES

LIST OF FIGURES

ABSTRACT

In the past, systematic studies of the mechanisms of heterogeneous crystal growth, as well as the structure and nature of the solid/liquid interface, have proven somewhat difficult. In this thesis, a novel molecular dynamics simulation methodology has been employed to create conditions allowing steady-state crystal growth/melting to be studied. This methodology is used to examine solid/liquid crystal faces of model atomic potentials (LJ) and ice/water model systems. Extensive sets of simulations were performed with several different potential models exploring different conditions of temperature gradient and growth velocity. Profile functions of various quantities across the interface are key results of these simulations; as measured in the moving frame these functions are effectively averaged over the atomic/molecular detail of the interface and become smooth. This characteristic allows for new ways of interpreting and utilizing profile functions. When the derivative of these profile functions is taken with respect to the z-dimension, consistent peaks that characterize the freezing/melting interfaces are obtained. Consequently, the position and width of an interface are easily identified and quantities such as the interfacial energy are directly obtained.

In addition, the mechanisms of crystallization and melting are explored using averaged configurations generated during these steady-state runs, where subsequent tagging and labeling of particles provide many insights into the detailed atomic/molecular behaviour at the freezing and melting interfaces. The interfaces of the atomic and ice/water systems are generally found to be rough and the microscopic structure of the freezing and melting interfaces are observed to be very similar. Large structural fluctuations with solid-like and liquid-like characteristics are apparent in both the freezing and melting interfaces.

The behaviour observed at a solid/liquid interface under either growth or melting conditions reflects a competition between ordering and disordering processes. The findings in this thesis are also able to reconcile the different behaviours exhibited by different interfacial measures and to address the onset of asymmetry in the growth rates at high rates of crystal growth/melting.

LIST OF ABBREVIATIONS AND SYMBOLS USED

Abbreviations

AFM	atomic force microscopy
ASW	amorphous solid water
BCF	Burton Cabrera Frank
BF	Bernal Fowler
CCD	coupled cluster device
CF1	central force model
DFT	density functional theory
FCC	face centered cubic
HCP	hexagonal close packed
HDA	high density amorphous
LJ	Lennard-Jones
LDA	low density amorphous
MD	molecular dynamics
NMR	nuclear magnetic resonance
SFG	sum frequency generation
SHG	second harmonic generation
SPM	scanning tunneling microscopyy
STM	scanning tunneling microscope
TEM	transmission electron microscopy

Roman Symbols

a	Radius of spherical particle
a_o	Gaussian width
A_{obs}	Experimentally observable macroscopic property

A	Area
A_{int}	An instantaneous property
C	Square of curvature function
C_n	Fraction of solid blocks over total number of blocks
C_p	Constant pressure heat capacity
C_v	Constant volume heat capacity
c_m	Mean heat capacity of the melt
D	Diffusion coefficient
D_s	Self-diffusion coefficient
d	Interlayer spacing
dA	Small unit area change
dw	Small change in work
E	Energy of the system
E_l	Energy of the liquid region
E_s	Energy of the solid region
e	Interfacial excess total energy
E_{int}	Energy of the interfacial region
E_{vap}	Vapourization energy
F or f	Helmholtz free energy
$\mathbf{F}_{ij}$	Force on particle i, due to interactions with particle j
$\mathbf{F}_i$	Force on particle i
$\mathrm{F}[\rho(\mathbf{r})]$	Helmholtz free energy functional
$\mathrm{F}_{\text{excess}}[\rho(\mathbf{r})]$	The excess free energy functional
$\mathrm{F}_{\text{ideal}}[\rho(\mathbf{r})]$	Ideal gas free energy functional

f_e	An effectiveness factor
$G(N,C_n,T)$	Free energy
g	Excess Gibbs free energy
g_N	Degrees of freedom
$G_c(z_i)$	Weighting function for the heat sink
$G_h(z_i)$	Weighting function for the heat source
g_{HH}	Radial distribution function
$G_l(z_i)$	Localizing weighting function
g_{OH}	Radial distribution function
g_{OO}	Radial distribution function
$g(r,\dot{r},t)$	Non-holonomic constraint
$g(r)$	Radial distribution function
$G(\hat{q}_c)$	Real and continuous function that minimizes at the centroid
H	Hamilton's function
I_C	Intensity of Raleigh line
h	Planck's constant
I_B	Intensity of Brillouin limn
I_c	Ice I – cubic ice
I_h	Ice I – hexagonal ice
Ih10$\bar{1}$0	Hexagonal ice with 10$\bar{1}$0 crystal face
Ih0001	Hexagonal ice with 0001 crystal face
Ih11$\bar{2}$0	Hexagonal ice with 11$\bar{2}$0 crystal face
Ic001	Cubic ice with 001 crystal face
Ic111	Cubic ice with 111 crystal face

Ic011	Cubic ice with 011 crystal face
$I(k)$	X-ray intensity
K_i	Kinetic energy of particle i
$\mathbf{k}$	Wave-number
k_B	Boltzmann constant
$\mathbf{k}_f$ or $\mathbf{k}_{\text{scatter}}$	Scattered wave-vector
$\mathbf{k}_i$ or $\mathbf{k}_{\text{water}}$	Incident wave-vector
$\mathbf{k}_{\text{refracted}}$	Wave-vector of the refracted light
L_0	Change in internal energy
l	Latent heat of fusion per atom
L	Difference in activation free energies of solid and liquid
m	Particle's mass
N	Number of particles (molecules) in the system
N_m	Number of particles comprising a complete monolayer
N_{ad}	Number of adatoms
N^i	Total number of particles of type i
N^i_{int}	Total number of interfacial particles of type i
N^i_l	Total number of liquid particles of type i
N^i_s	Total number of solid particles of type i
N_{solid}	Number of solid particles
P	Pressure (except in Appendix B where it is the number of orientations)
$\mathbf{p}^N$	Momenta microstate of a N particle system (in a three dimensional space)

$\mathbf{p}_i$	Momentum of particle i
$(\mathbf{p}_1,\cdots,\mathbf{p}_N)$	Momenta microstate of a N particle system (in a three dimensional space)
q	Heat
q_O	Charge on oxygen atoms
q_H	Charge on hydrogen atoms
$\mathbf{q}$	Vector describing the difference between the scattered and incident wave-vectors
Q_{ens}	Partition function
Q	Coupling parameter
Q_t	Thermal bath relaxation parameter
q_c	Orientational centroid
$\boldsymbol{Q}$	Quaternion
Q_k	Charge on site k on molecule i
Q_L	Actvation free energy of the liquid
Q_l	Charge on site l on molecule i
q_t	Quaternion for each molecule
Q_S	Actvation free energy of the solid
q_j	Quaternion parameter j=0,1,2,3
$\mathbf{r}_{x,y,z}$	Components of rotation matrix
$\langle R^2 \rangle$	Mean square displacement
R	Net growth rate
R_F	Freezing rate
R_F°	Freezing rate at equilibrium
R_M	Melting rate

R_M°	Melting rate at equilibrium
$\bar{r}$	Arithmetic mean of four radial distances
$\dot{\mathbf{r}}$	Velocity
r	Distance
r_i	Position of particle i
$\mathbf{r}$	Position vector
$\mathbf{r}_{ij}$	Distance vector between particle i and j
r_I	Ratio between spectral intensities
r_k	Radial distance from the central molecule
r_{kl}	Distance between sites k and l
r^N	Position microstate of a N particle system (in a three dimensional space)
$\ddot{\mathbf{r}}_i$	Acceleration of particle i
R_g	Gas constant
$\mathbf{R}$	Rotation matrix
$(\mathbf{r}_1,\cdots,\mathbf{r}_N)$	Position microstate of a N particle system (in a three dimensional space)
$(\mathbf{r}^N,\mathbf{p}^N)$	Phase space point of a N particle system (in a three-dimensional space)
s	Excess entropy
$\mathbf{s}_{x,y,z}$	Components of rotation matrix
S_g	Local tetrahedral order parameter
S_k	Local radial distance order parameter
$\mathrm{S_s}$	Entropy of solid
$\mathrm{S_l}$	Entropy of liquid

S_{int}	Entropy on interface
$S(\mathbf{k})$	Structure factor
T	Temperature
T_c	Temperature of heat sink
$T_{c;o}$	Target temperature of the cold thermostat
T_i	Temperature of the melt
T_e	Equilibrium temperature
T_h	Temperature of heat source
$T_{h;o}$	Target temperature of the hot thermostat
T_l	Local temperature
T_m	Thermodynamic melting temperature
t	Time
$\mathbf{t}_{x,y,z}$	Components of rotation matrix
U	Potential energy
U_{HH}	Potential energy due to hydrogen interactions
U_{LJ}	Lennard-Jones potential energy
U_{OO}	Potential energy due to oxygen interactions
U_{OH}	Potential energy due to oxygen-hydrogen interactions
$U(r)$	Potential energy as a function of coordinates
V	Volume
V_s	Total volume of solid particles of type i
V_l	Total volume of liquid particles of type i
V_a	Velocity of growth along the a-axis
V_c	Velocity of growth along the c-axis

V_i	Total volume of particles of type *i*
V_{int}	Total volume of interface particles of type *i*
v_p	Pulling velocity
v	Velocity
v_i	Velocity of particle *i*
$V(\mathbf{r}^N)$	Potential energy
w_{ens}	Weight function
x, y, z	Cartesian axes
xx,yy, zz	Tensor components
x_e	Effective thickness
z_i	Particle *i* position on the z-coordinate
z_o	The center position of the thermostatted region
z_η	Coordination number of the crystal
$Z(N,C_n,T)$	Partition function

Greek Symbols

α_c	Thermostatting multiplier of cold
α_h	Thermostatting multiplier of hot
α	Jackson's alpha parameter
β	Inverse of temperature in energy units
ΔT	Supercooling
ΔS	Change in entropy
ΔH_f	Heat of formation

ΔS_{tot}	Total change in entropy
ΔE_{tot}	Change in total enrgy
ΔE_0	Change in internal energy due to the attachment of an atom
ΔE_1	Change in internal energy due to the interaction of an atom with atoms in the monolayer
ΔG_{tot}	Total change in free energy
ΔG	Change in free enrgy
ΔV	Volume change
ΔH_{cryst}	Heat of crystallization
$\Delta\mu$	Chemical potential difference
η_0	Normal interface bonds
η_1	In plane bonds
η	Viscosity
Λ	De Broglie wavelength
Γ^i	Surface excess number of particles of type *i*
Γ	Point in phase space
$\Gamma(q_c,q_i)$	Arc length between centroid orientation and individual quaternions
μ_i	Chemical potential of particle *i*
$\Omega[\rho(\mathbf{r})]$	Grand canonical ensemble as a functional of particle density
$\nu(\mathbf{r})$	Single particle density
$\rho(\mathbf{r})$	Particle density
ρ_{ens}	Probability density distribution
γ	Excess interfacial free energy

λ	Thermostatting multiplier (except in Chapter 5, λ is wavelength)
γ_c	Interaction energies in the Temkin model
γ_T	Conservation of momentum term
$\dot{\lambda}$	Constraint or friction coefficient
ε	Well depth
σ	Diameter of particle
ε_o	Dielectric constant
ε_{LJ}	Well depth for LJ
κ_B	Adiabatic compressibility
κ_T	Isothermal compressibility
κ	Thermal conductivity
λ_d	Diffusional mean free path
5	Density
$\sum(z)$or $\sum$	2D order parameter
ω	Frequency
ω_i	Different frequencies *i-1,2*
ω_T	Total frequency

ACKNOWLEDGMENTS

I would like to express my respect and many thanks to my supervisor Professor Peter G. Kusalik who has been incredibly supportive and patient over the years and for being a great inspiration. I would also like to express my sincerest gratitude and love to my beloved Susan for her continued support, perseverance and help in completing the thesis.

I would also like to thank Lisandro for many engaging conversations and his great passion for science. I would like to thank Edward and John for all their help.

Finally, I would like to thank all my teachers past and present for supporting me over these many years.

CHAPTER 1
INTRODUCTION

The creation of our planet, over some five billion years ago, has involved among other significant events, numerous melting and freezing processes [1]. These fundamental transitions are still a normal part of our every day lives in both the natural and industrial worlds. Today we appreciate and marvel at the fact that these processes are responsible for creating the earth's crust and continuing to shape it from deep inside the earth or on the surface through ice floes [2]. In industry, a large proportion of commercial solid materials start out as liquids that are frozen into configurations to suit the demands of practical utility in modern existence.

The melting of a solid or the solidification of a liquid can be easily characterized by thermodynamics, however the complex microscopic interactions of matter and energy [3] involved in these processes are less well defined. The production of a latent heat by the freezing phase transition was recognized as early as the 18^{th} century by Fahrenheit and Lowitz [4]. This heat is generated at the boundary between the solid and liquid phases, called the interface, and is conducted away by one or both phases, dependent on prevailing conditions (experimental or natural). During a reversible phase change, the free energies of both phases are equal. The free energy of the system is a continuous function of pressure and temperature during such phase changes, but other thermodynamic quantities such as the internal energy, entropy, volume and heat capacity undergo discontinuous changes. Such a phase change can be defined as a first order phase transition [5].

Despite thermodynamic descriptions to address bulk macroscopic properties like melting and freezing, even for a common liquid like water elementary questions pertaining to the mechanisms involved with constituent molecules organizing or arranging themselves in a liquid are not well characterized. Answers to these questions are at present far from complete [6]. These are some of the cogent issues that will be dealt with in this thesis, from the perspective of a solid in contact with its melt.

Water is a compound that is required by all life on earth and is found in all the varied ecosystems throughout our biosphere. It covers two-thirds of our planet in liquid form and is trapped in solid form at the poles of our planet. Water vapour is very active in our atmosphere and is by far the most important factor in all kinds of weather phenomena. Water is ubiquitous; it is the most abundant naturally occurring inorganic substance on our planet. The unique properties of water stem from its ability to form relatively strong hydrogen bonds to its neighbours in a tetrahedral arrangement [7]. This structure allows some unique solid phase behaviour to be seen. Therefore much inquiry has gone into elucidating its structure and behaviour at the molecular level.

There are many important chemical reactions and physical processes that occur at the phase boundaries in water [8]. Knowledge of the interfacial properties is fundamental in many natural and technological processes. Of the three interfaces of the phases of water, perhaps the best characterized, through experimental and theoretical work, is the vapour/liquid interface [9,10]. Many systems that would benefit from a better understanding of their interfacial regions, including biological membranes and water in contact with material surfaces. Ice surfaces are important for meteorology of clouds, rheology of ice sheets, the prevention of freezing hazards in society, food preservation

and cryobiology [11]. The properties of water are of great importance to many diverse fields, making it the most extensively studied substance [12,13]. Despite enormous efforts to understand the complexity of water, complete understanding of this substance still is elusive.

The challenge to a physical chemist is to attempt to understand this enigmatic substance and its phase behaviour. At the very least, thermodynamics furnishes a macroscopic gauge on solidification and melting, providing quantifiable descriptions. Posing a simple question as to whether solidification and melting are inverse processes should then be easily answered. In light of equilibrium macroscopic considerations the answer seems obviously "yes". Now turning to a microscopic description to discover the relationship between these processes, the principle of microscopic reversibility may be invoked. This principle, first justified by Lars Onsager in 1931 [14], states that under equilibrium conditions any molecular process, and its reverse, take place on the average with the same frequency. Some have tried to interpret this principle by considering for example the motion on a particle of a system of particles. Such a particle can be provided exact coordinates, velocities and accelerations. Classically, the particular trajectory traversed by such a particle may be reversed, tracing the same path backwards. In other words, if time were allowed to be reversed, the particle (or particles) should in principle follow the reverse of its original trajectory. As a consequence, since freezing and melting are apparently (macroscopically) reversible, should this imply the underlying microscopic processes are?

Let us consider another example. If N (non-interacting) gaseous molecules occupied a volume V at a particular temperature, then the probability of locating the N

molecules in a volume $0.5V$ would be 0.5^N. Since N is usually of the order of 10^{23}, the probability of witnessing this event is incredibly small [15]. Similarly, the probability of a disordered collection of molecules at a solid/liquid interface (the site of crystallization) becoming localized to form a lattice layer might be expected to be considerably lower than the melting of a layer of molecules (due to the much larger number of possibilities). Clearly, probabilistic considerations appear to violate microscopic reversibility. The present thesis will attempt to reconcile this seemingly apparent contradiction.

In addition to considerations of the nature of the freezing and melting processes and how they may be microscopically related, this thesis will also examine the region where these processes occur, that is the solid/liquid interface. The elucidation of the possible interfaces between the solid, liquid, and gas phases has certainly experienced many advances [3,16,17]. The solid/gas interface has been well-characterized by experiments [18,19,20] and computer simulation [21]; its importance to technological applications has motivated much of the interest in understanding the solid/gas and solid/vacuum interfaces [22,23,24]. The liquid/gas interface has been successfully characterized by statistical mechanical theories [25] and generally serves as a basis for characterizing the other interfaces [19]. In contrast, the solid/liquid interface, generally, is not as experimentally accessible [26]. These interfaces are difficult to probe directly as most techniques tend to focus on the chemical species of the solid or the reactions taking place in the bulk liquid [27]. Macroscopically the solid/liquid interface is a sharp and distinct boundary, but at the microscopic level this entity is less well defined [3]. Many processes important to chemists, like ionic adsorption, electrodeposition, nucleation, growth of a crystal and heterogeneous catalysis, all occur at liquid/solid interfaces [3,27].

It is also unclear whether comparing equilibrium and non-equilibrium conditions changes the interfacial structure and how the processes of freezing and melting may be affected. The interface is a region, generally, believed to be a few atomic or molecular diameters wide [3]. Such an interface is described as a buried interface as it is bounded by two condensed phases. Furthermore, its properties are also believed to be distinct from the bulk phases, and it is expected that particles at the interface experience asymmetric forces due to the inhomogeneous environment. The asymmetry of the forces across the interfacial region may significantly affect the inherent interfacial structure and physical properties. It may also impact the dynamic properties of the atoms or molecules [3,6,27].

In this thesis, the solid/liquid interfaces of model atomic and water systems, as well as their crystallizing and melting characteristics, will be investigated by molecular dynamics simulations. The atomic model simulations will involve 001, 011 and 111 solid/liquid interfaces of FCC and BCC crystals with Lennard-Jones and inverse sixth power potentials. For the solid/liquid interfaces of water, the faces 001, 011 and 111 of cubic ice I and the faces 0001, $10\bar{1}0$ and $11\bar{2}0$ of hexagonal ice I will be explored with the TIP4P [28], SPC/E [29] and TIP4P-Ew [30] potential models of water. The aim of this part of the study is to examine the growth characteristics and the relationships of the two forms of ice I. Moreover, the study will serve to test and advance new computer simulation methodologies for the investigation of fundamental crystal growth physics.

Some of the numerous studies, from the theoretical and experimental perspectives, carried out to probe the solid/liquid interface and its role in crystal growth will be discussed in Chapter 2. It will be clear from these discussions that the solid/liquid interface has proven to be a difficult region to characterize or describe successfully.

Chapter 3 will examine the use of computer simulations to investigate the solid/liquid interfaces, providing a survey of previous computer simulation studies and their findings. Moreover, a new methodology developed to overcome the difficulties faced by other researchers will also be discussed in Chapter 3. Chapter 4 will present the results from non-equilibrium crystal growth studies of atomic systems. By introducing innovative profile functions, interfacial structure during crystal growth (or melting) will be characterized; in addition an effective visualization procedure for capturing the details of microscopic processes responsible for freezing and melting will be presented and discussed. In Chapter 5 properties of solid and liquid water are examined, along with experimental solid/liquid interfacial studies and examinations of ice growth from liquid water. In addition to the discussions of experimental techniques to investigate the interfaces, a review of computer simulation studies of the ice/water interface is presented, along with the application of the present methodology to ice growth and melting. The results from this work will be reported and examined in detail in Chapter 6, where the connections between hexagonal and cubic ice, the analysis of profile functions and visualization of detailed mechanisms of crystal growth and melting will be explored. Chapter 7 will present conclusions from these simulation studies and comment on the insights provided by these investigations to the issues raised in this chapter. Finally, Chapter 8 will offer suggestions of future work relevant to this thesis.

CHAPTER 2
THE SOLID/LIQUID INTERFACE

2.1 THERMODYNAMICS OF THE LIQUID/SOLID INTERFACE

2.1.1 Introduction

The interface between bulk phases is certainly an interesting entity. Important issues concerning its structure and properties were first addressed by Thomas Young [31,32] in 1805. He provided an intuitive approach in characterizing the interface, in which he proposed that the mechanical properties of such a "surface" may be related to those of a hypothetical membrane. Such a stretched membrane would posses a surface, which could be called the "surface of tension". The surface (or surface layer) Thomas Young had envisioned was a stretched membrane (of infinitesimal thickness) separating two bulk homogenous liquids [31]. Defay et al. [32] modified Young's initial ideas and proposed that the microscopic properties of two bulk phases are uniform until they reach such "a surface layer" of finite thickness. Defay et al. [32] also claim that if the detailed forces were known at the interface, in principle the surface of tension (or interfacial tension) can be identified unambiguously. However, the greatest success in describing the solid/liquid interface certainly belongs to Gibbs, who successfully applied thermodynamics to interfaces.

2.1.2 Gibbs definition

In 1878, J. W. Gibbs [3] provided a general formalism for understanding the bulk properties of interfaces; this approach has formed the basis of many theoretical and experimental techniques to investigate interfaces through thermodynamics [33,34]. When two bulk phases (solid and liquid) of a mono-component system are in contact, it is assumed that the environment at the interface is different from either of the two bulk phases. Although there may be some density and local pressure variations in the interfacial region, thermodynamics can be used to characterize the interface. A thermodynamic treatment begins by imagining an arbitrary dividing surface separating the two bulk phases [6]. The thermodynamic parameters of the two bulk phases are then uniform up to the dividing surface of the interface. To enable a derivation of a result for the single-component system, the extensive properties for a multi-component system are re-expressed as

$$E = E_{sol} + E_{liq} + E_{int}, \tag{2.1}$$

$$V = V_{sol} + V_{liq} + V_{int}, \tag{2.2}$$

$$S = S_{sol} + S_{liq} + S_{int}, \tag{2.3}$$

and

$$N^i = N^i_{sol} + N^i_{liq} + N^i_{int}. \tag{2.4}$$

where E is the energy, V is the volume, S is the entropy and N^i the number of particles. In the above expression the subscript *int* indicates properties of the interface, *sol* the solid and *liq* the liquid regions. The work required, δw, to form a unit area of interface, δA, defines γ, the excess interfacial free energy, where

$$\delta w = \gamma \delta A. \tag{2.5}$$

Chandler [36] has pointed out that besides defining the surface tension (or interfacial excess free energy) as Helmholtz free energy per unit area, the definition of γ also can be considered the force constant in the restoring force that restricts the increase in the surface area.

Using the above definitions, the interfacial region has an interfacial excess total energy, e, and entropy, s, associated with it. These quantities are derived from the Euler Equation [35],

$$\gamma = e - Ts - \sum \mu_i \Gamma^i, \tag{2.6}$$

when the excess interfacial volume is zero. In Equation 2.6, Γ^i is the surface excess number of particles of type i, T is the temperature and μ_i is the chemical potential of particles of type i.

For a system at thermal and chemical equilibrium, Gibbs showed that the chemical potential of the i^{th} component in both the solid and liquid phases will be equal, along with the temperatures. Since the excess Helmholtz free energy, f, is given by

$$f = e - Ts, \tag{2.7}$$

and the excess Gibbs free energy, g, is given by

$$g = \sum_i \mu^i \Gamma^i, \tag{2.8}$$

Equation 2.6 now becomes

$$\gamma = f - g. \tag{2.9}$$

The choice of the location for the dividing surface between the bulk phases will dictate the numerical values of the thermodynamic parameters. For a single-component system,

Gibbs then assigned the dividing surface to a position where Γ is zero. This simplifies Equation 2.9 to

$$\gamma = f \ . \tag{2.10}$$

Equation 2.10 is an expression for the interfacial excess free energy for a single-component system.

The Gibbs definition provides a clear account of applying thermodynamic ideas to the interface, despite containing no information pertaining to microscopic interfacial structure or how such a structure at the interface will correlate with the interfacial energy. Clearly, Defay et al. [32] have noted, if the (detailed microscopic) forces at the interface were known then the position and nature of the interface could be characterized. In Chapter 3, the definition of the interface, a key issue in this thesis, will be further explored. Only after the microscopic structure of the solid/liquid interface is made lucid, will its role in crystal growth be understood.

At present, there is not a generally accepted molecular theory of the solid/liquid interface and therefore of crystal growth. The next section will explore theoretical attempts to understand the phenomena of crystal growth through a range of varied microscopic theories and models .

2.2 SURVEY OF RELEVANT MICROSCOPIC THEORIES AND MODELS

2.2.1 Introduction

Crystal growth from the liquid state has been of interest for more than a 100 years, both from a fundamental [3,37] and applied point of view [38,39]. Because of the

significance of the topic there have been numerous attempts to offer detailed explanations through models and theories of crystal growth phenomena [37] and the general discussions of crystal growth are voluminous [40,41,42]. However, in the following discussions only those theories relevant to this thesis will be presented. Many of the ideas presented are generally developed from solid/vapour crystal growth considerations, since more information has been available from such systems. The following discussions will highlight relevant issues of the solid/liquid interface and its intrinsic role in crystal growth.

One of the early approaches to crystal growth were surface energy theories. These trace their origins to the postulation of Gibbs [43] and Curie [44], which, simply stated, assumes that the shape of the growing crystal is dictated by the minimization of the surface energy (this assumption is true provided the crystal is in equilibrium with its surroundings at constant temperature and pressure). The crux of this idea has been supported by Wulff [45], who showed that the equilibrium shape of a crystal is related to the free energies of the surface. Subsequently, Laue [40] added that all possible faces must be taken into account to determine the crystal face with the minimum surface free energy. Currently, surface energy theories of crystal growth [40] appear not to be generally accepted. Although the ideas from these theories are often used in predicting equilibrium morphologies, in applying continuum theories (discussed in this chapter) and in predicting preferred growth directions (and crystal habits), their success is still mixed [46]. In addition, the determination of surface free energies (interfacial free energies) and their role in crystal growth has still not been fully understood [45].

Another approach has been to describe the general thermodynamics of the interfacial system. Since it is well known that the process of crystallization is accompanied by the liberation of heat due to the latent heat of crystallization, the rate of heat transfer from the crystal face to the melt or liquid is thus an important consideration. As a result, the surface of the melt is believed to be at a higher temperature than the melt in some cases. If the temperature of the solid/liquid interface is denoted by T_i and the temperature of the melt given by T, the rate of removal of heat resulting from an undercooling $(T_i - T)$ close to the interface is given by

$$\frac{dq}{dt} = \frac{\kappa}{x_e} A(T_i - T), \tag{2.11}$$

where κ is the thermal conductivity and x_e the effective thickness for the transfer of heat [40]. Tamman [47] has also provided an expression for the maximum rate of crystallization which can be observed at a temperature higher than that required for maximum nucleation. The maximum rate is predicted to occur at a melt temperature T, given by

$$T = T_m - \frac{\Delta H_{cryst}}{c_m}, \tag{2.12}$$

where T_m is the melting point, and ΔH_{cryst} is the heat of crystallization and c_m is the mean heat capacity of the melt. Equations 2.11 and 2.12 are marginally successful in reproducing the behavior of a few different systems under varying conditions [40]; the lack of success suggests much more is occurring at the interface giving rise to a clamant need for a detailed account of the surface or interface of a crystal to be undertaken.

A theory of crystal growth that incorporates surface processes of a crystal was first suggested by Volmer [48]. He reasoned that growth of a solid from vapour occurs at

the surface of the solid by an adsorbed layer of atoms or molecules for a given crystal. Other central contributors to this notion include Brandes [49], Stranski [50] and Kossel [51]; Stranski and Kossel's work now feature prominently in modern discussions and theoretical developments in solid/vapour growth [52]. In this model of crystal growth, atoms or molecules close to the crystal (vapour, liquid or melt) will attach themselves to positions on the surface where the attractive forces are greatest. In this regard, the interface is considered to contain distinct sites; Figure 2.1 shows the step, ledge, terrace and kink model of a crystal surface. These different sites have distinct energies associated with them. Crystal growth is believed to occur with the attachment of atoms on a surface that leads to a step-wise build up of the layer until the whole surface is completed (for a detailed discussion see ref [41]). The process is repeated with the formation of a critical nucleus of atoms or molecules, which serves an important function by providing new reactive sites.

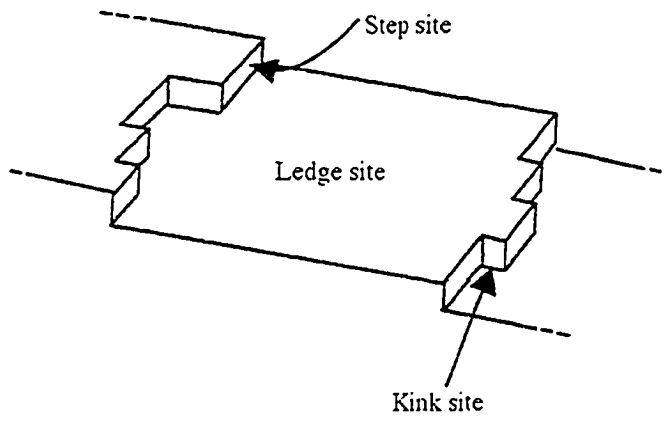

Figure 2.1 A schematic of a three-dimensional crystal surface, showing a ledge (terrace) site, a step site and a kink site (adapted and modified from ref. [53] fig. 4.4, pg. 28).

This mechanism of the growth of crystals appears in reality to be valid for only a few systems [42]. Furthermore, imperfections of the crystal structure always occurred to some degree. One particular type of growth imperfection, the screw dislocation (shown in

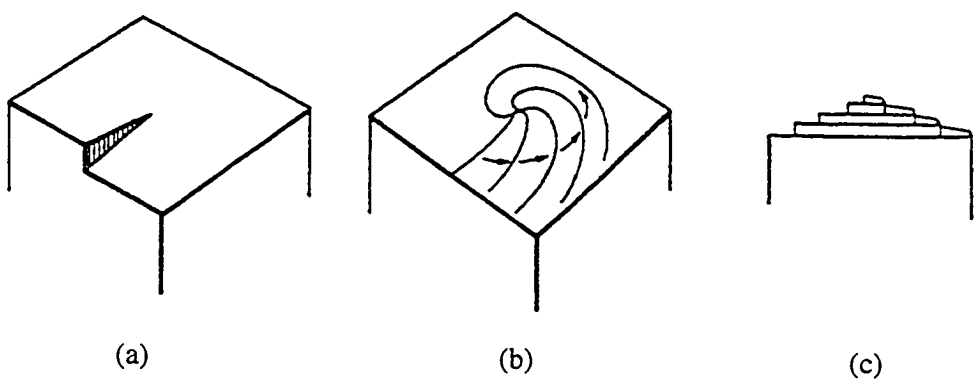

Figure 2.2 The schematic diagram illustrates the development of a growth spiral which starts from a screw dislocation. (a) A screw dislocation, (b) movement of the growth spiral, (c) final appearance of a growth spiral (adapted and modified from ref. [40] fig. 5.7, pg. 115)

Figure 2.2) is more important than others. Frank [55] proposed that the existence of such a screw dislocation circumvents the need to invoke the formation of a two dimensional nuclei in layer-by-layer crystal growth. The mechanism of crystal growth, for this model, begins with the formation of a screw dislocation followed by the attachment of more particles at a constant rate (the step grows at some constant linear velocity); the angular velocity associated with various points in the step is different causing the step to twist into a spiral as shown in Figure 2.2(b). This mechanism of spiral growth and related surface growth theories were introduced in the landmark publication of Burton, Cabrera and Frank [56]. These growth spirals have been observed on different length scales and are observed in vapour and solution crystal growth [39]. The rate of growth of the spiral

growth mechanism is $R \propto \Delta T^2$ [53]. Growth spirals have been observed in macroscopic samples of polycrystalline ice for example [57], yet their formation and link to microscopic mechanisms is far from understood due to the lack of information on the solid/liquid interface.

2.2.2 Wilson-Frenkel theory

The theory formulated by Wilson [58] and Frenkel [59], one of the earliest theories concerned with growth of a crystal from its melt, has been reasonably successful. Compared to other models of growth, this model assumes that growth occurs at any point on the crystal via the arrival of an atom from the liquid. The implicit assumption here is that the interface must be "rough" for every site to be a possible growth site. Thus, the calculated growth rate is derived from the rate that arriving atoms become solid at the interface. This type of growth is defined as 'continuous' growth.

At equilibrium, the interface is assumed to have equal rates of atoms leaving the surface and sticking to the surface. The net growth rate, R is then given by

$$R = R_F - R_M, \tag{2.13}$$

which is the difference between the freezing, R_F, and melting, R_M, rates. If the activation free energies for the solid and liquid phases are given by Q_S and Q_L, respectively, then the rate can be given in an exponential form with an explicit temperature dependence,

$$R = R_F^0 \exp\left(-\frac{Q_L}{k_B T}\right) - R_M^0 \exp\left(-\frac{Q_S}{k_B T}\right). \tag{2.14}$$

At the melting point T_m, R = 0, and by using

$$L = Q_S - Q_L \tag{2.15}$$

Equation 2.14 under equilibrium conditions becomes

$$\frac{R_F^0}{R_M^0} = \exp\left(\frac{-L}{k_B T_m}\right). \tag{2.16}$$

Replacing R_M^0 in Equation 2.14 with Equation 2.16, the following result is obtained

$$R = R_F^0 \exp\left(-\frac{Q_L}{k_B T}\right)\left[1 - \exp\left(\frac{L}{k_B T_m} - \frac{L}{k_B T}\right)\right]. \tag{2.17}$$

If $\Delta T = T_m - T$, at small undercoolings, $\frac{L\Delta T}{k_B T_m T} << 1$, the Wilson- Frenkel Equation is given by

$$R = R_F^0 \exp\left(-\frac{Q_L}{k_B T}\right)\frac{L\Delta T}{k_B T_m T}. \tag{2.18}$$

Q_L in earlier formulations of this expression was related to the self-diffusion coefficient, D, which is in turn inversely proportional to the viscosity, η, given by the Stokes-Einstein Equation [60,61],

$$D = \frac{k_B T}{6\pi\eta a}. \tag{2.19}$$

This implies that the rate, at all undercoolings, can be expressed as

$$R \propto \frac{1}{\eta}\left[1 - \exp\left(\frac{L\Delta T}{k_B T_m T}\right)\right]. \tag{2.20}$$

In the most recent form of the Wilson-Frenkel Equation, L is replaced with a latent heat of fusion per atom, l, which is an experimentally measured quantity [62]. The modified Equation is given as

$$R = f_e d \frac{D_s}{\lambda_d^2}\left[1 - \exp\left(\frac{l\Delta T}{k_B T_m T}\right)\right], \tag{2.21}$$

where d is the interlayer spacing, λ_d is the diffusional mean free path and f_e is the effectiveness factor, which is a statistical term that accounts for the probability of incorporation into the crystal. Equation 2.21 is believed to hold for systems close to equilibrium. Another formulation of the Equation 2.21 is due to Jackson [63] who included an entropy factor to obtain

$$R = f_e d \frac{D}{\lambda_d^2}\exp\left(-\frac{\Delta S}{k_B}\right)\left[1 - \exp\left(\frac{l\Delta T}{k_B T_m T}\right)\right]. \tag{2.22}$$

Jackson's modification was used by Grabow et al. [64] who demonstrated in a simulation study of silicon solidification and melting that Equation 2.22 performed better than the unmodified Equation 2.21. Although the Wilson-Frenkel treatment contains microscopic notions in its construction (like diffusion barriers, competing processes and probabilistic terms) to account for microscopic growth, it is still essentially a thermodynamic approach. The theory is not amenable to high growth rates and may be missing other still unknown critical factors.

2.2.3 Jackson theory

The Jackson theory of the solid-liquid interface [65,3], though simple, has had some success in predicting interfacial properties as it explicitly incorporates some microscopic details of the interface. In simplifying this approach, several approximations are made in this model. Jackson proposed a two-level model of the interface that takes into account only nearest neighbour bonds in the solid and is based on a simplified Bragg-Williams statistical model [66], where molecules are assigned mean rather than

individual properties. The starting point of this model assumes that the interface is atomically smooth or singular; atoms are then added to this single layer until a complete monolayer is formed. The surface now has become a layer thick and is atomically smooth again; the total number of atoms in a monolayer is given by N_m.

The formation of bonds in this model are of two types: normal bonds between adatoms and the solid/liquid interface, given as the change in internal energy as an atom is attached to the surface, ΔE_0, and in plane bonds among adatoms, given as the change in internal energy associated with the interaction of the atom with other adatoms on the monolayer, ΔE_1. The total energy, ΔE_{tot} is given by the sum of these two contributions. Similarly, the entropy change also consists of two terms, the first a change upon solidification and the second the entropy of mixing at the interface. Again the total entropy, ΔS_{tot} can be expressed as a sum of these two contributions. Jackson then writes that the total free energy change associated with adding N_{ad} adatoms to the solid/liquid interface is given by

$$\Delta G_{tot} = \Delta E_{tot} - T\Delta S_{tot} + P\Delta V. \tag{2.23}$$

If the number of "half bonds", z_η , in the bulk crystal structure is essentially the coordination number of the crystal, then z_η will be given by the sum of the maximum number of in plane bonds, η_1, established between pairs of adatoms plus twice the number of normal interface bonds, η_0, that develops between the adatom and the interface.

In order to derive an expression for ΔG_{tot}, Jackson begins with the change in internal energy, L_0, associated with the transfer of one atom from the bulk liquid to a solid site on a singular surface for N_{ad} given by

$$\Delta E_0 = -L_0\left(\frac{2\eta_0}{z_\eta}\right)N_{ad}, \tag{2.24}$$

where the change in internal energy is given as a fraction of normal bonds over the total number of bonds. The factor of 2 accounts for the internal energy change that a solid atom will undergo with the addition of an atom from the liquid. The second energy term,

$$\Delta E_1 = -L_0\left(\frac{2\eta_1}{z_\eta}\right)\left(\frac{N_{ad}}{N_m}\right)\frac{N_{ad}}{2}, \tag{2.25}$$

involves the internal energy change with the surface adatoms and also accounts for any adatom site with on average N_{ad}/N_m nearest neighbour adatom sites filled. Then the total energy can be given by,

$$\Delta E_{tot} = -L_0\left(\frac{2\eta_0}{z_\eta}\right)N_{ad} - L_0\left(\frac{2\eta_1}{z_\eta}\right)\left(\frac{N_{ad}}{N_m}\right)\frac{N_{ad}}{2}, \tag{2.26}$$

The total entropy is expressed as [65],

$$\Delta S_{tot} = -\frac{\Delta H_f}{T_e}N_{ad} + k_B \ln\frac{N!}{N_{ad}!(N_m - N_{ad})!} \tag{2.27}$$

where in the first term T_e is the equilibrium temperature for the phase change and the second term corresponds to the configurational entropy. Ignoring the $P\Delta V$ term in Equation 2.25 (considered insignificant at ordinary pressures) and substituting Equations 2.26 and 2.27 for ΔE_{tot} and ΔS_{tot}, respectively, the total free energy change becomes

$$\begin{aligned}\Delta G_{tot} = &-L_0\left(\frac{2\eta_0}{z_\eta}\right)N_{ad} - L_0\left(\frac{\eta_1}{z_\eta}\right)\frac{N_{ad}^2}{N} \\ &-T\left[-\left(\frac{L_0}{T_e}\right)N_{ad} + k_B N \ln\left(\frac{N}{N - N_{ad}}\right) + k_B N_A \ln\left(\frac{N - N_{ad}}{N_{ad}}\right)\right]\end{aligned}. \tag{2.28}$$

Simplifying the third term in Equation 2.28 using Stirling's approximation, rearranging and making the assumption that $T = T_e$, one can obtain

$$\frac{\Delta G_{tot}}{Nk_B T_e} = -\alpha\left(\frac{N_{ad}}{N}\right)\left(\frac{N_{ad}}{N} + \frac{2\eta_0}{\eta_1}\right)$$
$$+\alpha\left(\frac{N_{ad}}{N}\right)\left(\frac{z_\eta}{\eta_1}\right) - \ln\left(\frac{N}{N-N_{ad}}\right) - \left(\frac{N_{ad}}{N}\right)\ln\left(\frac{N-N_{ad}}{N_{ad}}\right) \quad , \tag{2.29}$$

where the α factor is defined as

$$\alpha \equiv \frac{\Delta S_f}{R_g}\left(\frac{\eta_1}{z_\eta}\right). \tag{2.30}$$

The first factor in Equation 2.30 is the thermodynamic factor (where R_g is the gas constant) and the second factor is a geometric term where again $z_\eta = 2\eta_0+\eta_1$ for the interface model.

The dependence Equation 2.29 on the ratio N_{ad}/N is shown in Figure 2.3. If $\alpha < 2$, the ΔG_{tot} is a minimum at $N_{ad}/N_m = 0.5$ and the solid/liquid interface is considered rough. Conversely, if $\alpha > 2$ the ΔG_{tot} is a maximum at $N_{ad}/N = 0.5$ and the interface is considered smooth. Consequently, the solid/liquid interfacial energy can be considered an excess energy and/or deficient entropy present at the interface. In this way, the structure of the interface may be approximately characterized by the so called "alpha" factor with $\alpha > 2$ described as atomically smooth with few vacancies or adatoms, or $\alpha < 2$ described as atomically rough with many vacancies and adatoms. The benefit of the "alpha" factor is embodied in its correlation with the complexity (roughness) of the crystal interface. Another observation that can be made from the findings of this model (from inspection of Figure 2.3) is that rougher interfaces ($\alpha < 2$) have lower free energies than smoother interfaces.

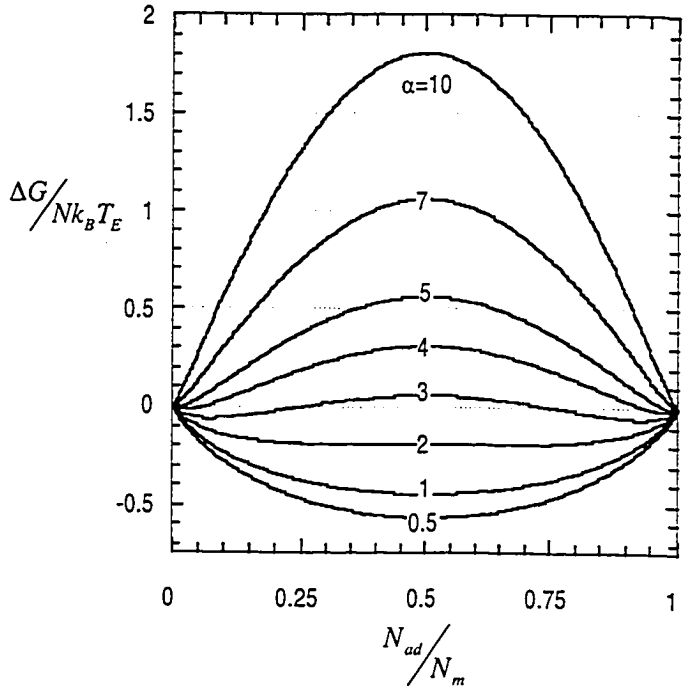

Figure 2.3 The excess free energy, $\Delta G/Nk_BT_E$, plotted as a function of the fraction of occupied sites, N_{ad}/N_m. The "alpha" factor shows that the roughening transition occurs at $\alpha = 2$.

2.2.4 Temkin's model

The Temkin model [67,3,53] is a slightly more advanced model than that of Jackson. It is an n-layer model, where the number of layers itself is considered to be a variable to be used in the minimization of the free energy. The Temkin model holds for applications to solid/fluid interfaces, where the fluid can be considered a vapour, any solution or a melt. Figure 2.4 shows the solid and liquid phases represented as blocks of equal size. Furthermore, there are no restrictions on where the interfacial region is located (which is an important distinction from the Jackson model). The free energy, $G(N,C_n,T)$ is then given by [42]

$$G(N,C_n,T) = -kT \ln Z(N,C_n,T), \tag{2.32}$$

which depends on the configuration of atoms at the interface through the term

$$C_n = N_{solid}/N \tag{2.33}$$

for the fraction of solid blocks and $(1- C_n)$ for the fraction of fluid blocks. In Equations 2.32 and 2.33 N is the total number of blocks (particles), T the temperature and Z is the partition function. The bond energies in this model system stem from the contributions of three interaction energies: sides of each solid block, ϕ_{ss} sides of each fluid block, ϕ_{ff}, and sides of fluid and solid block, ϕ_{sf}. The final result from this approach, with the explicit partition function evaluated and simplified, provides an equation of the form

$$\frac{\Delta G}{Nk_BT} = \frac{\Delta\mu}{k_BT}\left[\sum_{n=-\infty}^{0}(1-C_n) - \sum_{1}^{\infty}C_n\right] + \gamma_c\sum_{n=-\infty}^{\infty}C_n(1-C_n) + \sum_{n=-\infty}^{\infty}(C_{n-1}-C_n)\ln(C_{n-1}-C_n), \tag{2.34}$$

where $\Delta\mu$, is the chemical potential difference of atoms in the different phases and γ_c includes the interaction energies of the blocks. At equilibrium $\Delta\mu = 0$, and it can be shown that γ_c equals the α term in Jackson's model. In this case Temkin's model reduces to Equation 2.29 (Jackson's model) if a single disordered layer is considered. The α (γ_c) value from the Temkin model has very similar interpretations in predicting whether an interface is smooth or rough, although the transitions from smooth to rough are less well defined than in the Jackson model.

Although the Temkin and the Jackson models are rather simple models, they are successful in predicting the roughening transition that is the effective temperature below which the interface is smooth and above which the interface is rough on an atomic scale. In fact, in modern day constructs used to describe crystal growth, Jackson's α parameter has an important place. It can indicate the relative ease of the production of surface sites with many favourable binding sites required for the formation of a layer. Consequently, a

low α parameter indicates an expedited growth rate as available sites are present.

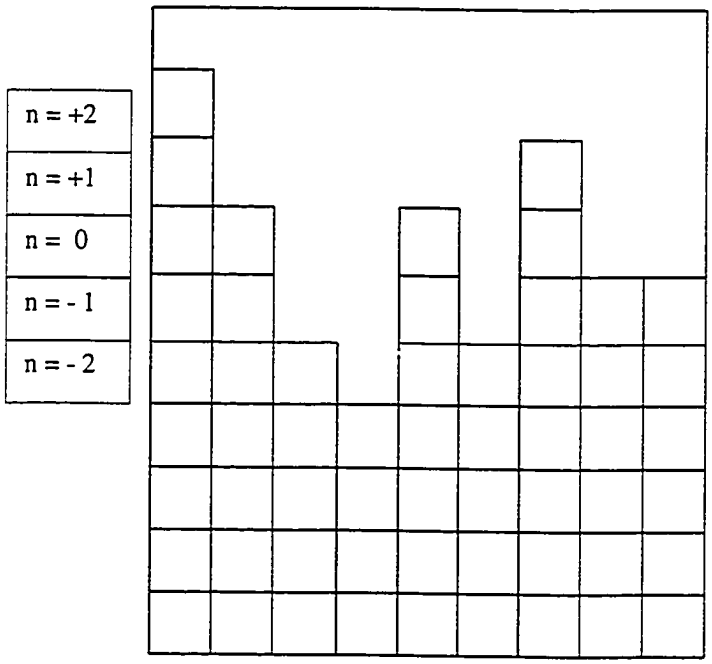

Figure 2.4 A schematic of the Temkin model, showing 5 transition layers at the interface. The index n indicates the positions of the solid blocks. Only solid blocks are shown.

Conversely, a high α parameter retards growth rates and mechanisms that create favourable sites are envisaged for crystal growth to commence. However, it should be pointed out that the microscopic details of the Temkin or Jackson models have not been confirmed experimentally [3,45,52].

2.2.5 Density Functional theory (DFT) and other continuum methods

The use of DFT applied to solid/liquid interfaces was pioneered by Haymet and Oxtoby [68] and Klupsch [69] independently. The general framework for this theory relies on statistical mechanics, where the free energy, Ω, of the grand canonical ensemble

is related to a given spatially dependent single particle density, $\rho(\mathbf{r})$. The use of the grand canonical ensemble originates from the different densities associated with the bulk solid and liquid. A system at a given constant temperature, T, with an external single-particle potential, $v(\mathbf{r})$, and at a fixed chemical potential, μ, is treated as a unique functional, $F[\rho(\mathbf{r})]$, of the density distribution, and is expressed as

$$\Omega[\rho(\mathbf{r})] = F[\rho(\mathbf{r})] + \int dr[v(\mathbf{r}) - \mu]\rho(\mathbf{r}). \tag{2.35}$$

$F[\rho(\mathbf{r})]$ is the intrinsic Helmholtz free energy functional and is made up of two parts

$$F[\rho(\mathbf{r})] = F_{ideal}[\rho(\mathbf{r})] + F_{excess}[\rho(\mathbf{r})]. \tag{2.36}$$

The ideal term, $F_{ideal}[\rho(\mathbf{r})]$ (or the ideal-gas free energy functional), represents in the absence of internal interactions the free energy of a non-uniform system and is known exactly. It can be explicitly expressed as

$$F_{ideal}[\rho(\mathbf{r})] = \beta^{-1} \int dr \rho(\mathbf{r})\{\ln \rho[(\mathbf{r})\Lambda^3] - 1\}, \tag{2.37}$$

where $\beta = 1/k_B T$ and Λ denotes the de Broglie wavelength (thermal wavelength). In contrast, the excess free energy contribution, $F_{excess}[\rho(\mathbf{r})]$, contains the particle interactions and is only approximated in calculations. Its true functional form is unknown [70]. With a reasonable approximation of the excess free energy, the total free energy given by Equation 2.35 can be minimized.

The challenge in using DFT for describing the solid/liquid interface is to furnish a reasonable free energy functional form in such calculations; this can take the form of perturbative or non-perturbative approximation methods. In the perturbative approach, the excess free energy around the homogeneous bulk density is treated as a Taylor series expansion in powers of the density deviation. The expansion involves all the higher order correlation functions of the fluid and it is generally found that correlation functions

beyond two particle interactions are unknown. If the free energy is locally dependent on one or more order parameters, sharp interfaces results. In order to correct for this unphysical result, truncations at second order are applied in most practical applications [71]. Truncation at the lowest order gives the square gradient approximation. However, these truncations introduce errors to the calculations. For example, when the density change becomes too abrupt, the model fails. To overcome this problem, non-perturbative approaches, which incorporate the two particle correlation functions and higher terms, are applied in an approximate manner [72]. As an example, the weighted density approximation [73] is based on the notion that the free energy should be evaluated at the weighted density averaged over the immediate surroundings rather than at the instantaneous local value of the density, which changes very rapidly through space. However, the results pertaining to solid/liquid interfaces obtained in this manner are inconsistent with computer simulation results [74]; the choice of the excess free energy functional gives reasonable results in some cases and not in others [35]. In addition, DFT has not been successful in describing detailed microscopic crystallization [75].

Other phenomenological continuum methods use coupled differential equations based on the change of an order parameter that is a functional of the free energy. This functional resembles the expression for the square gradient approximation and are sometimes called the Landau-Ginzburg or Cahn-Hillard Equations [76,77]. The chosen order parameter could involve the density or some other change that distinguishes the phases. As an example, Harrowell and Oxtoby [78] used such a method to demonstrate that for two surfaces with the same surface tension, different growth rates are calculated due to the difference in the underlying crystal structure results.

If DFT and the continuum methods discussed so far can be considered to be intermediate between macroscopic and microscopic considerations, then microscopic solvability theory [79] neglects the interfacial structure altogether, thus excluding microscopic behaviour. This approximation is rationalized by arguing that the pattern formation at the face of a growing crystal (micrometer or larger) is much larger than the scale of the interface (nanometer). In a related approach, called phase field theory, the interface structure is also neglected and the phase field variable changes smoothly from 1 to 0 as the interface is crossed [80]. These approaches have resulted in micro and macro scale studies of dendrite and pattern formation [81]. As these theories do not specifically deal with microscopic growth conditions, they will play only a tangential role in the discussions in subsequent chapters.

2.2.6 Conclusions

The theories discussed above address micro, meso and macroscopic crystal growth and interfacial behaviour. From the models and theoretical approaches surveyed it is clear that theoretical modeling of the solid/liquid interface contains much complex behaviour that requires further investigation. A comprehensive account of the interface must include the interfacial energy, latent heat of crystallization, structural inhomogeneities and fluctuations of the interfacial structure. In fact, the importance of such fluctuations has resulted in the application of renormalization group techniques to fluctuations at the interface [82]. None of the approaches discussed in this chapter have considered all these effects in their interfacial descriptions. As was also discussed, these theoretical descriptions have had varying success in describing different properties of

interest. For example, Jackson's [65] and Temkin's [67] methods have led to the understanding of the phenomenon of the roughening transition where lateral growth seems to be transformed to continuous growth. When the surface is rough, continuum theories have shown fluctuations to be important. However, theory needs to be guided by experiments that may offer more clues and cues from which better theoretical approaches can be developed. The final section of this chapter will examine the use of some important experimental techniques to probe the solid/liquid interface.

2.3 IMPORTANT EXPERIMENTAL TECHNIQUES

2.3.1 Select experimental techniques

There are many experimental techniques used to explore liquids [83,84] and solids directly [85,86]. Moreover, over the last 20 years, the burgeoning of surface characterization techniques has provided much information about the solid/vapour and solid/vacuum interface [87]. In stark contrast, there have been few experimental techniques applied specifically to look at the solid/liquid interfacial region and to elucidate the equilibrium interface or microscopic freezing and melting behaviour [87]. In this section some important techniques are described briefly.

X-ray techniques

X-rays have been an effective tool in providing detailed descriptions of crystal and liquid structure [84,86]. The wavelengths of X-rays, typically 0.1 nm (compared to about 0.3 nm for an atomic spacing in crystals), are thus able to infer the structure of a crystal by the diffraction of the X-rays, which provides information on internal symmetry

[88]. For liquids, the diffraction patterns show short-range spatial correlations characteristic of liquid structure. The use of X-rays to probe surfaces became a reality with the availability of powerful synchrotron radiation sources, as the signal from a surface is of order 10^6 less than from a bulk [89]. Therefore X-rays from synchrotron radiation can access the interface of a solid/liquid system [89]. The key property that X-ray scattering of interfaces probes is the distribution of the electron density profile of the liquid at/near the interface. This distribution can be obtained from the X-ray intensity, $I(\mathbf{k})$, given by the relationship

$$I(\mathbf{k}) \propto \int \left| \rho(\mathbf{r}) \exp(i\mathbf{q} \cdot \mathbf{r}) d\mathbf{r} \right|^2 , \tag{2.38}$$

where $\rho(\mathbf{r})$ is the local electron density at position $\mathbf{r}$, $\mathbf{q} = \mathbf{k}_f - \mathbf{k}_i$ with $\mathbf{k}_i$ the incident wave vector scattered elastically from a material and $\mathbf{k}_f$ the scattered wave vector that is detected. A typical experiment involves specular reflection of the X-rays from the interface at varied angles. The intensity is related to the structure factor, $S(\mathbf{k})$, which in turn under Fourier transformation provides the $g(\mathbf{r})$ [83,84] as shown by the relationship

$$S(\mathbf{k}) = 1 + \rho(\mathbf{r}) \int \exp(-i\mathbf{k} \cdot \mathbf{r}) g(\mathbf{r}) d\mathbf{r} . \tag{2.39}$$

The microscopic details of the interaction of the liquid with the crystal may change the relative stability of different growth faces, which may affect changes [90] in growth rates and local concentration gradients. X-ray scattering can offer insights into this behaviour since it can detect the ordering in the liquid (layer ordering) without interfering with the processes inherent at the interface. Such layering over a small distance has been observed in a number of experimental systems [91]. The direction of layer ordering is perpendicular to the surface, but lateral ordering is also believed to exist. The lateral ordering is expected to be much weaker as the liquid near the interface is

under the influence of the two-dimensional periodic potential of the solid [92]. However, it is possible in principle to uncover the full ordering characteristics of the liquid near the crystalline interface [93]. Yet, the effects are weak and the signal-to-background ratio in an experiment is often poor due to the presence of the liquid, which implies that the thinner the liquid portion of the sample, the easier it will be to carry out the experiment. The experiments that have provided some of the most detailed information of this type have been on a simple model system [94,95]. Furthermore, there are other complicating factors in the growth of crystals, including impurities that may be present in the liquid and possible pre-ordering of the growth units that may be observed at the interface [96,97].

Transmission Electron Microscopy (TEM)

In transmission electron microscopy, a high-energy beam of electrons is appropriately accelerated and focused on a sample [98,99]. The wavelength of the electron beam is much smaller than that of visible light. Images formed in this manner yield magnifications of details up to 10^6 X with resolution better than 1 nm [100]. The images generated can be observed with fluorescent screens, on photographic film and with a CCD camera linked to a computer. Furthermore, the analysis of the X-rays produced by the interaction between the accelerated electrons with the sample allows the determination of the elemental composition of the sample with high spatial resolution. In general, the shorter the wavelength, the better the resolution. For crystals with interplanar spacing greater than 0.12 nm, crystal structure, symmetry and orientation can be determined. A TEM is able to image the atomic arrangement of a single crystal and to identify the Burgers vector for a dislocation. In addition, structural examination of

defects, including stacking faults, interstitials, precipitates and vacancies, is possible. In a related technique called scanning electron microscopy (SEM) [98], as with TEM, samples are subjected to a beam of electrons, but instead of the electrons being transmitted through the sample, the beam is "scanned" across it creating a 3-dimensional image on a computer. The mapped topography is useful in surface structure analysis, it allows such topographs to be provided much quicker, however the resolution may be poorer. In addition, a large field of observation can be acquired at a time, which is another key feature of SEM [101]. Yet, no microscopic observations of crystal growth or solid/ liquid interfaces have been achieved with this technique.

The use of TEM to investigate solid/liquid interfaces is thus far limited to a few model experimental systems. As an example, Al-Si liquid with an Si solid [102] has been investigated. Observations of a transition layer at 2 nm resolution were made, with growth rates measured at 20 nm/s. Partial ordering of the liquid in front of the interface was also observed, with two-dimensional ordering within the first layer of the liquid. The authors observed cooperative organization, but did not clarify the mechanism involved. They mentioned that structural and compositional changes are strongly correlated at the interface as well. They also attempted to identify the interfacial position from the available data. The timescales of their measurements were limited to the microsecond range.

Scanning Probe Microscopies (SPM)

In scanning tunneling microscopy (STM), an atomically sharp metallic tip is brought very close to a conductive sample [103]. Changing the position in the lateral (x,y) plane allows continuous scans across the sample surface and by changing the

vertical (z) position it allows for the change of the desired tip-sample distance. When that distance is small enough (10 - 0.1 Angstroms) and voltage is applied between the sample and the tip, a tunneling current (1 - 0.1 nA) can be observed. This current is dependent exponentially on the tip-sample separation. Thus, if a feedback loop is used for the adjustment of the vertical position to keep the current constant, the tip-sample distance can be kept constant with relative ease. Alternatively, the z-coordinate could be held constant and the tunneling current recorded, the current being essentially proportional to the density of electronic states in the sample. The first method essentially maps constant density of states contours and the second method maps the actual density of states. The contrast in STM images reflects both topography and electronic effects. In solid/liquid interfacial studies, this technique is used to investigate the electrode/electrolyte surface [104], as well as mesoscopic scale systems [105]. However, its application to a buried solid/liquid interface has not yet been successful. In addition, van Hove [87] has pointed out in a review on atomic scale surface determination that the imaging mechanism in STM applied to solid/liquid interfaces "is not clear" and thus findings from detailed analysis could be questionable.

A related technique, atomic force microscopy (AFM), can image non-conductive materials [102]. Moreover, this technique can provide details on the topography of an atomic or molecular surface. The resolution of AFM is up to 10 pm and images from samples in air and liquids can be obtained. An extension of AFM is its use in Phase Imaging, this provides nanometer scale information about surface topography often missed by other SPM techniques. This is achieved by mapping the phase of the cantilever oscillation during an AFM scanning mode (Tapping Mode), detecting such properties as

surface composition, adhesion, friction and viscoelasticity. In addition, AFM has been used to provide images of the solid side in solution growth [106]. Despite its sensitivity it has not provided any mechanisms or dynamics of crystal growth, it is thus limited to surface investigations.

Non-linear optical techniques

Second harmonic generation (SHG) [107,108] is a second-order non-linear optical process, where two laser beams at the same frequency, ω, impinge on a sample, simultaneously interacting and generating a sum frequency in a non-linear medium, 2ω. In sum frequency generation (SFG), the two laser beams have different frequencies ω_1 and ω_2, and generate radiation at the sum frequency, $\omega_T = \omega_1 + \omega_2$. As second-order non-linear optical processes, these methods are electric-dipole forbidden in a centrosymmetric medium, but allowed at interfaces where the centrosymmetry is broken [109]. The induced non-linear polarization originates from the dominant contribution term that results from the interaction of electric-dipoles with the optical electric field. Therefore the light that radiates at SH or SF frequency is generated exclusively from the layers that are associated with the interface. Consequently, the sensitivity of the SHG and SFG techniques are not restricted by the optical penetration depth, as other more conventional optical techniques are [110]. This characteristic makes SHG and SFG sensitive to the properties of interfaces, especially the solid/liquid interface.

Although SHG and SFG have not had the projected success that was predicted for their use at the solid/liquid interface, they have been used to describe molecules at solid/water interfaces [111] and to reveal ordering at the interface of monolayers [112]. They have not been able to probe a solid/melt system nor provide microscopic details of

freezing or melting phenomena at the interface. From their few select applications, it is obvious that the use of this methodology is limited at this time.

2.3.2 Conclusions from experiments

When a crystal grows from a solution or melt, the actual growth must occur at the solid/liquid interface. For a complete understanding of the atomic-scale processes that occur, knowledge of both the crystal surface and the liquid structure near the crystal interface is of paramount importance. The liquid may influence the growth and the resulting crystal shape in various ways. From the techniques described, it has been shown that they can and have worked together in providing some key insights into the solid/liquid interface. X-ray techniques and TEM have shown ordering of the liquid at the interface next to the solid lattice layer. There appears to be some pre-freezing phenomena at the solid/liquid interface [97,101], however the authors are rather nebulous about providing any details. X-ray techniques, SFM and TEM provide only averaged images of atomic density and hence have not been able to yield dynamical information in the pico or nanosecond timescales. In contrast, SHG/SFG seem interface specific and the laser pulses are in the femtosecond timescales (which could provide fundamental dynamical information), yet no new experiments on microscopic crystal growth appear to have been performed. In fact, many of the results reported from experimental studies to date have corroborated the findings of computer simulations of atomic systems over 20 years ago: these will be reviewed in detail in the next chapter.

CHAPTER 3
COMPUTER SIMULATION

3.1 MOLECULAR DYNAMICS METHODOLOGY

3.1.1 Introduction

Computer simulation techniques in the study of condensed matter now seem commonplace with the rapid development of modern computer technology. Yet, it was only in the 1950's that two landmark pioneering publications, the first by Metropolis et al. [113] and the second by Alder and Wainwright [114], indelibly laid the foundation for the Monte Carlo method and molecular dynamics, respectively. Since then, there have been numerous advances in both methodologies [115], but the essential ideas that have given both methods their ubiquity and utility remain intact. Computer simulations have provided a bridge between the abstract theoretical construct of statistical mechanics to the macroscopic level of experimental measurements of thermodynamics. In bridging the gap of the microscopic domain of atoms and molecules to macroscopic measurements, computer simulations have contributed and continue to contribute detailed and important insights into the inner workings of particles of matter and their fascinating interactions [116].

In order to establish the connection between molecular dynamics (via statistical mechanics) and thermodynamics, consider a system of N atoms [117]. The positions and momenta of the atoms are given by $\mathbf{r}^N \equiv (\mathbf{r}_1,\cdots,\mathbf{r}_N)$ and $\mathbf{p}^N \equiv (\mathbf{p}_1,\cdots,\mathbf{p}_N)$, respectively. These can be thought of as coordinates in a $6N$ dimensional space or, more commonly,

termed phase space. A particular point in phase space can be defined by the abbreviation, $\Gamma = (\mathbf{r}^N, \mathbf{p}^N)$. Therefore, for a particular instantaneous property, A_{int}, the value can be written as the function $A_{int}(\Gamma)$. If the system evolves in time, so that Γ changes, $A_{int}(\Gamma)$ will also change as a result. The experimentally observable "macroscopic" property, A_{obs}, is then given by the time average of $A_{int}(\Gamma)$ taken over a long time interval, t_{obs}:

$$A_{obs} = \lim_{t_{obs} \to \infty} \frac{1}{t_{obs}} \int_0^{t_{obs}} A_{\text{int}}(\Gamma(t))dt. \tag{3.1}$$

The time evolution of $A_{int}(\Gamma(t))$ for a large number of molecules or atoms is rather complex, thus the time average given above can be replaced by the ensemble average for a closed system; this is the essence of the ergodic hypothesis [36]. The ensemble average can be regarded as a collection of points, Γ, where in phase space, these points are associated with a probability density distribution, ρ_{ens}, given by

$$\rho_{ens}(\Gamma) = \frac{\exp[-\beta H(\Gamma)]}{\int\int \exp[-\beta H(\Gamma)] d\mathbf{r}^N d\mathbf{p}^N}, \tag{3.2}$$

where the Hamiltonian of the system is given by

$$H(\Gamma) = \frac{1}{2m} \sum_{i=1}^{N} |\mathbf{p}_i|^2 + U(\mathbf{r}^N) \tag{3.3}$$

and $\beta = 1/kT$ for a closed system at constant temperature, T, and U the potential. A_{obs} can then be expressed as

$$A_{obs} = \sum_{\Gamma} A(\Gamma)\rho_{ens}(\Gamma). \tag{3.4}$$

The above expression may be recast by replacing ρ_{ens} by a 'weight' function, $w_{\text{ens}}(\Gamma)$, that satisfies [118]

$$\rho_{ens}(\Gamma) = Q_{ens}^{-1} w_{ens}(\Gamma), \tag{3.5}$$

with

$$Q_{ens} = \sum_{\Gamma} w_{ens}(\Gamma). \tag{3.6}$$

Q_{ens} is called the partition function, which acts to normalize the probability density. Therefore, in the canonical ensemble (constant N, V and T), the probability density is proportional to

$$\exp[-\beta H(\Gamma)], \tag{3.7}$$

with the partition function expressed in quasi-classical form given by

$$Q_{NVT} = \frac{1}{N! h^{3N}} \int\int \exp[-\beta H(\Gamma)] d\mathbf{r}^N d\mathbf{p}^N. \tag{3.8}$$

Since the partition function is a dimensionless quantity, the integral in Equation 3.8 must be divided by a parameter that contains the dimensions of phase space [119]. Planck's constant, h, is chosen for two reasons. The first being it has dimensions of a length multiplied by momentum, therefore a division by h^{3N} formally satisfies the requirement for Q to be dimensionless. The second reason is due to the uncertainty principle, where $h=dpdr$ is the element within which one is unable to be sure that the energy has varied. The 1/N! term stems from the indistinguishability of particles [15]. The appropriate connection to a thermodynamic function is through the Helmholtz free energy [120],

$$f = -\frac{1}{\beta} \ln Q_{NVT}. \tag{3.9}$$

Relationships to other thermodynamic functions are easily obtained with the appropriate differentiation.

With the connection established between statistical mechanics and thermodynamics, the link between statistical mechanics and molecular dynamics is made

through the equations of motion, particularly Hamilton's equation of motion. Formally this link is established by Liouville's theorem which states that the rate of change of phase space density, ρ, experienced by a fixed point in phase space is given by

$$\frac{\partial \rho}{\partial t} = -\sum_{i=1}^{N}\left(\dot{\mathbf{r}}_i \frac{\partial \rho}{\partial r_i} + \dot{\mathbf{p}}_i \frac{\partial \rho}{\partial \mathbf{p}_i}\right) \tag{3.10a}$$

which depends explicitly on time. However, an alternative formulation can be derived from a phase space point traveling in space, the rate of change of phase space density, ρ, in this case is now 0, after substituting Equation 3.10a in Equation 3.10b for $\partial\rho/\partial t$,

$$\frac{d\rho}{dt} = \frac{\partial \rho}{\partial t} + \sum_{i=1}^{N}\left(\dot{\mathbf{r}}_i \frac{\partial \rho}{\partial r_i} + \dot{\mathbf{p}}_i \frac{\partial \rho}{\partial \mathbf{p}_i}\right) = 0, \tag{3.10b}$$

where $\dot{\mathbf{r}}_i$ is the velocity and $\dot{\mathbf{p}}_i$ is the force. This result also satisfies the condition that at thermodynamic equilibrium the ensemble average is time independent, hence the phase space density does not explicitly depend on time [119].

3.1.2 Dynamical equations

In molecular dynamics, the time evolution of a collection of interacting atoms or molecules is followed by solving the equations of motion for each particle [115]. This motion can be described by the Newtonian equation,

$$\mathbf{F}_i = m_i \ddot{\mathbf{r}}_i, \tag{3.11}$$

where $\mathbf{F}_i \equiv -\nabla_r U(\mathbf{r}^N)$ is the force exerted on atom i, m_i the mass, $\mathbf{r}_i$ the position vector of particle i, and $U(\mathbf{r}^N)$ is the interaction potential function of atom i that includes all particles. The Newtonian equation can be written in Hamiltonian form,

$$\frac{\partial \mathrm{H}}{\partial \mathbf{p}_i} = \frac{\mathbf{p}_i}{m} = \dot{\mathbf{r}}_i \tag{3.12}$$

and

$$\frac{\partial \mathrm{H}}{\partial \mathbf{r}_i} = \frac{\partial U(\mathbf{r}^N)}{\partial \mathbf{r}_i} = -\dot{\mathbf{p}}_i. \tag{3.13}$$

Hamiltonian equations give 6N first order differential equations as opposed to Newton's 3N second order equations. In principle the latter lend themselves to more efficient algorithms to solve for the motion of individual particle trajectories. In a typical molecular dynamics simulation, the motion of a phase space point (or the trajectories of the particles) is followed in time. To allow numerical treatment, time is discretized and the equations of motion are solved (numerically) at each step in time, to provide positions and momenta for all the particles. The number of time steps can typically vary from thousands to millions, depending on the system of interest.

There are two principal techniques utilized to solve the equations of motion: the predictor-corrector and the Taylor series methods. Modifications of these two principal methods are also used [121]. All these methods allow one to obtain numerical solutions to differential equations. As an example, a general predictor-corrector algorithm is outlined below [116]:

a) at a time t, use the current positions and current velocities and their time derivatives to predict new positions and velocities at a new time ($t + \delta t$);

b) at the new positions, forces are evaluated;

c) utilizing these forces, correct the positions, velocities and their derivatives;

d) finally, variables of interest are calculated and time averages are performed; the process now iterates by returning to step a).

In this way, the dynamics in the system is evolved, one time step at a time. Phase space is adequately sampled in a typical molecular dynamics simulation after a sufficient amount of time has elapsed depending on the nature of the system and the lifetimes inherent to the properties under investigation.

3.1.3 Modifications to the equations of motion

In simulation studies, the need to investigate systems beyond constant N, V and E (which describes the microcanonical ensemble) conditions is of more practical interest. It is well known that Hamilton's equations conserve energy [61], and moving to other ensembles requires the equations of motion to be modified. One approach to accomplishing this task has been to introduce thermostats, which were originally developed to facilitate non-equilibrium simulations. The first such thermostats were introduced by Hoover [122] and Evans [123], who proposed them simultaneously and independently. Today, thermostats are routinely used in many ways for many kinds of simulation studies [121].

One approach to the theoretical framework of thermostats in molecular dynamics is to modify the equations of motion by addition of a damping or friction term. This method can be justified by deriving the equations of motion using Gauss' principle of least constraint [124]. This principle states that when a dynamical system is subjected to constraints, it will follow trajectories, which will differ minimally in a least squares sense from the unconstrained trajectories. These constraints can be considered to be on a hypersurface called the constraint plane. As an example of the use of Gauss' principle, consider a system of Cartesian coordinates and velocities at time t. The actual physical

acceleration of a function C, which is a set of accelerations as shown in Equation 3.14, corresponds to a minimum [61].

$$C = \frac{1}{2}\sum_{i=1}^{N} m_i \left(\ddot{\mathbf{r}}_j - \frac{\mathbf{F}_i}{\mathrm{m}_i} \right)^2 \tag{3.14}$$

Equation 3.14, will give 0 as a minimum when there are no constraints and the particles in the system will evolve under Newton's equations of motion. A constraint equation will be applied to Equation 3.14 to obtain the appropriate constraint relationships. As an illustration, a non-holonomic constraint equation for which the kinetic energy is fixed (i.e. constant temperature) is

$$g(\mathbf{r},\dot{\mathbf{r}},t) = \sum_{i=1}^{N} \frac{\mathrm{m}_i \dot{\mathbf{r}}_i^2}{2} - \frac{3Nk_BT}{2} = 0. \tag{3.15}$$

This enables particles in the system to conform to this fixed kinetic energy, if the kinetic energy deviates, it will be acted on in a manner that does not cause significant deviations of the trajectories. Differentiating $g(\mathbf{r},\dot{\mathbf{r}},t)$ with respect to time yields

$$\sum_{i=1}^{N} \mathrm{m}_i \dot{\mathbf{r}}_i \cdot \ddot{\mathbf{r}}_i = 0. \tag{3.16}$$

Equation 3.16 is now an acceleration form of the constraint equation, which can now account for a set of accelerations being acted on by a constraint in Equation 3.14 as shown below

$$\frac{\partial}{\partial \ddot{\mathbf{r}}_i}\left(\frac{1}{2}\sum_{j=1}^{N} m_j \left(\ddot{\mathbf{r}}_j - \frac{\mathbf{F}_j}{\mathrm{m}_j} \right)^2 + \lambda \sum_{j=1}^{N} m_j \dot{\mathbf{r}}_j \cdot \ddot{\mathbf{r}}_j \right) = 0. \tag{3.17}$$

The next step involves minimizing equation 3.17 subject to the constraint (Equation 3.16) to obtain the equation

$$m_i\ddot{\mathbf{r}}_i = \mathbf{F}_i - \lambda m_i\dot{\mathbf{r}}_i \quad , \tag{3.18}$$

where the form of the thermostatting multiplier

$$\lambda = \frac{\sum_{i=1}^{N}\mathbf{F}_i \cdot \dot{\mathbf{r}}_i}{\sum_{i=1}^{N} m_i\dot{\mathbf{r}}_i^{\,2}} \tag{3.19}$$

satisfies the kinetic energy constraint. Equations 3.18 and 3.19 are referred to the Gaussian isokinetic equations of motion. The implementation of these constrained equations of motion (that maintain a constant kinetic energy in the simulation) would require a minor modification to a standard MD program [121].

In addition to the Gaussian thermostat described in the previous paragraph, another much used thermostatting procedure is the Nosé-Hoover thermostat [125]. The basic constraint equation resembles the equation given in Equation 3.18. However, the difference is in the form of the thermostatting multiplier, λ or the constraint (termed a 'friction' coefficient) which now also evolves in time according to

$$\dot{\lambda} = \frac{\sum_{i=1}^{N}\frac{p_i^2}{m} - g_N k_B T}{Q_t}, \tag{3.20}$$

where g_N is the number of degrees of freedom and T is the temperature. The term in the denominator, Q_t comprises a thermal bath relaxation variable. The Nosé-Hoover thermostat samples the canonical ensemble (where the thermal-equilibirum kinetic energy is not constant and fluctuates about its average value) whereas the Gaussian thermostat samples the isokinetic ensemble.

Other ensembles that can be simulated include the isothermal-isobaric and the isobaric-isoenthalpic ensembles. The use of a barostat, to simulate constant pressure

conditions, is vital in simulation studies of these ensembles; Anderson [126] was the first to introduce a barostat in MD simulations. The method involves coupling the system to an external (volume) reservoir. Constant pressure conditions are maintained by a feedback mechanism similar to that of the Gaussian and Nosé-Hoover thermostats but which now allows the volume to fluctuate appropriately.

With the different ensembles that can now be sampled in molecular dynamics simulations, a wide variety of problems have become accessible to investigators. The next section will outline some properties that can be garnered from molecular dynamics.

3.1.4 Analysis of data from molecular dynamics

A molecular dynamics simulation produces trajectories of its particles and the particles composing the system of interest are typically contained within a simulation cell. Periodic boundary conditions, where a simulation box is surrounded by images of itself, are applied to mimic bulk behaviour [115]. This is done so every particle in the simulation cell is unaffected by boundary constraints, which would be problematic if bulk behaviour is desired [116]. Properties of interest are then calculated in various ways to generate useful data that may be compared to experimental results.

The temperature of the system is compared to the thermodynamic temperature through the equipartition theorem [116],

$$\sum_{i=1}^{N} \frac{1}{2} m \mathbf{v}_i^2 = \frac{3}{2} N k_B T, \tag{3.21}$$

where the sum is over all particles in the system, m is the mass, $\mathbf{v}_i$ is the velocity, N is the number of particles and T is the temperature. The pressure is calculated from the virial theorem [121],

$$P = \frac{Nk_BT}{V} - \frac{1}{3}\sum_{all\ pairs}\left(\frac{-\mathbf{r}_{ij}\cdot\mathbf{F}_{ij}}{V}\right), \tag{3.22}$$

where P is the pressure, V is the volume, $\mathbf{r}_{ij}$ is the distance vector between particles i and j, and $\mathbf{F}_{ij}$ is the force between the particles.

For interfacial systems, it is interesting and important to examine average properties at various positions through this heterogeneous environment. Properties of interest, such as the density and the diffusion constant, are recorded as profiles and become functions of z, the distance perpendicular to the interfacial surface. The method of obtaining the density profile, for example, begins with partitioning the simulation box into thin slices such that the atomic or molecular density within a particular range of z values is averaged over the x and y directions [115]. These partitions are called slabs or bins and in past studies have usually corresponded to solid particle lattice in the simulation box. This coarse binning, which is necessitated by the combination of a static interface and the inherent molecular structure across it, severely limits the quality of these functions as will be discussed below.

As another example, diffusion constants can be calculated from the mean square displacements of the particles in each slab. The diffusion constant, D, is then obtained through the Einstein relation,

$$6Dt = \langle R^2 \rangle, \tag{3.23}$$

where t is the time. In principle, profile functions of any other system property, such as the energy or pressure, can be similarly extracted, but are always recorded in the z direction of the simulation box [116].

In order to further characterize an interfacial system of interest other probes have been used. These include functions that enable structural information, both translational and orientational order, to be determined. The form of these functions can vary from simulation to simulation, dependent on the particular structural features of interest. One simple structural function commonly used is the radial distribution function, $g(r)$ [116]. This function describes the average environment that surrounds an atom or molecule in the system. For a model water system, this approach can yield g_{OO}, g_{HH} and g_{OH} distribution functions. The g_{OO} function provides primarily translational information within slabs of a water system, while the g_{OH} function can provide molecular orientational information when combined with other radial functions like g_{OO} and g_{HH} (examples of these functions are shown in Figure 5.3). Other functions that can be used to probe the local orientational order follow the dipole moments of the water molecules, the O-H and H-H vectors [49]. Therefore various properties can be calculated, some trivial to obtain others almost impossible, depending on the investigators needs.

3.2 SOLID/LIQUID INTERFACE OF SIMPLE MODELS

3.2.1 Model potentials

The interaction of atoms expressed in its most rudimentary form involves only pairs of atoms interacting over a range of separations. Such simple models [116,120] have been used to investigate solid, liquids and gases. Moreover, they have been used to investigate crystal growth and the properties of a solid/liquid interface. Three of the

simplest potentials used in these studies have been the hard sphere potential, the inverse-power potential and the Lennard-Jones potential. The hard sphere potential is given by

$$\begin{aligned} U(r) &= \infty \qquad r < \sigma \\ &= 0 \qquad r > \sigma \end{aligned}, \tag{3.24}$$

where σ is the diameter of the particle and r the separation. This potential is strictly a repulsive potential and was important in early simulations of phase transitions [127]. The inverse power potential, given by

$$U(r) = \varepsilon(\sigma / r)^n, \tag{3.25}$$

has made important contributions to the understanding of first order phase transitions through theory [128] and simulations [129]. For example, it has been used to show that the repulsive part of the potential energy is critically important in the freezing process of simple systems. By far, the most widely studied potential for solid/liquid simulations is the Lennard-Jones potential given by

$$U(r) = 4\varepsilon\left[\left(\frac{\sigma}{r}\right)^{12} - \left(\frac{\sigma}{r}\right)^{6}\right]. \tag{3.26}$$

where ε is the well depth of the attractive potential and σ describes the particle diameter. This potential reproduces well the properties of the rare gas elements, for example argon. It has also been widely used to build molecular interaction potentials [130]. The following discussions will examine the use of these simple potentials in simulations of solid/liquid interfacial and in studies of crystal growth.

3.2.2 Hard-sphere simulations

This model has been an important system in the early development of theoretical models for the solid/liquid interface [131,114]. Yet, there have been very few simulations of a true crystal/liquid interface in a hard-sphere system. Despite the challenges presented by this model, it offers a couple of attractive features. Firstly, it is relatively simple to implement in simulations and it has been employed in the development of a DFT theory for solid/liquid interfaces. Secondly, it has been established that the freezing behaviour of a dense simple fluid is reliant primarily on the repulsive component of the interaction potential; the attractive part of the potential simply becomes a perturbation to the repulsive component. Hence, a system of hard-spheres with an effective diameter [132] can be often used to model the atoms and molecules in such studies.

The first hard-sphere simulation of a solid/liquid interfacial simulation was by Kyrlidis and Brown [74]. They simulated an FCC hard-sphere solid/liquid system of 3000 particles by Monte Carlo methods for the 111, 110 and 001 interfaces. The chief goal in their study was to compare the density profiles obtained with results they determined from various density functional theories. Interfacial widths of 4-5 σ, 4 σ and 5-6 σ were calculated for the 100, 110 and 111 interfaces, respectively. An interesting observation was the increase in density profile peak spacing between layers in the interfacial region for the 100 face, which was not explained by the authors. Another study by Mori, Manabe and Nishioka [133], addressed the same systems using molecular dynamic simulations with approximately 3000 atoms. However, due to the short simulation times, the authors were not able to provide estimates for the interfacial widths.

A few years later Davidchack and Laird [134] estimated from the data of Mori et al. [133] that the widths for all the three interfaces were ~ 5.5 σ.

Davidchack and Laird [134] also investigated the hard-sphere crystal/melt interface with molecular dynamics, with the aim of carrying out larger (~10^4 atoms) and longer simulations to quantify the hard-sphere interface of 100 and 111 crystal faces with different structural and dynamical measures. They also observed the increase in the lattice spacing within the density profile of the 100 system and not the 111 system, which corroborates the findings of Kyrlidis and Brown [74]. The data from the profiles of density, pressure and surface stress seem to be quite sensitive to the different binning regimes (coarse versus fine grained), which makes their interpretation difficult. With the aid of density contour maps, the x-y planes perpendicular to the interface were observed and the actual transition from liquid to solid was found to occur between roughly 2-3 transition layers instead of the 7-8 crystal planes suggested by the density profile data. The diffusion constant profile appeared invariant to crystal face. Solid and liquid domains were observed to coexist on the same layer with a high degree of mobility on a subnanosecond time scale.

3.2.3 Inverse-power potential simulations

There have been no simulations reported to date on crystal growth utilizing inverse power potentials. The simulations that have been undertaken involve solid/liquid interfacial studies only. One of the first such studies was by Cape and Woodcock [135]. They investigated a Face-Centred Cubic (FCC) 100 crystal/liquid interface utilizing the inverse-twelfth-power-potential. The system was comprised of 7680 particles with the

coexistence density and temperature taken from previous simulations of bulk phases. The density profile of the system suggested 6-7 lattice spacings for the width of the interface. Trajectory plots indicated that there were "liquid-like" fractions of particles in the interface nearer to the bulk liquid and "crystal-like" fractions closer to the bulk crystal. The diffusion constant profile indicated an interfacial width of 5 lattice spacings. Tallon [136], in a subsequent study, investigated the FCC 111 interface of the inverse twelfth-power potential crystal/liquid interface with 6480 particles. The primary aim of his simulation work was to characterize the interfacial region. The width of the interface of the 111 system was found to be about 5 lattice layers. His analysis of the individual layers within the interface suggested that in a given layer "crystal-like" and "liquid-like" domains did not coexist.

The next important study was by Laird and Haymet [137] who investigated the crystal/melt interface for an inverse sixth-power potential. They simulated Body-Centered Cubic (BCC) 100, 110 and 111 systems. The values of the coexistence temperature and densities were chosen to match the bulk properties on the phase coexistence line. The simulation consisted of 3430, 3500 and 3600 particles for the 100, 110 and 111 crystal/melt systems, respectively. The analysis of the density profile revealed an interfacial width of 6.4 σ (9 lattice planes), which agreed with a previous smaller simulation study [138]. As was observed in previous studies, the diffusion constant gave an interfacial width of 3.8 σ (5 lattice spacings). Widths of 9 σ and 7 σ were obtained from the density profiles, and 3.9 σ and 4.0 σ from the diffusion profiles of 110 and 111 faces, respectively. Yet, the diffusion constant values for all three interfaces were almost the same. The authors proposed that the apparent differences

between these measures may be due to strictly geometric considerations rather than true differences of the various interfaces.

All these studies have consistently indicated a difficulty in interpreting the differences in the estimate of the widths. None have adequately provided a plausible reason for the discrepancies. Furthermore, the discrepancy over the presence of "crystal-like" and "liquid-like" domains in an interfacial layer appears problematic.

3.2.4 Lennard-Jones simulations

Lennard-Jones systems have provided the most detailed insights into the solid/liquid interface to date. Initial investigations were concerned primarily with equilibrium interfaces. Among the first to perform simulations of a LJ crystal/liquid interface were Ladd and Woodcock [139] who carried out a three-phase simulation to obtain the LJ triple point. Among other interesting results, they provided a static profile of the density across a crystal/melt LJ face-centred cubic 001 face; the profile revealed that the 001 crystal/melt interface was very broad with an interfacial width estimated to be 9-10 lattice spacings (7-8σ). In a subsequent paper Ladd and Woodcock [140] investigated transport and thermodynamic properties of interfacial systems. Using profile plots of diffusion constants measured in two-dimensional layers, an interfacial width of 5 lattice spacings was estimated. Another quantity of interest examined in this work was the surface stress. However, the noise in their data generated difficulties in interpreting the results. Toxvaerd and Praestgarrd [141] also investigated the equilibrium LJ FCC 001 interface and calculated an interfacial width of 7-8 lattice spacings. In yet another study [142] investigating the same system with a modified LJ potential, a width of 3-4 lattice

spacings was extracted. All these simulation studies appear to predict different widths for the equilibrium (001) interface. Other simulations [143,144] of the FCC 111 crystal/melt interface with modified LJ potentials had similar problems with consistently identifying the width of the interface. The need for a systematic study of the LJ crystal/melt interface became clear. To this end, the first detailed systematic simulation study of the FCC 111 and 001 interfaces was performed by Broughton, Bonissent and Abraham [145,146]. Their simulations, under triple-point conditions, yielded similar density profiles for both crystal faces and an estimate of the interfacial width of 6-8 lattice layers. Estimates of 3-4 lattice layers were obtained for both faces if the diffusion constant was used as the measure. The diffusion constant profile was found to be invariant to crystal orientation, a finding in accord with the observation of Laird and Haymet [147] using the inverse R^6 potential.

The next set of important equilibrium studies of the LJ FCC crystal/melt interfaces for the 001, 011 and 111 crystal faces is that of Broughton and Gilmer [148,149,150,151,152,153]. In order to investigate whether fundamental differences of the three interfaces existed, bulk [148], transport [149] and dynamical properties [150] were examined in detail under triple-point conditions. Properties of the crystal/melt and crystal/vapour interfaces were also obtained. An interfacial width of approximately 3σ was obtained for crystal/melt interfaces for all three crystals faces, based on data from radial distribution functions, nearest neighbour fractions and angular correlation functions [152]; this result is considerably smaller than the width as estimated from the density profile. This trend was also observed for the inverse sixth-power system investigated by Laird and Haymet [147] and the hard-sphere simulations of Davidchack and Laird [134].

Simulations of steady-state crystallization were first investigated by Broughton, Gilmer and Jackson [154] and later by Burke, Broughton and Gilmer [155]. In these simulations, periodic boundary conditions were applied only in the x and y directions, with crystal growth/melting occurring in the z-direction. They created a non-equilibrium system where the interface between the solid and liquid regions was created at the center of the simulation box with two heat baths at each end. They maintained steady-state growth by introducing a particle flux in the system. Liquid particles were introduced into the system and moved towards the growing interface, where they became solid and were eventually removed from the system at the opposite end. Thus, the whole system appeared to move at this velocity, which was chosen to maintain the interface at the center of the box.

The findings of Broughton et al. [154] and Burke et al. [155] revealed that the 111 system has in general no preference for either FCC or HCP stacking, with stacking faults occurring in about half the layers grown. The presence of these two (competing) lattice types was identified as being responsible for the slower growth of 111 as compared to the 001 face, the latter showing no dual lattice structure. An important conclusion from these simulation studies was that during crystallization atoms in a layer grow by a "cooperative motion of the atoms". The non-equilibrium methodology used in their work enabled the creation of conditions appropriate for steady-state freezing but not melting. In addition, these studies could not make any predictions of the interfacial widths under these growth conditions nor locate the interfacial dividing plane in their steady-state systems, both of which Burke et al. [155] claimed were difficult.

Another group of significant papers focused on the LJ crystal/melt system were those of Briels and Tepper [156,157,158,159]. They employed equilibrium and non-equilibrium techniques in the simulation of the crystal growth of LJ FCC 001 systems. Briels and Tepper [156] developed a methodology to calculate growth rates near equilibrium (low growth velocities) that exploited a solid/liquid recognition function to characterize the appropriate fluctuations in local order. They discovered that these fluctuations in the equilibrium simulations, together with Onsager's regression hypothesis, predicted growth rates similar to those obtained from non-equilibrium simulations [156]. Then through a series of three papers, Briels and Tepper [157,158,159] investigated the role of lattice imperfections in crystal growth and melting rates of a LJ FCC 001 interface close to equilibrium. The first of these studies [157] explored small superheatings and supercoolings with respect to the equilibrium melting temperature. They concluded that any asymmetry in the freezing and melting curves was due to lattice imperfections found in the crystallizing interfaces (in contrast to the melting interfaces). In subsequent simulations [158,159], when imperfections were incorporated into the melting interfaces, the asymmetry vanished. In their follow up investigation [158], they utilized their recognition functions to identify two linear growth regimes: a short-time regime related to interface relaxation rates and a long-time regime associated with the macroscopic limit of growth and melting. They concluded that short simulations will give the former growth regime, which could be confused with crystal growth and so lead to apparent slope discontinuities arising from improper equilibration of the solid/liquid interface. In their third paper [159], Briels and Tepper concluded that long runtimes, long observation times and large box sizes were required to avoid confusion of interfacial

relaxation rates with growth rates. The aforementioned studies by Briels and Tepper, however, did not address issues such as widths, positions and structure of the interface, nor how these might change from equilibrium to non-equilibrium conditions.

Recently Huitema et al. [160] revisited the problem of characterizing the interface of a growing LJ crystal/melt system through a Monte Carlo simulation method. In these growth simulations, the initial configuration of the rectangular system was half liquid and half solid and crystallization proceeded until the whole simulation box was crystalline. In these simulations the x and y dimensions of the rectangular simulation box were held fixed, with the z-dimension able to fluctuate. To discriminate solid from liquid, they have used an order parameter which exploits symmetry properties of the local environment for the 001, 011 and 111 faces. They concluded that all three interfaces were rough and vary little with temperature. The profile functions they obtained for the density of the system were virtually identical to those of Broughton and Gilmer [153] and they similarly obtained interfacial widths for all three crystal orientations of the same magnitude. They also found the interfacial widths were independent of undercooling. The microscopic picture of growth as described by Huitema et al. [160] for the 111 and 011 faces consisted of ordering of the particles in the layers in front of the interface along with hopping of atoms from layers further away to layers closer to the interface. In addition, the apparent density of the layers in front of the interface was observed to increase by about 10% on solidification. In contrast, the 001 face exhibited no such increases in the apparent density of layers. However, the distance between layers became smaller upon ordering of the particles in the layers. The authors concluded that this provided a faster growth mechanism. Since the Monte Carlo simulation algorithm employed by Huitema et

al. [160] does not describe a true trajectory for the system, it is unclear the extent to which their work advances our understanding of the detailed mechanisms of atomic crystal growth. Thus, several issues remain unresolved, all dealing with the nature of the interfacial layer and the mechanism of crystal growth. Other important properties of the solid-liquid interface, such as its interfacial energy (or the interfacial tension), can be determined once detailed information on the nature of the interface is explored.

Broughton and Gilmer [153] were among the first workers to calculate the interfacial free energy of the solid/liquid interface The surface free energies [153] for the different faces were found by employing a rather involved thermodynamic integration method that used a series of cleaving potentials in a four step process to calculate the reversible work necessary to form the interface. The calculated values obtained were 0.34 $\pm$ 0.02, 0.36 $\pm$ 0.02 and 0.35 $\pm$ 0.02 (units in ε/σ^2) for the 001, 011 and 111 interfaces, respectively. Broughton and Gilmer [153] thus were able to claim that the interfaces were isotropic within their error bars and they postulated, based on these results, that the equilibrium interfaces of the crystal were approximately spherical. More recently, Davidchack and Laird [161] calculated the surface free energies using a similar procedure. They have reported that the surface free energies (interfacial tensions) decrease in the order 100 > 110 > 111. Their technique employs computer simulations to calculate a continuous thermodynamic path that can be integrated from a starting system of an independent bulk liquid and a bulk solid to a final state containing the interface. The methodology they employed, where planar cleaving walls were utilized as opposed to cleaving potentials to separate the phases, is an extension of the procedure used by Broughton and Gilmer [153]. One of the important approximations of Davidchack and

Laird [161] was to treat the interface as a planar entity, despite their own observation that the interface is generally "rough" on a short time scale. However, they justified this assumption by claiming that the fluctuations in the interfacial position should average out to a planar surface.

In a recent study by Morris and Song [162], the order of interfacial free energy differences matched those of Davidchack and Laird [161]. The method used by Morris and Song [162] examines the "fluctuations in the height of the interface". Utilizing an order parameter that distinguishes particles as solid, liquid and interfacial particles, this method then provides a reference point from which to calculate the height of the interface. This approach assumes the interface to be a line that can be used to demarcate solid from liquid and it is the deviations from this reference point that describe the average interface. The interfacial energy as defined in Morris and Song's [162] study is the energy required for fluctuations, thus low interfacial energy is equated to smaller fluctuations.

3.2.5 Conclusions from atomic studies to date

Computer simulations have provided important insights and detailed descriptions of solid-liquid interfaces. These interfaces are the regions where the melting and freezing processes occur. Yet, it is only after the position and structure of the interface has been characterized that detailed accounts of its role in freezing and melting can be understood. The results from the different studies discussed above agree that different order parameters provide different measures of the interface, with dynamical measures like the diffusion constant profile indicating a narrower interface (~3σ) than structural measures

like the density profile (~6σ). The apparent differences between these measures have not been adequately explained and there is no agreement on the widths of the different crystal faces. In addition, the detailed structure of the interface is not well characterized, which obfuscates any attempt to render the mechanisms of freezing and melting in a perspicuous manner. Moreover, very few simulations have addressed crystal growth directly, as there has been no systematic examination of crystal growth and melting.

Beyond model simulations, there has been little theoretical work aimed at providing insights into the solid/liquid interface. Williams, Moss and Harrowell [163], using coupled Landau-Ginzburg equations based on a mean-field approximation of the FCC lattice gas with nearest and next nearest neighbour interactions, have attempted such a study. The focus was on the relationship between particle interactions and packing geometries and the intrinsic properties of the non-equilibrium interface, specifically interfacial structure and interface mobilities. They found that the surface tension of the 001 face was lower than that of 111, and they also determined that the structural fluctuations of the 001 face are larger than those of 111. In addition, they identified the importance of the dynamics of interfacial transients manifested through the crystalline fluctuations in the liquid next to the solid. The observations by Williams, Moss and Harrowell [163] suggest that fluctuations are an integral part of the equilibrium and non-equilibrium solid-liquid interface. In light of these observations, the claim that the interface is planar (at the molecular scale) by Davidchack and Laird [161] is perhaps questionable. Furthermore, descriptions of a (microscopically thin) *surface* that separates solid and liquid are unrealistic as it implies some complex static 3 dimensional surface.

The unambiguous classification of particles at this surface as solid or liquid certainly becomes very challenging indeed.

Clearly, what is needed is a new paradigm to define and describe what the interface between a solid and liquid is, with an unambiguous means of defining an interfacial width. The following section will begin to address some of these outstanding issues, utilizing a new methodology to perform non-equilibrium simulations.

3.3 NEW MD SIMULATION APPROACH

3.3.1 Methodology

The novel methodology employed in this work consists of two related but distinct aspects. The first is concerned with how temperature is controlled in the simulation. Specifically, it involves the incorporation of a heat source and a heat sink into the system; these are regions that experience local temperature control. It should be noted that in a standard thermostatted molecular dynamics simulation, temperature would be controlled uniformly across the entire system or interface [116]. To implement these local thermostats, local temperatures, T_l, are defined by

$$\frac{3}{2}k_B T_l = \frac{\sum_i G_i(z_i)K_i}{\sum_i G_i(z_i)}, \tag{3.27}$$

where the localizing weighting function,

$$G_l(z_i) = \exp -[a_o(z_i - z_o)^2], \tag{3.28}$$

is assumed to be a Gaussian for convenience, K_i is the kinetic energy of particle i, z_i is its position in the z direction, z_o defines the position (or center) of the thermostatted region

and a_o is the Gaussian width. Equations 3.27 and 3.28 effectively restrict the temperature measure, T_l, to a lateral "slice" of the system, where this slice is characterized by a soft boundary.

The introduction of the local thermostats correspondingly alters the equations of motion. These become

$$\dot{\mathbf{p}}_i = \mathbf{F}_i - \left[\alpha_h G_h(z_i) + \alpha_c G_c(z_i)\right]\mathbf{p}_i + \gamma_T\left[G_h(z_i) + G_c(z_i)\right], \tag{3.29}$$

where $\mathbf{p}_i$ is the momentum and $\mathbf{F}_i$ is the force on particle i,

$$\alpha_h = \frac{1}{Q}\left(T_h - T_{h;o}\right) \tag{3.30a}$$

and

$$\alpha_c = \frac{1}{Q}\left(T_c - T_{c;o}\right) \tag{3.30b}$$

are thermostatting multipliers denoting the heat source and heat sink, respectively, Q is a coupling parameter that determines the response of the multipliers, $T_{h,o}$ and $T_{c,o}$ are the desired (target) temperatures for these regions, and

$$\gamma_T = \frac{\sum_i \left[\alpha_h G_h(z_i)\mathbf{p}_i + \alpha_c G_c(z_i)\mathbf{p}_i\right]}{\sum_i \left[G_h(z_i) + G_c(z_i)\right]}. \tag{3.31}$$

The third term in Equation 3.29 is used to ensure that the total momentum of the system remains conserved. The simple Berendson [164] thermostats represented by equations 3.30a and 3.30b are sufficient for present purposes. The above equations describe the motion of a particle within the simulation cell under the influence of the heat sink and source. If this particle is well away from the thermostatted regions, (i.e. G(z) ~ 0) Equation 3.29 essentially reduces to its Newtonian form, i.e.

$$\dot{\mathbf{p}}_i = \mathbf{F}_i. \tag{3.32}$$

In this way, heat is able to enter one part of the system while being removed from another part (in a very controlled manner). Moreover, any latent heat generated (removed) by crystallization (melting) can be effectively removed (added). When both the heat sink and heat source are operating, a thermal gradient is created giving rise to a heat flux through the system. The presence of this thermal gradient is key to the present methodology.

The second component of this methodology makes a non-equilibrium steady-state approach to the simulation of crystal growth possible. It exploits the simple fact that during a MD simulation the positions of the heat source and heat sink can be changed, if desired. By moving the heat source and sink together through the system, at some sufficiently slow pre-set speed, the crystal can be effectively forced to grow under non-equilibrium steady-state conditions. As full periodic boundary conditions are applied to the simulated system, the movement of the thermostats could eventually cycle through the entire system several times and so a given particle could experience several changes of state during any particular simulation run.

A key feature of this methodology is the ability to generate a true steady-state for a given temperature gradient and velocity of the local thermostats. The system will be heterogeneous with both solid and liquid phases present. Therefore, under steady-state conditions, it will contain two interfaces: a freezing interface and a melting interface, as illustrated in Figure 3.1. Under these conditions, temperature, density, energy and structural profiles can be obtained within the moving frame of the system (i.e., of the heat source and heat sink). The principal benefit of obtaining profiles from within the moving frame is that the system will then have sampled all possible positions of the interface

relative to the underlying molecular structure of the crystal. As a comparison, a static density profile of an equilibrium FCC 001 system is shown in Figure 3.2(a), while the

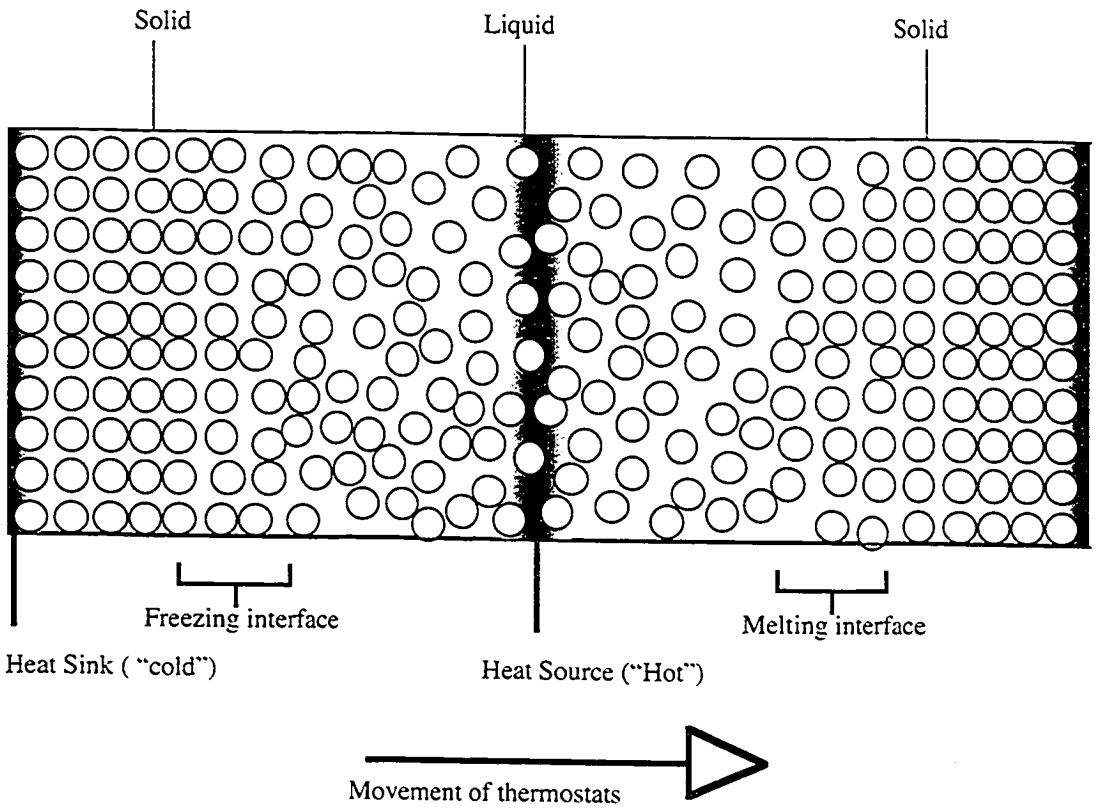

Figure 3.1 A schematic diagram showing a typical simulation cell. The heat source and the heat sink are the locations of the local "hot" and "cold" thermostatted regions, respectively. The shaded area represents the extent of the local influence of the thermostats on the system. The arrow shows the direction of movement of the thermostats that then drives the freezing and melting interfaces. Note that periodic boundary conditions are applied in all three Cartesian directions.

density profile obtained in the moving frame of a growing system is presented in Figure 3.2(b). In Figure 3.2(b) and in all subsequent moving frame profile functions, $z = 0$ corresponds to the position of the heat sink. The large oscillations in the former function in the solid region of the system (see Figure 3.2(a)) reflect its static nature. In the past,

[145,160] profile functions, such as that shown in Figure 3.2(a), were used to carry out analysis on such systems (e.g. to estimate interfacial widths). More recently, smoothing procedures have been utilized to help refine such functions [165]. These procedures, though useful, add some uncertainty to the interpretation of the resulting functions. The functions obtained within the present approach will be inherently smooth when averaged sufficiently. Thus, they allow for more direct comparison with experimental and other theoretical results, and will be very useful in characterizing the average interface.

3.3.2 Computational details

Simulations were performed on atomic (spherical) systems where the particles interact through the pairwise additive Lennard-Jones (LJ) potential or an inverse R^6 potential. Both BCC and FCC crystal structures were examined, although the latter was much more extensively studied. A limited number of simulations were carried out for BCC and FCC systems with the inverse R^6 potential to explore possible model and crystal structure dependence. The most extensively studied systems, and the primary focus of this study, will be those with FCC crystals and the LJ potential; any exceptional behaviour manifested by the inverse R^6 potential systems will be reported in the relevant sections in the next chapter. Table 3.1 summarizes the crystal structures investigated, along with the potential and system size used for each of the three crystallographic faces (001, 011 and 111) considered in the present study. Employing the various systems as described in Table 3.1, in excess of 200 simulations were performed with different temperature gradients and growth velocities as summarized in Tables 3.2 and 3.3, respectively. In Tables 3.2 and 3.3, and throughout Chapters 3 and 4, all quantities are

given in the reduced units appropriate for the Lennard-Jones potential [120,116]. In these simulations the potential was truncated and shifted at a cutoff radius, $r_{cut} = 2.5$. Periodic boundary conditions were applied in all three Cartesian directions. The reduced timestep, Δt, used in the simulations was 0.005.

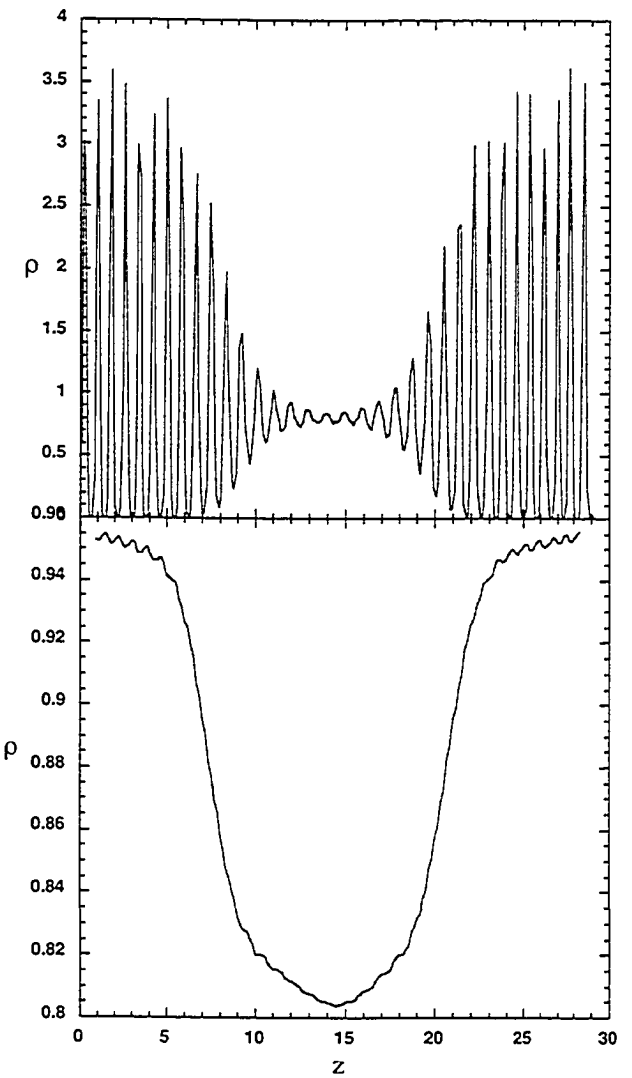

Figure 3.2 Density plotted against the z-coordinate for a LJ 001 crystal/melt system. (a) Static equilibrium system profile; (b) profile obtained in the moving frame of a steady-state system with a small gradient at a low velocity of 0.006.

Table 3.1 Summary of the different potentials and crystallographic faces of FCC and BCC lattices investigated. The number of particles along with the steady-state system dimensions (in brackets) are given.

Interface	Number of Particles (reduced box dimensions)		
	LJ-fcc	$1/R^6$- bcc	$1/R^6$- fcc
111	2880 ($9.16\sigma \times 11.9\sigma \times 30.57\sigma$)	2592 ($8.79\sigma \times 7.61\sigma \times 21.5\sigma$)	2880 ($9.16\sigma \times 11.9\sigma \times 30.57\sigma$)
110	2304 ($9.15\sigma \times 9.71\sigma \times 29.54\sigma$)	2880 ($8.79\sigma \times 8.28\sigma \times 22.17\sigma$)	-----
100	2448 ($9.70\sigma \times 9.70\sigma \times 29.93\sigma$)	2688 ($8.29\sigma \times 8.29\sigma \times 21.94\sigma$)	2448 ($9.70\sigma \times 9.70\ \sigma \times 29.93\sigma$)
111 (big)	4320 ($13.17\sigma \times 11.87\sigma \times 30.26\sigma$)	-----	-----
110 (long)	3456 ($9.15\sigma \times 9.71\sigma \times 43.23\sigma$)	-----	-----
110 (big)	4608 ($13.72\sigma \times 12.94\sigma \times 29.50\sigma$)	-----	-----
100 (big)	4352 ($12.95\sigma \times 12.95\sigma \times 29.46\sigma$)	-----	-----

The ability to determine crystalline order across an interface is an important aspect of this study. Other workers have used structural functions that have focused on local order around a given particle [156]. An order parameter that can be used as a measure of crystalline order within a particular 2-dimensional slice of the system is

$$\Sigma(z) \equiv e^{-(i\mathbf{k}_{2D}\cdot\mathbf{r}_{2D})}, \tag{3.33}$$

where $\mathbf{k}_{2D}$ is a two-dimensional wave-vector commensurate with the unit cell structure

Table 3.2 Temperature gradients employed in the present simulations along with the corresponding temperatures of the heat source and heat sink. All temperatures are in reduced units.

ΔT	T(hot)	T(cold)
0.6 (very large)	0.90	0.30
0.4 (large)	0.85	0.45
0.2 (moderate)	0.72	0.52
0.1 (small)	0.67	0.57

Table 3.3 Velocities under which non-equilibrium steady-state simulations were undertaken together with other related simulation parameters. Note that velocities are given in reduced units.

Velocity	10^3 timesteps to move 1σ	Total run length (10^3 timesteps)
0.002	100.0	1500
0.006	33.33	500
0.02	10.00	300
0.06	3.333	300
0.08	2.500	250
0.09	2.222	200
0.12	1.666	200
0.16	1.250	100
0.2	1.000	100
0.3	0.666	100
0.4	0.500	100
0.45	0.445	100
0.5	0.400	100
0.6	0.333	100

and $\mathbf{r}_{2D}$ is the position vector (x,y) of the particle within the two-dimensional slice. This measurement of long-range order is performed perpendicular to the z-direction, the direction of crystal growth (heterogeneity) and of the movement of the thermostats. This function has been found to be a good discriminator of local crystalline order in these simulations.

The procedure for the creation of an initial equilibrium crystal/liquid interface consisted of several steps. First, the crystalline solid at its estimated melting temperature, T_m, was equilibrated at constant pressure. The single barostat being employed allowed for scaling of all three dimensions of the simulation cell. Next, the local thermostats were turned on with their temperatures set appropriately to melt roughly half the system. A thermal gradient was generated across these systems thus facilitating the generation of solid/liquid interfaces. During this stage the x and y dimensions of the simulation cell were held fixed, while the z dimension was allowed to change to maintain the corresponding component of the pressure tensor. The heat source and heat sink were then turned off and the system was allowed to equilibrate. The final (uniform) temperature of the system then provided a new estimate for its melting temperature. The above steps were repeated several times until the melting point could be consistently reproduced to within 0.0005. The equilibrium melting temperature thus obtained was 0.6201 ± 0.0005 at a pressure of 0.01 ± 0.005 for the three interfacial orientations of the LJ FCC systems. This result is in excellent agreement with previous simulations [145]. Similar procedures were performed for the $1/R^6$ systems with reduced melting temperatures of 0.6024 ± 0.0005 and 0.5962 ± 0.0005 for BCC and FCC systems, respectively, at a pressure of 47 ± 1 in excellent agreement with the phase diagram as described by Laird and Haymet [147].

Crystal growth simulations were continued from configurations of equilibrium simulations at the point where half the system melted (or from slower growth steady-state runs). The thermostats (and hence the gradient) were left on and were then moved at various fixed velocities (as indicated in Table 3) to obtain the desired steady-state growth rates of the different crystal faces. After an initial equilibration period during which constant z-pressure was maintained, the simulations were performed under constant volume conditions. However, the average z-pressure was carefully monitored to determine if the pressure deviated significantly from our preset value for the different simulations; if so, the system was re-equilibrated until the z-pressure was consistently reproduced. Simulation runs were continued until the steady-state growth conditions were adequately sampled, typically representing a full system length of crystal growth. Profile functions for the energy, density, pressure (in x, y and z), temperature, and the two-dimensional solid order parameter, Σ, were obtained along the z-dimension of the simulation cell to help characterize the system. These profile functions were obtained from numerical histograms with bin widths of approximately 0.113 σ.

For the investigation of possible system size effects three significantly larger ("big") systems were also examined and are included in Table 1. A single system that was roughly 50% longer was included in our simulation study to confirm that the two interfaces did not interact with one another and that their behaviour was otherwise independent.

CHAPTER 4
COMPUTER SIMULATIONS OF GROWTH OF LJ CRYSTALS

The results obtained from computer simulations, applying the methodology described in the last chapter, are presented here [166]. The non-equilibrium methodology generates unique profile functions, which are different from those described in Section 3.2. The following discussion will examine the profile functions followed by a detailed investigation of atomic configurations.

4.1 CHARACTERIZATION OF STEADY-STATE MELTING/FREEZING

4.1.1 Profile functions from non-equilibrium simulations

Profile functions from a typical steady-state LJ simulation are shown in Figure 4.1. The results given are for a FCC 001 system with a small temperature gradient and a low velocity (as defined in Chapter 3). One key feature of these profiles is that the functions are relatively smooth. In Figure 4.1(a), the temperature profile in the moving frame is a characteristic "carat" shape, with the maximum corresponding to the position of the heat source and the position of the minimum corresponding to the heat sink. The z-pressure profile appears essentially flat with very small oscillations in the vicinity of the interface, apparently stemming from the transition from solid and liquid. However, no systematic trend was observed in this detailed behaviour in the pressure. In Figure 4.1(b), the energy profile shows higher potential energy in the liquid than in the solid region, as expected. This function exhibits a characteristic "bell-shaped" energy profile, as obtained

at a small gradient and low velocity. The structural order parameter, Σ, also clearly demarcates the solid regions (for z roughly 0-5 σ and 23-30 σ), the liquid (roughly 9-19 σ) and the transitions between solid and liquid. These values are typical for steady-state systems

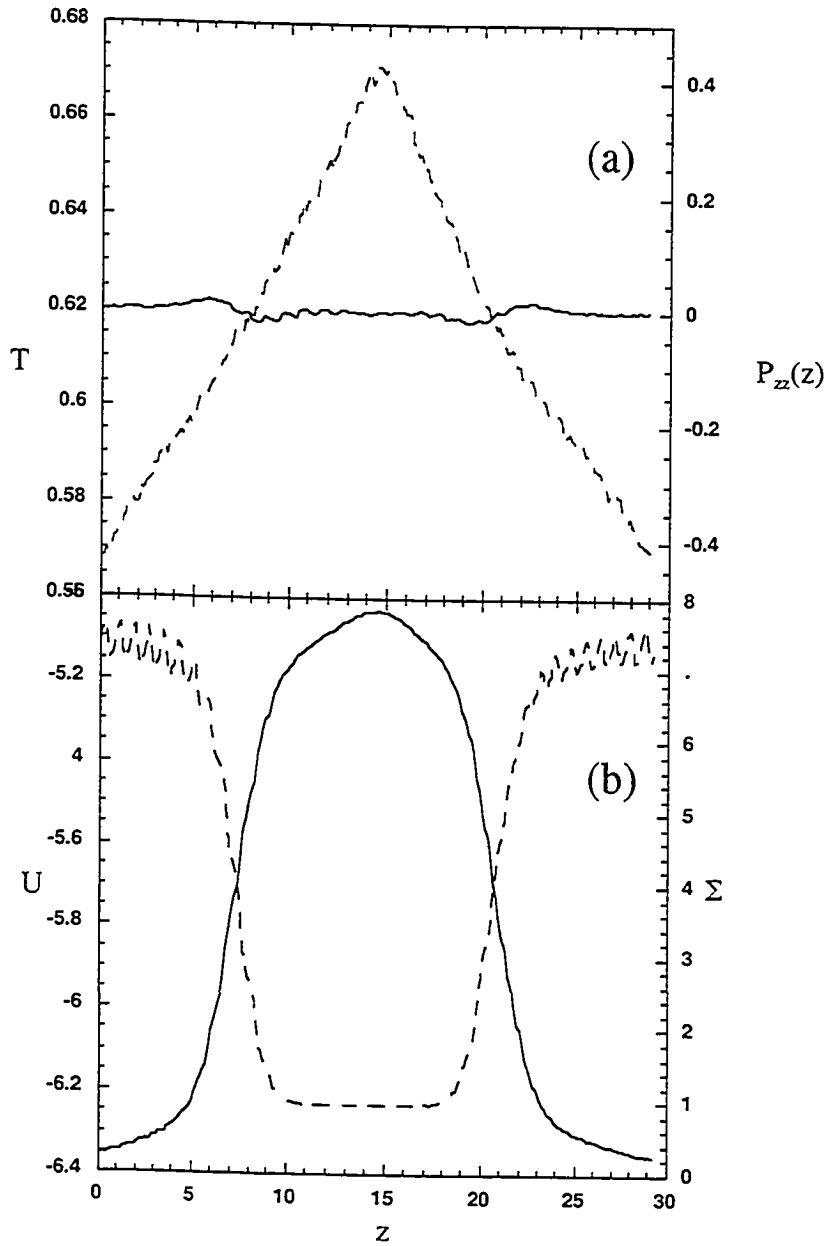

Figure 4.1 Profile data for: (a) the z-component of the pressure, $P_{zz}(z)$ (solid line), and the temperature, T (dashed line), and (b) the Σ order parameter (dashed line), and the energy, U (solid line). All profiles are in the moving frame of a LJ 001 steady-state system at a small gradient and a velocity of 0.006.

where the solid, corresponding to the left most part of the profile function, ends with the freezing interface and the melting interface is found further to the right. The Σ order parameter can be seen to be very sensitive within the 2D crystalline order of the solid/liquid system. One of the additional benefits of obtaining functions in this manner (in the moving frame) is that consistent profiles throughout a simulation run confirm that a stable steady-state has indeed been established.

Through direct inspection of the energy and Σ profiles all regions in the steady-state system are easily identified. However upon closer inspection, the precise positions and widths of the two interfaces are still difficult to pinpoint. Thus, although Figure 4.1 is useful and informative, it still does not allow for a systematic way of determining interfacial widths or of defining the center (or position) of the interface [160,167], which is one of the goals in the present work. With this in mind, when the derivative of an energy (or Σ) profile is taken with respect to the z-coordinate, two clear extrema are observed, one peak and one valley (henceforth referred to as "peaks") that correspond to each interface. Examples of this behaviour are shown in Figure 4.2(a). Similar peaks at essentially the same positions are exhibited in Figure 4.2(b) by the derivative of the Σ order parameter. The positions of the extrema in Figure 4.2 are used to define the middle of the freezing and melting interfaces and the widths of the peaks to correspond to the interfacial width. Furthermore, it is useful to point out that the derivative of the energy function can be interpreted as an average force in the z-direction experienced by a particle at that position in the system.

In general, one finds that the derivatives of the energy and Σ order parameter profiles are sensitive measures of the changes occurring in the interfacial region. They

also appear quite symmetric and conveniently remove most of the effects of the temperature gradient present in these systems.

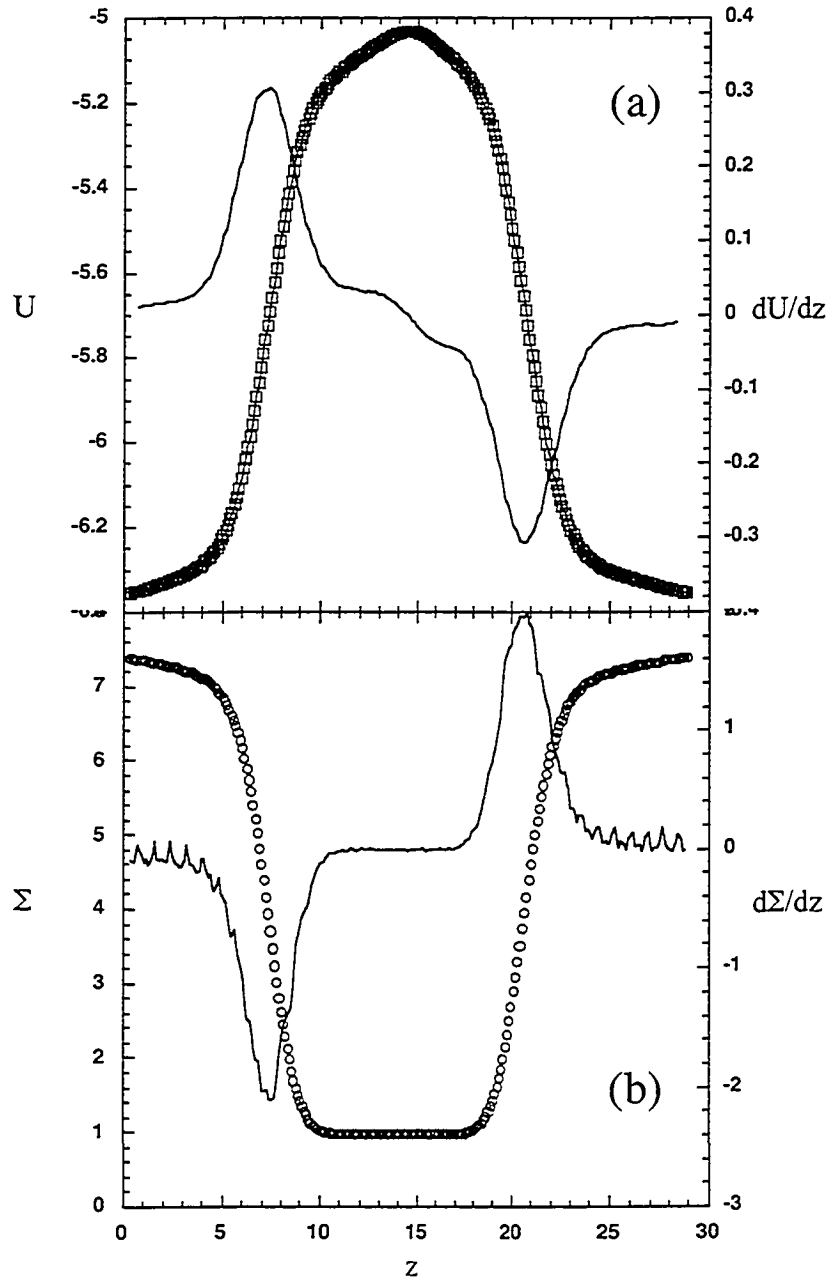

Figure 4.2 Energy and structural parameter profiles together with their derivatives with respect to z. The squares in (a) and the circles in (b) represent the original profile data, while the solid lines are their respective derivatives. The peaks/valleys correspond to the positions of the freezing and melting interfaces. The widths of the peaks correspond to the interfacial widths. The system shown is the LJ 001 steady-state system with a small gradient and at a low velocity of 0.006.

While these profile functions and their derivatives generally improve our description of the interface, the precise edge of any peak is still not well defined. To improve the analysis of the profile functions, seven point smooths were performed on the raw data. The peaks in the derivative functions were subsequently fit to Gaussian-like forms, involving a Gaussian to which a linear (ramp) function has been added to account for the influence of the temperature gradient. With the aid of these functional forms more precise predictions of the interfacial widths can be obtained. In particular, the interfacial width is defined as two standard deviations to both sides of the peak position (accounting for 95% of the total peak area). The values obtained in this manner agree well (with respect to the observed trends) with other more crude estimates (such as measuring the width at half height). In this way, a means of consistently measuring the widths and positions of peaks, such as those shown in Figure 4.2 corresponding to the interfaces has been established. It should be noted, however, that the widths from the energy functions are consistently 1-1.6 σ larger than the values obtained from the Σ order parameter functions, although both functions agree in their predicted positions. Galej et al. [168] have argued that different measures of interfacial widths cannot be expected to give the same values. A further discussion of these differences will be addressed later in this section.

Simulations of "big" and "long" systems, as given in Table 3.1, were also performed and the profile functions obtained show no significant differences with those of standard sized systems. The widths of the interfaces and the positions of the peaks are readily reproduced by the larger and longer systems. Moreover, the time required to reach steady-state was approximately the same. This invariance to system size validates the

current systems within the present methodology. The use of small systems and short runtimes to study crystal growth has been questioned by Briels and Tepper [159]. They have observed with their methodology that true growth rates could be confused with interfacial relaxation. Thus, they claim that long runtimes and bigger systems are needed to avoid the confusion. In simulations undertaken in the present study (in which crystal growth is being driven by a thermal gradient), no such simulation artifacts were noted. In fact, steady states were realized in relatively short simulation runs (see Table 3.3).

4.1.2 Velocity dependence

For a particular gradient, it is interesting to investigate the impact of growth (or melting) rate on the nature of the interface. Figure 4.3 shows interfacial widths for small gradient systems at low and high velocities. The energy profile becomes skewed to the left as the velocity is increased (0.02 and 0.16 for 111 and 001, respectively) in contrast to low velocity (0.006) where the energy profiles appear symmetric. It can be seen in Figure 4.3 that the distance between the freezing interface and the heat sink at high velocities is considerably smaller than at low growth velocities. This behaviour can be rationalized by the expectation that more rapid growth demands a deeper supercooling. This trend is observed with all systems at conditions of faster growth. At the melting interface, the melting temperature is shifted to higher temperatures with increased velocity; these shifts are always smaller than the corresponding shifts for the crystallizing front. Therefore, for a given gradient, one always encounters the upper bound in the crystal growth rate first. Table 4.1 summarizes the maximum growth rates attained for the LJ FCC systems at specific gradients. The maximum growth rates achieved for the

different FCC faces are consistent with those observed in previous studies [155]; with argon parameters for ε and σ, the maximum growth rate for the LJ 001 system is approximately 80 m/s. The growth rates for the different crystal faces increase in the order $111 < 011 < 001$.

Table 4.1 Maximum observed steady-state growth rates (in reduced units) for the various crystallographic faces and gradients examined for LJ FCC systems.

Interface	**Gradients**			
	0.6	0.4	0.2	0.1
111	0.16	0.16	0.12	0.06
110	0.3	0.2	0.12	0.09
100	0.5	0.2	0.2	0.09

Figures 4.3(c) and 4.3(d) show the derivatives of the energy and Σ order parameter profiles, respectively. Plots such as these provide data for interfacial positions and widths. Examination of this data reveals that there appears to be no systematic effect on the interfacial width with increasing velocity for a given gradient. The $1/R^6$ potential systems that were investigated as part of this thesis were observed to exhibit comparable behaviour, with similar maxima.

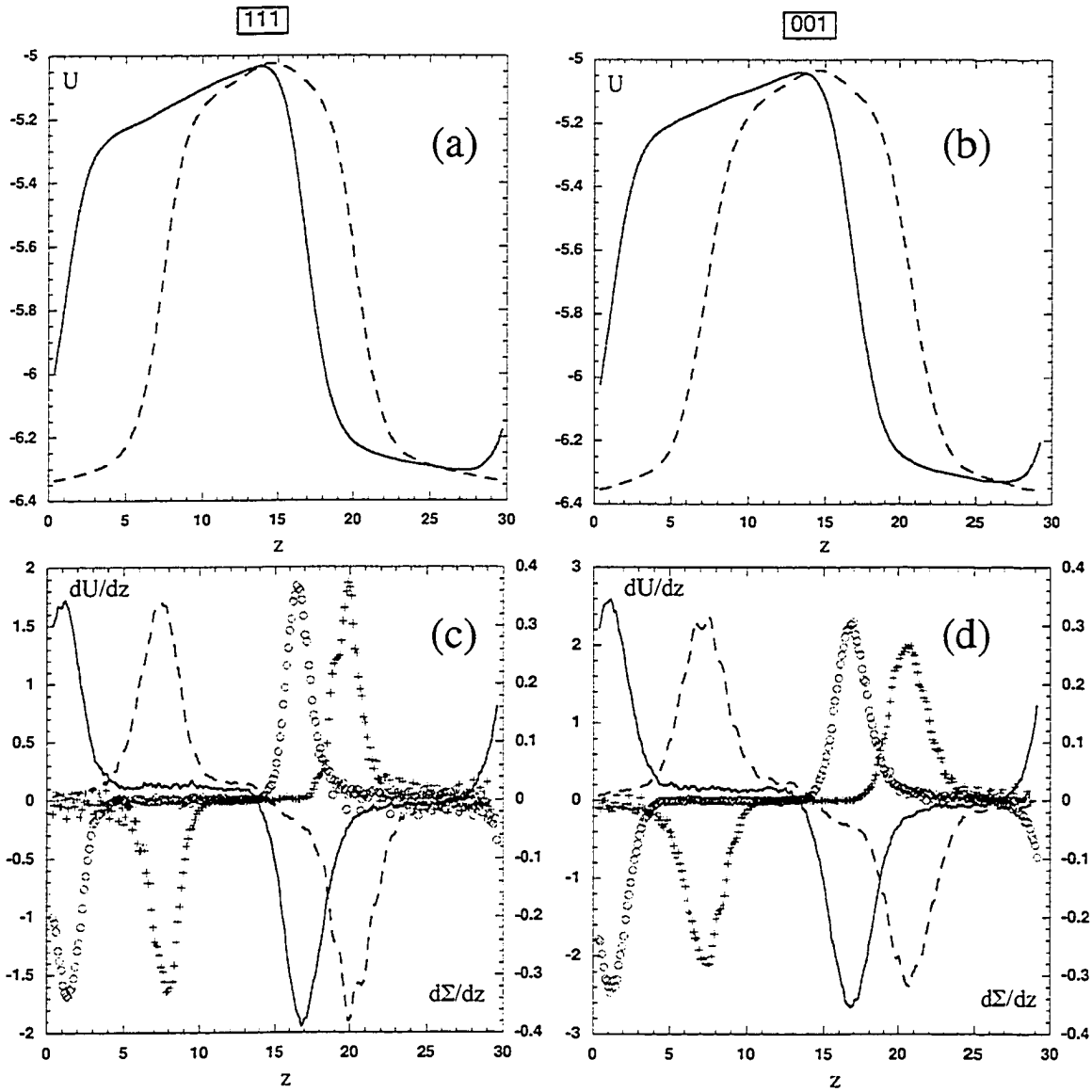

Figure 4.3 Energy profiles for the 111 (a) and 001 (b) LJ steady-state systems with small gradients at low (dashed) and maximum (line) velocities. The corresponding derivatives of U and Σ (circles-low velocity, crosses-high velocity) are shown in (c) and (d).

4.1.3 Gradient dependence

The gradients used in the present study are described in Table 3.2; Figure 4.4 examines the dependence of the interfacial properties on temperature gradient. It can be seen from Figure 4.4 that the shape of the energy curve becomes flattened when comparing a small to a large gradient system. For the smallest gradient shown in Figure

4.4, the energy curve reasonably approximates the plateau regions expected for the solid and liquid regions. Further insights can again be obtained by examining the derivatives of these profile functions. The derivatives shown in Figure 4.4(b) clearly show the features associated with the interfacial regions. The slight shifts of the melting and freezing interfaces (apparent for the different gradients) simply reflect the system finding its desired melting temperature on the temperature profile. Inspection of the derivatives of the Σ order parameter and the energy (see Figure 4.4(b)) reveals that the gradient has only a small impact on the interfacial thickness, with the interfaces becoming slightly narrower with increasing gradient. Similar results were observed for all crystal orientations. This dependence is not unexpected as larger gradients should tend to confine the interface to a smaller region. Because of the more rapidly varying temperature, some structural fluctuations at the growing and melting interfaces are restricted in large gradients causing these interfaces to be narrower. Small gradients do not confine these structural fluctuations resulting in slightly wider interfaces. Figure 4.5 shows the temperature gradient dependence of interfacial width as obtained from the derivative of the Σ order parameter and the energy. It is clear from Figure 4.5 that the interface becomes somewhat broader with a smaller gradient. This trend suggests that the zero gradient (equilibrium) interface may be slightly (less than 0.5σ) wider than those recorded here. Yet it is important to point out that the apparent temperature gradient dependence is small relative to the sensitivity to the employed measure.

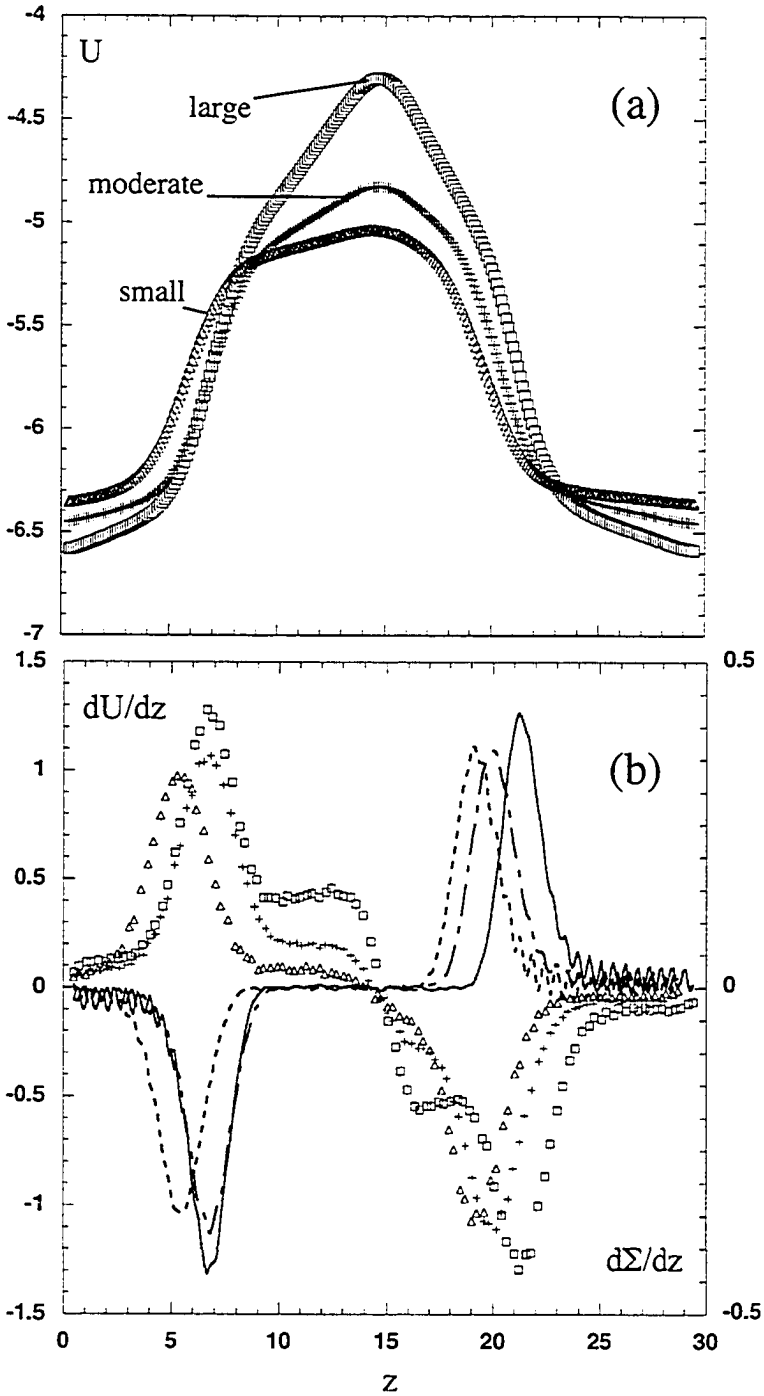

Figure 4.4 (a) Energy profiles at different gradients (as defined in Table 3.2) for steady-state LJ 001 systems at low velocity (0.02). (b) The derivatives of the energy as well as the Σ order parameter profiles at large-(squares and solid lines), moderate-(crosses and dash-dot lines) and small-(triangles and dash lines) gradients, respectively.

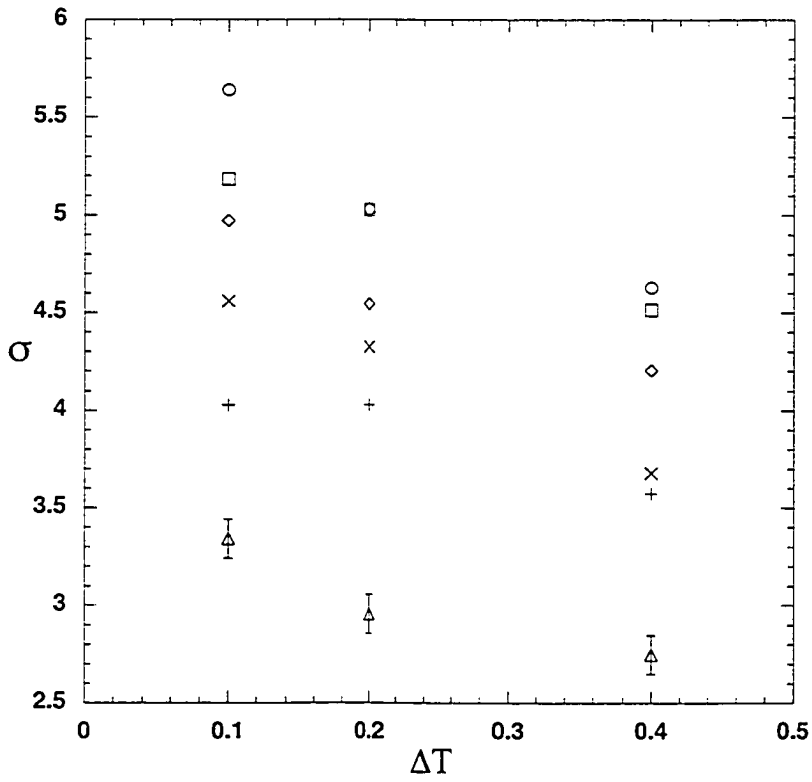

Figure 4.5 Dependence of interfacial widths on crystal face and on gradients. Results for 001 (circles), 011 (squares) and 111 (diamonds) systems are obtained from the derivative of the energy profile, while the Xs, crosses and triangles represent the corresponding derivatives of the Σ order parameter. Representative error bars are included for the 111 crystal face.

4.1.4 Comparison of crystallographic faces

As mentioned above, the growth rates observed in this work agree well with those recorded in previous studies [154,155]. Observations have confirmed that the maximum velocities for 011 are approximately 25 % slower, and for 111 are about 70 % slower, than for FCC 001 crystal faces. It is important to note that measured growth and melting rates have been simultaneously achieved under steady-state conditions, where the

movement of the heat source and sink in the present simulations has been used to drive the systems.

The energy profiles of the three FCC faces for two different sets of gradient/velocity conditions are shown in Figure 4.6. Results for a large gradient (0.4) and a velocity of 0.006 are compared in Figure 4.6(a), while Figure 4.6(b) shows data at a velocity of 0.12 with moderate gradient (0.2). These functions indicate that the interfaces associated with all three crystal faces generally appear to be rather similar; this observation is consistent for all the profile functions examined in this study. Obviously, as was already noted above, small differences do appear particularly at high velocities for each crystal face. The interfacial widths derived from the derivatives of the energy range from 4.6 - 5.6 σ, 4.5 - 5.2 σ and 4.2 - 5.0 σ for 001, 011 and 111 crystal faces, respectively (the uncertainty in these values is estimated to be $\pm$ 0.1 σ). The widths obtained using the derivative of the structural order parameter are consistently narrower by 1.0, 1.1 and 1.6 σ for 001, 011 and 111 faces, respectively. The interfacial widths obtained from the structural order parameter agree with previous equilibrium estimates, if measures dependent on transport and local structure are compared [146,153]. Huitema et al. [160], through the use of filtering techniques applied to static density profiles, obtained interfacial widths also in agreement with the present values. The derivatives of the energy predict a wider interface, in accord with the results of Broughton, Bonissent and Abraham [145]. The widths obtained in this thesis for the 001 face comprise 6-8 layers while the 111 face is found to contain 5-6 layers. Thus, the overall agreement of the present interfacial widths with those in the literature is good.

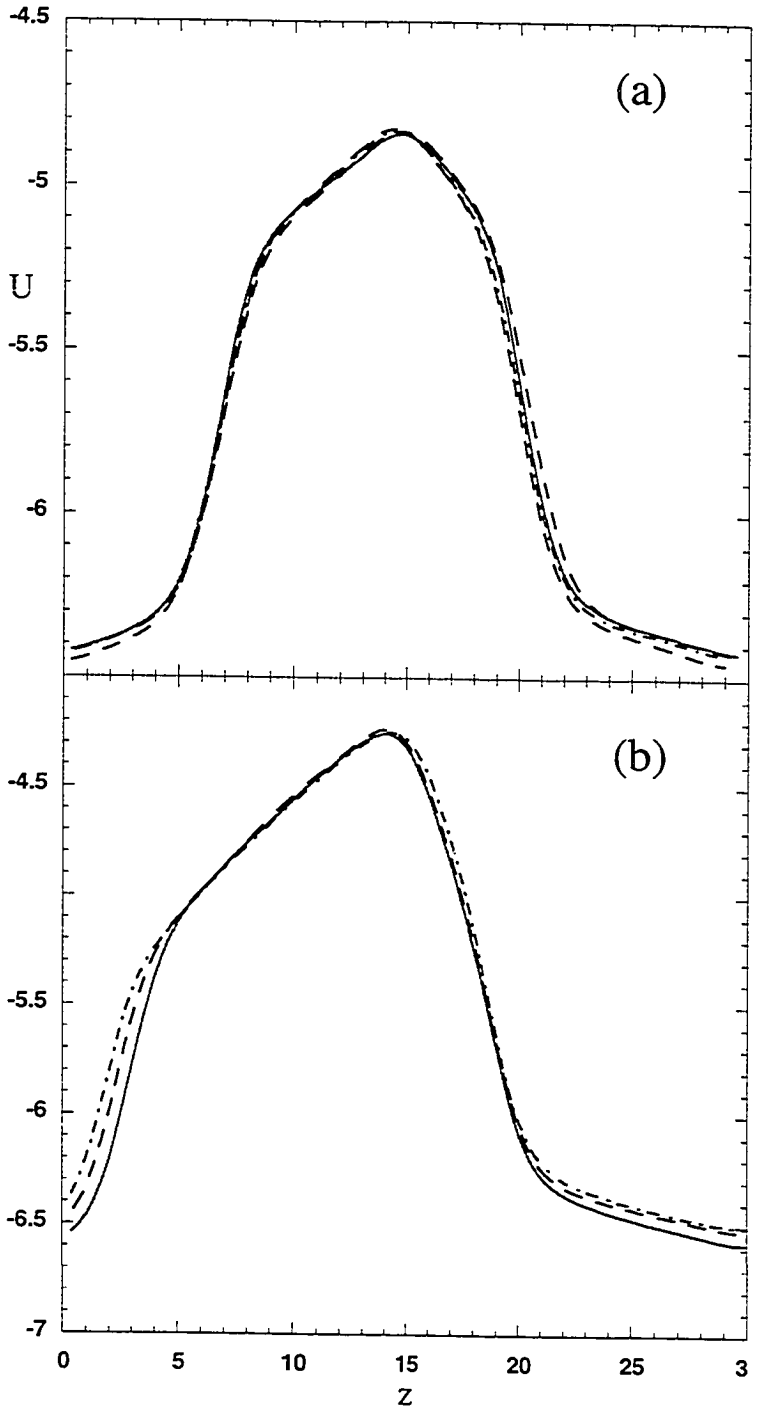

Figure 4.6 Energy profiles for the three crystallographic faces 001 (lines), 011 (dash) and 111 (dash-dot). (a) Moderate gradient with a low velocity of 0.006. (b) Large gradient with a high velocity of 0.12.

From the data provided by simulations presented here, a dependence of the interfacial width on the crystallographic orientation can be discerned. In particular, the 001 crystal face appears to be consistently the widest interface followed by the 011, and then the 111 crystal faces. This observation differs from the findings of Huitema et al. [160], and Broughton, Bonissent and Abraham [145] where they were able to observe interfacial differences. The former study [160] did not investigate true steady-state growth conditions and, moreover, suffers from poor statistics. Additionally, both studies have used static density profiles to extract interfacial widths, which appear to make it rather difficult to resolve more subtle effects such as crystal orientation. The determination of the interfacial widths of the LJ crystal/melt systems in their work are the most accurate to date, at least under non-equilibrium steady-state conditions. The detailed atomic structure of the interfaces will be described in the next section to help reconcile the differences in the interfacial widths.

4.1.5 Melting and freezing interfaces

Melting and freezing temperatures were extracted from the positions of the interfaces (as determined from the derivatives of the energy profiles) together with the known temperature profiles. The values obtained for moderate gradient systems are plotted against the velocity in Figure 4.7. Using these melting and freezing points, a thermodynamic melting point (the zero velocity temperature) can be extracted for all three-crystal faces. The agreement in the values for the three faces is excellent; the melting temperatures from Figure 4.7 are 0.612 ± 0.005, 0.613 ± 0.005 and 0.618 ± 0.005 for the 001, 011 and 111 systems, respectively. In general, the melting temperatures of all

BCC and FCC systems obtained in this manner were found to be essentially invariant to the choice of the crystal face and the magnitude of the temperature gradient, although the uncertainty associated with the melting temperature increases with larger gradients. The temperatures were also in very good agreement with the converged values determined initially for the various equilibrium systems, as described in Section 3.3.2. Comparison of these melting temperatures with those obtained in previous studies [146,147] for Lennard-Jones and $1/R^6$ systems show similar excellent agreement.

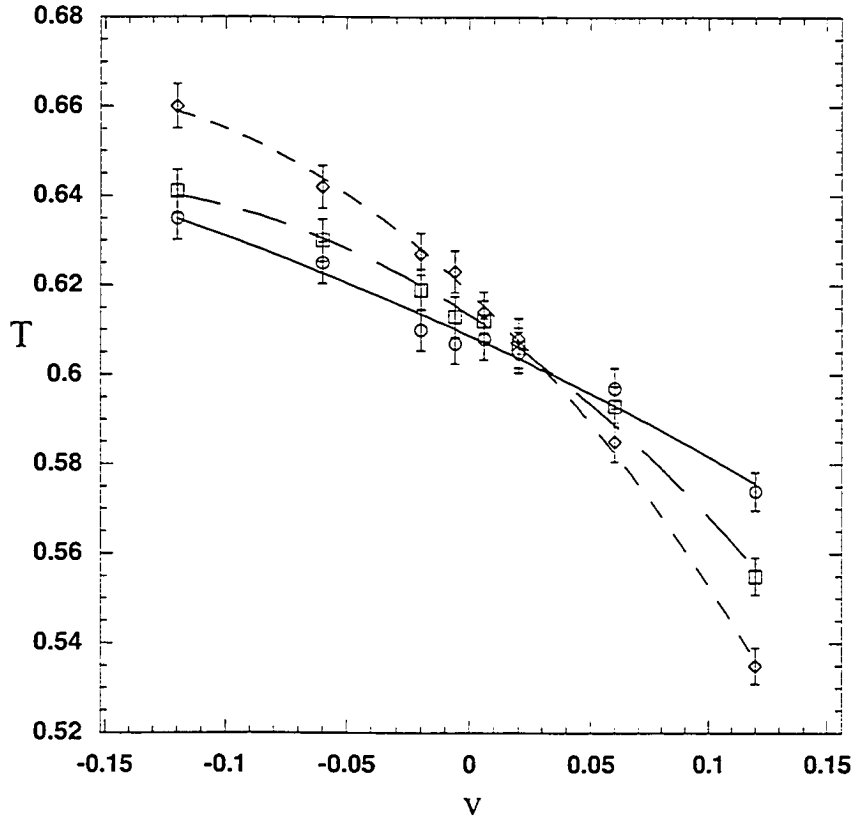

Figure 4.7 Dependence of melting and freezing temperatures on crystallizing velocities, v, for the 001 (circle), 011 (square) and 111 (diamond) crystal faces. The lines represent the best quadratic fits to the data.

Further inspection of Figure 4.7 reveals that the melting temperatures of the 111 face is shifted to higher temperatures with increasing velocity, followed by the 011 and the 001 crystal faces; the crystallizing temperature is observed to decrease in the same order. The same behaviour was observed for all the gradients examined in this study. This trend implies that for the 111 face, crystallization occurs at higher temperatures and melting occurs at lower temperatures for a given velocity in comparison with 001 interfaces. Thus, for a given temperature gradient, the maximum growth rate of 001 will occur at much higher velocities. The data in Figure 4.7 agrees very well with data from Figure 2 of Burke et al. [155].

The data in Figure 4.7 for all three crystal faces is consistent with apparent linear behaviour (with continuous derivatives) close to zero velocity, in accord with agreements made in ref. 155, and deviations from linearity appear to occur as high velocities are approached. The asymmetry in crystallizing and melting temperatures observed at high velocities reflects the growth/melting rate behaviour discussed earlier. Zero velocity can again be understood as the equilibrium limit for the system, where at both the crystallizing and melting fronts the ordering of atoms is occurring at the same rate as the disordering of atoms. Hence, no slope discontinuity will be observed close to equilibrium. Away from equilibrium one of these basic processes will dominate. For example, under conditions appropriate for crystal growth one can visualize that ordering processes are occurring faster than disordering processes [3]. The structural fluctuations observed in the equilibrium and non-equilibrium simulations have confirmed this behaviour. Thus, as one would expect, ordering and disordering are different and distinct

processes, occurring at both melting and crystallizing fronts, which will be further explored later in this chapter.

4.1.6 Interfacial tension

The simulation methodology of this study allows the direct calculation of average forces in the z direction (perpendicular to the interface) as the z-derivative of the energy profile described in section 4.1.1. Interestingly, what emerges from taking this derivative is a profile function representing a detailed account of the average forces through the interface [32], as described in Section 2.1; these forces enable the procurement of the interfacial tension as the (maximum) force per particle (hence diameter) from this methodology. Table 4.2 lists the values of interfacial tension recorded at different gradients. There is an apparent increase in interfacial tension values with increasing gradient, however this can be shown to be the result of a baseline shift that is due to the influence of the temperature gradient on the energy profile. If these gradient effects are removed and the interfacial tension values are extrapolated to zero gradient, the obtained values are approximately 0.02 lower than smallest gradient values given in Table 4.2 for all the faces. Whereas gradient dependence makes it somewhat difficult to estimate accurately absolute values for interfacial tensions, this method permits the determination of the differences between values for the various faces (i.e. the anisotropy) with considerable confidence.

These values generally agree with those obtained by Broughton and Gilmer [153] and more recently by Davidchack and Laird [161] and Morris and Song [162]. The values obtained here show that the 001 crystal face has a consistently higher value of the

interfacial tension at all gradients than the 111 face. This observation is in accord with the fact that the interfacial widths of 001 are much larger than those of the 111 face; the latter face appears to be a narrower and smoother interface that exhibits less structural fluctuations (this observation is confirmed by Williams, Moss and Harrowell [163]). The values for interfacial tension and for width of the 011 interface are between those of the 001 and 111 crystal faces.

Table 4.2 Interfacial tensions obtained from steady-state LJ FCC systems. Estimated errors in the last digit are given in parentheses.

Gradient / Crystal faces	0.4	0.2	0.1
001	0.42(1)	0.36(1)	0.31(1)
011	0.43(1)	0.36(1)	0.34(1)
111	0.45(1)	0.39(1)	0.36(1)

The present results disagree with those of Davidchack and Laird [161] and Morris and Song [162]) suggesting the surface free energies (interfacial tension) decrease in the order 001 > 011 > 111. The technique used by Davidchack and Laird [161] uses computer simulation to calculate a continuous thermodynamic path that can be integrated from a starting system of bulk liquid and solid to a final state containing the interface. Davidchack and Laird [161] have claimed to have extended and improved upon the

procedure of Broughton and Gilmer [153], where they have used planar cleaving walls as opposed to cleaving potentials to separate the phases. One of the key approximations of Davidchack and Laird [161] was to consider the interface to be a planar entity. After stating in their paper that the interface should be generally "rough" on a short time scale, they added that the fluctuations in the interfacial position should average out to a planar surface; this statement on the microscopic structure of the interface appears contrary to my observations: the interface is inherently a dynamic entity that fluctuates in position and structure and, therefore, will always be "rough" on the molecular scale. The planar interface assumption (constraint) of Davidchack and Laird [161] may be a contributing factor in their values. The rationale of the calculations undertaken by Morris and Song [162] contain some deficiencies. For instance they indicate that the instantaneous position of the interface can be defined and used as a reference point yet have no means to confirm this measure. In this thesis, a method to unambiguously define the interface has been developed that hitherto has not been available. Additionally, Morris and Song claim that the presence of increased fluctuations, about a reference point, over the total simulation time indicates and confirms a high interfacial free energy. Chandler [36] has made the contrary statement, namely, that if there is less free energy available to maintain a surface, then greater fluctuations will result to break down such a surface.

4.2 MECHANISMS OF CRYSTALLIZATION

4.2.1 Details of analysis

The systems chosen for this section were 'big' systems given in Table 3.1 typically subjected to a moderate temperature gradient and were studied at a moderate velocity

(0.06). These conditions were chosen because they have been previously shown to be well suited for the examination of the crystallization and melting behaviour of LJ systems. Where appropriate, results obtained for higher velocity and larger gradient systems will be also be discussed [169].

a) Representative configurations

Analysis of system configurations will be a key component of the present study since one of its goals is to provide a systematic and consistent microscopic description of the mechanisms involved in crystallization and melting. In MD simulations, the many trajectories of all the particles of the system are followed in time, where at every time step their positions will change. To facilitate viewing of the behaviour important to the present study, an averaging procedure was required to effectively remove the thermal motions of the particles so that any net translational motion could be more easily observed. This approach consequently allowed a far more complete characterization of the interfacial region and permitted atomic-level details of the freezing and melting processes under steady-state conditions to be examined. This was accomplished by maintaining rolling averages of particle positions over 80 timesteps and, subsequently, dumping these averaged coordinates (an averaged configuration) every 750 timesteps; typically, a sequence of a few hundred such configurations was produced. This optimum averaging procedure was selected based on the smallest time window and lowest frequency of dumps necessary to capture the essential physics of the system. For visualization purposes, the multiple files produced were then animated to view the time-dependent behaviour of the particles in a single layer, as many layers or as a whole

system. For visualizing the microscopic behaviour of the atoms during crystal growth and melting, standard visualization software was used in conjunction with software developed by the present author to facilitate visualization of the physical processes within the systems being investigated.

One means of elucidating the critical structural aspects of the interface was to superimpose the derivatives of the energy and Σ profile functions on a series of representative time-averaged configurations of the corresponding steady-state atomic system; an example of which is shown in Figure 4.8. In this figure, the atomic structure is apparent as overlapping circles. This representation facilitates observation (and distinction) of the solid-like and the liquid-like regions. In this way, the structure of the crystallizing and the melting interface has been probed. The degree of crystalline character through the interface has been ascertained and the extent of structural fluctuations monitored at growing or melting fronts. Such sets of the averaged configurations also allow the examination of the nature of the fluctuations that can occur in an interface during steady-state growth or melting. They also provide important insights into the meaning of interfacial widths as defined by the derivatives of the energy and Σ profiles.

b) Slice identification and monitoring

In the analysis of the averaged configurations from simulations performed in this study, slicing of the "crystal" at the interface was performed in two ways. The first approach involved slicing the system near the interface into layers as determined visually. These layers, or slices, were then inspected systematically to identify and label the atoms

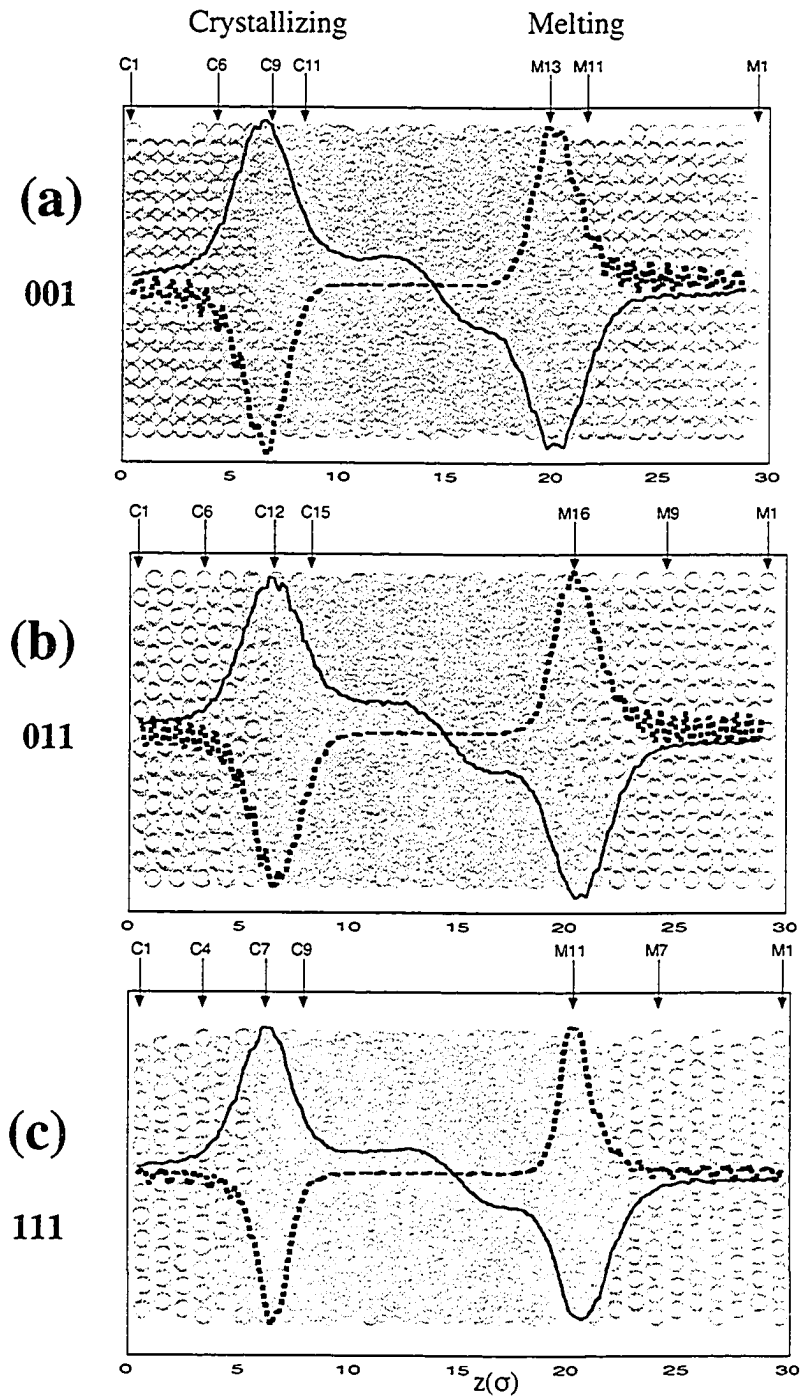

Figure 4.8 Representative averaged configurations of 001 (a), 011 (b) and 111 (c) steady-state systems. Derivatives of the energy and Σ profiles for each system are superimposed as solid and dashed lines, respectively. The position of the crystallizing and melting interfaces are as indicated for each system along with the layer numbers used in the texts. The layers are labeled in ascending order from the solid to the liquid side for both interfaces.

in a particular layer. The percentage of crystalline character present in slices through the interface was obtained from the corresponding values of the Σ order parameter at the appropriate position. The degree of crystalline character of a slice was then simply the percentage relative to the Σ value of the bulk solid for a particular system. It was also useful to superimpose 2 or 3 consecutive layers and to check visually for possible correspondence of the order (crystallinity) within successive layers (for example, see Figure 4.9(b)). The interfacial layers that will be discussed in the next section are labeled "C" for those at a crystallizing interface and "M" for a melting front, where their numbers indicate their positions relative to the solid side of the interface, as shown in Figure 4.9(a). The labeling of slices for any particular system is consistent throughout this section (for example, for the 001 system in Figures 4.9, 4.10, 4.11 and 4.12). An alternative method that was used in the analysis of the formation (or disappearance) of layers involved the indexing (or tagging) of particles. As an example, let us assume that a set of averaged configurations from a particular segment of a system trajectory has been produced. The final averaged configuration is examined and the particles that compose the layers of the *crystal* near the interface are indexed (tagged).

For visual identification, the particles that compose each of these slices are labeled a different colour. It is then possible to follow the behaviour of the tagged particles throughout the full series of averaged configurations, thereby allowing one to monitor at the atomic level how the process of crystallization occurs. This method also affords detailed insights into the way neighbouring slices might influence the slice of

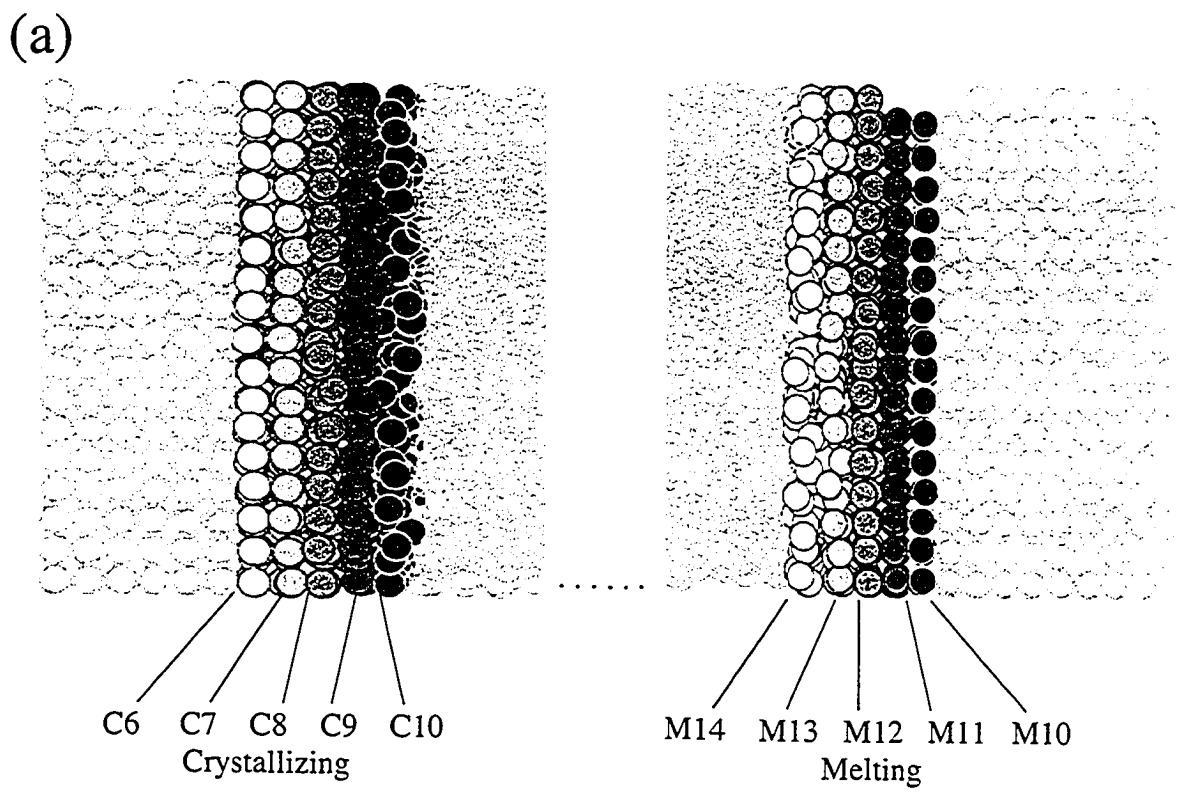

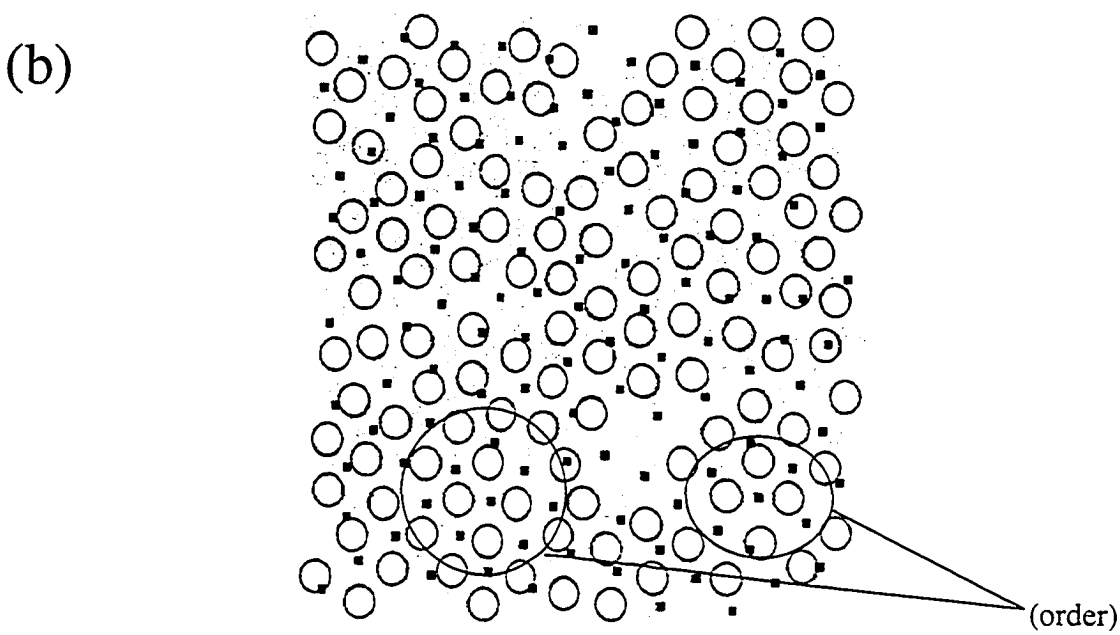

Figure 4.9 (a) Layers of the crystallizing (C6-C10) and melting (M10-M14) interfaces of an averaged configuration of a LJ 001 FCC system. Five slices are identified and labeled (shaded differently) for each interface with the layer numbers as given in Figure 4.8. (b) The forward view of three layers: C10 (small squares), C9 (open circles) and C8 (filled circles). Areas showing crystalline order have been identified.

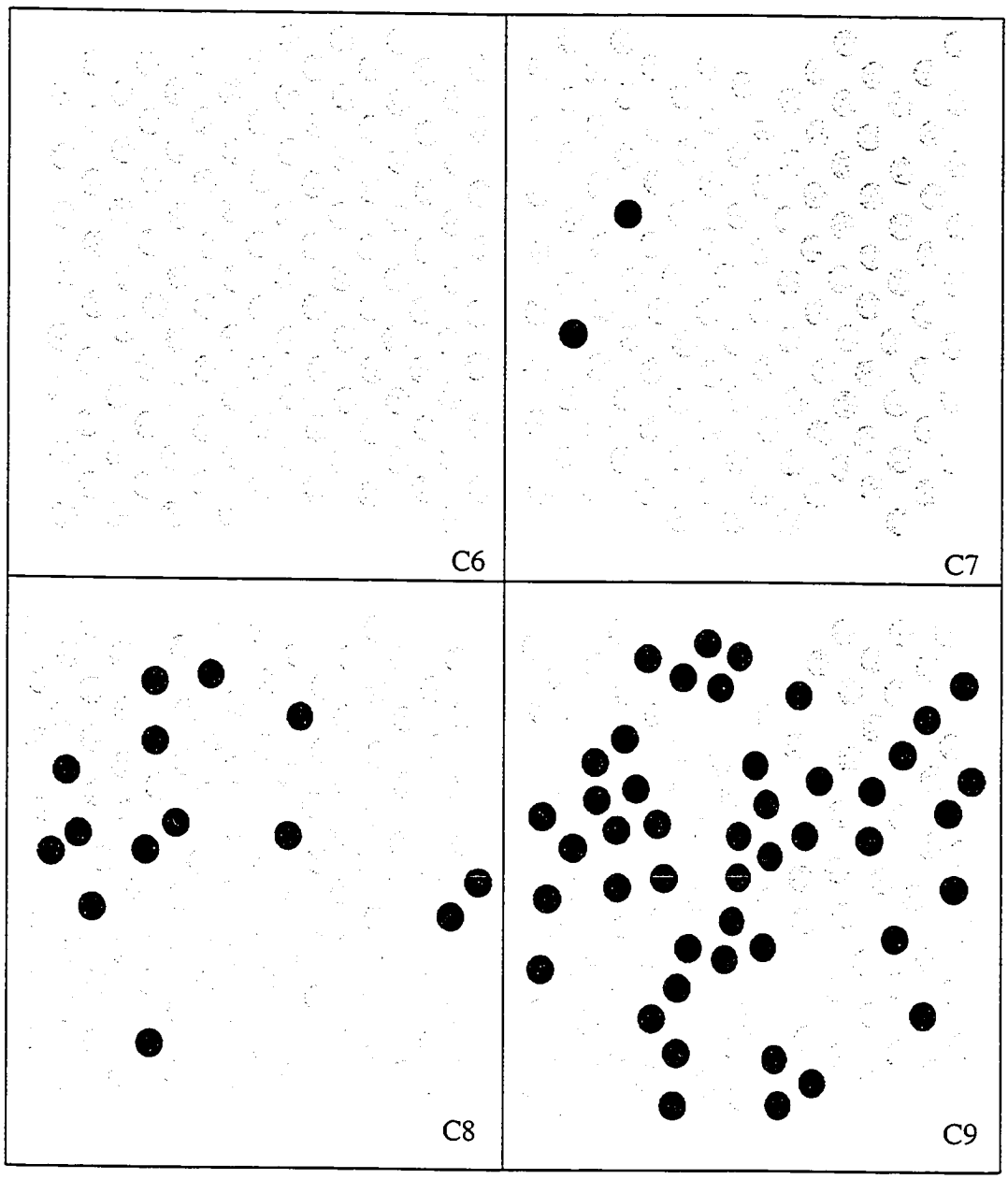

Figure 4.10 Averaged configurations of four consecutive slices through the crystallizing interface of the same LJ 001 FCC system as in Fig. 4.9. Layers are labeled as in Figure 4.9. The dark atoms are transient particles as defined in the text.

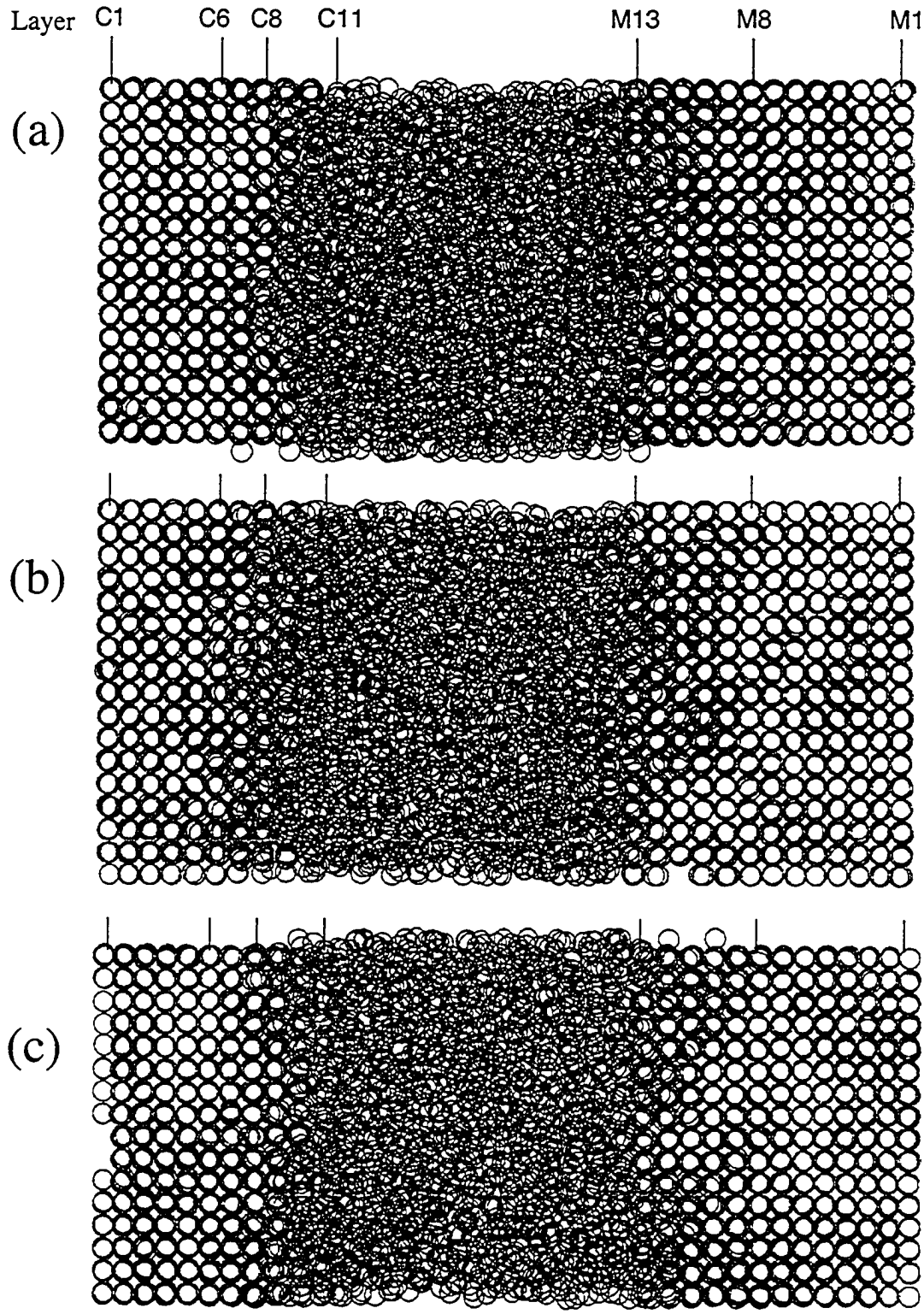

Figure 4.11 Three averaged configurations of the LJ 001 FCC system (same as Fig. 4.9). Particles are shown as open circles and the numbering of the layers are identical to Figure 2(a) (same as Fig. 4.9): (a) represents an arbitrary initial frame 0, (b) frame 43 and (c) frame 50, where each frame is separated by 750 timesteps.

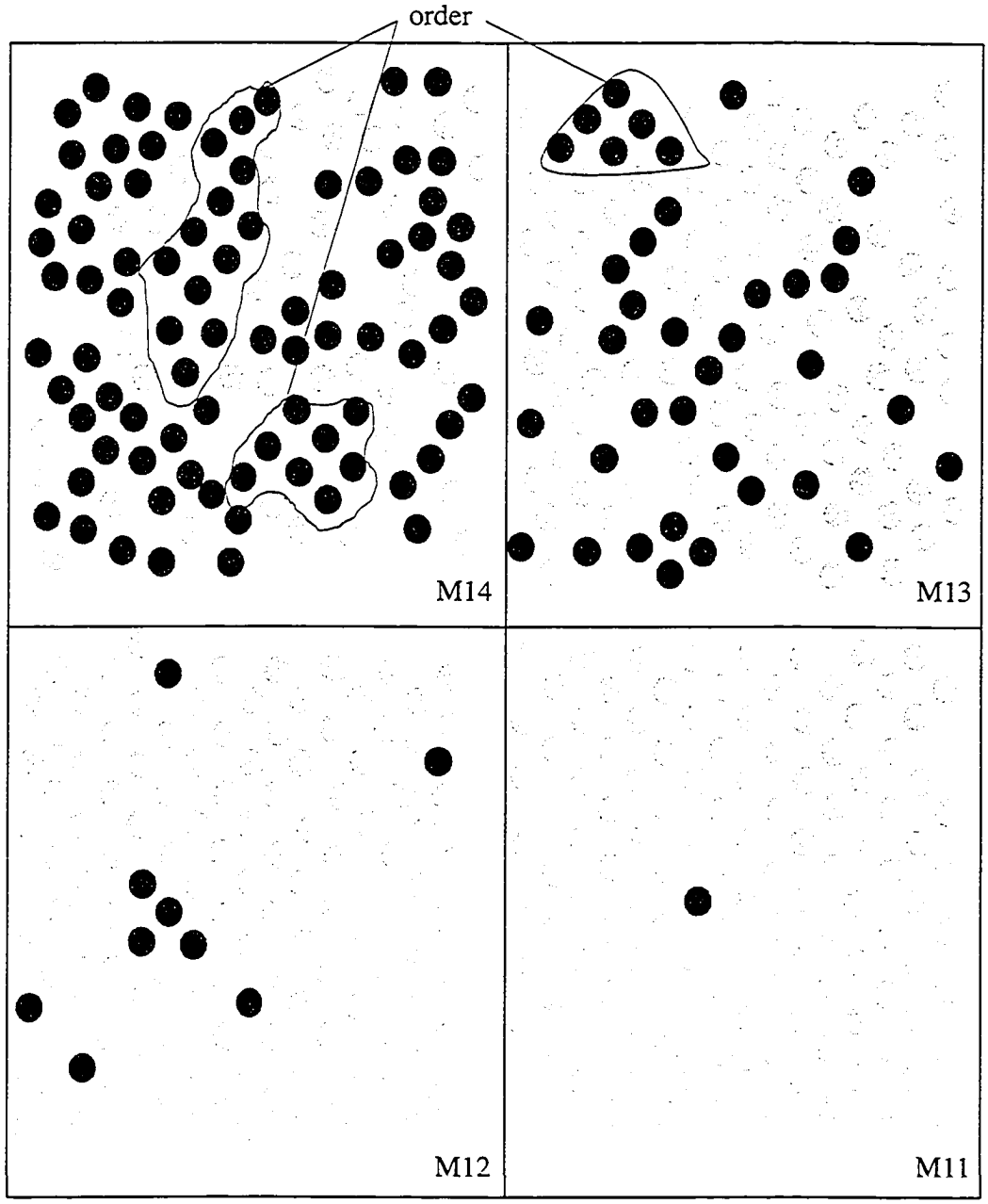

Figure 4.12 Averaged configurations of four consecutive slices through the melting interface of the LJ 001 FCC system (same as Fig. 4.9). Layers are labeled as in Figure 4.9. The dark atoms are transient particles as defined in the text. The identified areas show crystalline order.

interest the analogous (inverse) labeling scheme was also employed at the melting interface

The visualization of slices is performed in two ways. The first is to inspect (display) only the tagged particles from the simulation. This allows one to identify possible nucleation sites that may form during crystal growth and provides a detailed view of how these particles interact and form an ordered layer. The second approach involves examination of one or a few layers of the system where tagged and untagged atoms are coloured appropriately. This procedure was adopted because the process of crystallization (and melting) involves the cooperative behaviour of many atoms/molecules [153,160], where there are considerable exchanges of particles between layers. The visualization method allows the formation of a layer to be followed along with the impact that adjacent layers may have on the crystallization of the layer of interest. Analogous analyses were performed on the melting interface.

In following a particular sliced layer through time during freezing/melting using the above procedures, it was possible to establish an equivalent analysis through inspecting the various slices of an averaged configuration of a particular interface; the various slices of any particular averaged configuration exhibit essentially the same stages that a specific slice goes through during the process of freezing/melting. In subsequent discussions, the focus will be on the averaged configuration method (although both approaches were utilized in investigations of the behaviour). As an example, Figure 4.10 shows four slices of a crystallizing interface, or alternatively, it can be viewed as different stages a slice would experience in forming a crystalline layer.

4.2.2 Interfacial structure of the 001, 011 and 111 crystal

To facilitate their identification, the various layers in a steady-state system have been uniquely labeled. For the 001 interface being specifically examined here, these layers are C6-C10 and M10-M14 for the crystallizing and melting interface, respectively, as shown in Figure 4.9(a). The averaged configuration illustrated in Figure 4.9 is representative of the 001 interface presented in Figure 4.8(a). The structural fluctuations typical of the 001 interface are depicted in Figure 4.10; a comparison of these three averaged configurations reveals that the 001 interface undergoes large structural changes during steady-state growth. Similar structural changes were also observed by Moss and Harrowell [170]. It is clear that the structural fluctuations observed in Figure 4.10 will contribute to the apparent thickness of the interface. Widths of 5.2σ (7-8 atomic layers) and 4.2σ (5-6 atomic layers) are obtained for this interface if the derivatives of the energy and Σ profile functions are used, respectively.

A similar analysis can be applied to the 011 interface. Estimates of its interfacial width are about 5.0σ (8-9 atomic layers) and 4.0σ (6-7 atomic layers) if the derivatives of the energy and Σ function are employed, respectively. As with the 001 face, large structural fluctuations are observed at the 011 interface, as can be seen in Figure 4.13.

However, the fluctuations here appear primarily in the form of 111 microfacets on the crystal front. These microfacets were observed in all averaged configurations examined for this crystal face (see Figure 4.13).

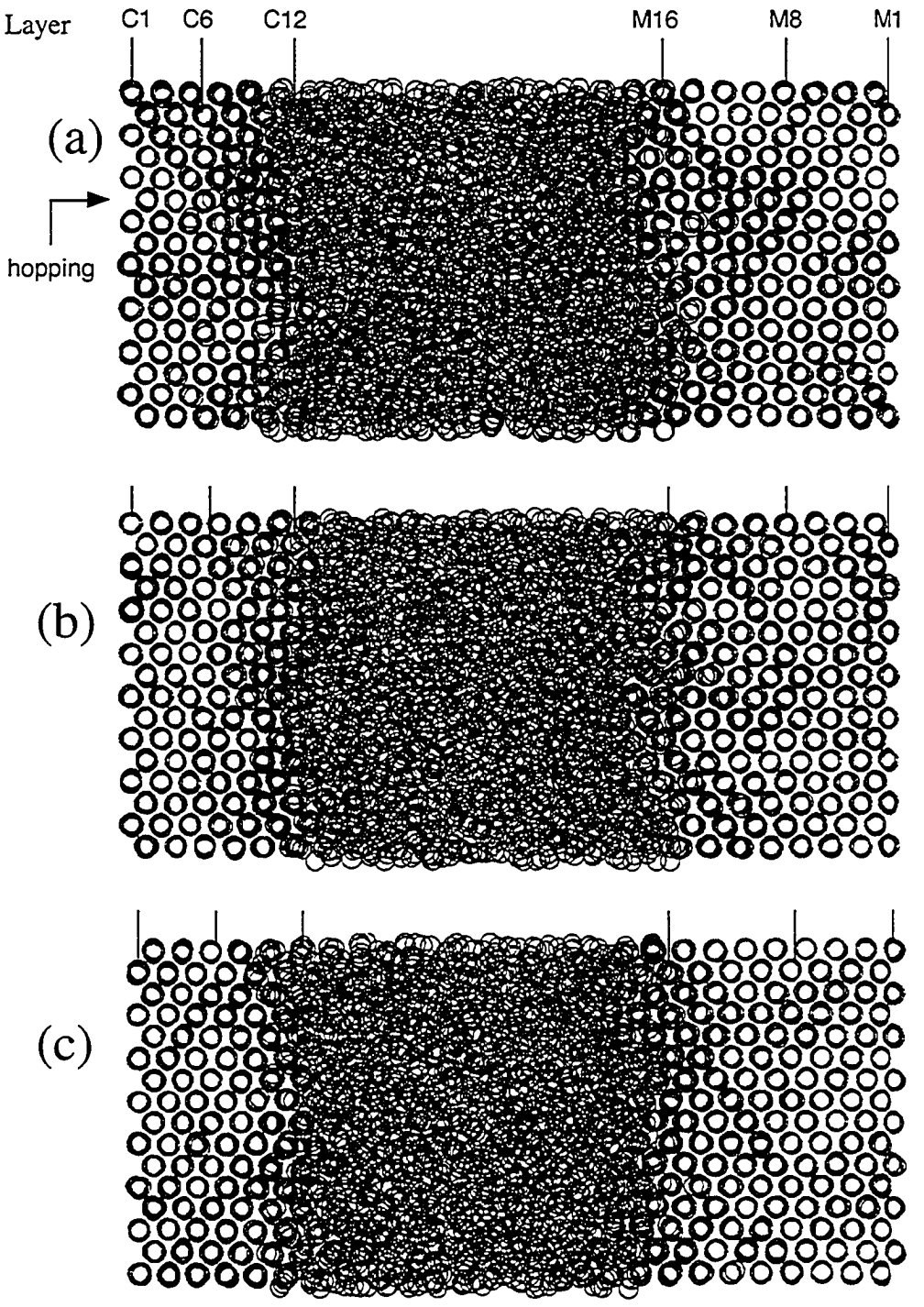

Figure 4.13 Three averaged configurations of the LJ 011 FCC. Particles are shown as open circles and the numbering of the layers are identical to Figure 4.8(b): (a) represents an arbitrary initial frame 0, (b) frame 32 and (c) frame 45, where each frame is separated by 750 timesteps. The arrow in (a) identifies the row where atom hopping is observed to occur in layer 6.

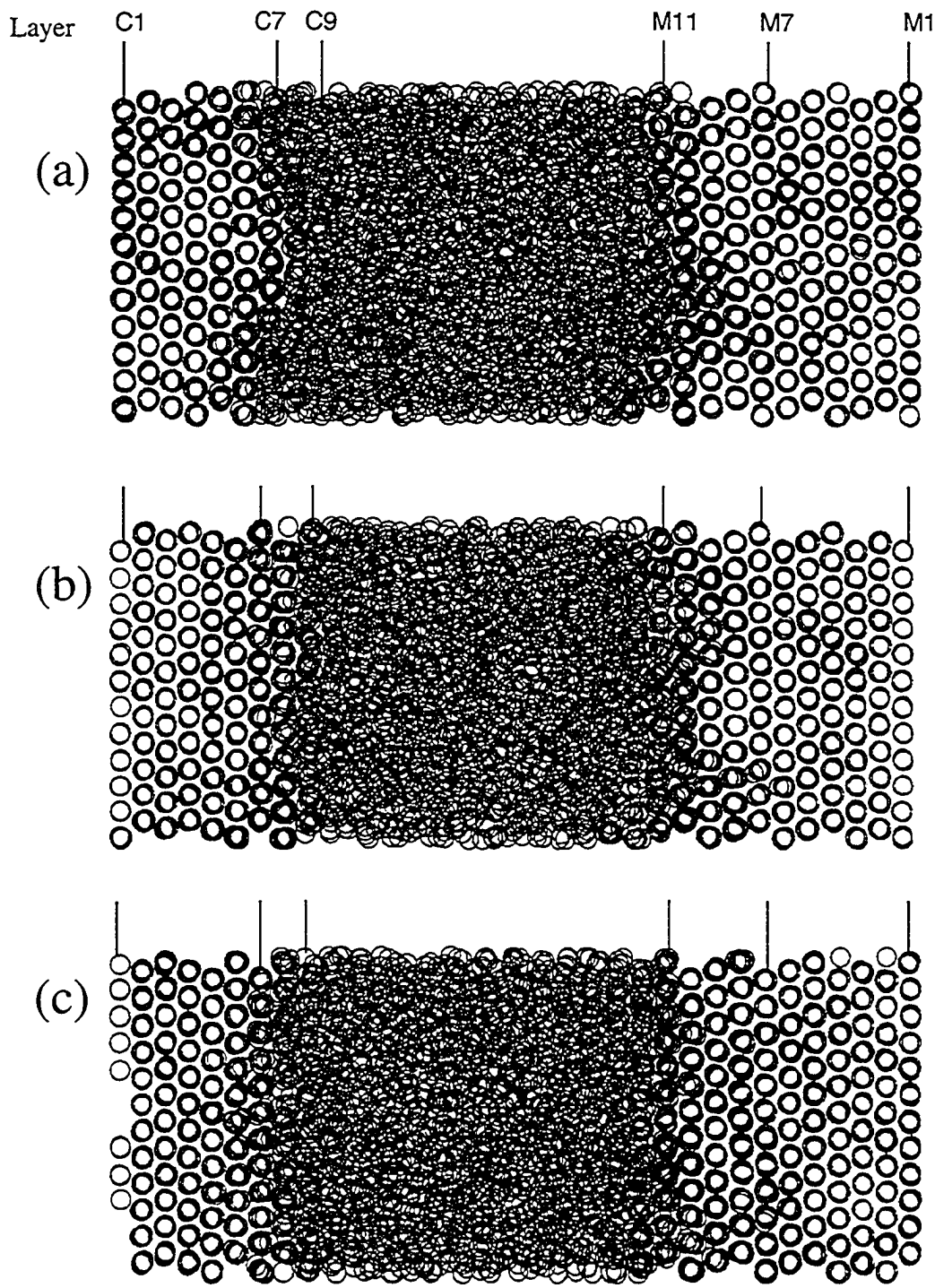

Figure 4.14 Three averaged configurations of the LJ 111 FCC. Particles are shown as open circles and the numbering of the layers are identical to Figure 4.8(c); (a) represents an arbitrary initial frame 0, (b) frame 11 and (c) frame 50, where each frame is separated by 750 timesteps.

Interfacial widths of 4.8σ (5-6 atomic layers) and 3.2σ (3-4 atomic layers) are obtained for the 111 interface if the derivatives of the energy and Σ profile functions are utilized, respectively. The magnitude of the structural fluctuations apparent in the 111 solid/liquid interface (see Figure 4.14) is much smaller than for the 001 and 011 interfaces. This observation of a reduced structural fluctuation is consistent for all the 111 configurations examined during my analysis.

The extent of the structural fluctuations can be linked to the interfacial tension for each of the various crystal faces, where the magnitude of the structural fluctuations at the interface can be understood [36] as being sensitive to the free energy cost in forming a unit area of "interface". The interfacial tension of the 111 crystal face is higher (therefore the free energy cost of increasing surface area is higher) [163], consistent with the smaller structural fluctuations occurring within this interface [145]. Examining the 001 and 011 faces, their larger fluctuations now reflect the lower free energy cost in forming a unit area of interface. These faces have been also observed [154] to grow faster than the 111 crystal face. The mechanism of crystal growth for these different faces appears bound to their "structural fluctuations", which in turn are determined by their interfacial tensions. The next section will explore these issues in further detail.

4.2.3 Freezing and melting mechanisms of 001, 111 and 011 crystal faces

In order to provide a detailed microscopic account of the freezing and melting behaviour for the various crystal faces, information from averaged configurations will be used to illustrate specific characteristics of melting and freezing. The analysis will commence from the liquid side of the interface and move through the centre of the

interface towards the solid. Generalizations of interfacial behaviour on freezing and melting have been made based on extensive observations of steady-state systems under various conditions of gradient and velocity.

001 crystal face

The layers C6-C12, as shown in Figures 4.8(a), 4.9(a) and 4.10, represent the various stages that a slice undergoes during crystallization, as well as capturing the environments influencing the ordering processes. The outermost layer of the crystallizing interface will be examined first. This layer, C12 in Figures 4.8(a) and 4.11, exhibits no obvious atomic layering. At this position, near the liquid edge of the interface, patches of order (transient entities undergoing continuous fluctuations) are just beginning to appear. In layer C11 (see Figures 4.8(a) and 4.11), there is some apparent solid-like behaviour, where on average between 0-10% of solid order (as defined in section 4.2.1) is observed and the order here may persist to form a crystalline layer.

At C10 larger solid patches, which tend to persist longer (see Figures 4.9 and 4.11(c)) with large structural fluctuations are apparent; this layer between 10-50% of solid order has been observed. Inspection of layer C9 reveals that at least half of this slice appears crystalline (see Figures 4.8(a), 4.9 and 4.10), although sometimes (see Figure 4.11(a)) considerably less order in this layer is observed. It is clear from Figure 4.8(a) that C9 corresponds to the middle of the interface. In Figure 4.10, the atoms of layer C9 are labeled black and grey, where the grey (tagged) atoms are those that are still present in the final crystalline layer (as described in section 4.2.1). Hence, black particles are those atoms that do not end up in the final crystalline layer. Figure 4.10 (C9) clearly

shows that many of these (black) atoms are in crystalline positions. Such black atoms are thus only transient occupants of crystalline positions, even though the degree of crystalline order in C9 is between 50-80%. These (black) atoms will eventually reside in adjacent layers, primarily C10. This hopping, or exchange, of atoms between layers is a critical dynamical feature of the solid/liquid interface.

Inspecting layer C8, in Figures 4.9, 4.10 and 4.11, shows that it appears almost completely crystalline with a few defects. However, there are still some transient (black) atoms in crystalline positions, indicating that this layer is not truly crystalline and will continue to undergo some exchanges of atoms with adjacent layers. Layer C8 also still contains some distortions of its crystal structure with an estimated 80-100% crystalline order present. Moving now to C7, we see in Figure 4.10 that there are still a few transient (black) atoms in what otherwise appears to be a well-ordered crystalline layer. The particle hopping still occurring in C7 almost exclusively involves exchanges with the layer C8 (closer to the liquid). Examination of layer C6 (see Figures 4.8, 4.9 and 4.10) shows no transient (black) atoms in this layer that lie on the solid edge of the interface. This layer is almost fully crystalline with particle hopping occurring only rarely, where such events appear to be triggered by structural distortions in the adjacent (liquid-side) layers. Clearly, the present approach of tagging atoms has allowed detailed observations of atomic behaviour that might otherwise be easily overlooked.

The mechanism by which the 001 face crystallizes can now be discussed in terms of the descriptions given above. As is evident in Figure 4.9(b), there are "fingers" of order that extend through the interface, across layers, revealing that the interface is a complex, three-dimensional and dynamically fluctuating entity. It is this behaviour,

characterized by constant structural fluctuations where atoms collectively take up and leave crystalline positions, that is inherent to the growing interface.

Shifting the analysis to the melting process, the method of analysis is analogous to the crystallizing interface, with the discussion of the melting interface commencing on the solid side. Figures 4.8(a) and 4.9(a) identify the two outer layers, M10 and M11, of the melting interface. Minor distortions of the crystal layer are observed coupled with observations of atomic hopping, as shown in Figure 4.12 (M11); these particle exchanges can be seen to be the first stage of melting. The layer M12 exhibits more distortions and defects with more incidences of atom hopping. At the centre of the interface (M13) (see Figures 4.8(a), 4.11 and 4.12) a layer with only partial solid order is seen. In addition to particles leaving (exchanging), further disordering of the layer is observed; there is evidence indicating that particles are reorganizing into (new) ordered structures distinguishable in M13, as shown in Figure 4.12. Continuing through the interface the last two layers, M14 and M15 are similar in structure to the first two layers (C10 and C11) of the crystallizing face. In M14 the majority of the remaining crystalline order is accounted for by transient (black) atoms that make up (new) ordered clusters within the melting interface, as can be seen in Figure 4.12.

Naively, one could argue that freezing and crystallizing are just opposite processes. This would be consistent with observations that profile properties (such as width) are the same for the crystallizing and melting interfaces. However, within a crystallizing (or melting) interface I note that two separate and competing processes are operative, namely ordering and disordering. Therefore, at a melting front, the disordering processes are occurring faster than the ordering processes. Thus, the structure of layer

M13 (see Figure 4.12) is very similar to that of C9 (see Figure 4.10) where both of these layers are at the center of their respective interfaces and contain 50-80 % of solid order.

There also exists a clear asymmetry [155] in the freezing and melting rates despite the similarity of the interfaces, with melting occurring at faster rates than freezing at higher velocities. This can be understood by again comparing the layers C9 (Figure 4.10) and M13 (Figure 4.12) at the middle of their respective interfaces. They both show evidence of structural fluctuations, and comparatively equal content of solid-like and liquid-like behaviour. Within C9, different fragments of several crystal structures, including FCC and some HCP clusters can be identified. Consequently, before this layer can fully crystallize, there needs to be a collective organization of its atoms into a crystalline structure that is commensurate with layer C8. This necessitates that there be sufficient time for the desired structures to appear (as collective fluctuations) and for the undesirable structures to be eventually eliminated. For the melting layer, M13, no such additional time is required, as the defects and mismatched crystal structures will not hinder (and presumably aid) the melting of the layer.

111 crystal face

The crystallization of the 111 interface is examined in Figures 4.14, 4.15 and 4.16. The freezing process of the 111 crystal face begins to occur with a few transient patches of order forming in C9 at the liquid edge of the interface (see Figure 4.15), which can be either FCC or HCP in nature. These transient patches, also observed by Burke et al. [155], undergo considerable fluctuations and so are similar in behaviour to those within the 001 interface. From the averaged configurations shown in Figure 4.14, no

discernable layer is observable at C9. Moreover, crystal patches have not been observed to persist in C9. At C8 (see Figures 4.15 and 4.16) there appears to be different (competing) sub-lattice structures as a result of structural fluctuations. It is at C8 that the first crystal layer structure is observed, with at least a partial layer evident in Figure 4.14(b), but on average only between 10-50% solid order is present and none of the crystalline clusters appear to traverse the whole layer. As can be seen in Figure 4.16, transient (black) atoms occupy both crystalline (majority) and non-crystalline positions in this layer. In addition, layer C8 was found to influence strongly the solid-like fluctuations of layer C9.

Inspecting C7, slide dislocations and point defects can be found in this layer (see Figure 4.16). Figure 4.14 shows some distortion of the order within this layer, which is found to exhibit 50-80% of solid order. This layer can be identified as the center of the interface. However, exchanges of atoms are still clearly evident between C7 and adjacent layers. C6 as well as C5 appear structurally completely crystalline, yet particle hopping in these layers can still be observed. Minor distortions of C6 and C5 are still visually discernable, with the latter, which is now at the solid edge of the interface (see Figure 4.8(c)), showing much less distortion.

From Figure 4.15(b) one observes that C8 and C7 have commensurate crystalline order in the area indicated as region 1 and pockets of order elsewhere. However, it has been discovered that the structural fluctuations that dominate the behaviour at C9 are not usually commensurate with C8. In Figure 4.15(b), a discernable HCP cluster in region 2 and a FCC cluster in region 3 at C9 can be identified. Therefore, C9 can be characterized

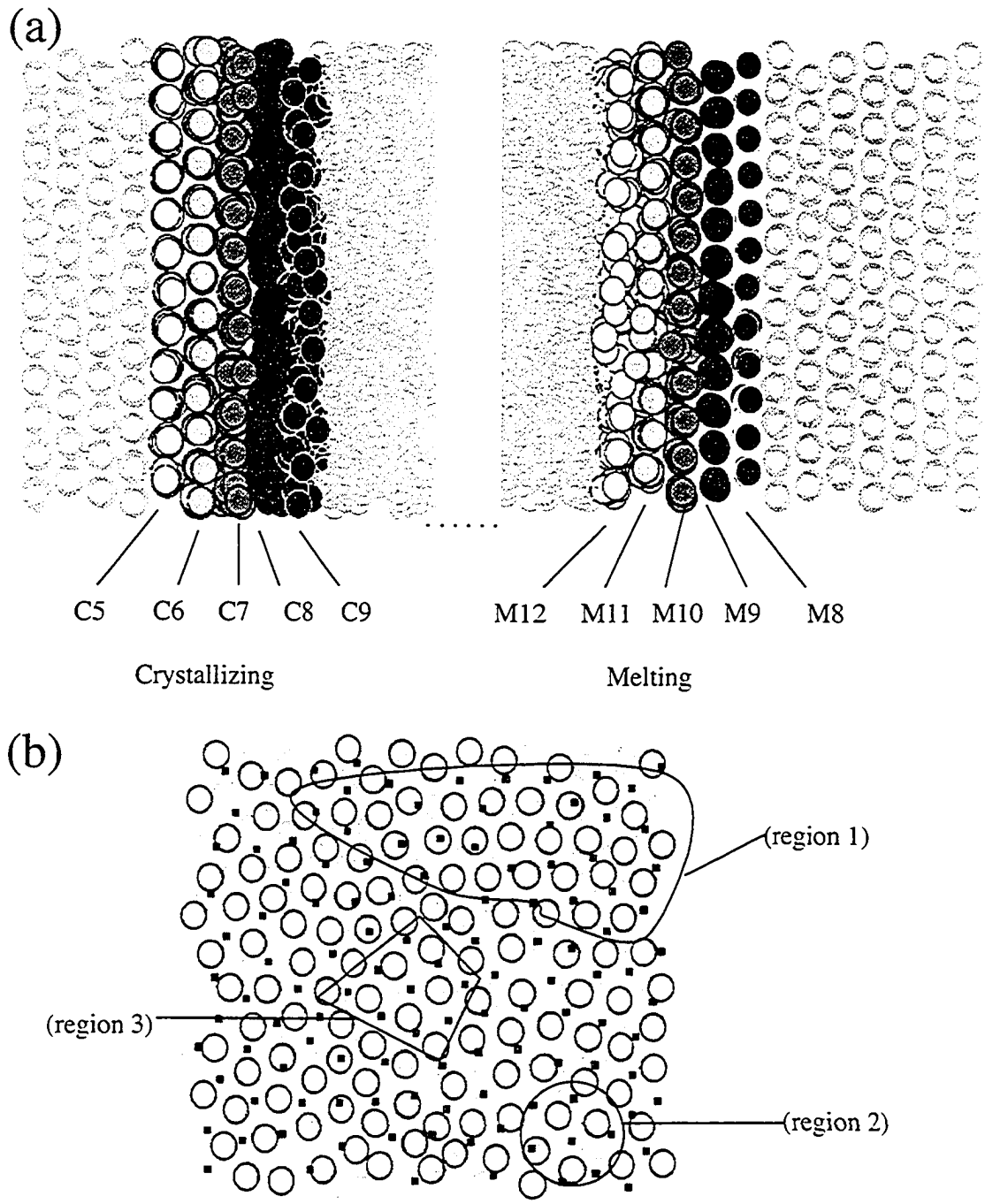

Figure 4.15 (a) Layers of the crystallizing (C5-C9) and melting (M12-M8) interfaces of an averaged configuration of a LJ 111 FCC system. Five slices are identified and labeled (shaded differently) for each interface with the layer numbers as given in Figure 4.8(c). (b) The forward view of three layers: C9 (small squares), C8 (open circles) and C7 (filled circles). Region 1 shows commensurate crystal structure between C8 and C7. Region 2 contains a HCP cluster and Region 3 shows a 001-FCC cluster.

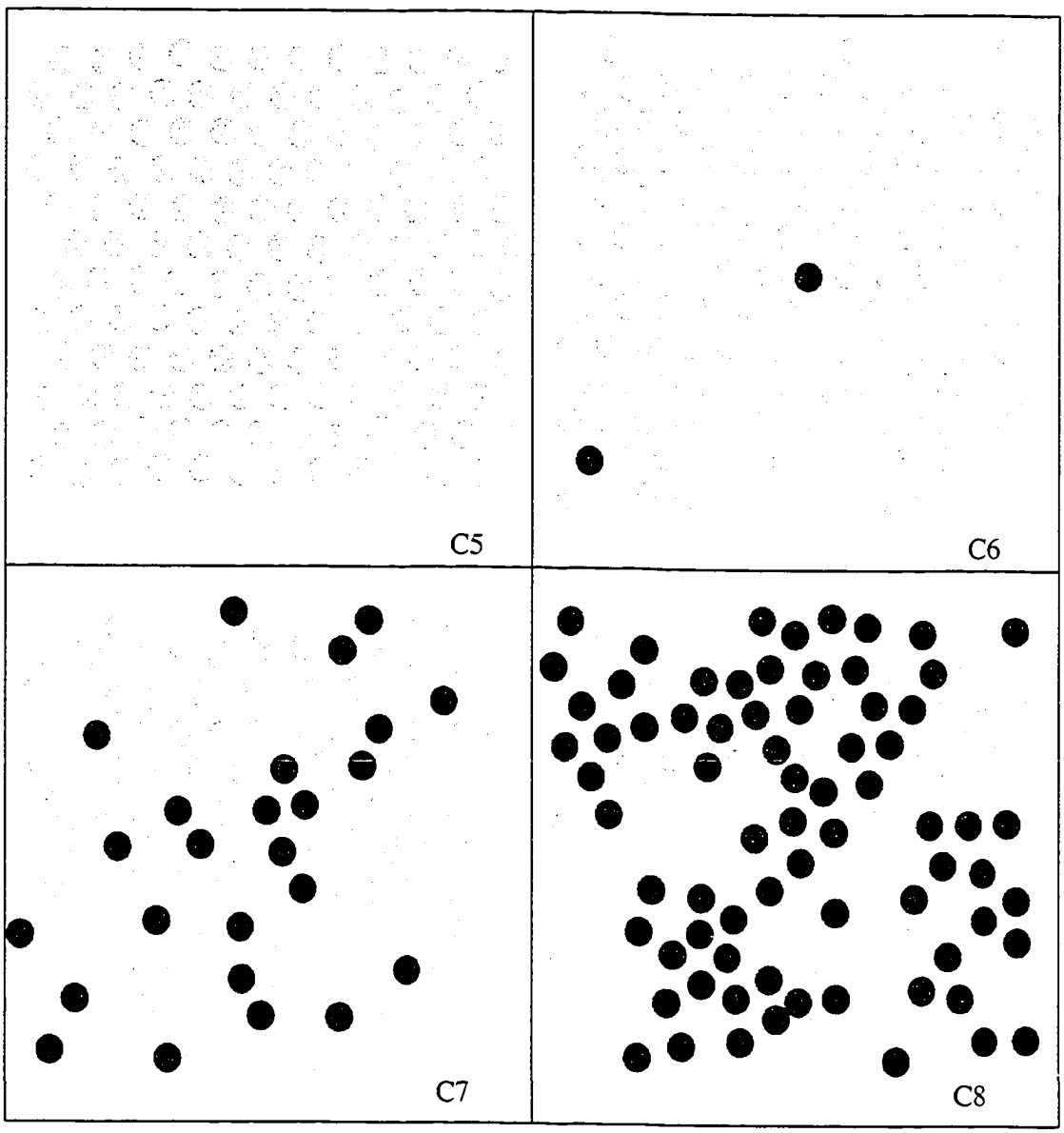

Figure 4.16 Averaged configurations of four consecutive slices through the crystallizing interface of the LJ 111 FCC system. Layers are labeled as in Figure 4.15. The dark atoms are transient particles as defined in the text.

as the layer with the most apparent dynamic fluctuations, where these fluctuations are sampling many related crystal structures. In contrast to the 001 face, no fingers of order are discernable extending through the interface. Hence, the conclusion here is that the 111 interface is sharper (for example it has no layer with 0-10% of solid order) than the 001 interface.

The above analysis suggests that for the 111 face, crystal growth properly begins with layer C8, where it takes considerable time to match correctly the structure within layer C7 (which resides at the center of the interface). This annealing behaviour has been seen by Burke et al. [155] in their descriptions of crystal growth of the 111 crystal face. However, they did not identify the fluctuation in solid structure within C9, the layer before C8, which is the origin of crystal nuclei that may grow into a crystal layer (only in a few cases).

The structure of the 111 melting interface is very similar to that of the 111 crystallizing interface. In essence, the same behaviour is observed within layers M8-M12 as was described for C5-C9, but in the former layers the disordering processes appear to dominate. Not surprisingly then, the melting process for the 111 face is as described for 001, with the same mechanism operative and responsible for the asymmetry between the freezing and melting rates.

011 crystal face

The behaviour at the 011 crystal face is in many respects rather similar to that of the 001 interface. Examining layer C14 in Figure 4.17 at the liquid edge of the crystallizing interface (see Figure 4.8(b)), one finds behaviour analogous to that seen with the 001

interface with patches exhibiting crystalline character apparent; FCC, HCP, and 011 structures are observed. Only the 011 structures persist and grow if they are commensurate with the underlying crystalline structure. The crystalline order in C14 varies between 0 and 10%. At layer C13, considerably more crystalline character (between 10-50%), as shown in Figures 4.17(b) and 4.18, can be found. The latter figure also reveals a HCP cluster as indicated. From Figure 4.13, evidence of 011 layers is just becoming discernable at C13. At C12 more crystalline order is observed, about 50-80% as shown in Figure 4.18. It is at layer C12, at the center of the interface (see Figure 4.8(b)), that clear layers are observed in Figure 4.13(b). There are also transient (black) atoms in crystalline positions apparent in C12 in Figure 4.18. Inspection of C11 reveals point defects; this layer is 80-100% crystalline and only a few transient (black) atoms are observed in Figure 4.18. Finally, at C10 the layer is essentially crystalline with occasional atom hopping occurring (see Figure 4.13 although not evident in Figure 4.18). The extent of fluctuations in the 011 interface is similar to that seen in the 001 interface, with atom hopping occurring as far as layer C6 (indicated in Figure 4.13(a) with an arrow) due to structural fluctuations.

As is the case of 001, the melting front of a 011 face is similar to its crystallizing face with similar interfacial structure and structural fluctuations (compare M13-M17 to C10-C14 in Figure 4.17(a)). The explanation for the asymmetry for the freezing and melting rate is also analogous to that of the 001 crystal face.

(a)

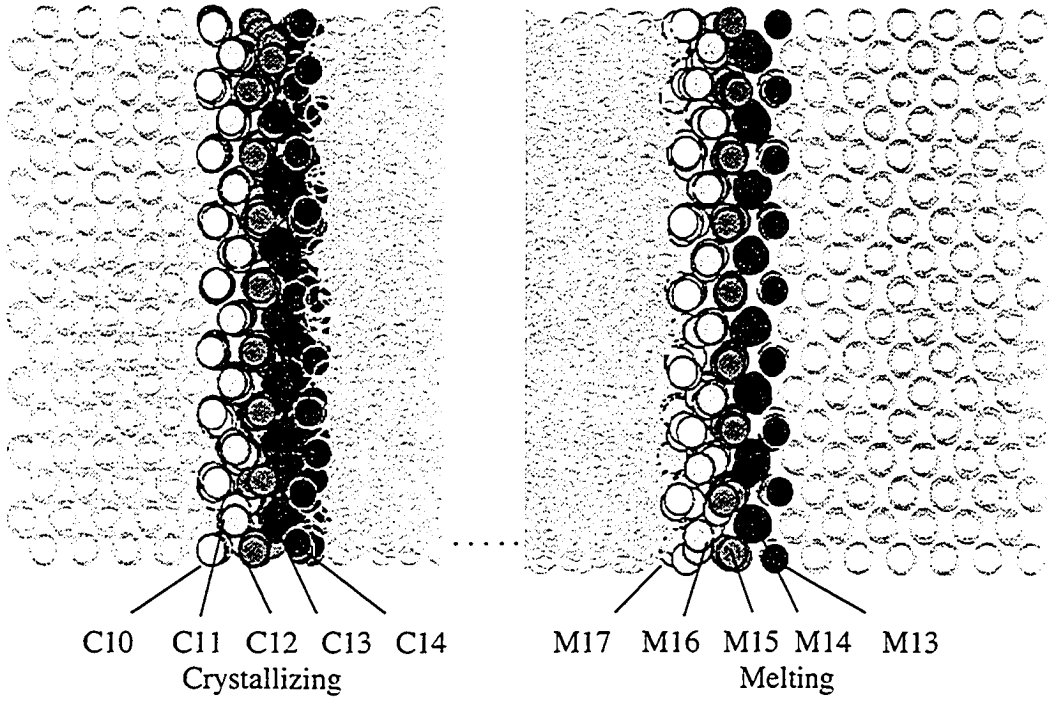

(b)

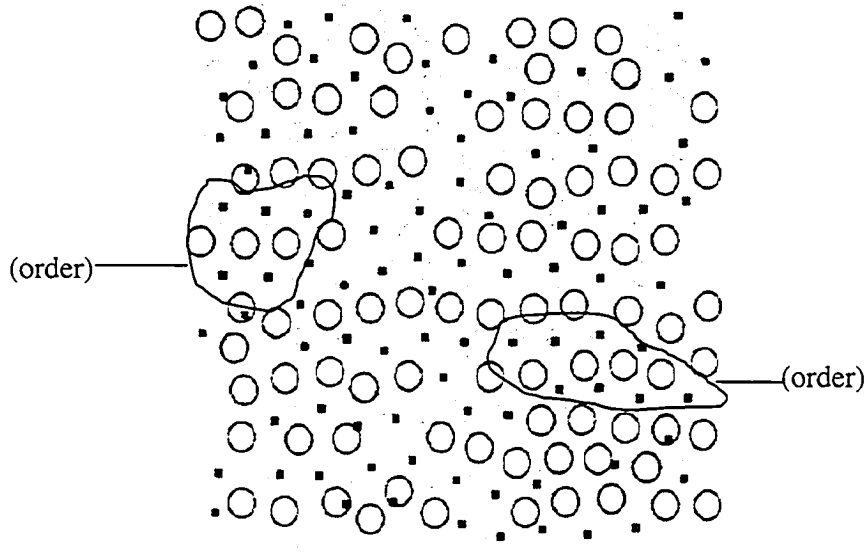

Figure 4.17 (a) Layers of the crystallizing (C10-C14) and melting (M17-M13) interfaces of an averaged configuration of a LJ 011 FCC system. Five slices are identified and labeled (shaded differently) for each interface with the layer numbers as given in Figure 4.8(b). (b) The forward view of three layers: C14 (small squares), C13 (open circles) and C12 (filled circles). The identified areas exhibit crystalline order.

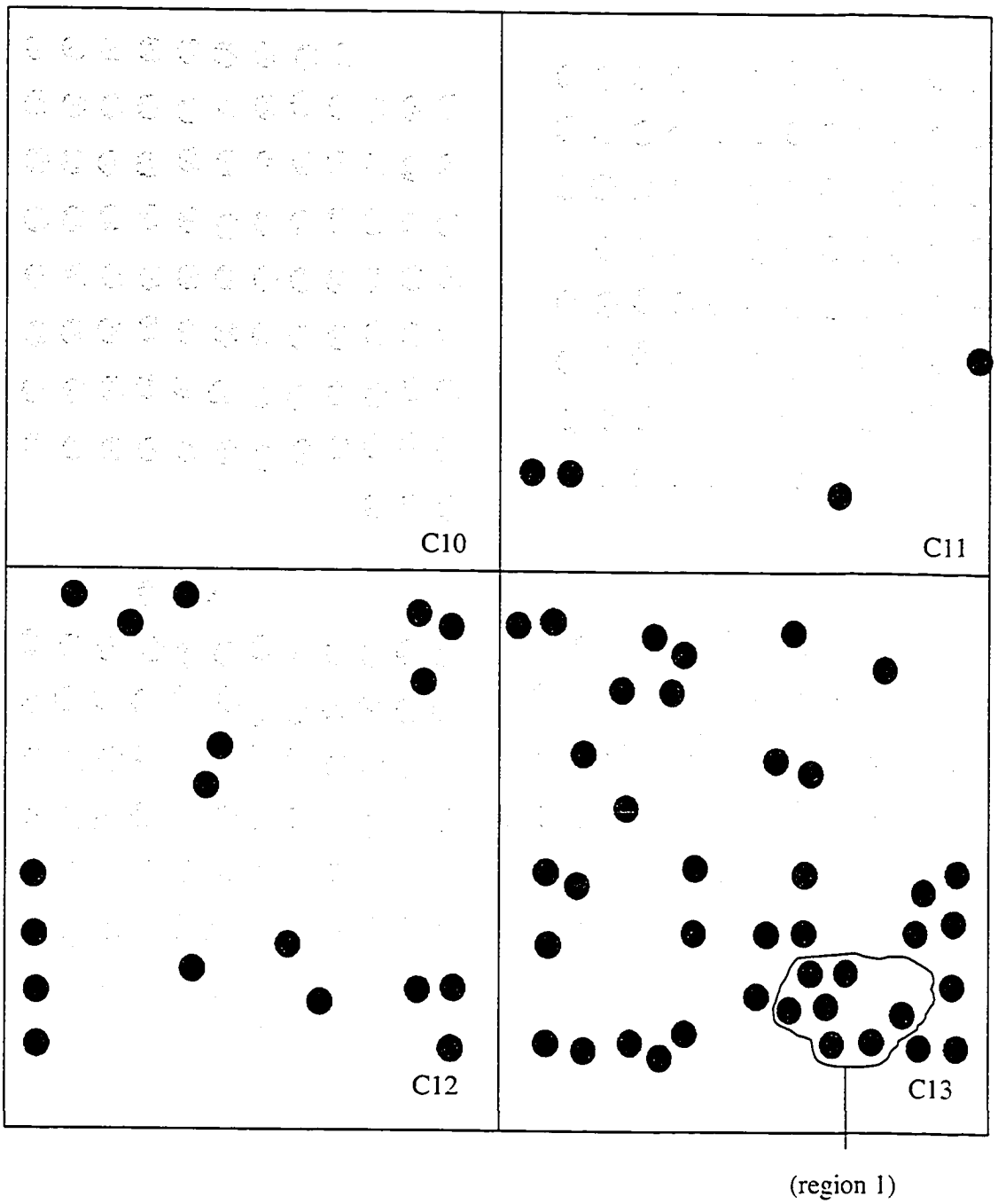

Figure 4.18 Averaged configurations of four consecutive slices through the crystallizing interface of the LJ 011 FCC system. Layers are labeled as in Figure 4.17. The dark atoms are transient particles as defined in the text. Region 1 shows an HCP cluster.

4.2.4 Comparison of interfaces

An explanation can now be provided for why the values from the two measures of interfacial width are different for the 001, 011 and 111 interfaces. The Σ function measures 2D crystalline order, so if a particle exchanges between two layers occurs, the structural measure will be relatively insensitive to this event. In contrast, the energy function will be sensitive to the energy changes that must be part of the hopping process at either the crystallizing or melting faces. The importance of particle hopping on the solid side of the interface explains the slight asymmetry, as observed in the shape of the peak in the derivative of the energy profile function. The consequence of this observation impacts the utility of the Lindemann criteria [171,172] used to categorize the melting process of a heterogeneous system. Melting as described in this section begins with particle hopping; consequently, the mean square displacement criterion employed in the Lindemann procedure may not be adequate to capture the one (or few) particle(s) that hops and may underestimate the initial onset of the melting process.

Hopping has been observed within all the interfaces in this LJ study. This behaviour has also been observed by Huitema et al. [160], but they did not provide a specific account of the role of these atoms. In addition, they do not describe clearly where the interface is located in their simulation and the extent of hopping in relation to this position during crystal growth and melting. The observations made in this section show that hopping behaviour is part of both the freezing and melting phenomena, manifested as ultimately a disordering process; a fluctuating (defective) layer next to a crystalline layer appears to be a sufficient condition. The overall numbers of these transient atoms diminishes as one traverses the interface from the liquid side to the solid side, although

their relative influence increases. Atom hopping can be understood as originating from thermal motion and fluctuations in the local structural environment at the interface.

It is ultimately the collective behaviour of many atoms at the interface that determines whether (net) freezing or melting is observed. The basic mechanism by which freezing occurs at the different crystal faces begins with solid-like structural fluctuations within an otherwise liquid region at the edge of the interface. These ordered clusters are transient entities, however if they match the underlying crystal structure, they may persist and grow. The ordered structure that finally forms may not necessarily contain all its original atoms as significant occurrences of particle exchanges have been noted. These transient atoms, as have been defined in this thesis, can take up clear crystalline positions, however they are observed to ultimately hop to adjacent layers even though the layer (or cluster) from which it originated may otherwise appear crystalline and even defect free. This behaviour indicates that liquid-like characteristics can persist well into the solid side of the interface. The growth at the interface, in general, is not governed by 2-dimensional layering but rather a dynamic 3-dimensional ordering process that can subtend several layers, where the ordered structure can extend to the edge of the interface. These protrusions of order can extend from a true crystalline layer across three to four layers of the interface towards the liquid, as seen in Figures 4.9(b) and 4.17(b) for the 001 and 011 faces, respectively. 001 and 011 are the widest interfaces, where the former is slightly wider. The crystallizing process is faster for 001 than for the 011 crystal face as the latter appears to sample FCC and HCP structures (in addition to 011 features) which need to be eliminated before a complete layer can be formed. However, as pointed out in the previous section, lower interfacial tension and wider interfaces allow the 001 and 011

interfaces to grow faster than the 111 crystal face. In contrast, less pronounced protrusions or more confined structural fluctuations within the 111 interface, due to its higher interfacial tension, contribute (in addition to the annealing of different crystal types) to the slower growth of the 111 crystal face.

CHAPTER 5
PROPERTIES OF LIQUID WATER AND ICE

5.1 WATER

5.1.1 The physical properties of water

The literature on liquid water is vast in extent. This subsection will focus only on some relevant details of liquid water pertinent to this thesis. Consequently, the discussion that follows is a limited overview of the many interesting aspects of liquid water.

The properties of water are of great interest to many areas of study. It is of no surprise that the thermodynamics has been well studied; Figure 5.1 [173] shows the P-V-T surface of water adapted from Steam Tables [174]. Knowledge of its vapour and liquid saturation behaviour is important in the properties of steam for power generation, for example. In fact, the properties of water are important in many other areas of research and technology [13] and even a cursory look at the properties of water reveals something unique about water.

The liquid range of water, which is 100 K at 1 atm, is indicative of strong intermolecular attractions compared to other low molecular weight liquids [12a]. Partial evidence for this behaviour is the relatively small value for the latent heat of fusion which is only 15% that of the latent heat of vapourization. This constitutes evidence that there is significant order in liquid water preserved from the solid state. The primary intermolecular force in water is hydrogen bonding. Hydrogen bonding is best described as being essentially electrostatic in origin [173] and represents the interaction between the

hydrogen atom of one molecule and the oxygen of a neighbouring water molecule. This strong, yet highly-directional intermolecular attraction, is directly and indirectly responsible for the unusual properties of water.

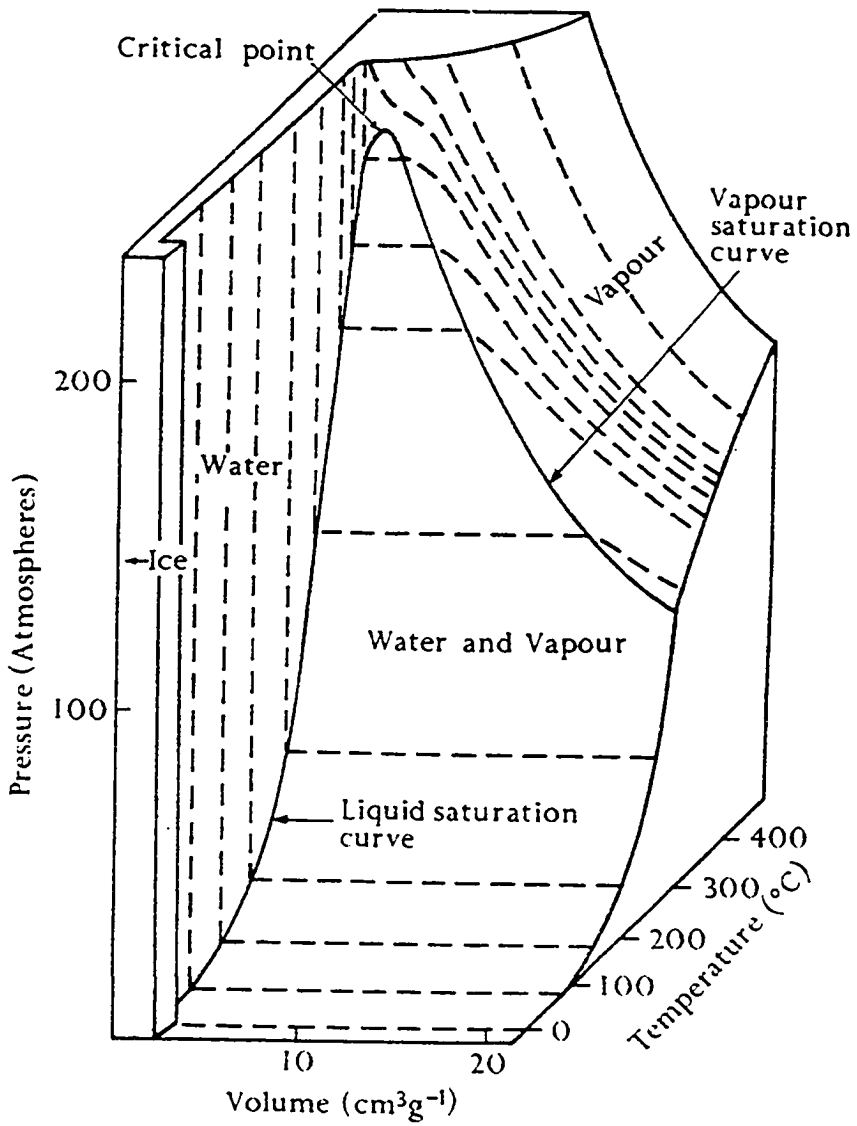

Figure 5.1 A diagram showing the surface of the pressure-volume-temperature relationships of water. The dashed lines indicate isotherms. (from ref. [173] fig. 2.6, pg. 59)

Other interesting properties of liquid water are its large heat capacity (75.2 J mol^{-1} K^{-1}), which is 50% greater than values for its vapour and solid states, and the density

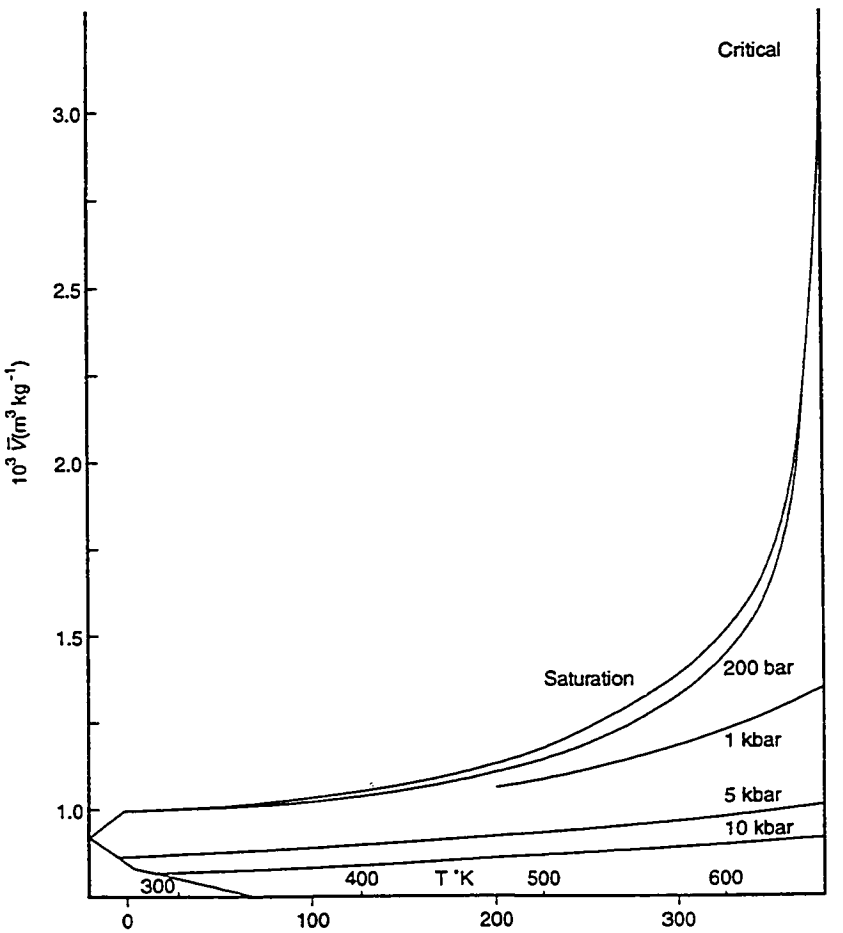

Figure 5.2 Volume of liquid water as a function of temperature at different pressures. (from ref. [12a] fig. 5, pg. 381)

which reaches a maximum at 3.98 °C [175]. At temperatures close to the critical point (at lower pressures), water behaves more like other low molecular weight liquids (see Figure 5.2). It is at low pressure, 1-200 bar, and low temperature range that the anomalous behaviour observed for water, like minimum compressibility and maximum density, is

most pronounced. Water perhaps appears more like other low molecular weight liquids where its transport properties, like thermal conductivity and diffusion, are concerned.

5.1.2 The structure of liquid water

The local environment of the water molecule has been probed by x-ray and neutron diffraction techniques [12a]. Neutron diffraction experiments are carried out with a thin sample of water subjected to radiation with a wavelength, λ. The wavelength that is chosen matches the order of the molecular spacings in the liquid. The measurements of neutron diffraction experiments yield the intensity of the scattered radiation as a function of scattering angle. Similar measurements of scattering intensity are performed in x-ray diffraction experiments. Fourier transform is applied to the data from both types of experiments to provide the radial distribution function, g(r), which is the average number of molecules (or atoms) found at a particular distance from a specific reference position. The radial distribution function provides information on near neighbour distances and coordination numbers. The correlation functions for O-O, O-H and H-H are shown in Figure 5.3, with g_{OO} determined from x-ray diffraction, whereas g_{OH} and g_{HH} have been obtained from neutron diffraction [13]. Separations corresponding to a value of g(r) > 1, indicate preferred atomic spacings. Other useful information contained in these correlation functions are coordination numbers, obtained by integrating the correlation functions of Figure 5.3 over a specific range (for example, to their first minima).

5.1.3 Supercooled water

Bulk liquids can be supercooled below their freezing temperatures where they can exist as metastable liquids. In the absence of nucleation centres, kinetic stabilization

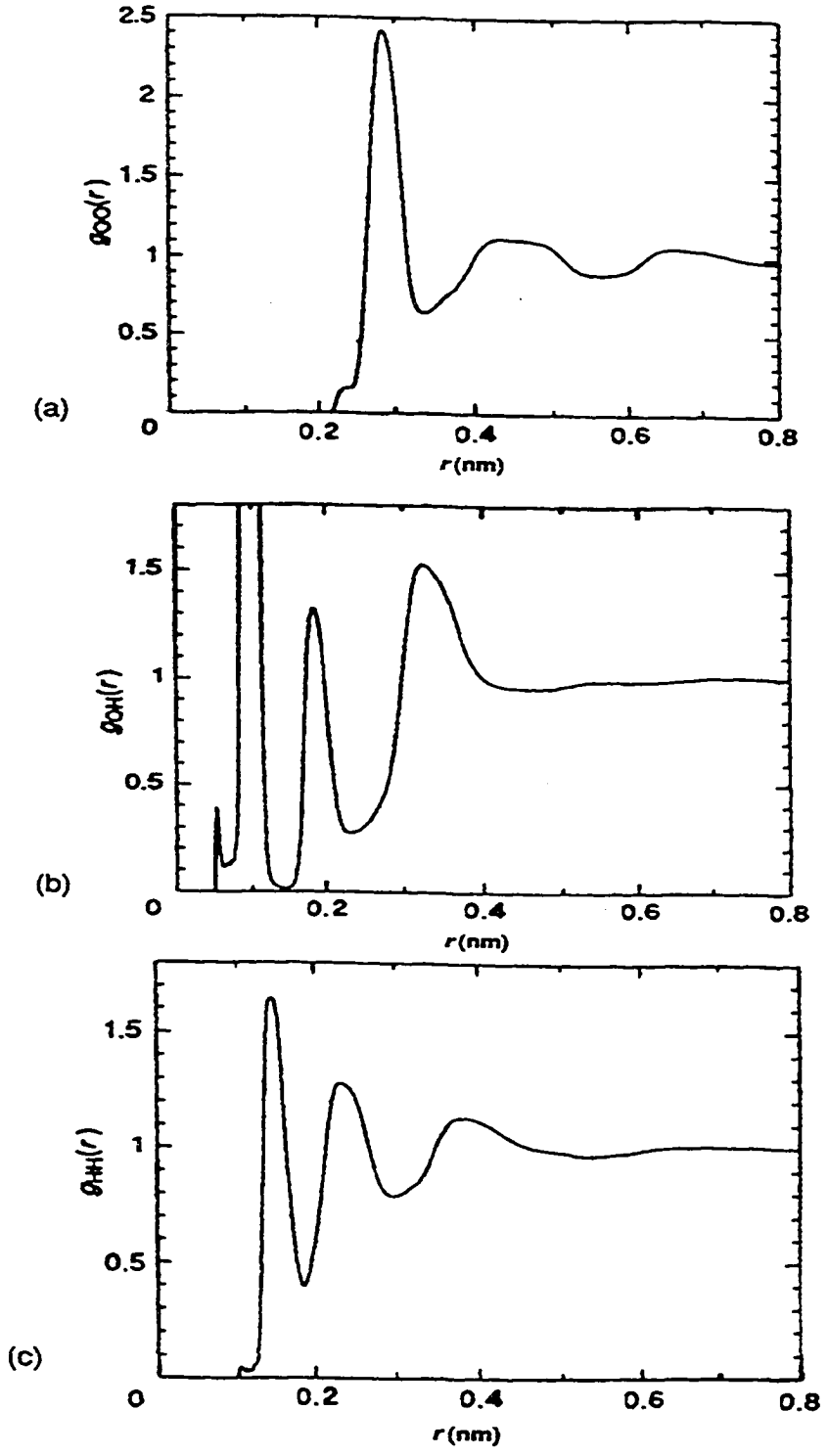

Figure 5.3 Radial distribution functions, $g_{ab}(r)$, for water at room temperature. r is the distance between a pair of atoms, a and b (from ref. [13] fig. 4.1, pg. 45).

allows the liquid phase to persist on cooling instead of the thermodynamically favoured solid phase. With further cooling, supercooled liquids can undergo a glass transition into

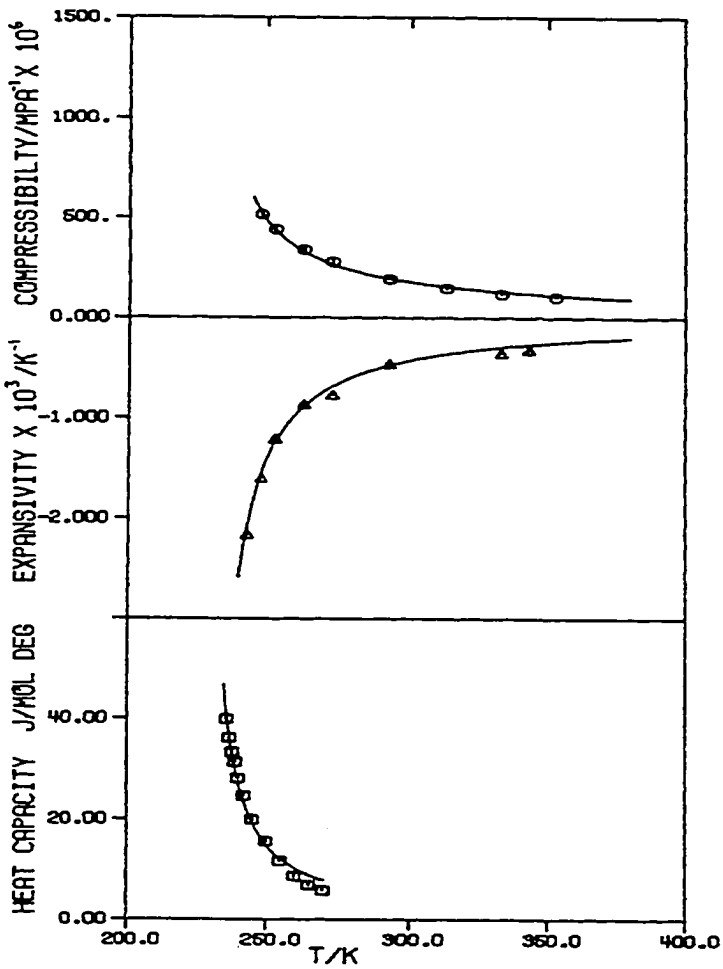

Figure 5.4 The temperature variation of three intensive thermodynamic properties of supercooled water. The temperature dependence of the compressibility, expansivity and heat capacity are shown. (from ref. [173] fig. 30.a, pg. 73).

an amorphous solid. The density of supercooled water falls from about 1.000 g/cm^3 at 0°C to 0.985 g/cm^3 at – 34 °C. Extrapolation of the density versus temperature curve of supercooled water shows that its density approaches that of ice I at - 45 °C. Figure 5.4 shows the anomalous compressibilty and expansivity data of supercooled water. Some

investigators believe that this behaviour may be indicative of a thermal anomaly [12c]. The apparent rapid increase in C_p upon cooling to -38 °C (see Figure 5.4) has not been fully explained.

5.2 ICE

5.2.1 Structure of hexagonal and cubic ice (I_h and I_c)

In the natural terrestrial environment, the only form of ice observed is hexagonal ice, I_h [176]. However, eleven other polymorphs of ice have been identified, as will be discussed in the next sub-section. The structure of ice I_h has been elucidated by x-ray and neutron diffraction experiments. Every oxygen atom is located at the center of a regular tetrahedron formed by its four neighbouring oxygen atoms. The distance between oxygen atoms is 2.76 Å, with a bond angle of 109.28° and a O-H bond distance of 1.01 Å [13], as seen in Figure 5.5 at 273 °K . The next nearest neighbours are at a distance of 4.5 Å. All water molecules in ice I_h are hydrogen-bonded to four nearest neighbours where the O-H bonds of the molecule point toward the oxygen atoms of two of its neighbours. The hydrogen bonds are directed along the O--O vectors joining the water molecule to each of its four nearest neighbours. The bonding just described follows the Bernal-Fowler ice rules [12]. The open lattice that is formed has hexagonal rings as shown in Figure 5.6. This structure is isomorphic with ZnS, the so-called wurtzite structure.

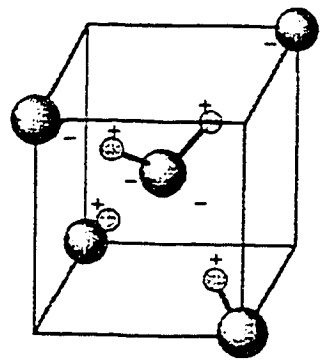

Figure 5.5 Diagrammatic local structure of a water molecule surrounded by four tetrahedrally arranged neighbours. The negative signs show the partial charges on the oxygens. The positive circles are the hydrogen positions. The oxygen sites are located in the middle of the cube and on the corners of the cube (modified from ref. [13] fig. 4.3, pg. 35).

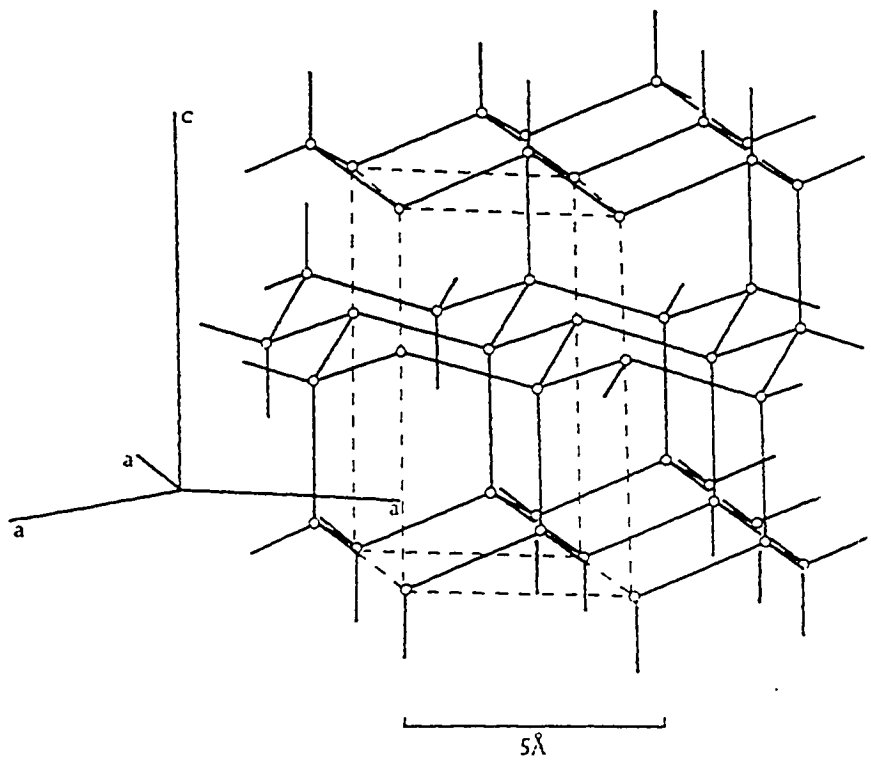

Figure 5.6 Structure of hexagonal ice with the crystallographic axis and dimensions shown. The circles correspond to oxygen positions and the lines are drawn to show the oxygen vectors (bonds). The dotted line indicates a unit cell of hexagonal ice (from ref. [173] fig. 3.1, pg. 72).

In ice I_h, all permutations of the H-bonding are observed, thus there is a random pattern of hydrogen orientations in an ice crystal [173]. This random arrangement is referred to as proton-disordered. The net dipole moment of a bulk sample of such an ice crystal is zero as a result. Proton ordering can occur at high pressures and/or low temperatures. Ordering occurs in ice I_h because the crystal possesses residual entropy due to its proton-disordered arrangement. Proton ordering causes a net polarization of the crystal due to all the electric dipole vectors of the molecules pointing in one direction. Thus a ferroelectric transition to the ice XI, a polymorph of ice [178] (discussed in the next sub-section) can occur. Antiferroelectric crystals have also been studied [179] in theoretical modelling where there are local domains of proton ordering within a crystal, such that the net dipole moment of the whole crystal is zero. Proton-disordered, ferroelectric and antiferroelectric ice crystal models [180,181] should prove useful in studying the properties of crystallization of ice from its melt or near walls or inside cavities.

Cubic ice is a metastable form of ice I. It is not known to exist on the surface of the earth, however there is evidence that it exists in the upper atmosphere and is transformed to hexagonal ice in the formation of snow [182]. Its oxygen atom structure is identical to the arrangement of carbon atoms in a diamond lattice, as shown in Figure 5.7. It has the same bond distance and bond angles as I_h. Ice I_c can be produced in the lab when high pressure polymorphs of ice are depressurized at 77 K, and subsequently warmed to about 160 K. Another way to produce cubic ice is when low density amorphous ice is warmed to a temperature of 170 K, where an irreversible transition to ice I_c occurs [176]. A more detailed discussion of the relationship between ice I_c and I_h is given in section 5.2.5.

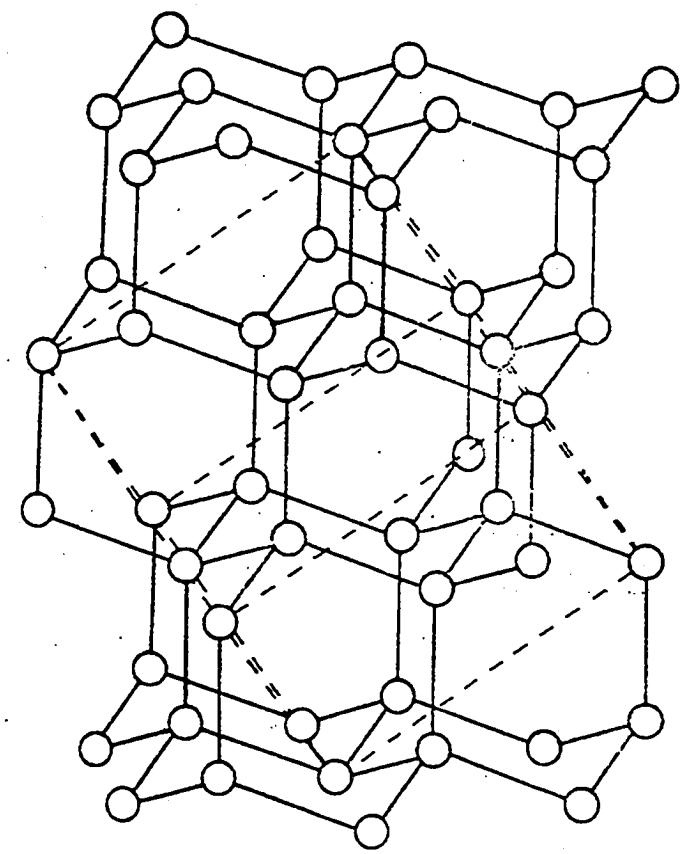

Figure 5.7 Structure of cubic ice with the dotted lines indicating the position of the cubic unit cell. The circles are the oxygen sites and the lines are drawn to show the diamond lattice. (from ref. [173] Fig. 3.10, pg. 91).

5.2.2 Polymorphs of ice

As mentioned earlier, there are twelve polymorphs of ice presently known; the phase diagram shown in Figure 5.8 indicates all the polymorphs except ice X, ice XI and ice XII [13]. Each polymorph is stable (or metastable) over a limited pressure and temperature range. Each water molecule in these structures is hydrogen bonded to four nearest neighbours as in ice I, but high pressures cause distortions in hydrogen bond

angles and bond lengths (necessary to achieve higher density). For example in ice V hydrogen bond donor angles range from 84° to 135° compared to 109.28° in ice I; the O--O vector distances here are between 3.28 to 3.46 Å [176]. At higher pressures, ice VII and VIII have a water molecule surrounded by eight nearest neighbours with O--O vector distances of 2.92 Å. Four of these neighbours are hydrogen-bonded to the central molecule while the other four are a part of a (pressure-induced) interpenetrating tetrahedral lattice Another high pressure induced form is ice XII, discovered at pressures of 300 Gpa. Ice VI, VII and VIII are among the densest forms of ice known. The compactness of their structures is due to two interpenetrating fully hydrogen-bonded frameworks. These frameworks are interpenetrating but not interconnected [12a]. A proton ordering is also seen with ice VI, giving rise to ice X.

Ice II,VII and IX are proton-ordered polymorphs. Another proton-ordered ice phase was discovered in experiments with ice I, where D_2O was doped with KOH [178]. A thermal transition was discovered at 72 K; the new phase was designated ice XI. Thus it can be clearly seen that the phase behaviour of ice is complex.

5.2.3 Amorphous solid water

In addition to the crystalline forms of water, another solid form of water exists, called amorphous solid water (ASW). This form of water is metastable and has no crystalline order and is also described as glassy or vitreous water. ASW has at least two distinct forms, high density amorphous (HDA) and a low-density amorphous (LDA). There is some dispersion in the nearest neighbour separation, but the source of the disorder in LDA stems from deviations of the O-O-O angles from 109.5°. The range of

the deviations is about 8°, sufficient to destroy the correlations between the positions of the molecules separated more than 7 Å. Nonetheless, the short-range order of the four nearest neighbours is essentially preserved [12c].

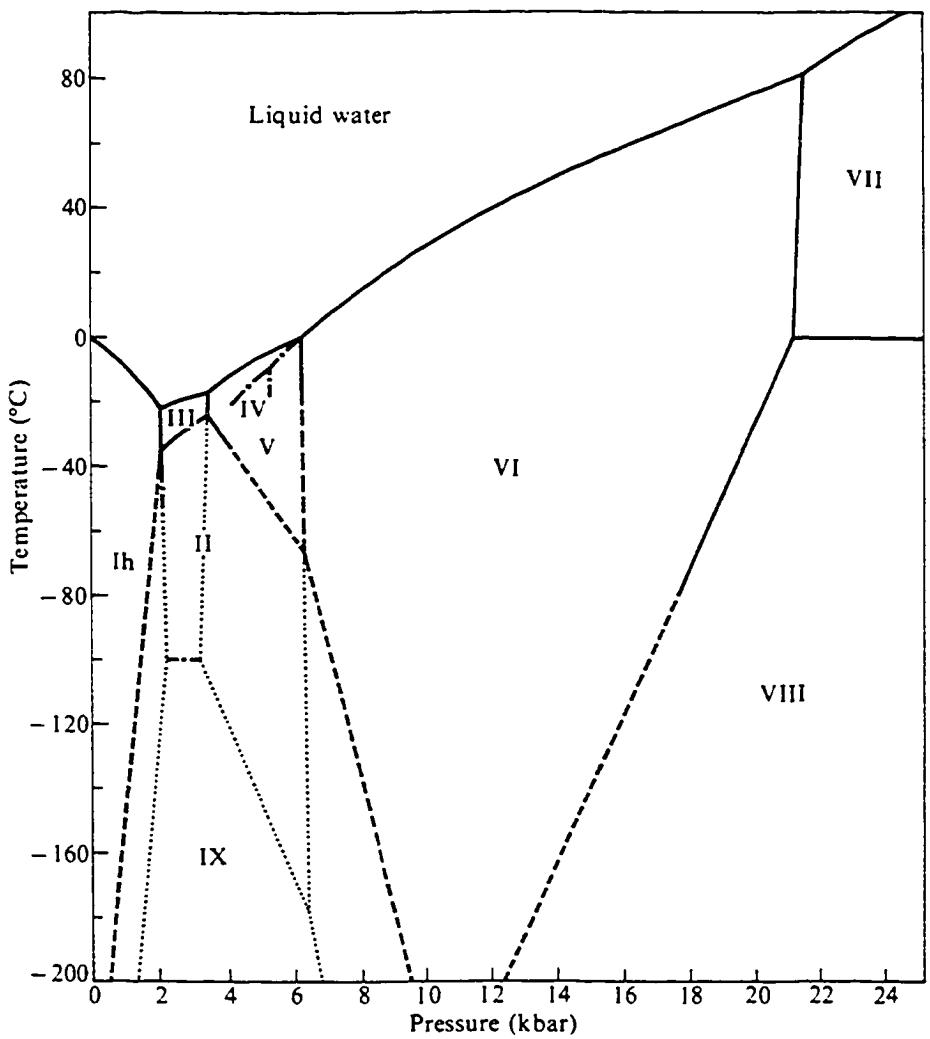

Figure 5.8 A temperature - pressure phase diagram showing the majority of the polymorphs of ice. (from ref. [12a] fig. 1, pg. 117).

5.2.4 Crystal planes of cubic and hexagonal ice

In this thesis several different crystallographic planes of hexagonal and cubic ice will be discussed. A brief description of the relevant crystal structures with their Miller indices will be examined. Figure 5.9 shows three crystal planes of cubic ice along with their corresponding Miller indices. Miller indices are obtained from taking the reciprocals of the orientation of a plane with respect to the coordinate axes a, b and c defining the unit cell and then normalizing the fractions obtained to simple whole numbers [183]. The three planes of ice I_h discussed in this thesis are shown in Figure 5.10. The (0001) plane is termed the basal face or plane, and the $(10\bar{1}0)$ plane is termed the prismatic face or plane. In addition, there are six possible faces of the hexagon and hence there are six descriptions of the prismatic plane. This also holds true for the third crystal plane shown in Figure 5.10, the $(11\bar{2}0)$ plane.

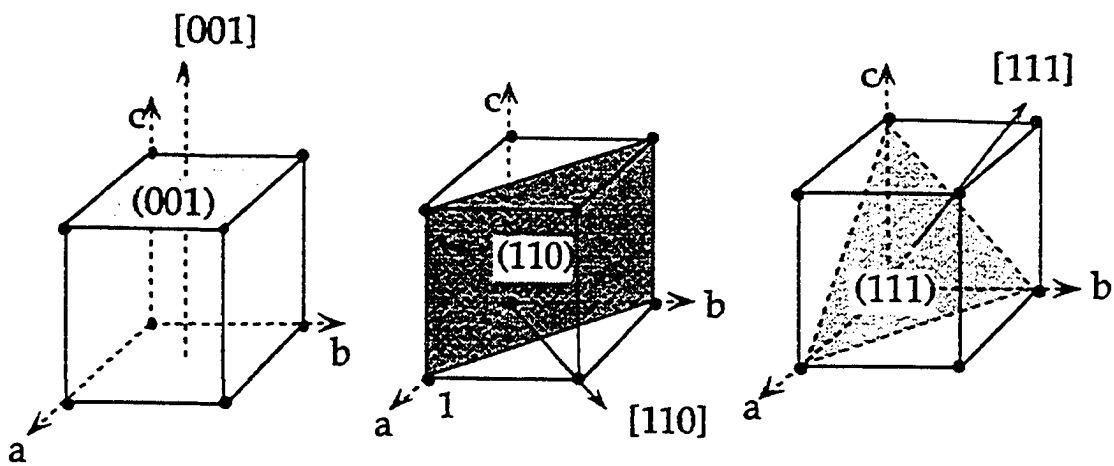

Figure 5.9 The planes of three Miller indices investigated in this thesis for the cubic structure (cubic ice) (from ref. [181] fig. 2-22, pg. 158).

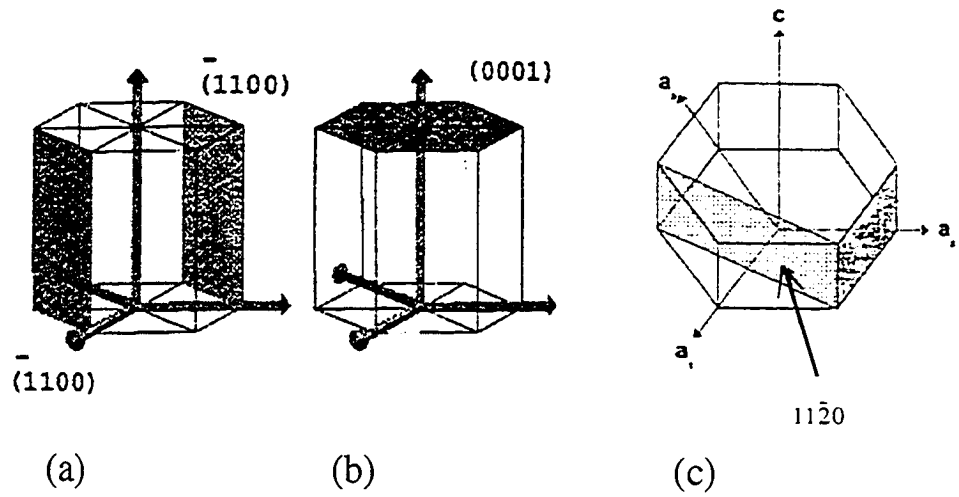

Figure 5.10 The three crystal planes of hexagonal ice investigated in this thesis (a and b, from ref. [180] fig. 2-30, pg. 167 ; c from ref. [165] fig. 1, pg. 3734)

5.2.5 Exploring the relationship of hexagonal and cubic ice

Cubic ice is similar in many ways to hexagonal ice, as has been discussed above, yet the former ice structure is metastable with respect to the hexagonal form [184]. The enthalpic difference between the two ices is small, determined to be ~40 J mol^{-1} [185,186]. In fact, it has been argued that cubic ice may be formed in the upper atmosphere, where it is responsible for the observation of Scheiner's halo; this is a rare halo which occurs at ~28° from the sun or moon [182]. Such observations then raise questions as to the possible roles that cubic ice may play in the formation of hexagonal ice in nature.

It has been found [187,188,189] that in polycrystals of snow there may be a misorientation in the c-axis of about 70° and that the a-axes of the crystals coincided with each other. In another experiment [190], where supercooled droplets of water were placed on the basal plane of ice I_h, it was found that as the temperature was lowered the same

misorientation of about 70° of the c-axis occurred. In addition, spontaneous freezing of a water droplet showed that the polycrystalline droplet had the same 70° misorientation [191]. There have been numerous explanations for this phenomena; but one suggestion invokes a cubic ice model as a possible explanation of the experimental observations [192]. The reason is due to the fact that two cubic 111 crystal planes occur at an angle of 70.54°. Consequently, this model proposes that during the nucleation process, an embryo with the structure of ice I_c is produced. Hexagonal ice subsequently grows from the (111) faces of the cubic crystal embryo. This model is based on the fact that the basal plane of hexagonal ice is the same as the (111) plane of cubic ice. However, the study did not address the initial formation of the cubic embryo or probe directly for cubic structure. Studies with other materials have shown some intriguing results. It was discovered [193] that a ZnS crystal formed as a cubic crystal below a certain transition temperature subsequently grew as a hexagonal crystal above the transition temperature. This result agrees with the model proposed for ice, where the hexagonal crystal forms from a cubic embryo. In yet another study [194], it was shown by electron diffraction that a ZnO crystal had a cubic core with a hexagonal pattern around the core.

In a study by Mayer and Hallbrucker [195], it was discovered that cubic ice could be obtained from the liquid directly. The experiment involved rapidly quenching aqueous droplets ~3 μm in diameter on a cryoplate and using x-ray diffraction to analyze the samples. Another experiment by Bartell and Huang [196] showed that rapid crystallization of supercooled water clusters with diameters roughly 74 Å also produced cubic ice. Other studies [197,198] using computer simulation have produced cubic ice directly from water, with the application of a strong electric field. Very recently, Murray

et al. [199] have obtained cubic ice at 235 K, claiming that heat dissipation was critical in forming cubic ice homogeneously from small water droplets. The connection between cubic and hexagonal ice in nature, especially from nucleation to growth of the macroscopic ice crystal, clearly needs to be explored further.

5.2.6 Physical properties of ice

The physical properties of ice represents a rather large body of information [176,200,201], therefore the discussion below will highlight only a few of the physical properties.

The dielectric constant, ε_0, of ice increases with a decrease in temperature. There is also a larger value of ε_0 parallel to the c-axis of ice I_h than perpendicular to it. Moreover, ε_0 is larger at 0°C for ice than for liquid water, even with the decrease in the volume of liquid water at melting. Other polymorphs of ice also show high dielectric constants, which indicate that the molecules in these crystals can change their orientations [176] in response to an electric field. When an electric field is applied to ice I and the frequency increased to above 10 kHz, the dielectric constant falls from about 100 to 3.2. The relaxation frequency associated with this change in behaviour is a measure of the frequency of the molecular reorientation. Crystal defects are primarily responsible for this behaviour; the defects are primarily due to impurities in the crystal. Impurities play a large part in the electrical conductance of the crystal; when there is a temperature increase, the conductance increases exponentially [13]. The self-diffusion constant in ice is another property that involves crystal defects in the lattice, with a self-diffusion value of 2.8×10^{-11} $cm^2 s^{-1}$ [173] over the temperature range of -10 to -35 °C.

5.3 ICE GROWTH IN LIQUIDS

5.3.1 Crystal growth

The topic of ice crystal growth encompasses many time and length scales. Growth of ice results from the freezing of the liquid or condensation of the vapour. A common consideration for both processes involves transport of water molecules to the region of growth and the incorporation of these water molecules to the crystal. Other similarities are the transport of latent heat away from the growing interface. If the crystal growth of ice is ongoing in the presence of another component besides water, the considerations of crystal growth in this case engenders further complications as there may be competing processes at the surface of the growing crystal. The next section will be focused on ice growth from the pure liquid, addressing growth parallel and perpendicular to the c-axis of ice I_h. The focus will be on experimentally derived growth rates of ice [176].

5.3.2 Growth parallel and perpendicular to the c-axis

Although there has been much experimental data collected on ice growth in supercooled water, the rates of ice growth discussed here are obtained in the 1950's and 1960's [175.176]. These results are still valid today as few experiments since then have added any substantial information on growth rates [202]. In the literature [202,203], studies pertaining to ice growth have focused on possible mechanisms of ice growth from microscopic and macroscopic considerations with the latter studies significantly more abundant [176,202,204]. This is a testament to the difficulties faced in unraveling the complexities of ice growth at the microscopic level. In light of this, only a small number

of relevant macroscopic mechanistic results, particularly dealing with dendritic growth (if pertinent to microscopic growth) will be discussed. However, there still exists considerable challenges in interpreting these results stemming primarily from the lack of information surrounding the theory of crystal growth from a melt.

The experimental techniques used in the following discussion of growth studies are primarily of three types: fine bore capillary [205,206], thermal wave [207,208] and directional growth experiments [209]. In fine bore capillary experiments sufficiently slow growth can be monitored in small diameter capillary tubes that are placed in a well-regulated constant temperature heat bath [205]. The temperature of the heat bath is very close to the equilibrium freezing temperature with the rate of evolution of latent heat assumed to be slow enough that the heat can be effectively channeled away by the small temperature gradients present in the system [206]. In addition, the interface temperature is considered to be the same as the bath temperature.

In the thermal wave technique, a solid-liquid interface is located in a system that is under a temperature gradient that is held fixed. An additional heat flux that varies sinusoidally in time is also introduced into the liquid [207]. The net result of this set-up is to cause the interface to move back and forth and thereby act as a heat source and heat sink. Thus, the latent heat wave will be out of phase with the applied thermal wave. Measurements are made, employing thermocouples (located on both sides of the interface), of the amplitudes and phases of the thermal wave. In principle, both the growth rate and the interface supercooling can be determined.

In a directional growth experiment, the apparatus as originally designed by Jackson and Hunt [210] is shown in Figure 5.11. The two ends of the growth cell are held at different temperatures, T_h (hot) and T_c (cold). A temperature gradient is

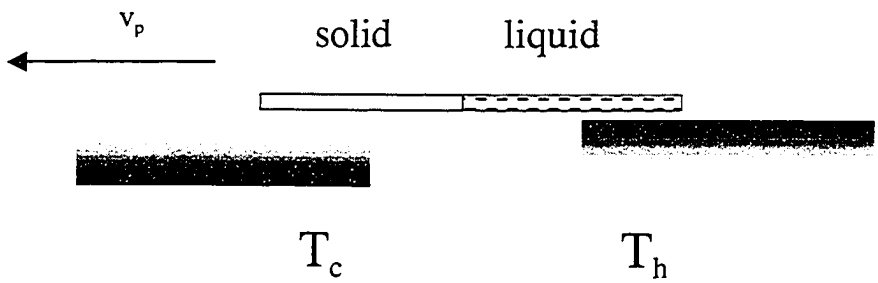

Figure 5.11 Diagrammatic representation of a directional growth apparatus. T_c is the temperature of thermal sink and T_h is the temperature of thermal source. v_p is the pulling velocity used to induce crystallization.

established along the z-axis of the growth cell. The growth cell is placed in a slider that can be moved along the z-direction by mechanical means so constant pulling velocities can be achieved to induce crystallization (see Figure 5.11). The corresponding growth of the sample can be viewed with a microscope and consequently recorded for analysis. Interferometry is typically used to analyze the samples [211]. Measurements were made of ice growth perpendicular to the c-axis of ice I_h by Kost [212] using the capillary wave-technique. He investigated the growth velocities, V_a, of ice dendrites, as shown in Figure 5.12. He proposed that the temperature of the interface was the same as that of supercooled water, however this claim has been called into doubt. Hallett [213] under water supercoolings of -20°C measured the free growth of ice in supercooled water and

obtained the results also shown in Figure 5.12. He proposed that the growth rate perpendicular to the c-axis is given by the empirical relationship

$$V_a = (0.0008 \pm 0.0001) T_s^{(1.9 \pm 0.05)}, \qquad (5.1)$$

where V_a is in m/s and T_s is the supercooling of the water. The empirical relationship of Hallet [213] is quantitatively in agreement with growth velocity measurements made in the decades preceeding his work in which the data can all be described by a growth law of the form,

$$\text{velocity} = A(\Delta T)^m, \qquad (5.2)$$

where m varies from 1.3 to 2.2 for different experiments. Other important work was contributed by Miksh [214] who discovered that there was no slope discontinuity during the transition of freezing to melting. He examined the rates of freezing and melting of an ice-water mixture by altering the temperature by as little as 3×10^{-6} K from the equilibrium freezing temperature. The results were interpreted as showing that the notion of a surface nucleation mechanism for growth perpendicular to the c-axis could be ruled out as growth was claimed to be limited by the rate at which heat could be removed from the growing interface and not by interface kinetics.

To investigate the anisotropy of growth perpendicular to the c-axis, Nagashima and Furukawa [215], using a directional growth apparatus have observed anisotropic growth kinetics between the Ih$11\bar{2}0$ and Ih$10\bar{1}0$ crystal faces. They have discovered that the kinetic supercooling (or kinetic coefficient defined as a constant of proportionality between the interface supercooling and the solidification velocity [46]) was a minimum at the $11\bar{2}0$ direction and maximum at the $10\bar{1}0$ direction. They observe that the anisotropic interface kinetics increased with increasing growth velocity. They have made

the argument that these results can be qualitatively compared to free growth experiments in supercooled water. They further note that the anisotropic interface kinetics stabilize

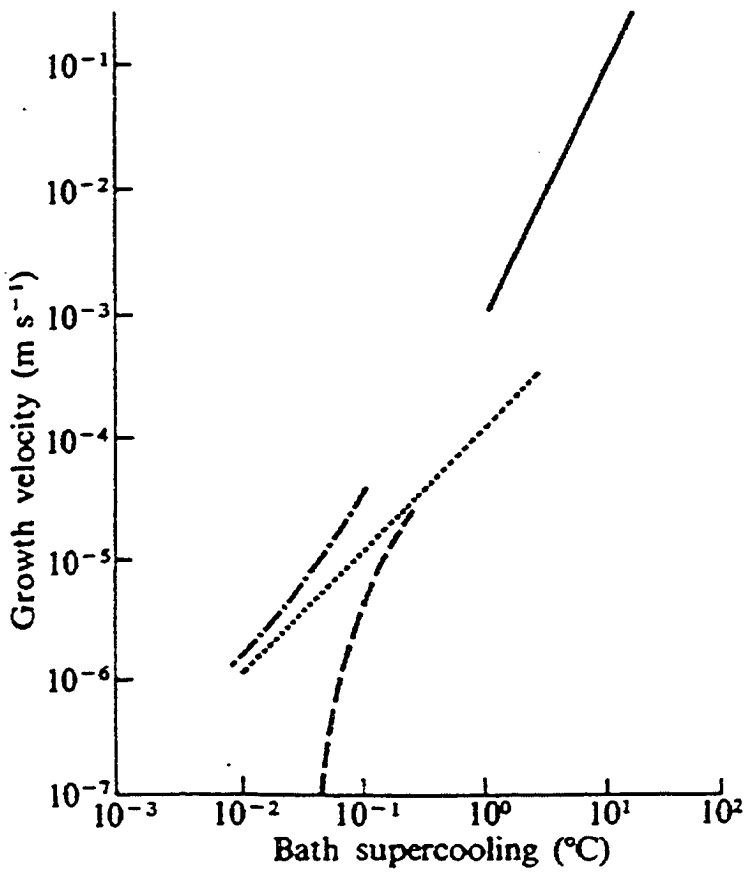

Figure 5.12 Growth velocities of ice perpendicular (V_a) and parallel (V_c) to the c-axis. The various lines represent independent growth experiments from Hallet (V_a-solid line-1964), Hillig (V_c-'imperfect crystals'-dotted line-1958), Kost (V_c-dash dotted line-1958) and Hillig (V_c-'perfect crystals'-dashed line-1958) (from ref. [176] fig. 9.10, pg. 584).

the growth of the dendrite tip in the $11\bar{2}0$ direction. Using a high-pressure growth apparatus in supercooled water, Moruyama [216] has found that under high pressures, 160 MPa, a roughening transition occurs for the prism face of ice at 257 K. Above 257 K

crystal growth rates change from approximately quadratic to linear in the supercooling, with the prism facets disappearing and a rounded crystal forming.

In measurements for growth along the c-axis, Hillig [206] used the finebore capillary technique to measure rates for bath supercoolings from 0.2 to 2.4 K; his measured growth rates are shown in Figure 5.12. The data was fit to the empirical relationship,

$$\text{velocity} = 0.0003 \exp(-0.35/\Delta T), \tag{5.3}$$

where ΔT is the supercooling. It was argued that this law is consistent with a surface nucleation mechanism with growth proceeding by a step mechanism. Moreover, they claimed that further evidence supporting this suggestion was observed when the interface was damaged. Growth rates as much as 300 times faster were seen for supercoolings of 0.03 K. For supercoolings of 0.65 K a dislocation mechanism was suggested. Sperry [217,218,209] used a modified capillary technique to improve obtaining the interface temperature. For supercoolings between 0.04 and 0.07 K, the growth rate increases rapidly and for supercoolings between 0.07 and 0.2 K the growth rates appeared to vary with ΔT^2 and so a screw dislocation mechanism was proposed. Thus, a consistent mechanistic description of crystal growth of this face is unclear from the experimental evidence.

Shimada and Furukawa [219], using in-situ observations of disc ice crystals grown in supercooled water performed with an interferometric optical system, discovered that under identical conditions two growth regimes of the whole crystal occurred. The first (type I) identified by measuring the change in radius (prism) and height (basal), exhibited similar growth rates in the prism face and the basal faces. In type II, they

observed an initial period of significant prism growth relative to the basal face; after a period of time similar growth rates of the two faces were once again observed. In a subsequent study by Yokoyama, Sekerka and Furukawa [220] a numerical technique modeling the growth of a disk crystal was attempted; they concluded that the type I crystal "probably" grew by screw dislocations on the basal plane based on growth rate data, consistent with the study by Michaels et al. [221] employing optical microscopy in capillary tubes. Growth of type II crystals was believed to proceed by two-dimensional nucleation on the basal plane. The justification provided for the latter mechanism was due to the sensitivity to supercooling. However, in a recent experiment by Teraoka et al. [222], measuring the growth of a single ice crystal measured by an interferometer, it was shown that growth velocity (V_c) along the c-axis face was not dependent on supercooling but on time (t) and could be fitted to the empirical relationship,

$$V_c = 0.010 \times t^{-0.67}. \tag{5.4}$$

A recent study by Maruyama [223], at high pressures discovered a ΔT^2 dependence for growth of the basal face, again believed to be consistent with a screw-dislocation mechanism.

The general consensus from this plethora of experiments appears to be that the growth rate of ice perpendicular to the c-axis (prism) is much greater than that parallel to the c-axis (basal). Jackson et al. [209] have suggested that the difference in growth behaviour must be related to the structure inherent in the growing interfaces. They argued that growth parallel to the c-axis must involve three molecules each making a single bond to the layer of ice below. These molecules must be present on three neighbouring sites (not nearest neighbour sites), before a fourth molecule can be added which can make one

bond to each. Therefore, the four molecules are bound to each other and to the crystal and any one of the molecules must break at least two of these bonds before it can leave the solid. In contrast, for growth perpendicular to the c-axis, a molecule with a single bond to the crystal can be joined by another molecule with a bond to it and to the crystal. The result is two molecules with three bonds as compared with basal growth parallel to the c-axis where we have four molecules and six bonds. Therefore, Jackson [209] argues that the probability of occurrence of such an arrangement of a four molecule group is smaller than the two molecule group of the prism face and hence the prism face can grow faster than the basal face. However, Jackson's suggestion ignores the presence of a liquid which forms hydrogen bonds to these molecules.

The experiments thus far are inconclusive in clarifying a mechanism for ice growth perpendicular and parallel to the c-axis. In addition, the literature is unclear on which face is faster the Ih$\langle 11\bar{2}0\rangle$ or Ih$\langle 10\bar{1}0\rangle$ crystal face. The role of the latent heat of crystallization and its impact in these studies cannot be underestimated. Murray et al. [199] discovered cubic ice in supercooled droplets, after effectively dealing with the removal of latent heat. Maruyama [223] also discovered different growth rates as a result of using different materials for the growth cells. The removal of latent heat is a critical consideration in ice crystal growth studies. The results in Chapter 4 have demonstrated that this problem can be effectively dealt with and consequently will be applied in ice/water systems.

5.4 SOLID/LIQUID INTERFACE OF WATER

5.4.1 Survey of experimental techniques

In section 2.3 of this thesis, several experimental techniques were discussed in the investigation of liquid/solid interfaces in general. These techniques were only applicable to selective systems, under particular conditions. For the ice/water interface only some optical techniques have proven to be successful.

The ice/water interface is the principal focus of this thesis; therefore, surface techniques like X-rays (particularly glancing-angle X-ray diffraction) [224], atomic force microscopy (AFM) [225,226], and scanning tunneling microscopy [102] used to investigate ice surfaces (ice/vapour) will not be discussed in this section. These experimental techniques have been used to explore the structure and dynamics of the quasi-liquid layer of ice surfaces and only findings relevant to results of this thesis will be presented in the appropriate sections. Moreover, there has been no application of these techniques to ice/water interfaces to date.

The optical techniques that have been used to probe the ice/water interface are briefly summarized below:

Ellipsometry - In this technique, a collimated light beam with a known polarization state is incident on a sample; the reflected light is then analyzed to check the polarization. From the incident and reflected polarization states, a ratio of complex reflection coefficients is obtained [227]. The ratio is then related to the structural and optical

properties of the sample under analysis [228]. In the experiments discussed below, the optical properties of the liquid, solid and the interfacial region were analyzed.

Rayleigh scattering - This occurs when monochromatic light is scattered by a medium where the diameter of the particles in the medium are smaller than the wavelength of the incident light [229]. The intensity is dependent on the wavelength, the scattering angle and the polarizability of the molecules. The frequency of the scattered beam is unchanged and its intensity is much higher than the accompanying Raman and Brillouin scattering in interfacial crystal/melt systems [230]. Rayleigh lines, as used in probing an interface, provide a check for dust contamination and the linewidths are related to the lifetimes of relaxational processes.

Raman scattering - This occurs when the polarizability of a bond varies with its length. The Raman effect is weaker than Rayleigh radiation, its intensity being about 10^{-5} times smaller than that of the incident beam. However, it can provide information on the vibrational modes of both solids and liquids [231].

Brillouin scattering - The spectrum obtained from this scattering process allows measurements of the linewidth and the frequency of thermally excited sound waves that provided information on sound absorption and velocity. Therefore, comparisons can be made of the spectra obtained in the solid, the liquid and the interface [232,233].

5.4.2 Summary of experimental results

Ellipsometry

Beaglehole and Wilson [234] have used ellipsometry to study the ice/water interface. The technique involved directing a ~550 nm light source at an angle to the interfacial layer and observing the change in polarization of the reflected light. The experiment was performed on the basal face and the prism face of hexagonal ice. In their experiment the average ellipticity was measured for both the crystal faces, and the anisotropy factor as well as the thickness of the interfacial layer were estimated. A value of 1 nm, obtained from computer simulation experiments [235], was used to calculate the anisotropy of the basal and prismatic face. They have interpreted their results as indicating that the prism face anisotropy is roughly twice that of the basal face, and have suggested this result indicates that the prism face is more structured than the basal face. They estimated the range of dielectric constants for the interface to be between those of ice and water.

Rayleigh, Raman and Brillouin scattering

Rayleigh scattering was used by Böni et al. [230] to probe the interfacial region. It was discovered that the linewidth of the scattered light was proportional to the square of the scattering vector, $\mathbf{k}_{scatter} = \mathbf{k}_{water} - \mathbf{k}_{refracted}$, where $\mathbf{k}_{water}$ is the vector reaching the detector, $\mathbf{k}_{refracted}$ is the vector of the refracted incident beam in water and $\mathbf{k}_{scatter}$ is the beam scattered from the interfacial region [236]. In addition, this relation is independent of wavelength. It was also found that there was an enhancement of the intensity of Rayleigh

light, up to four fold intensity, originating from a growing interface. The growth rate for the onset of enhanced Rayleigh scattering had to exceed a certain critical rate of 1.5 μm s^{-1}. The incident laser beam was applied from the water side of the interface. Rayleigh scattering was also used to ensure that there were no dust particles; this was accomplished by directing half the scattered radiation into a television camera to check visually for dust in the sample.

Brillouin scattering was used to confirm whether there was ice-like particles in the interface. From a comparison of the interfacial Brillouin spectra to that of bulk water and ice, it was concluded that there were no ice-like particles in the interfacial region. It was also confirmed that the scattering of the laser light was on the water side of the interface, with no enhancement from the Brillouin scattered light.

This experiment revealed that different grades of ice crystal (the grades were assigned visually, dependent on whether there were grooves on the ice crystal) gave different results for the proportionality between the scattering vector and the linewidth. To calculate the constant pressure, C_P, and constant volume, C_V, heat capacities, the isothermal compressibility, κ_T, and the adiabatic compressibility, κ_S, (of the interfacial water) Böni et al. [230] employed the Landau-Placzek [237] equation

$$r_l = \frac{I_C}{2I_B} = \frac{C_P - C_V}{C_V} \equiv \frac{\kappa_T - \kappa_S}{\kappa_S}, \tag{5.5}$$

where r_l is the ratio of the intensity of the Rayleigh line, I_C ,to twice the intensity of the Brillouin line, I_B. With the above equation the authors estimated the isothermal compressibility of the interface to be ~700 times that of bulk water. They also found that the value for the adiabatic compressibility was indistinguishable from that of bulk water.

Their estimate of the diffusion constant for water in the interface showed a marked decrease, ~10^5 times smaller than that of bulk water. The refractive index was calculated as being between that of water and ice. They also related the linewidth to the lifetimes of entropy fluctuations in the interfacial layer.

As an extension of the above study, Halter et al. [238] investigated the ice/water interface using both Raman and Rayleigh scattering techniques. To confirm the results of Böni et al. [230], a similar experiment was conducted with many modifications to the experimental set up. Similar findings were reported and Halter et al. [238] claimed that they were observing the same phenomena. The Raman spectra obtained showed that the interface was more water-like than ice-like, as no sharp Raman peaks associated with ice were found in the spectra. The O-O stretching band was also the same as for bulk water. Based on the Raman spectra, they estimated an upper limit of 2 % by volume of ice content in the interfacial region. The only anomaly was the discovery of a completely polarized line in the low frequency range of the Raman spectra of the interface. Halter et al. [238] tentatively assigned this anomaly to the formation and decay of some symmetric structure of a few H-bonded water molecules where the relaxation lifetime is half that of a typical H-bond. They also found the intensity of the Rayleigh scattering was about 500 times larger in the interfacial layer than the intensity of Rayleigh and Brillouin scattering in bulk water. They thus postulated that lower local density of the interfacial region could possibly be responsible for the anomaly and an enhanced Rayleigh line in the spectrum.

The interface width was estimated to be in the range of 3 – 200 μm, depending on the growth rate of the crystal. Halter et al. [238] also estimated the diffusion constant to be 7×10^{-8} cm s^{-2}. At low growth rates the interfacial region was described as thick

(viscous) and inhomogeneous (solid and liquid characteristics were indistinguishable) with optically non-resolvable regions immersed in bulk water. They stated that the local environment of a molecule is "water-like" with more H-bonds on average than in bulk water.

Both Böni et al. [230] and Halter et al. [238] have seen enhanced Rayleigh scattering at the ice/water interface under different conditions and it has been suggested that it is a universal phenomenon of crystal growth [239]. A 1986 paper by Cummings et al. [240], discussing a possible mechanism for the enhanced Rayleigh radiation, suggested that Brownian motion of precipitated microbubbles of gases, segregated at the growing interface, could be responsible for the enhanced radiation. It is known that the formation of microbubbles does occur during growth of a crystal from its melt, albeit an undesirable trait.

In a paper by Mesquita et al. [241], based on the suggestion of Cummings et al. [240], a biphenyl and naphthalene crystal/melt interface was investigated. It was quantitatively shown that the microbubble hypothesis was tenable. The model used by Mesquita et al. [241] associated Γ, the line width of Böni et al. [230] with the microbubble radius. To test the model, data from Böni et al. [230] were used and the model successfully reproduced their results.

In another experimental paper published by Brown et al. [240] at roughly the same time as Böni et al. [230], the results for Γ, were different. This study focussed on the prism face rather than the basal face examined by Böni et al. [230]. Brown et al. [242] suggested that the difference in the Γ values might be indicative of longer lived species in the interface at the prism face of hexagonal ice.

There is doubt at this time in interpreting the results of Böni et al. [230], Halter et al. [238] and Brown et al. [242], arising from the microbubble hypothesis [241]. In the 17 years, since the work of Halter et al. [238] these experiments have not been repeated. It remains unclear if microbubbles were present in these experiments, and if so, to what extent microbubbles may have affected the results obtained in these experiments.

5.4.3 Conclusions of experimental results

The small number of experimental studies reported in the literature is a testament to the difficulties faced in probing the ice/water interface; there is also a lack of a consistent description of the interfacial region. The light scattering experiments predict a very broad interface, possibly due to microbubbles or impurities forced to the front of the growing interface. It is also possible that non-equilibrium interfaces are broader than the equilibrium one. Another reason for the broad interface could be related to the wavelength of the light used. Therefore, better length resolution, and experiments that can be used to look at non-equilibrium and equilibrium interfaces, are needed.

Ellipsometry was useful in confirming a probable width of the interface, but ultimately had to rely on computer simulation results to confirm these estimates. Clearly, new experimental methods need to be developed to obtain a better picture of the interfacial region. There has been work done using second harmonic generation (SHG), optical scattering to probe the water/vapour interface [243] and the ice/vapour interface [244]; SHG has been seen as a possible technique to explore the ice/water interface. To date, only one study has claimed to have observed a signal from the ice/water interface [244], but the interpretation and the use of that experiment is doubtful as no other SHG

study (in the last ten years since reference [244]) has managed to obtain useful data from this technique applied to ice/water interfaces. Another experiment in the literature that has addressed the ice/water interface is a 1997 paper by Weglarz and Peemoeller [245]. It reported an observed coupling across the ice/water interface in a NMR experiment and the authors were hopeful that further work could be done. To date, no new experiments on the ice/water interface have appeared.

5.5 SIMULATIONS OF ICE

5.5.1 Relevant water models used in ice/water simulation

Numerous models of water have been developed and used in simulation studies over the last 30 years [246]. The two models commonly used in simulations of ice/water are the TIP4P [28] and the SPC/E [30] potentials; other important models recently developed are the CF1 model [247] and the TIP4P-Ew model [29]. These are all empirical force field models of water.

TIP4P [28] is a rigid four-site model, with an OH distance of 0.9572 Å and an HOH angle of 104.52°. The two hydrogen atoms each have a positive point charge of 0.52e. A negative point charge of -1.04e is placed along the HOH bisector at a distance of 0.15 Å above the oxygen. The fourth site of this model is a Lennard-Jones sphere located on the oxygen. The potential of interaction, U_{ij}, is then given by the sum of a coulombic term,

$$U_{ij} = \sum_{k}^{on\ i} \sum_{l}^{on\ j} \frac{Q_k Q_l}{r_{kl}}, \tag{5.6}$$

and a Lennard Jones (LJ) term,

$$U_{LJ} = 4\varepsilon_{LJ}\left[\left(\frac{\sigma}{r_{ij}}\right)^{12} - \left(\frac{\sigma}{r_{ij}}\right)^{6}\right], \tag{5.7}$$

where Q_k represents charge on site k on molecule i, r_{kl} is the distance between sites, ε is the well depth, and σ is the diameter of the site and r_{ij} is the distance between oxygen sites. The values of the LJ parameters ε and σ are 0.649 kJ mol^{-1} and 3.154 Å respectively, for the TIP4P model. A related but different model has recently been developed called the TIP4P-Ew model [29]. In this model the LJ parameters ε and σ are 0.680946 kJ mol^{-1} and 3.16435 Å, respectively. The negative point charge above the oxygen is –1.04844e at a distance along the HOH bisector of 0.1250Å and the charge on each of the hydrogen atoms is 0.52422e. Other aspects of the model are the same as that of TIP4P.

The SPC/E [30] is a rigid three-site model, with a HOH angle of 109.47° and an OH bond length of 1 Å. The hydrogen atoms each have a charge of 0.4238e. The oxygen atom carries a charge of –0.8476e and provides the centre of the Lennard-Jones interaction. The form of the SPC/E potential is the same as for the TIP4P (see Equations 5.6 and 5.7) but now where ε = 0.6517 kJ mol^{-1} and σ = 3.166 Å.

The CF1 model used by Duh et al. [247] in ice/water simulations is a flexible atom-based model. The vibrations inherent in the flexibility of the bond add a small

degree of polarization to the system. The CF1 potentials (hydrogen-hydrogen) U_{HH}, (oxygen-hydrogen) U_{OH} and (oxygen-oxygen) U_{OO} are given by

$$U_{HH} = \frac{36.1345}{r} + \frac{18}{1+e^{40(r-2.05C_2)}} - 17e^{-7.62177(r-1.45251)^2}, \qquad (5.8\ a)$$

$$U_{OH} = \frac{-72.269}{r} + \frac{6.23403}{r^{9.19912}} - \frac{10}{1+e^{40(r-1.05)}} - \frac{4}{1+e^{5.49305(r-2.2)}}, \qquad (5.8\ b)$$

and

$$U_{OO} = \frac{-144.538}{r} + \frac{26758.2C_1}{r^{8.8591}} - 0.25e^{-4(r-3.4)^2}, \qquad (5.8\ c)$$

where C_1 = 0.9 and C_2 = 1/1.1025. The distance r is measured in Å and the energy is in kcal mol^{-1}. The hydrogen atoms have a charge of q_H = 0.32983e and the oxygen atoms a charge of q_O =-2q_H. However, the latter model's behaviour in simulations of ice has not been thoroughly investigated.

These models have reproduced many physical properties of both liquid water and ice successfully despite their simplicity. A comparison of several standard properties of the TIP4P, TIP4P-Ew, SPC/E and CF1 models with experimental results are given in Table 5.1

Recently a new water/ice model designed for the explicit purpose of simulating water and ice was developed by Nada and van der Eerden [248]. This intermolecular potential for water contain six sites. It is TIP4P-like but with two additional charged sites to take into account electron lone pairs. As with the TIP4P and TIP4P-Ew models, the parameters of the model are changed to reproduce experimental properties. Some of the properties of this model are listed in Table 5.1. These models have been developed to investigate various properties of water and ice within reasonable computation times.

Ideally, a full quantum treatment of a many-bodied problem might be desirable, however this is clearly not practical at present. In addition, significant insights have been gained from simulations on ice and water with these models as the next section will show.

Table 5.1 A comparison of different thermodynamic properties of water for five water models at ambient conditions. The errors are given in brackets. (Adapted and modified from ref. [30] Table V)

	CF1	**SPC/E**	**TIP4P**	**TIP4P-Ew** *d)*	**Six-site model** *e)*	**Experiment**
T (K)	295.6	298	298	298	298	298
ρ (g cm^{-3})	0.997	0.997	1.002 (0.005)	0.9954	0.999 (0.08)	0.997
E_{vap} (kcal mol^{-1})	10.82 *a)*	9.90	10.10 (0.02)	9.982	9.95 (0.03)	9.92
P (kbar)	0.12 (0.03)	0.08 (0.04)	0.001	0.001	0.001	0.001
κ_T (10^{-3} kbar^{-1})	45	41.4 (2.0) *b)*	67 (13)	48.1	56 (8)	45.2
C_V (cal mol^{-1}K^{-1})	25 (10)	---------	20 (2)	19.2	24.7 (0.7)	17.8
ε_0	69 (11)	67 (10)	53 (2) *c)*	63.9 $\pm$ 0.9	----------	78.46

a) E_{vap} for CF1 is at 298 K, b) κ_T, for SPC/E is at 1.003, c) ε TIP4P is at 293 K, d) [30]. e) [248,249]

5.5.2 Survey of computer simulations in the literature

The simulations discussed in this section will focus primarily on ice/water interfaces and growth of ice from the melt. In addition simulation work providing information on the melting temperatures for different ice models will be briefly examined.

The first successful simulation of the ice/water interface was by Karim and Haymet [235,250]. To construct the initial ice/water interface they used separate, previously equilibrated samples of ice I_h and bulk water. The ice I_h system was in an antiferroelectric structure and its basal plane was brought into contact with the water system. At that point, there was extreme stress at the interface, in the form of localized hot regions, which had to be removed. Their solution involved fixing the positions of the solid section, and allowing the liquid to relax. All molecules with velocities twice that of the equipartition value were rescaled to the equipartition value. With the stresses removed, the solid section is assigned its original equilibrated velocities. The solid and liquid samples were then equilibrated with periodic velocity rescaling to obtain a mean temperature of 240 K. In constructing the interface periodic boundary conditions were applied in all three directions because bulk properties of the interface were being investigated. The system contained a total of 1440 molecules, using the TIP4P water model.

The equilibrium melting temperature was found to be 240 ± 1.5 K, with a pressure of -105 ± 118 atm. An interface thickness of 10-15 Å was estimated from density profiles, diffusion constant calculations and orientational correlation functions.

Orientational correlation functions, for the water dipole direction vector and a H-H direction vector, were used to provide a measure of solid order.

In a subsequent paper, Karim and Haymet [251] used the SPC/E model of water and employed the same elaborate technique to construct a stable interface. This study reproduced the properties determined in their first paper, with the exception of the melting temperature; the value was found to be 200 K for SPC/E. Their conclusion was that the observed melting temperature difference was due to the different models used, and that the similarity of the other results constitute evidence that the observed behaviour was representative of the actual properties of the real ice/water interface.

In 1995 two research groups independently reported studies of the ice/water interface. In one of these, Bàez and Clancy [252] used the SPC/E model and a simulation methodology based on Karim and Haymet to investigate the ice/water interface. They also estimated free energies of several ice polymorphs in their simulations. A lower energy, proton-ordered form of ice IX was produced, designated ice A, through these free energy simulations. They have also discovered that the SPC/E model predicts that ice II and ice A are more stable than ice I_h and I_c at low pressure. During their simulations of an ice A/melt system, they discovered a new structure, which they denoted as ice B, later identified as a quartz polymorph [252]. This form of ice is not known at present to exist in nature. Their simulations of ice B revealed that it is thermodynamically more stable than all the other polymorphs examined for the SPC/E model. Its growth, at a speed of 50 cm/s at 240 K, was observed. This growth is the first instance of ice growth reported in the literature. They concluded the paper by indicating that the SPC/E model is good for reproducing bulk liquid properties, however it fails in reproducing the relative stabilities

of the ice phases, recently confirmed by Vega et al. [253]. It is noteworthy that Bàez and Clancy [252] did not observe the interfacial growth of hexagonal or cubic ice.

The third important research group that has studied the ice/water interface is Nada and Furukawa [254]. They have used the TIP4P water model and techniques similar to those of Karim and Haymet [235,250] to investigate both the basal and prismatic planes of ice I_h. They obtained similar results to those of previous authors; they discovered that the interface was diffuse and had characteristics that were both ice-like and water-like. They did report an anisotropy between the basal and prismatic faces, with the basal face claimed to be thicker than the prism face. This anisotropy was interpreted from an analysis of self-diffusion data. Their results agree with the suggestion found in the experimental work of Brown et al. [242] that there may be longer lived species close to the solid, as well as the interpretation of Beaglehole et al. [234] that molecules near the prism interface are more structured than those at the basal interface. Unfortunately, no significant ice crystal growth was recorded and Nada and Furukawa concluded that the timescales of their simulations (100 ps) may have not been sufficient to observe crystal growth.

In a follow-up to their 1995 paper, Nada and Furukawa [255] once again investigated the ice/water interfaces of the prism and basal planes. They now employed a modified simulation methodology to take into account the removal of latent heat originating from the growth of the interface [256]. They started with a simulation box of bulk ice and melted half of it by increasing its temperature to obtain liquid water. During their simulation run, they fixed the temperature of the ice end of the simulation box to 0 K and the water end to 230 K. Periodic boundary conditions were applied in the x and y

directions only. They observed minimal ice growth (at best) over a time scale of 1 ns, although the prism face does have better overall order in the growth layer. They postulated, based on these results, that the basal plane grows by a *layer by layer* process. That is to say the growth is two-dimensional, one complete layer of the basal face must be completely filled, before the next layer can form. They claimed the prism face grows by a *collected molecule process*, although the description of this process is unclear in this paper. The anisotropy in the growth structure was interpreted as implying faster growth for the prism face than the basal face.

In their second paper, Nada and Furukawa [255], did not take into account boundary problems on the water side of their simulation box. They did not mention whether the boundary on the water side of their system was a vacuum or a wall. Both these situations would result in perturbations within the liquid. For example, one problem introduced by having a wall is that it might cause significant orientational ordering throughout the system [257]. On the solid side of their interface, where the molecules at the end of the simulation box was fixed on their lattice sites and was held at 0 K, the presence of a boundary was not significant. It is also interesting that during their simulations, they found an average temperatures of both systems to be about 5 K higher than the target temperature in their simulation; this increase in temperature was not satisfactorily explained.

They subsequently published a third paper in 1997 [258] to clarify their previous observations of the interfacial crystal growth. They again observed only minimal crystal growth. One might expect that under the right conditions for crystal growth, they would have certainly seen more significant growth (comparable to that seen in Bàez and Clancy

[252]). Based on the analysis of the data, Nada and Furukawa [258] concluded that translational order occurs before orientational order during crystal growth. They found that the prism face was geometrically rough whilst the basal face was a smooth surface.

A significant study by Hayward and Haymet [165] in 2000 addressed four ice/water interfaces, the basal (0001), the prismatic $(10\bar{1}0)$, the $(20\bar{2}1)$ and the $(11\bar{2}0)$ faces. They used the central force model (CF1) for this work. They attempted to characterize the interface using five order parameters within two-dimensional slabs: the translational, orientational (dipole vector of a water molecule and the z-axis) and local order (via the O-O coordination numbers) to examine structure; the average density and diffusion constants to explore the changes from the solid to the liquid. These five order parameters provide profiles through the interface. They used a criterion defined as the 10-90 value, where an order parameter changes from 10-90% of its value when moving through the interface from the bulk liquid to the bulk solid. They employed this criterion and their five order parameters to estimate the widths of the interface. The authors identified the center of the interface by using "what appear[ed] to be the center of the interfacial region" from inspecting the translational order parameter profile. According to their interpretation, the order parameter with the biggest 10-90 widths is the one that exerts the most influence on the interface. They concluded that in the prism interface, orientational structure and the dynamics of the water in front of it, dominate the interfacial properties more than in the other interfaces. In the basal interface, the translational order and average density of molecules are more important than the other factors. The water molecules within the basal interface are also dynamically more water-like. Hayward and Haymet [165] report that the other two faces are thinner and the ice

has less influence on the structure and dynamics of the water molecules in the interfacial region. Table 5.2 summarizes their calculated interfacial widths for the 0001, $10\bar{1}0$ and $11\bar{2}0$ faces of hexagonal ice. In a subsequent study [259], Hayward and Haymet investigated the orientational dependence of the molecules within the interface. The results for the orientational order parameters were very similar; the prism face however showed a slight but measurable difference from the three other interfaces, indicating its relative importance. They found that the water molecules were more orientationally ordered (i.e. akin to ice) in the *xz* and *yz* planes than in the *xy* plane for all the crystal faces. As Table 5.2 indicates, Hayward and Haymet [259] found that the basal face was wider than the prism and $11\bar{2}0$ faces for all their measures except the orientational order parameter.

The results of Hayward and Haymet [165,259] were generated from static interfaces. A key observation in Figure 5.13(a) is the fluctuations of structure at the transition of solid to liquid. Additionally, inspecting the density profiles provides little evidence to support whether one interface is broader than the other. The data they obtained from two-dimensional slabs for the five order parameters are a series of step functions. For example for the average oxygen density across the prism interface shown in Figure 5.13(b) is where the two step functions are their actual data. The non-uniform bins are allowed to change their dimensions with the expansion and contraction of the interface during the simulation whereas the uniform bin was held fixed. The continuous dashed line in Figure 5.13(b) is their smoothed representation of this profile. For the slab labelled P4, it is clear from Figure 5.13(b) that their smoothed function does not take into account the drop in density apparent in their original data. All Hayward and Haymet's

interpretations were made based on their smoothed functions of static profiles. One of the shortcomings of applying the smoothing procedure is that while it results in smooth curves, it is still limited by the coarse grain nature of the underlying bin structure, which is inherent in obtaining profiles in the static frame. Hence the resolution of their profiles of the interfacial boundaries is still crude and their ability to identify real differences in, for example the thicknesses of the interfaces, is questionable. Moreover, their general criteria for examining the different interfaces with the various order parameters indicate that they were investigating the change of different order parameters through the interface rather than measuring the width of the interface. This implies that the interface is dependent on which measure is used and there is no distinct entity as an interface. Further they do not provide a consistent physical account of the microscopic behaviour of the interface.

To explore possible model dependences from the work of Hayward and Haymet [165,259], Bryk and Haymet [260] explored ice/water interfaces with the SPC/E model. Only the basal and prism interfaces were investigated with 1920 water molecules. The equilibrated configurations were based on those of Hayward and Haymet [165]. Bryk and Haymet [260] obtained stable ice water interfaces in NVT MD simulations at a temperature of 225 $\pm$ 5 K, which they predict is the melting point of the model at 1 atm. They observed mass density oscillations at 220 K for the prism face, which was not observed for the basal face (see fig. 10 of ref. [260]).They interpreted this result as the possible formation of "slushy" solid or the perhaps even the growth of ice. Bryk and Haymet [260] employed different order parameters to quantify the interface and ended up with similar conclusions to those of Hayward and Haymet (the width is dependent on the

order parameter). Based on their averaging and smoothing techniques of the density profiles they obtained widths of 12.86 and 10.03 Å for the basal face and for the prism face based on the density profiles. A common thread that is evident from the work of Nada and Furukawa [254,255,258], Hayward and Haymet [165,259] and Bryk and Haymet [260] using different water models, namely TIP4P, CF1 and SPC/E, respectively, is that the interfaces as described by the density profile functions has 3 transition layers between bulk solid and liquid with fluctuations in structure within the interfacial region.

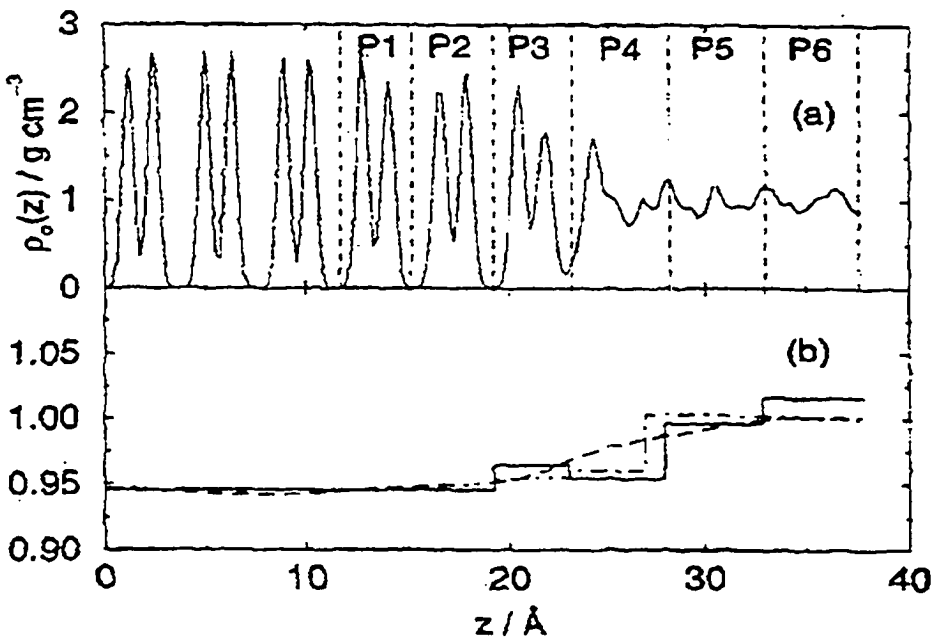

Figure 5.13 The oxygen density profile for the prism interface of Hayward and Haymet. a) The translational order profile, b) average density profiles for non-uniform (solid line) and uniform bins (dot-dashed line), with the smoothed function (dashed lines). (from ref. [165] Fig. 4)

Table 5.2 10-90 widths of the basal, prism and $11\bar{2}0$ for ice Ih as determined by Hayward and Haymet [259]. All results are in Å.

Crystal face / Order Parameter	Basal	Prism	$11\bar{2}0$
Translational	9.9	8.6	7.9
Average density	18.2	13.6	11.4
Diffusion	10.8	10.1	9.7
Orientational	5.7	7.7	7.5

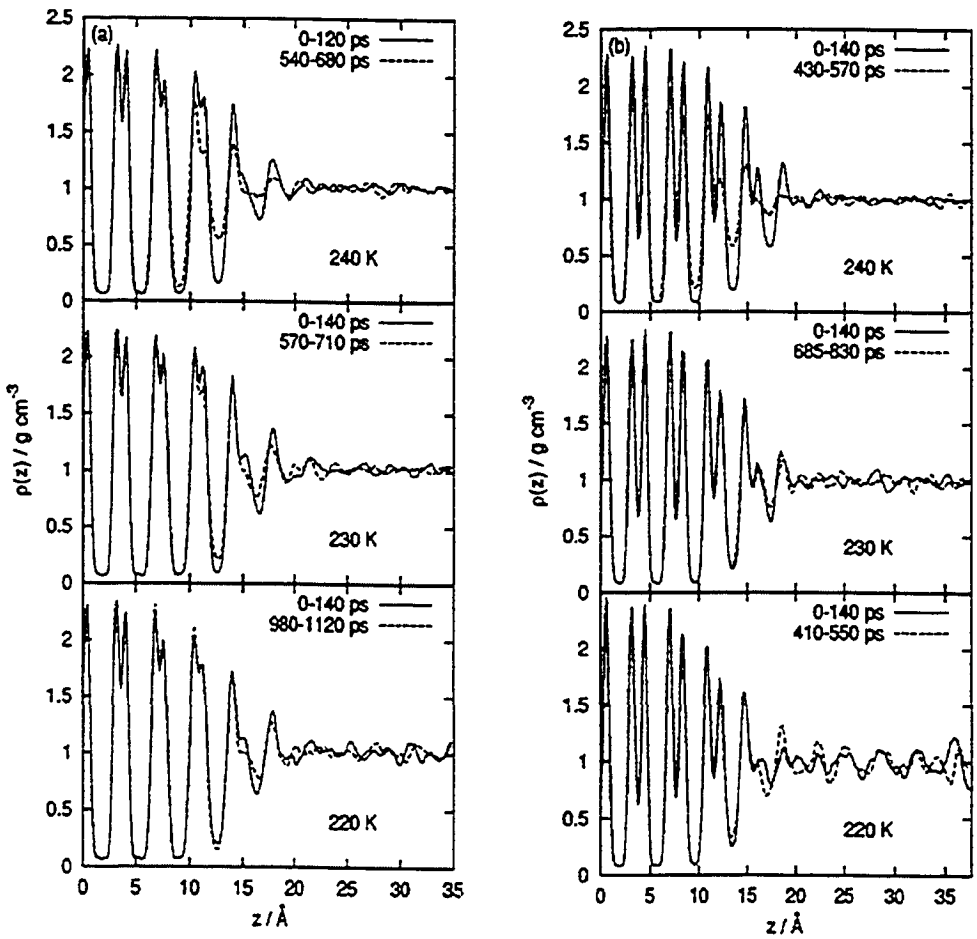

Figure 5.14 Mass-density profiles for the basal (a) and prism (b) ice/water interfaces. These are given at different temperatures estimated from two different time windows as indicated (from ref. [260] fig. 10).

In a recent study Nada et al. [249], using their newly developed six-site potential model [248] (see section 5.5.1), claimed to observe ice growth in a 2.7 ns simulation study for the prism face of ice. This new model was shown to have a melting temperature of 271 $\pm$ 9 K at 1 atm. Their simulation was set up similarly to Nada and Furukawa's [255] previous study with an ice system of 720 molecules sandwiched between two liquid systems of 360 molecules each. They claimed to have observed four layers of growth on one side and two on the other, where the highest growth speed was reported at 10 cm/s for the prism face. The prism face was claimed to be rough, with no change of interfacial structure, during the growth phase. Inspection of 10 ps snapshots revealed that as a layer is reorganizing its hydrogen bond network, it simultaneously induces a reorganization within the next layer towards the liquid. Therefore, their observation that the prismatic interface growth occurs by "kinetics of the reorganization of the hydrogen bonded network" over two layers, (which they claim) is qualitatively in agreement with the *collected molecular process* proposed by Nada and Furukawa [255].

5.5.3 Conclusions from computer simulations in the literature

There has been some important simulation work probing the ice/water interfacial region with several different water models. These simulations have certainly added to the understanding of selected aspects of structure and dynamics of the interfacial region. Haymet and co-workers [165,235,251,259,260] used the 10-90 criterion to define the position of the interface. This criterion provides an estimate of the interfacial thickness, but due to limitations of their profile data their interpretations are somewhat ambiguous. The use of several different order parameters has certainly demonstrated some interesting

properties of the interface through the change of these measures through the interface. Yet, their ability to use these various order parameters to define the interfacial width is certainly questionable. Nada and Furukawa [258], have neither focused on the location nor the thickness of the interfacial region, although they rely on a fixed interfacial boundary between the liquid and the solid in their analysis. Moreover, the growth that was reported by Nada and Furukawa [258], has since been ignored by the same group in their more recent paper [249]. There is sufficient justification in this new work to support a claim of having observed some new crystalline layers. Despite this observation, it still remains to be shown that the crystalline layers formed are not merely fluctuations of the structure within the 2.7 ns of the simulation. As is clearly evident in Bryk and Haymet's work [260], from Figure 5.14, fluctuations of structure can occur at the interface even after stable interfaces are created.

These simulations have provided useful information on the melting temperatures of the various models. If the melting temperatures of the various models are known precisely, simulations of crystal growth can be more easily attempted. The melting temperatures of several models relevant to this thesis are provided in Table 5.3; also included are estimates derived from calculations of free energies. There are some minor discrepancies between the melting temperatures from the various studies of TIP4P and SPC/E, exhibiting the difficulty of obtaining reliable simulation methods to predict melting temperatures. In addition, if melting and freezing temperatures are to be obtained from simulations, an effective means of determining the temperatures at the interfaces becomes necessary.

Table 5.3 Melting temperatures of disordered hexagonal ice for different water models at 1 atm. All temperature in Kelvins (K).

TIP4P [28]	240 ± 5 [250]	230 ≤ x ≥ 250 [261]	230 ± 5 [258]	232 ±5 [262]	229 [229]
SPC/E [30]	220 ± 5 [252]	215 ± 5 [263]	225 ± 5 [260]	-----	-----
TIP4P-Ew [29]	245.5 [253]	-----	-----	-----	-----
CF1 [247]	236 [165]	-----	-----	-----	-----
Six-site Potential Model [248]	271 + 9 [248]	-----	-----	-----	-----

The simulations that have been reported in the literature to date do not provide an unambiguous means for defining the position and width of the interface. Without doubt, clarification of the crystal/melt behaviour of water is a challenging task. The intrinsic fluctuations of the interfacial structure and subsequent analysis based on static profiles with their inherently discrete coarse-grained molecular structure has hampered investigations of the ice/water interface by computer simulations to date. Moreover, no steady-state growth simulations have ever been reported for ice growth, an indication of the difficulties that such a study entails. In a relatively recent homogeneous study of ice nucleation, Matsumoto et al. [264] reported ice nucleation and water freezing occurring after a 300 ns simulation. The temperature of the simulation was 230 K. The simulation size consisted of 512 TIP4P water molecules. It is a difficult result to interpret, as the authors were approximately at the melting point of the model. This should not have caused the system to solidify as the liquid was not supercooled contrary to their claims. (see Table 5.3). In addition, it is unclear whether there was significant crystal structure in the solidified system and the result was not reproducible.

5.5.4 Computational details of non-equilibrium steady-state simulations of ice.

The methodology developed for achieving steady-state crystal growth for the LJ systems was adapted and modified to ice/water systems in the present study. The simulations in this thesis were primarily performed using the TIP4P water model; however, simulations of TIP4P-Ew and SPC/E models were also used. Table 1 summarizes the crystal structures investigated, along with the potentials and system sizes used for each of the six crystallographic faces of Ice I (001, 011 and 111 for the cubic systems and 0001, $(10\bar{1}0)$ and $(11\bar{2}0)$ for the hexagonal systems) considered here. The various systems under the different conditions described in Table 5.4 resulted in 120 production simulations performed with different temperature gradients and growth velocities as summarized in Tables 5.5 and 5.6, respectively. In these simulations the LJ potential was truncated at a cutoff radius of half the box-width (in x and y dimensions) and the long range forces were treated with Ewald sums [115]. Plane-slab periodic boundary conditions [265] were applied with a reduced timestep of 1 fs.

Similar to the LJ systems, an order parameter to determine crystalline order across the interface was an important consideration. One of the order parameters employed was the Σ function given in equation 3.33, where again the two-dimensional wave-vector was commensurate with the unit cell structure of each of the six different crystal faces of ice and the vector (x,y) is the position of the molecule within the two-dimensional slice. This order parameter was then only sensitive to the center of mass positions in the two-dimensional slice and proved to be a good discriminator of local crystalline order in our ice simulations.

To complement the Σ function, an order parameter sensitive to the three-dimensional structure of the four nearest neighbours immediately surrounding a given water molecule was also used [266]. This order parameter is made up of two parts. The first part is concerned with the angular dependence of a tetrahedral arrangement,

$$S_g = \frac{3}{32}\sum_{j=1}^{3}\sum_{k=j+1}^{4}\left(\cos\psi_{j,k} + \frac{1}{3}\right)^2, \tag{5.9}$$

where ψ is the angle subtended at the central atom between the j^{th} and k^{th} intermolecular separation vectors (bonds), the factor 3/32 normalizes S_g to the range $0 \le S_g \le 1$, and the squaring ensures that the contribution from each bond angle is always ≥ 0. The second part focuses on the distances of the four neighbours in a tetrahedral arrangement, and is given by

$$S_k = \frac{1}{3}\sum_{k=1}^{4}\frac{\left(r_k - \bar{r}\right)^2}{4\bar{r}^2}, \tag{5.10}$$

where r_k is the radial distance from the central molecule to the k^{th} neighbour, $\bar{r}$ is the arithmetic mean of the four radial distances, and 1/3 is the normalizing factor. Both S_g and S_k return zero for a perfectly tetrahedral arrangement of the four nearest neighbours and a maximum value of 1 for complete deviations from the angular and the distance ideals. Chau and Hardwick [266] have used this order parameter in Lennard-Jones, ice and water systems and have demonstrated its success in indicating the geometric configuration of the molecules in their study. The simulations required proton-disordered ice lattices for cubic (001), (110) and (111), and the hexagonal (0001), $(10\bar{1}0)$ and $(11\bar{2}0)$ faces to be generated for use as initial starting points. Software was developed to generate proton-disordered ice lattices for both the cubic and hexagonal ice lattices as

outlined in Appendix A. These have been thoroughly checked to ensure that they comply with the Bernal-Fowler ice rules [177]. The dipole moments of the lattices were also calculated to determine the polarization of the samples, which was found to be less than 5%. After the generation of these ice lattices, the creation of an equilibrium ice/water interface was required. In order to achieve this, the crystal was initially allowed to relax at an estimated melting temperature believed to be 233 K for the TIP4P model, while a barostat was used to scale all three dimensions of the simulation cell to obtain zero pressure. This procedure ensured that the crystal was relaxed and free of any spurious stress effects before further simulations were undertaken. Next, the local thermostats were turned on with their temperatures set at appropriate gradients to melt roughly half the system. The barostat was applied only in the z-dimension to ensure that the pressure was maintained at 1 atm pressure, while the x and y dimensions of the simulation cell were held fixed.

As with the LJ systems, a thermal gradient was utilized for all the crystal faces investigated to generate water/ice interfaces. These interfaces were equilibrated with the thermostats still in operation for 200 ps. The systems were monitored to ensure that the ice/water interfaces were stable. Crystal growth simulations were subsequently undertaken with the movement of the thermostats at various fixed velocities as given in Table 5.5. However, unlike the LJ simulations, steady-state crystal growth was not easily achieved. For ice/water simulations the length of the simulations required to allow for the sampling of the entire system would be prohibitive, thus a steady-state condition was considered established when averaged profile functions were essentially unchanged after 13 Å of movement by the thermostats. This procedure can be justified by investigating

Table 5.4 Summary of the different potentials and crystallographic faces of hexagonal and cubic lattices of Ice I investigated. The number of particles along with the cell dimensions (in brackets) are given.

Interface	Number of Particles		
	TIP4P	TIP4P-ew	SPC/E
Ic111	1728 (17.9 Å × 30.1 Å × 96.0 Å)	1728 (18.0 Å × 31.0 Å × 96.1 Å)	1728 (18.0 Å × 31.1 Å × 99.3 Å)
Ic011	1152 (18.1 Å × 18.8 Å × 105.1Å)	1152 (18.2 Å × 18.6 Å × 106.8Å)	1152 (18.1 Å × 18.7 Å × 108.4 Å)
Ic001	1152 (19.0 Å × 18.9 Å × 98.0Å)	1152 (19.1 Å × 19.3 Å × 97.2 Å)	1152 (19.0 Å × 19.2Å × 100.8Å)
Ih0001	1344 (17.9 Å × 23.3 Å × 99.6 Å)	1344 (17.9 Å × 23.3 Å × 100.7 Å)	1344 (17.8 Å × 23.2 Å × 101.5 Å)
$Ih10\bar{1}0$	1248 (17.9 Å × 21.9 Å × 97.6 Å)	1248 (18.0 Å × 22.0 Å × 99.3 Å)	1248 (17.9 Å × 21.9 Å × 102.2 Å)
$Ih11\bar{2}0$	1584 (23.3 Å × 21.9 Å × 99.0 Å)	1584 (23.3 Å × 21.9 Å × 96.1 Å)	1584 (23.4 Å × 22.0 Å × 99.0 Å)
Ic001 (long)	768 (12.4 Å × 13.3 Å × 142.0 Å)	-----	-----
Ic001 (small)	512 (12.4 Å × 13.3 Å × 99.0 Å)	-----	-----
Ic001 (big)	2048 (25.5 Å × 25.4 Å × 98.0 Å)	-----	-----
Ih0001 (big)	2016 (26.9 Å × 23.3 Å × 99.3 Å)	-----	-----

Table 5.5 Temperature gradients employed for the different water models employed in the present simulations along with the corresponding temperatures of the heat source and heat sink. All temperatures are in Kelvin.

	ΔT	T(hot)	T(cold)
TIP4P	248.8 (very large)	349.8	101.0
	116.6 (large)	303.1	186.5
	85.5 (moderate)	264.3	178.8
	58.3 (small)	264.3	206.0
TIP4P-Ew	248.8 (very large)	349.8	101.0
	116.6 (large)	303.1	186.6
	101.1 (moderate II)	275.9	186.5
	85.5 (moderate I)	272.0	186.5
	58.3 (small)	275.9	217.6
SPC/E	258.6 (large)	344.8	86.2
	82.9 (moderate)	254.7	172.4

Table 5.6 Velocities used in non-equilibrium simulations along with related simulation details. The values for total run length assume growth/melting of at least 15 Å.

Velocity (cm/s)	Time required to move 1σ (ns)	Total run length range (ns)
3	10.0	40-60
8	4.0	20-40
16	2.0	10-30
24	1.3	6-10
30	1	5-8

steady-state LJ simulations where characteristics that manifest steady-state conditions were achieved before the thermostats had moved through the entire system. This observation was made through inspection of the various profile functions used as described in Chapter 4. Table 5.6 lists the simulations in which the establishment of steady-state crystal growth conditions was attempted. Profile functions for the energy, density, pressure (its xx, yy and zz components), translational and rotational temperatures, the two-dimensional solid order parameter Σ, the tetrahedral order parameter S_g, the radial order parameter S_k as well as the translational and rotational diffusion constant were obtained along the z-dimension of the simulation cell to enable the characterization of the system. Bin widths of approximately 0.274 Å were used to generate numerical histograms, which allowed profile functions to be generated.

For the investigation of possible system size effects two significantly larger systems were also examined with approximately 50% greater cross-sectional area, where details are included in Table 5.4. A single system notation of Ic001 approximately 50%

longer was included to verify that the two icc/water interfaces was otherwise independent and did not interact with one another.

CHAPTER 6
MICROMODELLING OF THE CRYSTAL GROWTH OF ICE

The characterization of the ice crystal growth involves methods developed in the analysis of the LJ systems. Thus, an analogous approach will be the starting point to the investigation of ice growth. Correspondingly, the subsequent discussions will use the two complementary methods based upon profile functions and molecular snapshots of averaged configurations.

6.1 PROFILE FUNCTION DESCRIPTIONS

6.1.1 Profile functions

The results presented below are primarily from steady-state systems. In the ice/water simulations undertaken in this thesis, steady-states are described both with respect to freezing and melting. Non steady-state systems refer to those simulations that have failed to crystallize. These systems, however, always achieve steady-state melting. To distinguish these ice/water systems, the term "pseudo steady-state melting" will be used in this thesis. In the following discussions, data from pseudo steady-state systems will be included where appropriate.

For the characterization of the interfaces, similar profile functions to those applied in the LJ systems will be utilized to describe the heterogeneous environments present in the simulations. Most of the profile functions here, as in the LJ simulations, are relatively

smooth functions. However, to facilitate detailed analyses, thirteen point smooths were applied in all functions presented here. All z-dimensions of profile functions will be given in Angstroms. Figure 6.1 compares raw and smoothed data of the S_k function and Σ order parameter for a typical system. Clearly, the smoothing does not change the form and behaviour of the profile functions. Moreover, the smoothed profiles become more amenable to further mathematical treatment (taking derivatives), facilitating detailed investigations.

Figure 6.2(a) shows the translational temperature and the density profiles with respect to the z-dimension of the simulation cell as obtained from a typical steady-state system for the $Ih10\bar{1}0$ at large gradient and a growth velocity of 8 cm/s. Such profiles are typical of steady-state ice/water systems. The density of the liquid is higher than the solid as is expected for water. From the density, ρ, regions corresponding to the liquid, the solid and the transitions from liquid to solid can be approximated. Figure 6.2(a) also shows the translational temperature profile of the steady-state, reminiscent of the temperature profile of the LJ system with its characteristic "carat" shape. The rotational temperature profile (not shown) is essentially identical to the translational temperature. In characterizing the steady-state system other useful profiles, such as the energy and Σ functions as shown in Figure 6.2(b), can be employed. The flat region of the Σ profile (roughly 25-75 Å) demarcates the liquid region, and the solid region corresponds roughly to 0-15 Å and 85-95 Å, with the other regions (~ 15-25 Å and 75-85 Å) described as the interfacial regions. The energy function shows the characteristic "bell-shape" as seen previously for the LJ systems. Regions characterizing the solid, liquid and interface in the simulation cell for a molecular system such as water are thus, easily identified.

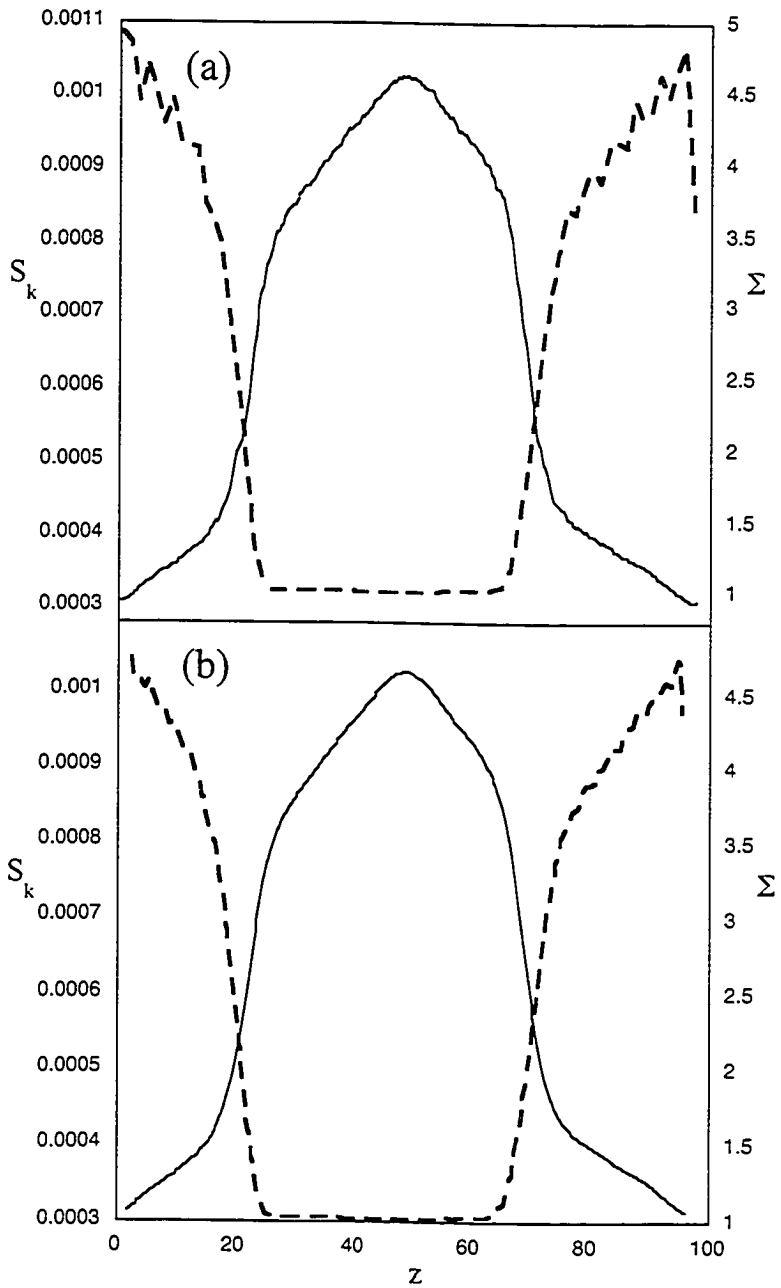

Figure 6.1 Profile data for: (a) the raw S_k function (solid line), and raw Σ order parameter (dashed line), and (b) the smoothed S_k function (solid line), and raw Σ order parameter (dashed line). Profiles are in the moving frame for a Ih10$\bar{1}$0 steady-system with a moderate gradient at a speed of 16 cm/s.

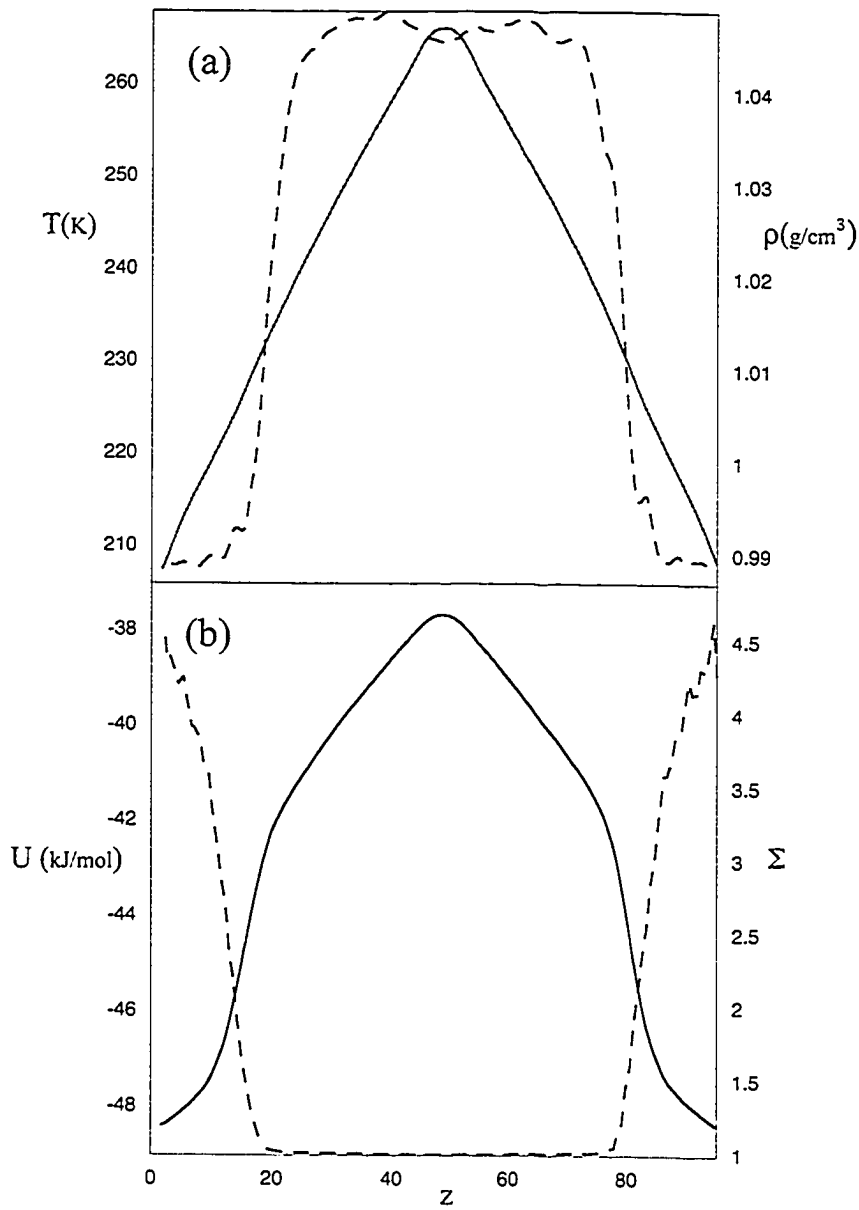

Figure 6.2 Profile data for: (a) the density, ρ, (solid line), and the temperature, T (dashed line), and (b) the Σ order parameter (dashed line), and the energy, U (solid line). All profiles are in the moving frame of Ih10$\bar{1}$0 steady-state system at a large gradient and a velocity of 8 cm/s.

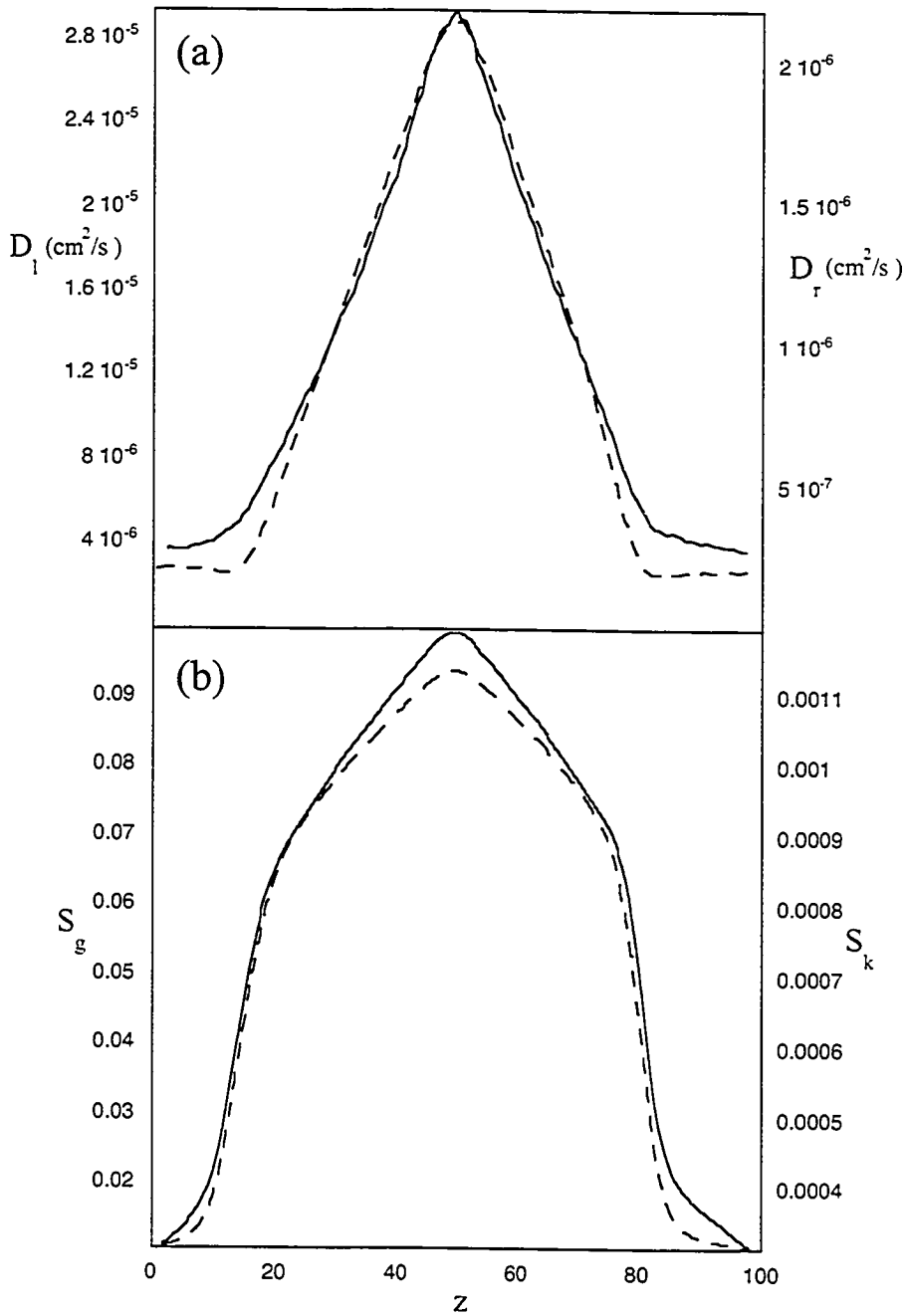

Figure 6.3 Profile data for: (a) the translational diffusion constant, D_l (dashed line), and the rotational diffusion constant, D_r (solid line), and (b) the S_g (dashed line) and the S_k functions (solid line). All profiles are in the moving frame of a Ih0001 steady-state system at a small gradient and a velocity of 8 cm/s.

The profile functions describe the heterogeneous environments of the other crystal faces equally well. Four other profile functions used to characterize these systems are shown in Figure 6.3 for the Ih0001 crystal/melt interface. The linear diffusion constant, D_l, and the rotational diffusion constant, D_r, are shown in Figures 6.3(a). The shape of these functions in the liquid region reflects the temperature gradient in the simulation cell and is consistent for all steady-state profiles in this study. The horizontal regions in both the translational and rotational diffusion constant profiles show that the flat horizontal regions demarcate the solid region. The values in the liquid are consistent with those reported in the literature [254] at corresponding temperatures. The solid regions should give a diffusion constant of essentially zero, however due to truncation errors in the calculation of the diffusion constant, values not consistent with a solid are obtained. The diffusion constant, however, is appositely used in describing general diffusive behaviour of molecules at the interface and is able to characterize liquid and solid nonetheless.

The S_ξ and S_k order parameter functions shown in Figures 6.3(b) are similar to the shape of the energy profile and identify similar boundaries for the different regions. This interesting characteristic implies that the local tetrahedral environment and the radial distances of a molecule's four nearest neighbours, as measured by the respective functions through a heterogeneous system (solid-interface-liquid) are very similar to the behaviour of the energy profile.

Pressure profiles for the Ih0001 crystal face at small gradient and a growth rate of 8 cm/s are shown in Figure 6.4. These profiles are typically less smooth (even after numerical smoothing) than in the LJ systems; however solid and liquid identification can be again made. The pressure profiles, (averaged over tens of nanoseconds in the moving

frame) are generally not well converged. More noise is evident in the interfacial region which typically shows negative pressures, as observed in Figure 6.4. Additionally, the values of the xx and yy components of the pressure tensor appear more negative than the zz component. Longer simulations must be undertaken to clarify the information from the pressure profiles.

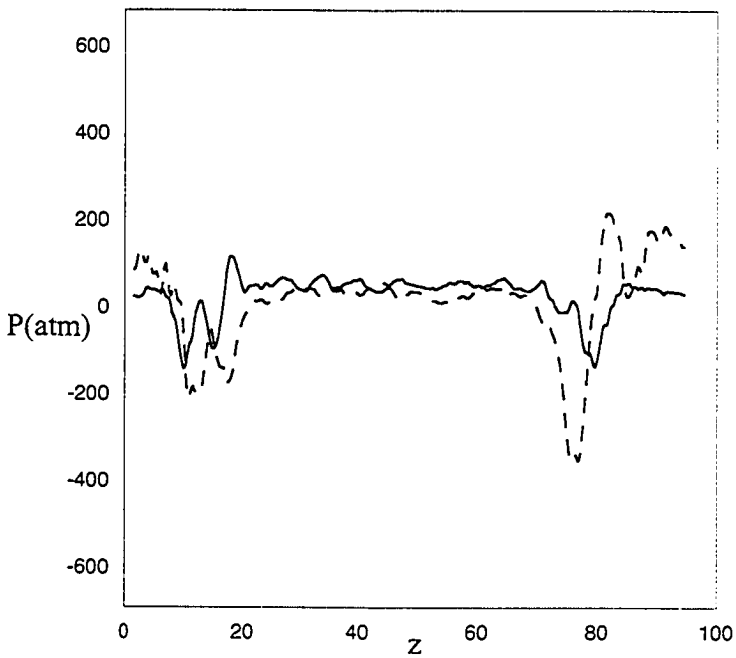

Figure 6.4 Profile data for the z-component of the pressure, $P_{zz}(z)$ (solid line), and the x-component of the pressure, P_{xx} (dashed line). All profiles are in the moving frame of a Ih0001 steady-state system at a small gradient and a velocity of 8 cm/s.

All the profiles described in this section indicate a consistency and reliability of these functions in characterizing the regions within the simulation cell. However, as was noted in Chapter 4 a more precise means of identifying the interface involves taking the derivatives of profile functions, such as the energy and Σ order parameter, with respect to the z-dimension of the simulation cell. Examples of these are shown in Figure 6.5(a) for the Ih0001 system at small gradient at 8cm/s. In addition, the derivatives of the S_g and

S_k order parameters with respect to the z-dimension are given in Figure 6.5(b). These profile functions unambiguously identify the positions and widths of the interfaces. For the calculation of the interfacial width, the z-derivative of the energy profile was used; although the Σ order parameter was used in the LJ analysis and proved to be a useful measure of the width (as noted in Chapter 4), these functions are found to be noisier in the ice/water system. They can be more aggressively smoothed (19-point smooths) to yield interfacial positions. However, because the increased smoothing can lead to overestimated widths no attempt to measure specific widths of these functions will be undertaken in this chapter. The derivatives of the S_g and S_k order parameters may be utilized to provide interfacial widths, but both functions were found to provide values for the width similar to those given by the z-derivative of the energy profiles. Therefore, the determination of interfacial widths discussed in the subsequent sections will use only the derivatives of the energy profile, along with the same method for calculating peaks for LJ systems as discussed in Section 4.1.

The derivatives of the density and energy profiles from LJ systems consistently describe the same positions and widths for the interfaces within the error bars. In contrast, the present ice/water simulations display quite different results. The peak in the derivative of the density profile, as given in Figure 6.6, differs by about 3.0 Å from the energy derivative; the density derivative appears to be shifted toward the liquid side of the interface. In this instance this shift, along with a similar shift in the Σ order parameter, may be indicating, interesting behaviour at the interface that will be explored in Section 6.2.

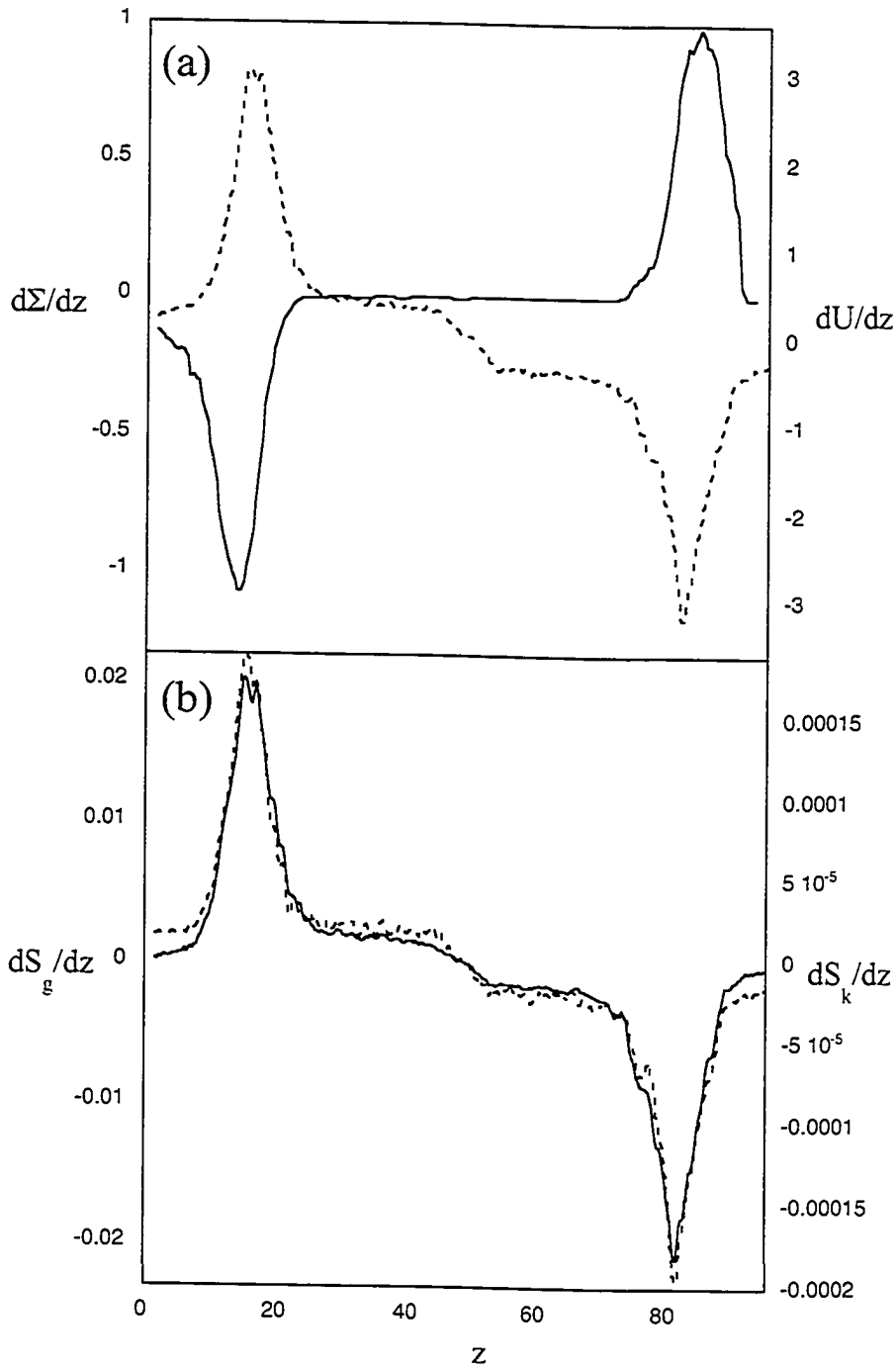

Figure 6.5 The derivatives of the energy and structural parameter profiles with respect to z. (a) The Σ order parameter (solid line) and the energy, U (dashed line). (b) The S_g function (solid line) and S_k functions (dashed line). The peaks/valleys correspond to the positions of the freezing and melting interfaces. The widths of the peaks correspond to the interfacial widths. The system shown is the Ih0001 steady-state system at a small gradient and a velocity of 8 cm/s.

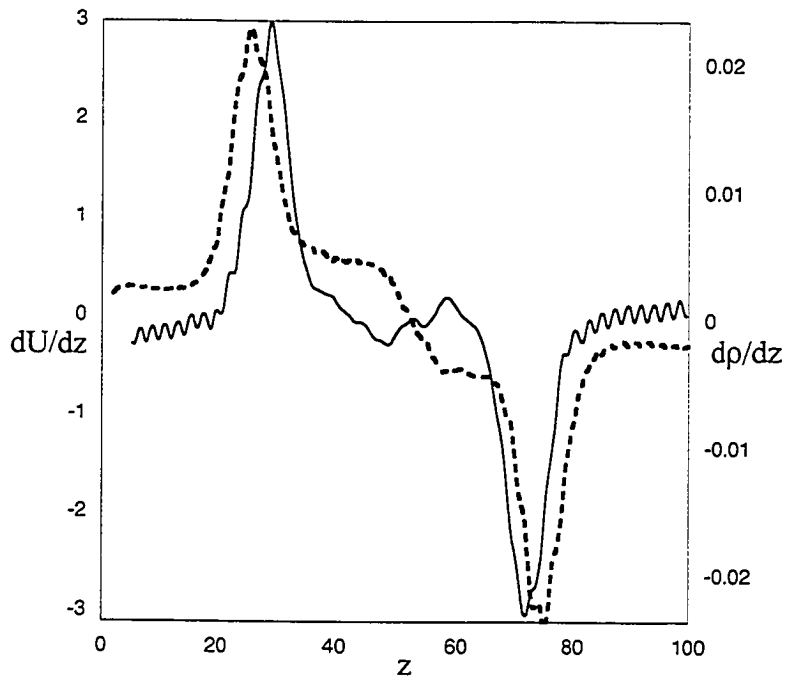

Figure 6.6 Comparison of the derivatives of the energy and density profiles. The density, ρ, is given by the solid line and the energy, U is given by dashed line. The system shown is the Ic011 steady-state system at a moderate gradient and a velocity of 16 cm/s.

The analysis of pseudo steady-state systems also allows for the extraction of interfacial widths and melting temperatures. Here we will use exclusively the melting interfaces of the system which contains at least 10 Å of "bulk" solid thereby minimizing the interaction of the two interfaces. The structural fluctuations inherent at the interfaces appear to couple for solid thicknesses of less than 10 Å. Figure 6.7 shows profiles of the derivative of the energy of a steady-state and pseudo steady-state melting interface of $\mathrm{Ih}1\,1\bar{2}0$ at 8 and 30 cm/s, respectively. Other than a shift in the peak for the latter system (which will be discussed in the section 6.1.2) the profiles appear to predict essentially

identical widths for the interface. This confirms the validity of these pseudo steady-state runs as well as the insensitivity of interfacial properties to the growth (melting) velocity.

As was found in the LJ simulation, no significant differences between simulations with our "big", "long" and normal sized systems (as defined in Table 5.4) were found. Figure 6.8 shows the z-derivatives of the energy profiles for two Ic001 systems. The positions of the peaks and the widths of the interface of the steady-state systems are in good agreement. Similar behaviour was observed for the Ih0001 systems that were examined. The slight shifts evident in Figure 6.8 can be understood as suggesting that the big system had not been fully equilibrated (the computation costs of the runs for these systems had necessitated much shorter runtimes). Inspection of the Figure 6.8 does show a strong similarity of widths for the normal and "big" systems.

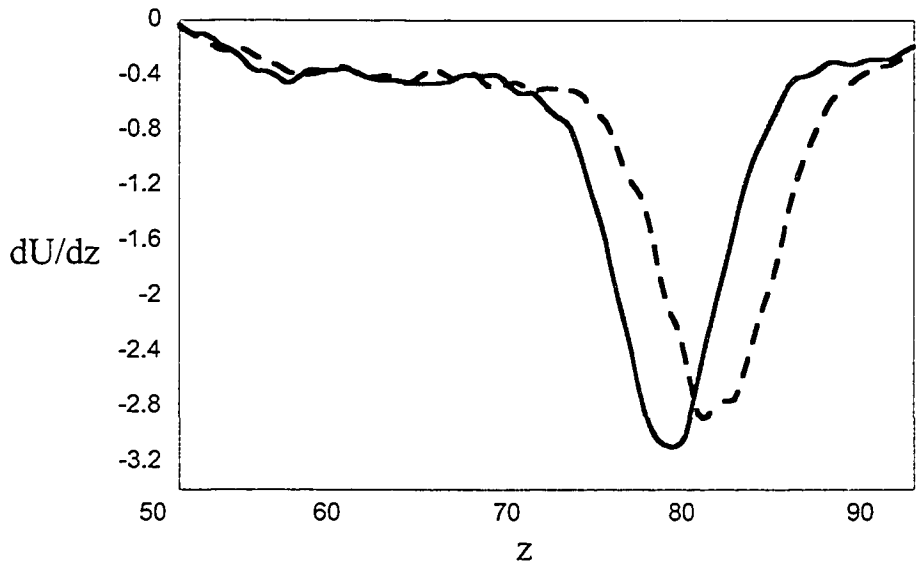

Figure 6.7 The derivative of the energy showing the melting interfaces of Ih$1\bar{2}10$ at 8 cm/s (dashed line) and 30 cm/s (solid line).

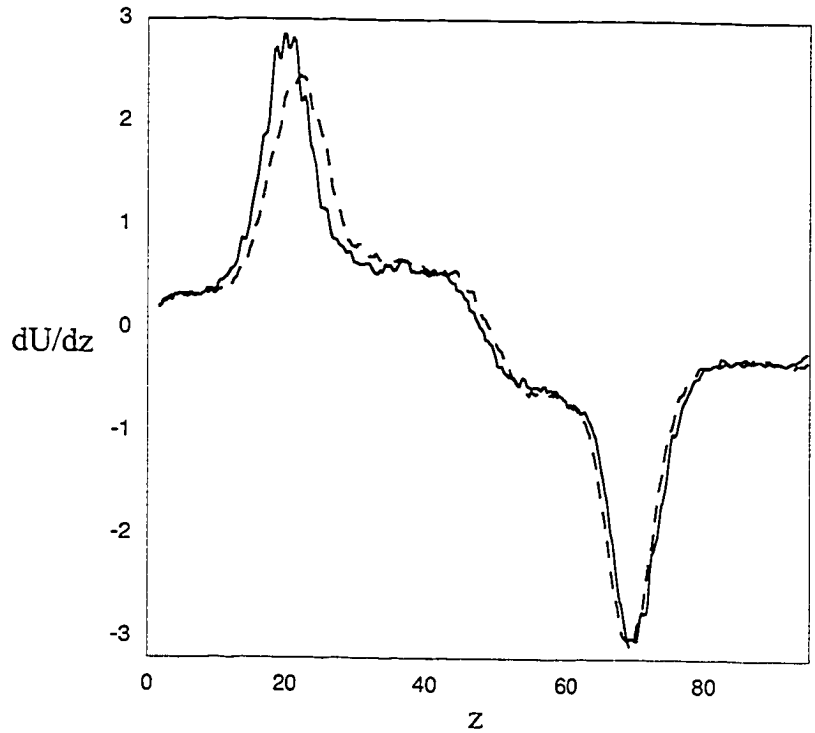

Figure 6.8 The derivatives of the energy showing the freezing and melting interfaces for Ic001, the solid line represents results for a standard system after a run length of 20 ns, while the dashed line is data collected over a 8.5 ns trajectory for a "big" system with moderate gradient at growth velocities of 16 cm/s.

6.1.2 Velocity dependence

As was observed for the LJ systems, different velocities impact the interface position at a particular gradient, as shown in Figure 6.9. In Figure 6.9(b) it can be seen that the energy function of Ih$10\bar{1}0$ is skewed slightly more to the left at a velocity of 8 cm/s relative to 3 cm/s. Unlike the atomic case, the increased velocity in this molecular system does not significantly affect the shape of the profile function, with minimal asymmetry observed. For steady-state runs for the different crystal faces there is typically a 8 - 10 K temperature difference in freezing and melting temperatures, for the velocities at 3, 8, 16 cm/s under a large gradient. There is a slight shift to lower temperatures for the

crystallizing interface and a shift to higher temperature for the melting interface at higher velocities. In addition, a similar shift is also observed when comparing pseudo steady-state melting data as shown in Figure 6.7. As was noted in the LJ system, higher growth rates will require greater supercooling. However, the magnitudes of the velocities examined for ice are much smaller than those in the LJ simulation study. Specifically, it can be noted that the growth rates of the LJ systems (if Ar units are assumed) are 500 times faster than the molecular system examined here.

Other profile functions like the S_g, S_k, D_l, D_r and Σ all exhibit shifts similar to those of the energy function, as illustrated by the S_g function in Figure 6.10. The interfacial widths show no significant change with increased velocity for all the gradients examined, utilizing both steady-state and pseudo steady-state data obtained from the melting interfaces.

It was found that the ice/water system is a much more challenging system in which to induce crystallization relative to an atomic system (LJ). With a molecular system like water, hydrogen bonding and the role of orientational order becomes critical. Such a system requires both translational (lattice site position) and orientational (hydrogen bonds) order to be satisfied by a solid molecule in the crystal.

It is now perhaps instructive to review the lack of success in previous simulation studies of ice growth. As was observed in the work of Nada and Furukawa [254,255,258], issues like removal of heat from the interface were critical issues in growth simulations. Previous studies of the ice/water system attempted to estimate interfacial positions from static profiles, which made locating the exact position of the interface challenging. In

addition, the majority of growth studies were limited to short timescales (on the order of fluctuations of the system) [157].

In the present work, although higher velocity simulations were attempted, no steady-states were achieved; however, growth of a few layers was observed (before the systems eventually melted) for the Ih$10\bar{1}0$, Ic011 and Ic001 crystal faces at 24 and 30 cm/s. Steady-state conditions were achieved for different crystal faces and conditions as summarized in Table 6.1. The growth rates obtained here for the TIP4P model agree well with experimental rates of ice growth (see Chapter 5, Figure 5.11). The growth rates of the different faces can be represented in descending order, Ih$10\bar{1}0$/Ic011/Ic001 > Ic111/Ih0001 > Ih$11\bar{2}0$. In the limited number of runs that employed other models all failed to achieve steady-state growth except for Ic011 with the TIP4P-Ew potential which showed steady-state growth with a moderate (II) gradient at 16 cm/s. A principal reason for the apparent lack of success with the use of the TIP4P-Ew model was the lack of information concerning its melting point. Based on properties of the model, a melting temperature of 260 K was estimated. Since we have determined that systems are very sensitive to the choice of gradient in relation to the melting temperature, it can be subsequently stated that the imposed gradients were far from ideal. Vega et al. [253] have emphasized the importance of knowing the melting temperature before crystal growth studies are attempted. In addition, the lack of success in observing crystal growth using the SPC/E model can be traced to its low melting point, which will affect viscosity and diffusivity considerations (although a systematic study was not attempted). Vega et al. [253] have also shown that the thermodynamically stable form of SPC/E ice at 1 atm is ice II, a high pressure phase. Even if work by Haymet and co-workers

[165,250,251,259,260] shows that apparently stable I_h interfaces could be constructed for SPC/E at its melting point, growth would certainly engender different considerations. Vega et al. [253] have also asserted that the best models for simulations of ice are TIP4P and TIP4P-Ew as they provide the most acceptable thermodynamic behaviour.

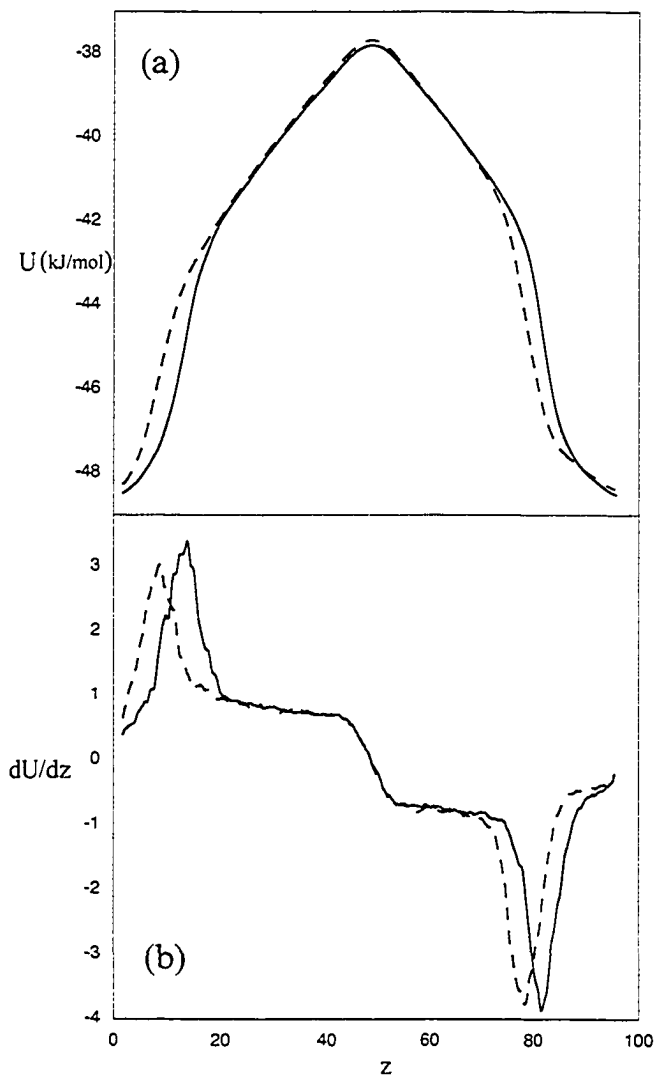

Figure 6.9 Energy profiles and the corresponding derivatives for $1h10\bar{1}0$ under a large gradient (a) 3 cm/s (solid line) and 8 cm/s (dashed line) for the energies, U and (b) their corresponding derivatives.

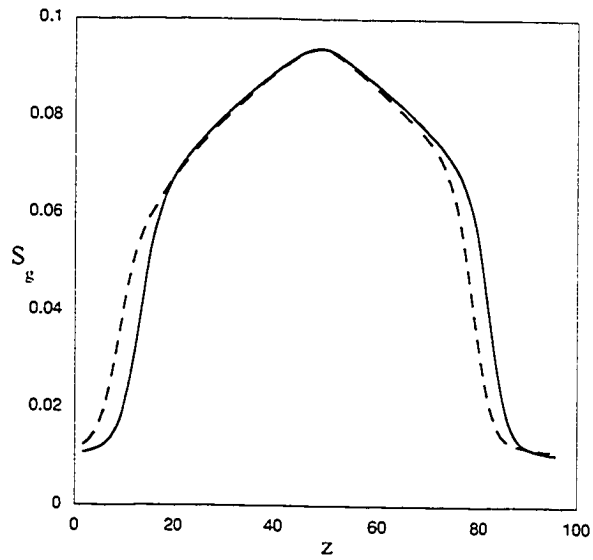

Figure 6.10 S_g profiles for Ih$10\bar{1}0$ at 3 cm/s (solid line) and 8 cm/s (dashed line) at a large gradient.

Table 6.1 Observed steady-state growth rates in cm/s for the various crystallographic faces and gradients examined with the TIP4P model.

Gradient / Interface	Very large	Large	Moderate	Small
Ic001	16	16,8,3	16	8
Ic011	16	16,8,3	16	8
Ic111	16	8,3	16	8
Ih0001	16	8,3	16	8
Ih$10\bar{1}0$	16	16,8,3	16	8
Ih$11\bar{2}0$	------	8,3	------	8

6.1.3 Gradient dependence

As was observed for the LJ systems, the different gradients examined in the present, ice/water simulations (see Table 5.5) all exhibit similar profile functions. The shape of the energy curve, shown in Figure 6.11(a) for a large and small gradient system at a growth velocity of 8 cm/s is relatively flattened for the latter system as expected. The slight shifts of the peaks in the derivatives of the energy and Σ profile functions of the small and large gradients (see Figure 6.11(b)) are caused by the system locating melting and freezing interfaces at their desired temperatures to achieve steady-state conditions. Similar changes in profile functions at large and small gradients can be seen for S_k and the linear diffusion constant in Figure 6.12. The S_g and S_k profiles, as well as their corresponding derivatives, are again very similar in shape to the energy profile function.

The impact of the gradient on the interfacial widths is again small, although interfaces are found to become slightly narrower with increasing gradient. Figure 6.13 shows the influence of the temperature gradient on interfacial widths, as obtained from the derivatives of the energy profile function. There is a consistent occurrence (previously observed for the LJ systems) of a larger gradient causing a narrowing of the interface and suggesting that at zero gradient the interface will be wider (coincident with equilibrium conditions). The interface as discussed in Section 4.1 is composed of two aspects, the transition of the structure from liquid to solid over a few transition layers and moving of the apparent "instantaneous centre" of the interface [82]. The presence of a larger gradient can again be understood as confining the magnitude of these fluctuations. However, the extent of the influence of the gradient on each of these components is unclear.

6.1.4 Comparison of crystallographic faces

The six ice crystallographic faces investigated can be divided in essentially 3 groups, (Ic011, Ic001, Ih10$\bar{1}$0), (Ih0001, Ic111) and (Ih11$\bar{2}$0). The steady-state conditions summarized in Table 6.1 indicate that the growth rates achieved can be given in decreasing order: Ic011 > Ic001 > Ih10$\bar{1}$0 > Ih0001, Ic111 > Ih11$\bar{2}$0. The results show that the prism face (Ih10$\bar{1}$0) is faster growing than the basal face (Ih0001), consistent with experimental observations [176]. The 11$\bar{2}$0 crystal face, which is also perpendicular to the basal face of ice, proved to be more resistant to steady-state crystallization than the basal face. Yet, in dendritic growth either from vapour or in liquid the 11$\bar{2}$0 face appears to be the preferred growth direction. The cubic faces of 011 and 001 are among the easiest faces to grow under a variety of conditions. This is consistent with observations from numerous studies as discussed in Section 5.2.5, that cubic ice seems to be the kinetically favoured phase at low temperature. Steady-state growth has been observed with the TIP4P-Ew model only for Ic011. Moreover, even for simulation runs that resulted in non steady-state crystal growth, the Ic011 and Ic001 systems exhibited much more growth than the other crystal faces with the exception of Ih10$\bar{1}$0. In contrast, the 111 cubic crystal face grows similarly to Ih0001, which is expected due to the similarity of these crystal faces as explained in Section 5.2.5.

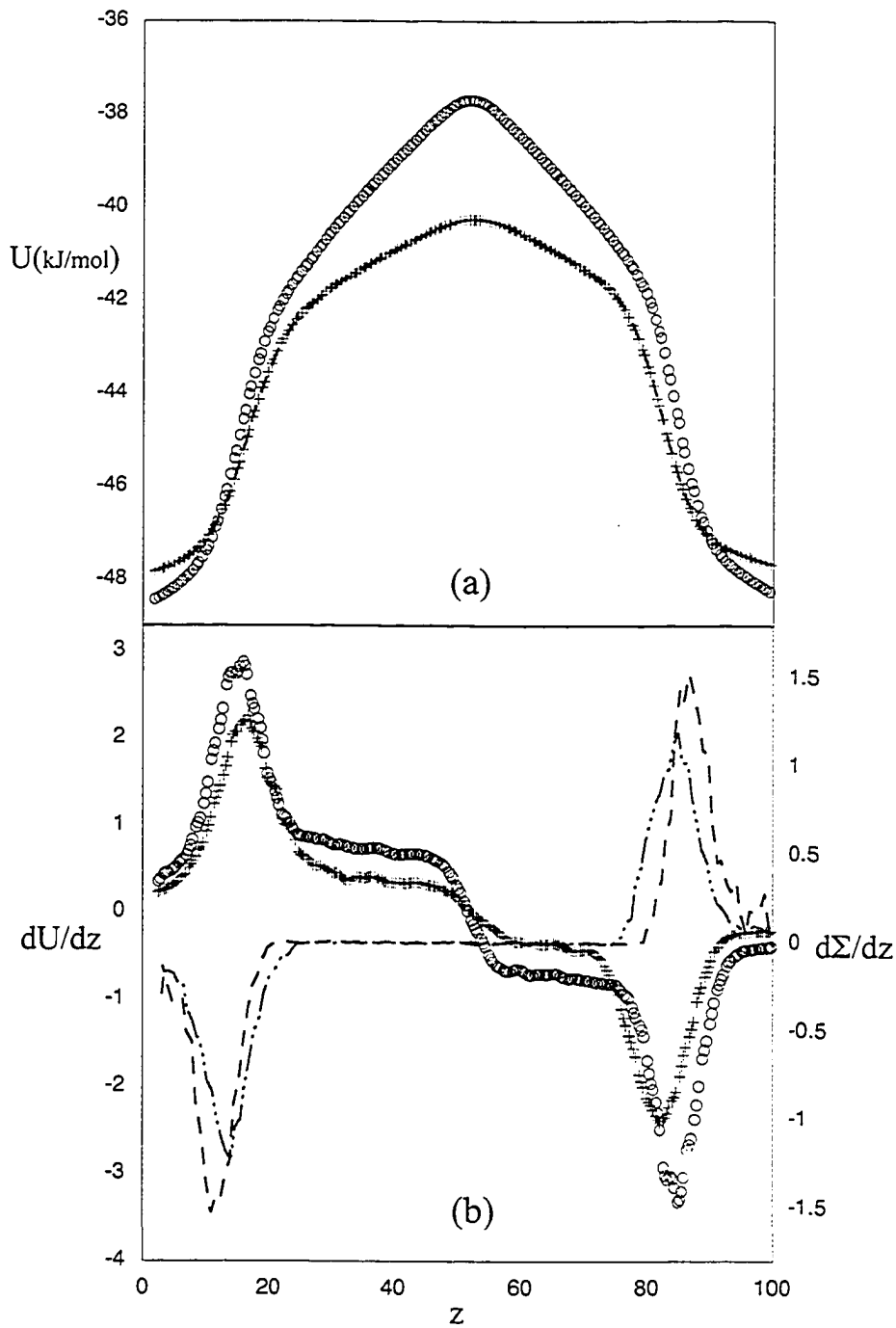

Figure 6.11 (a) Energy profiles at large (circles) and small gradients (crosses), for steady-state for Ih0001 at 8 cm/s. (b) The corresponding derivatives of the energy profiles as well as the derivatives of the Σ order parameter at large (dashed lines) and small (dash-dot lines) gradients, respectively.

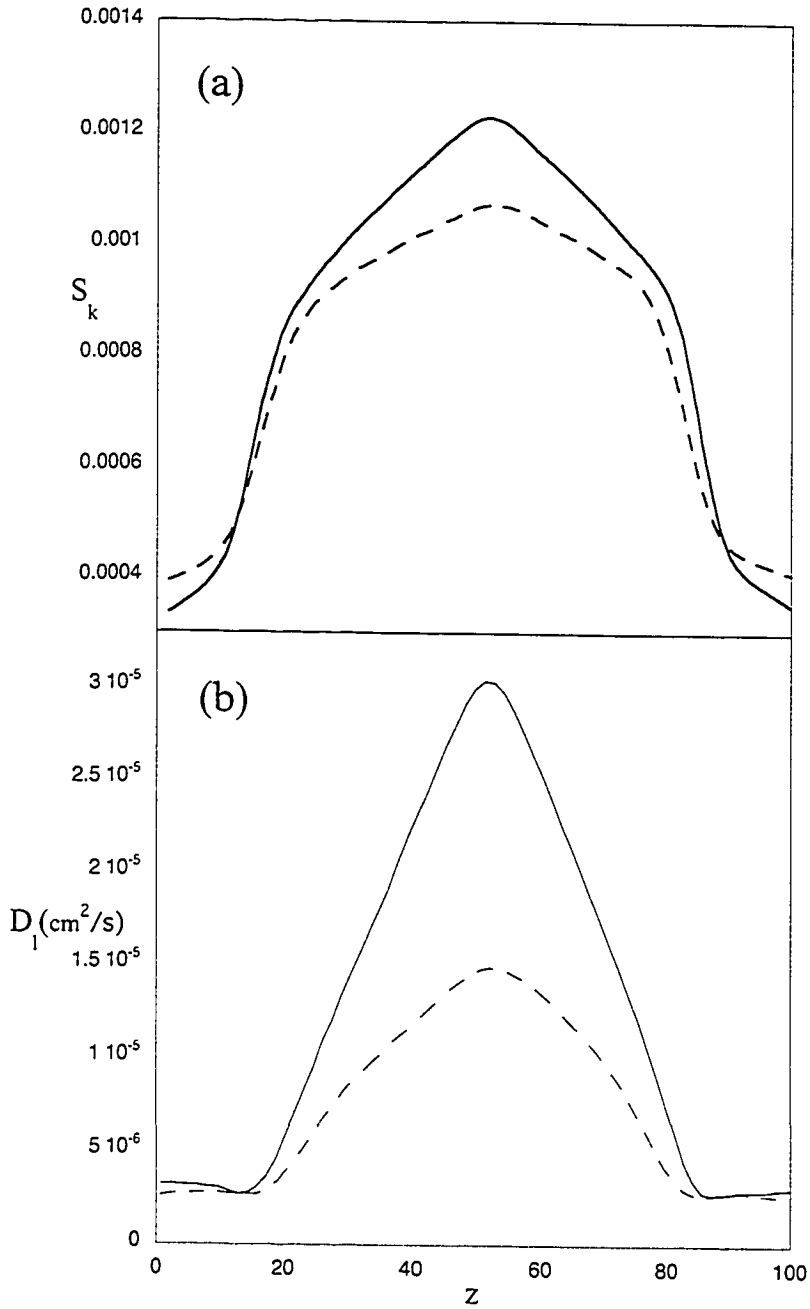

Figure 6.12 (a) S_k and (b) the linear diffusion profile functions at large (solid line) and small (dashed line) gradients for a steady-state of Ih0001 system at 8 cm/s.

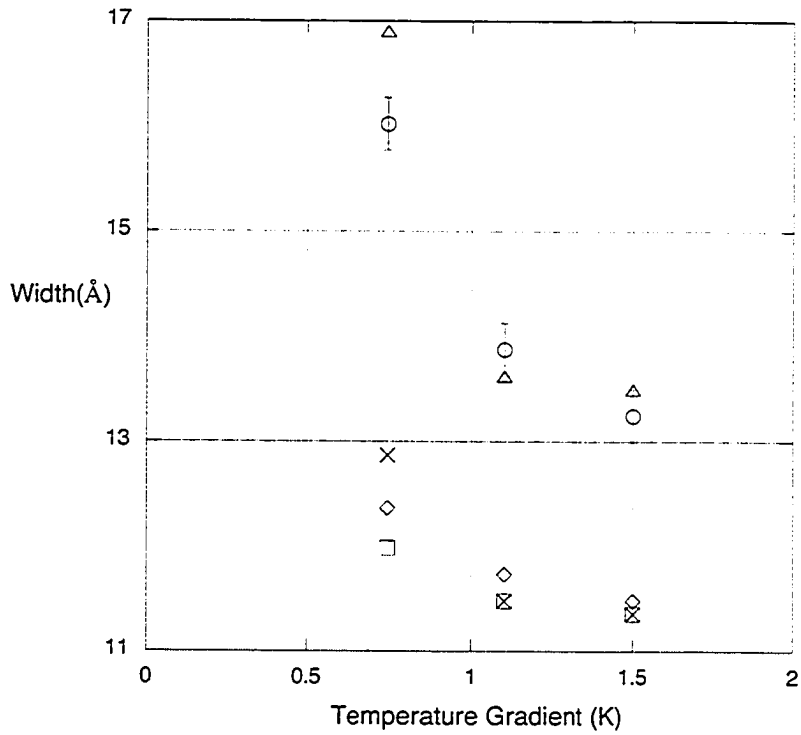

Figure 6.13 Dependence of interfacial widths on crystal face and on gradients for ice/water systems. Results for Ih0001 (squares), Ih10$\bar{1}$0 (diamonds), Ic111 (Xs), Ic001 (triangles) and Ic001 (circles) are obtained from the derivative of the energy profile. Representative error bars are included for the Ic001.

For a particular velocity and gradient, the interfaces of slower growing faces are shifted to lower temperatures, showing that deeper supercooling is needed as a driving force to sustain growth. Analogously their melting temperatures are shifted to higher temperatures. Interfacial widths of the various faces for the different models examined in this study are given in Table 6.2. The widths obtained from the S_g and S_k functions provide essentially identical results within the uncertainties. The results show that the interfacial widths in descending order are 110 > 001 > Ih11$\bar{2}$0 > Ih10$\bar{1}$0 > Ic111, Ih0001. Figure 6.13 compares results for the TIP4P model and indicates that Ic011 and

Table 6.2 Observed interfacial widths from the derivative of the energies for different models along with the standard deviations. All widths are given in Angstroms.

Crystal Face / Model	Ic001	Ic011	Ic111	Ih0001	Ih10$\bar{1}$0	Ih11$\bar{2}$0
TIP4P	13.8 ± 1.7	13.9 ± 2.2	11.4 ± 1.1	11.4 ± 0.4	11.7 ± 0.5	12.8 ± 0.6
TIP4P-Ew	14.5 ± 1.4	16.3 ± 3.4	10.7 ± 1.3	10.8 ± 1.0	11.6 ± 1.3	12.7 ± 0.8
SPC/E	13.7 ± 2.4	16.0 ± 4.0	11.5 ± 1.2	11.2 ± 0.7	12.0 ± 0.7	12.8 ± 0.6

then Ic001 are the widest interfaces. The data in Figure 6.13 also show that Ih10$\bar{1}$0 is slightly wider than Ih0001, with Ih11$\bar{2}$0 being wider than either Ih0001 or Ih10$\bar{1}$0. The width of Ic111 is indistinguishable from that of Ih0001, as expected, although the former crystal face appears to exhibit greater fluctuations (see Table 6.2). The fluctuations within the latter two crystal faces will be examined closely in Section 6.2.

The widths as presented in Table 6.2 agree in general with literature estimates for hexagonal ice. There is disagreement with predictions of the relative widths of the basal and prism faces of ice I_h. Hayward and Haymet [165,259] have argued, based on their analysis of static functions, that the basal face is wider than the prism. However, inspection of Figure 5.14 from Bryk and Haymet's [260] work displays more fluctuations occurring at the prism face than for the basal face. Even work by Nada and Furukawa [255] imply a wider face for the prism than for the basal face. Two key issues need be considered, the change of an order parameter value across the interface, and structural fluctuations of the interface over different time windows. Previous estimates of the interface have considered the former issue but have neglected the latter issue, thus

leaving out a key component in the behaviour of the interface. This problem is symptomatic of carrying out averages over static profiles. Static profiles do not adequately capture the second component of the interfacial behaviour as shown in Figure 5.14. Realization of this caused Bryk and Haymet [260] to remark that further investigation was needed to explain the behaviour. What occurs in static profile analyses at different time windows is the apparent shift in the "instantaneous centre" positions. These profiles are thus insensitive to such long-time behaviour. In addition, there are no reference points from which such meandering of the "instantaneous interface" can be followed. The approach in this thesis, considers both aspects contributing to the interfacial width because it utilizes averages within the moving frame of steady-state growth and melting.

The derivatives of the Σ order parameter, as was observed for the LJ systems, describe narrower interfaces. The widths obtained are ~ 4.7 Å smaller for Ic011, Ic001, Ih10$\bar{1}$0, Ih11$\bar{2}$0 and ~ 3.2 Å smaller for Ic111 and Ih0001 for all models. This behaviour is yet further indication that different measures will respond differently to structural fluctuations occurring within the interface. Further details of this behaviour will be explored in Section 6.2. The observation that the Σ order parameter predicts a narrower interface than the derivative of the energy is consistent with the observations from the LJ systems.

6.1.5 Comparison of melting and freezing trends

The melting and freezing temperatures for all steady-state simulations is easily obtained, as discussed in Section 4.1.5. Figure 6.14 shows the freezing and melting

temperatures plotted against velocity for large and moderate gradient systems. As was performed in the LJ systems, a thermodynamic melting temperature for the TIP4P model can be extracted from the zero-velocity temperature that should be common to all faces of a particular crystal. A melting temperature of 226 ± 1 K can be estimated in Figure 6.14 (a) from the large gradient for both ice I_h and I_c. The more limited values from Figure 6.14(b) suggests a somewhat higher melting temperature of 228 ± 1 K. It should be noted that a similar trend of a slight decrease in the apparent melting temperature with increasing gradient was observed in the LJ systems. Moreover, a somewhat narrow bulk solid region in the large gradient ice/water systems may have also had a small impact on its relative stability and hence slightly lowered the melting temperature. The temperatures determined in this work are within range of values reported by Vega et al. [253] (see Table 5.3).

The melting temperatures for the other models examined here cannot be treated in the above manner because fewer systems were studied and only 1 steady-state was obtained. However, as discussed in the section dealing with LJ systems, the structural fluctuations of the interface are somewhat restricted when a very large temperature gradient is used. Consequently, the position of the interface may be located rapidly in a pseudo steady-state melting system. Therefore, good estimates of the melting temperature may be obtained. For example, applying this rationale to the LJ systems with very large gradients, an average melting temperature of 0.62 ± 0.01 in excellent agreement with the previously calculated value in Chapter 4 was obtained. The melting temperature of TIP4P determined from the very large gradient data is 227 ± 2 K. Similarly, the estimated melting temperatures for SPC/E and TIP4P-Ew are 225 ± 5 K and 242 ± 2 K.

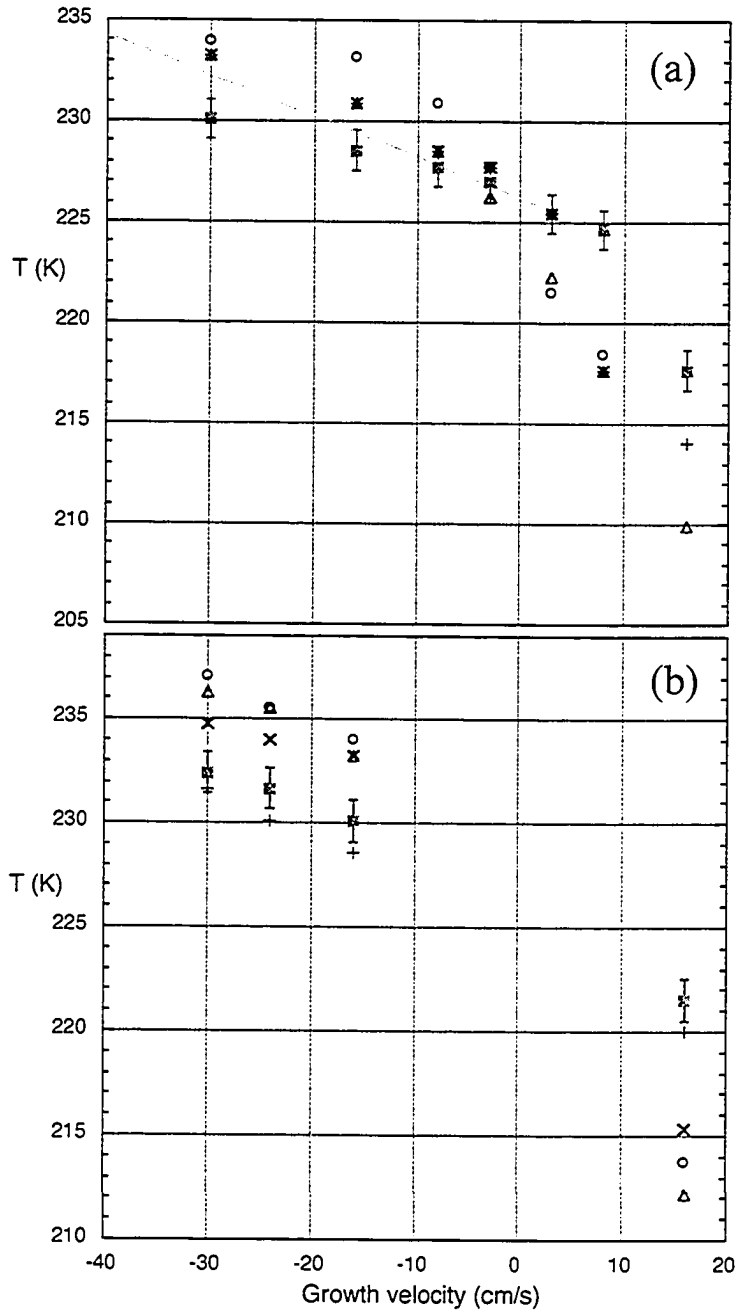

Figure 6.14 Dependence of melting and freezing temperatures on growth velocities for the Ih0001 (circles), Ih10$\bar{1}$0 (triangles), Ic111 (X's), Ic011 (filled squares) and Ic001 (crosses) at (a) large gradient and (b) moderate gradient. The line in (a) represents a linear fit to the four lowest velocity points to show deviations from linear behaviour. Representative error bars have been included with the Ic011 values.

respectively. Thus, this method predicts the melting temperatures for different models surprisingly well (see Table 5.3).

It should also be noted that Figure 6.14 is very similar to Figure 4.7 for LJ systems. In both plots the slower growing faces exhibit higher freezing temperatures than the faster growing faces with increasing velocity. The crystallizing temperatures of Ic001 and Ic011 appear generally higher than Ih0001, Ih10$\bar{1}$0 and Ic111. This trend suggests, that Ic011 and Ic001 require a somewhat smaller driving force to achieve the same rate of growth. Ih10$\bar{1}$0 also appears to have freezing temperatures slightly higher than Ih0001. The limited data available for Ih11$\bar{2}$0 (not shown) indicates that it is slower growing than Ic011/Ic001, but no significant distinctions can be made in comparison to the other hexagonal ices.

An asymmetry in freezing and melting temperatures is observed at high growth and melting velocities, as was observed in the LJ systems. In Figure 6.14, the temperature appears linear in the rate near zero velocity implying that there is no slope discontinuity at equilibrium. However, to ascertain the validity of this assertion, more extensive low velocity simulations need to be undertaken.

6.1.6 Interfacial tension

In an analogous way to the approach used for the Lennard-Jones systems the interfacial tension of the various ice/water system can be calculated. Table 6.3 shows the different interfacial tension values recorded at different gradients. As was observed for the LJ systems there is an increase in apparent interfacial tension values with increasing

gradient. Due to the relatively large error bars, the differences between the different faces of hexagonal ice are difficult to resolve. However, from the data two distinct trends in the interfacial tension appear. The faces Ih0001, Ih10$\bar{1}$0, Ih11$\bar{2}$0 and Ic111 have consistently higher interfacial tensions. In this respect, Ic111 behaves more like the faces of hexagonal ice. The other two faces of cubic ice Ic011 and Ic001, have consistently lower

Table 6.3 Interfacial tensions obtained from steady-state melting/freezing data for TIP4P. All data are given in units of mN/m. Estimated errors in the last digit are given in parentheses.

Gradient / Crystal faces	Large	Moderate	Small
Ic001	35 (3)	32(3)	30(3)
Ic011	34(3)	32(3)	26(3)
Ic111	40(3)	39(3)	33(3)
Ih0001	40(3)	37(3)	34(3)
Ih10$\bar{1}$0	38(3)	38(3)	34(3)
Ih11$\bar{2}$0	39(3)	39(3)	33(3)

interfacial tensions. This behaviour is consistent with the trend observed in the LJ simulation studies that the faces with the lowest interfacial tensions are also faster growing. Removing the effects of temperature gradient as was done in the LJ systems by

extrapolating to zero gradient reveals that for Ih0001, Ih10$\bar{1}$0, Ih11$\bar{2}$0 and Ic111 the average interfacial tension is 30 $\pm$ 3 mN/m and for Ic001 and Ic011 the average value is 24 $\pm$ 3 mN/m. The values obtained experimentally by W. B. Hillig [267] and Turnbull [268] for the interfacial tension of a hexagonal ice/water interface are 31.7 + 2.7 and 32.1 mN/m, respectively. For the cubic ice/water interface Huang and Bartell [196] estimated its surface tension to be 22 mN/m. These experimental values are in excellent agreement with the values determined in this thesis. Unfortunately, due to the relatively large error bars the anisotropy could not be distinguished between the different hexagonal faces. Longer simulation runs should be able to resolve the anisotropy between the faces of hexagonal ice. The results obtained here are the first of their kind obtained directly from simulations of steady-state crystal growth of a molecular system.

6.1.7 Significant observations from profile results

The profile functions for the ice/water interface have enabled consistent descriptions of its position and width to be determined under different gradient and velocity conditions. The interfacial widths obtained are in very good agreement with experimental [234] and previous simulation estimates [165,259]. The widths provided here are also the most accurate and precise to date. The width of the basal face is smaller than for the prism face, with the latter in turn smaller than for Ih11$\bar{2}$0. In general, the cubic 111 face is observed to be very similar to the basal face; this extends to growth rates, interfacial tensions and the interfacial widths. Ic001 and Ic011, however appear quite different from the face of hexagonal ice, with generally wider and more variable interfaces (The range of widths given in Table 6.2 (through the standard deviations)

provides a measure of the range of fluctuations possible for a particular interface). This finding will be examined in more detail in the next section.

The growth rates of ice recorded here are similar to the rates in experimental measurements (see Section 5.3) with the basal slower than the prism face of ice I_h. Curiously, the growth of the Ih$1\bar{1}20$ crystal face was more difficult to achieve; it appeared to be slower growing than either Ih$10\bar{1}0$ or Ih0001. Two of the faces of I_c, and especially Ic011, appear to grow faster than any other crystal face examined in this thesis. The growth rates of the different crystallographic faces based on the steady-states achieved can be used to comment generally on the relative ease of crystal growth of the various systems. The interface location in steady-state growth for a particular ice/water system should be the optimum position for crystallization at those conditions. It was also confirmed that the shifting of an interface to higher temperatures for a particular velocity and gradient is indicative of a faster growing crystal face.

Crystal growth is also observed to be stochastic in nature, with short intervals of growth typically punctuated with longer intervals of apparent stagnation (or even retreat). This would seem to indicate that critical low probability events must eventuate for growth to occur. Therefore, regardless of the growth velocity structural fluctuations are always occurring at the interface. Observations indicate no significant width changes associated with increased growth velocity. At small enough growth velocity, a particular system will be able to grow as the molecules at the interface are able to sample conditions conducive to growth.

The choice of an appropriate gradient is then dictated by two general considerations. The value of the gradient (expressed as a temperature change per

Angstrom) must be appropriately selected to achieve reasonable profiles in the moving frame. For ice/water this was found to be 1 Å / K. Smaller gradients give broader interfaces and significantly larger gradients (in addition to more dramatic skewing of the profile functions) confine the inherent width of the interface thereby restricting fluctuations that may facilitate growth. The other consideration involves the mean temperature within the system compared to the thermodynamic melting temperature of the model. Inspecting the data for steady-state growth runs reveals a lower melting point for the model than was initially assumed for a majority of the TIP4P simulations. For small and large gradients, the mean temperature for the systems is 6 and 18 K, respectively, above the determined thermodynamic melting point of the model. Therefore, these ice/water systems will have on average significantly more liquid than solid; this is confirmed from inspecting the configurations. This can be problematic, particularly at higher growth velocities where the necessary fluctuations of the interface can result in considerable thinning of the bulk solid region. Below a certain critical threshold, which was observed to be about 10 Å, the solid becomes considerably less stable and quickly melts.

The use of very large gradients for predicting melting temperatures was confirmed with the successful estimation of values for LJ systems, TIP4P, TIP4P-Ew and SPC/E. The melting temperature recovered for TIP4P-Ew is in excellent agreement with a recently reported value [243].

The next section will explore many outstanding issues raised in the foregoing discussions that required detailed investigation of averaged configurations.

6.2 MECHANISMS OF CRYSTALLIZATION

6.2.1 Methods of analysis

a) Representative configurations

The manner in which detailed molecular configurations for the different ice/water interfaces will be investigated is very similar to the methodology described in Chapter 4 (see section 4.2.1). Averaged configurations were produced by averaging, particle positions and orientations (in quaternions). Positions and orientations were sampled typically every 200 fs and these were averaged over trajectory segments of approximately 80 ps. The methods used to produce these averaged configurations of the center of mass positions and molecular orientations are outlined in Appendix B. For all the ice/water systems investigated, between 80 and 250 of such averaged configurations were produced spanning a time of 5 – 24 ns. The averaging procedure that was selected provided a reasonable vantage point to observe the complex processes of the microscopic mechanism of crystallization of water. The multiple configuration files were animated (similar to the LJ systems) to allow detailed time-dependent insights into single and multiple layer crystallizing and melting behaviour to be observed. Shorter time windows for averaged configurations were also examined but they offered no additional insights. The visualization procedure was identical to that used in the LJ systems.

As was done for the LJ systems, representative averaged configurations were superimposed with the derivatives of the energy and Σ profile functions of steady-state ice/water systems, as shown in Figures 6.15 and 6.16. Although crystal order is apparent in the configurations within the bulk solid regions of these figures, the distinction

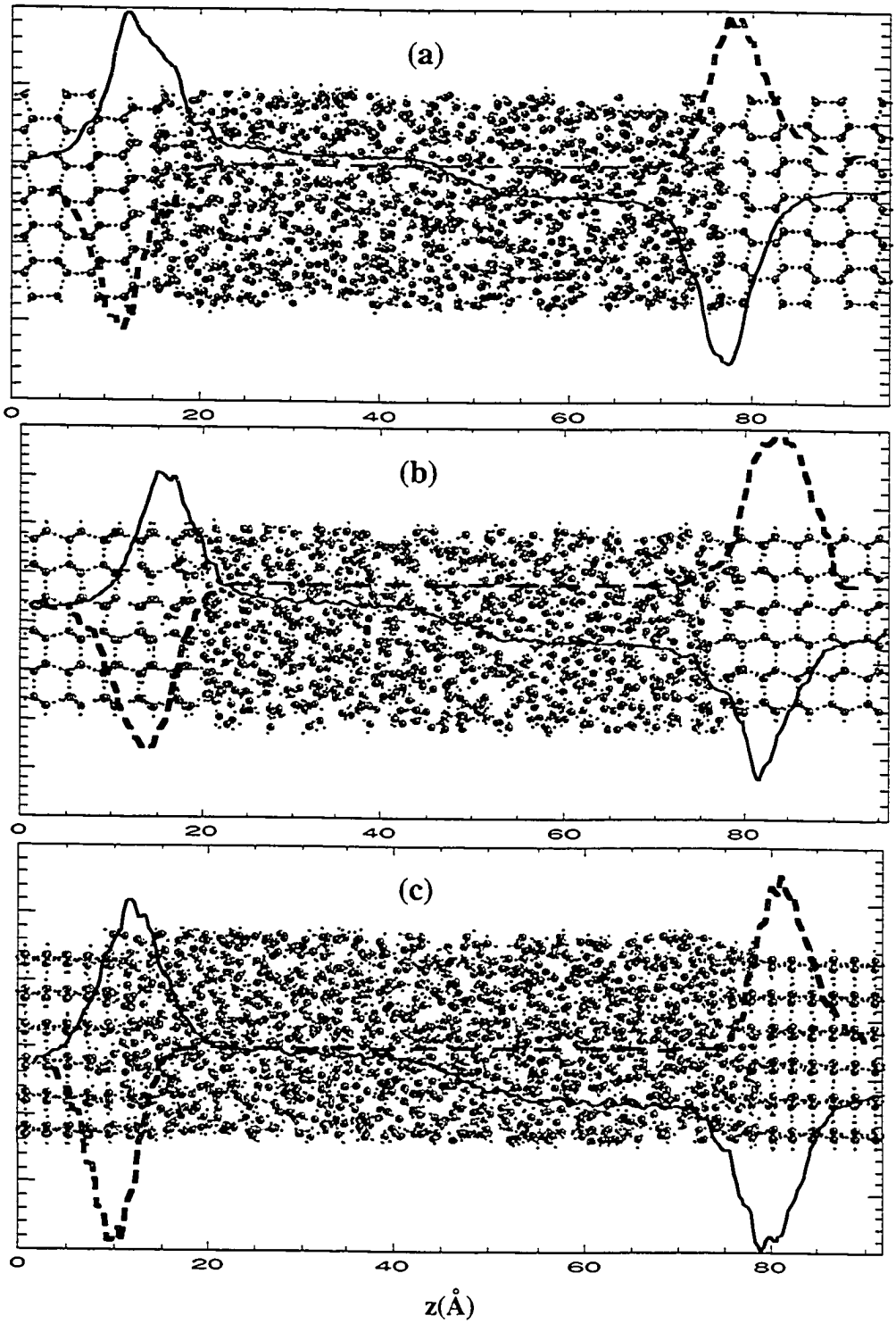

Figure 6.15 Representative averaged configurations of (a) Ih0001, (b) Ihl$0\bar{1}0$ and (c) Ihl$1\bar{2}0$ steady-state systems at a small gradient and a growth speed of 8 cm/s. Derivatives of the energy and Σ profiles are superimposed as solid and dashed lines, respectively.

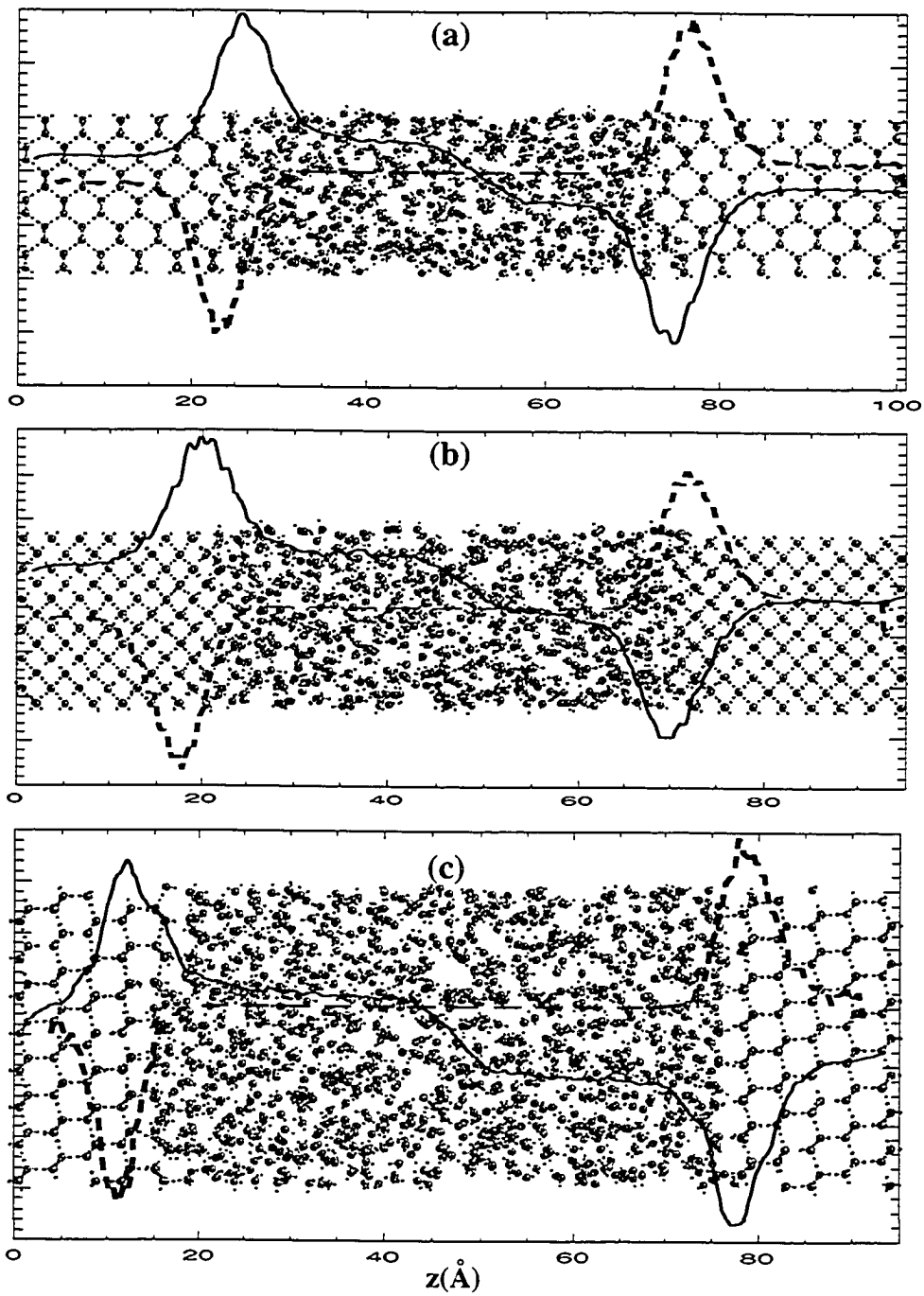

Figure 6.16 Representative averaged configurations of (a) Ic011 (moderate gradient at a growth speed of 16 cm/s), (b) Ic001(moderate gradient at a growth speed of 16 cm/s) and (c) Ic111 (large gradient at a growth speed of 8cm/s) steady-state systems. Derivatives of the energy and Σ profiles are superimposed as solid and dashed lines, respectively.

between solid and liquid molecules is far from obvious from inspection of the interface; within the present analysis, it is important to be able to make this distinction. To enable detailed molecular analysis, a molecule can exhibit solid behaviour in two ways. Specifically, a molecule can be translationally solid (fixed about a lattice position) or rotationally solid (fixed near a specific orientation, presumably due to hydrogen bonding). A molecule was labeled as "solid" in a configuration if the dispersion of instantaneous positions (or orientations) about their mean was below a particular threshold value (consistent with bulk solid behaviour). The labeling of molecules as translationally and rotationally either solid or liquid were generally exploited in visualizations of averaged configurations. Specifically, the various molecules in this section will be coloured as follows: translationally solid - red oxygen, translationally liquid - magenta oxygen, rotationally solid - white hydrogen and rotationally liquid - yellow hydrogen. Configurations of entire systems (such as Figure 6.17) will contain no tagging information; tagging, as discussed below, will be reserved for specific slices of such systems.

b) Slice identification and monitoring

The averaged configurations from the present ice/water simulations were investigated in a manner similar to the LJ systems, where slices were obtained at the growing and melting interfaces. The percentage of crystalline character for the various crystal layers through the interface was found not to be particularly useful due to the considerable fluctuations observed at the interfaces. Therefore, no attempt was made to quantify it (as will be noted in the next section). The method of identification of solid and

liquid molecules (as discussed above) facilitated the identification of crystalline layers identified in conjunction with visual inspection of such layers as well as referring to the underlying layer to ensure a commensurate crystalline pattern (as in the LJ systems).

The method of indexing (or tagging) molecules in a particular layer (or layers) was identical to the method used in the LJ analysis. Different layers were labeled with different colours. In addition, different colours were used for tagged molecules that were labelled either as solid or liquid with all other molecules in the layer retaining their previously described colour scheme. Tagged molecules replaced the red/magenta colour scheme for solid/liquid characterization with blue for solid and green for liquid. If two layers, or alternatively two planes in a layer, are tagged the other colour combination was gold for solid and silver for liquid. This method was applied to both the freezing and melting interfaces.

Unlike the LJ systems, there does not appear to be complete equivalence of following a particular layer of a system through time and inspecting the various slices of an averaged configuration at a specific time, due largely to the magnitude of fluctuations apparent in the molecular systems. Therefore, representative slices which remain fixed as the interface advances will be used to discuss crystal growth and melting. For example, Figure 6.17 captures the changes experienced by slices A and B with the advance of the crystallizing interface. All discussions on formation of a layer (or layers) will exploit such averaged configurations.

6.2.2 Interfacial structure

As discussed earlier in this chapter, the profile function for the Σ order parameter, which measures 2D crystalline order for the ice/water interface, predicts a narrower interface than the corresponding energy function. The position of the centre of the interface is understood as the position of the maximum in the derivative of the energy profile, i.e. the position of the maximum normal force. Moreover, one finds that the peaks in the derivative of the density profile are shifted roughly 3 Å ahead of the melting and freezing interfaces. The implication here is that the use of the centre of the density profile, as done by Hayward and Haymet [165], could result in a systematic error in the identification of the centre of the interface. The definition introduced in this thesis unambiguously identifies the position of the interface, even if the change in density is not commensurate with that of the energy, as is the case with the ice/water interface. The position of the peaks in the derivative of the Σ order parameter are shifted somewhat to the solid side, for all the interfaces, as shown in Figures 6.15 and 6.16. This is in contrast to the LJ systems (see Figure 4.8) where these functions are shifted slightly to the liquid side of the interface. This discrepancy was found to be due to atomic hopping, however in the ice/water interface this is obviously not the case (not due to molecular exchanges, because the shift is to the solid side of the interface). This interesting behaviour exhibited by the averaged profiles will now be examined at a detailed molecular level.

Inspecting Figures 6.15(a) and Figures 6.16(c) for Ih0001 and Ic111 interfaces, respectively, roughly 4 layers are observed at both freezing and melting fronts. The fluctuations apparent at the freezing interface for Ih0001 and Ic111 are shown in Figures 6.17 and 6.18, respectively. For the average configurations displayed in Figures 6.17(a)

and 6.18(a), the first two interfacial layers for both systems appear crystalline, with the third layer seemingly partially disordered and the fourth disordered with some crystalline characteristics. The fact that the z-derivatives of the energy, S_ε and S_k functions are consistent as interfacial measures indicate that at the edge of the liquid-side of the interface these measures are consistently detecting local ordered structures, which may not be evident in Figures 6.15(a), 6.16(c), 6.17 and 6.18. Figures 6.17 and 6.18 show that there are translationally solid-like molecules at the edge of the interface. Some of these are outside the defined interfacial region; they presumably originate from the presence of long-lived H-bonds arising due to the influence of the nearby interface. The density appears to be more sensitive since it has been observed that the derivative of the density profile is shifted somewhat towards the liquid side of the interface. The reduction of coordination near the interface and the associated density changes will be further examined when growth mechanisms are discussed.

Besides the obvious similarities between the Ih0001 and Ic111 faces evident in Figures 6.15(a), 6.16 (c), 6.17 and 6.18, there are interesting discrepancies. For instance, the derivative of the energy profile of the cubic 111 system is more asymmetric than that of Ih0001. The structural fluctuations of Ic111 includes partial ordering of layers at the interface as shown in Figure 6.18(b) with no such behaviour observed for the hexagonal system. Both systems do also show molecules with solid characteristics ahead of the interface.

Shifting to the other two faces of hexagonal ice, the $10\bar{1}0$ interface spans 4 layers (11.5 Å) and the $11\bar{2}0$ interface has 7 layers (12.5 Å), as shown in Figures 6.15(b) and 6.15(c), respectively. Representative structural fluctuations of the Ih$10\bar{1}0$ and Ih$1\bar{2}0$

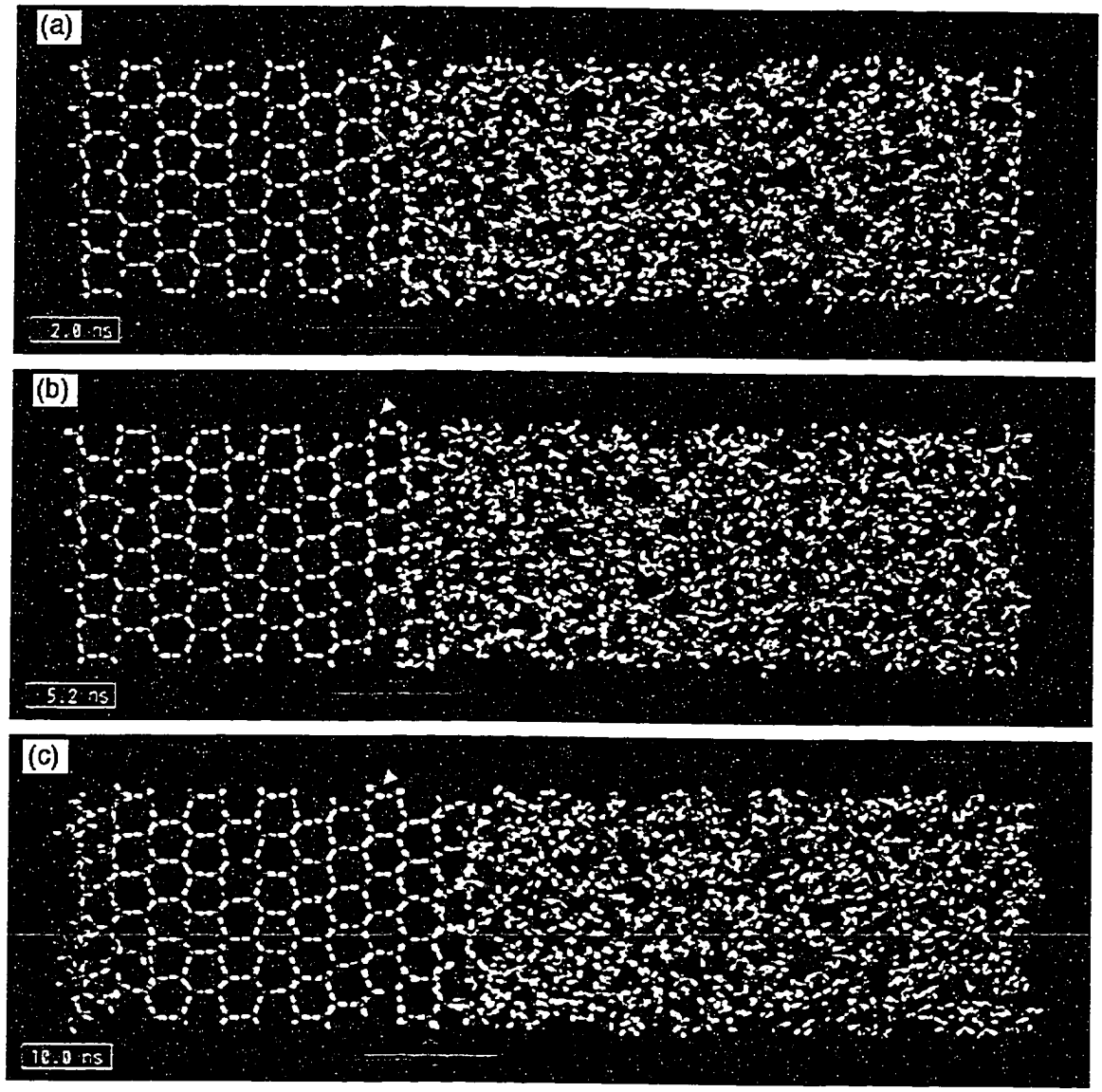

Figure 6.17 Three averaged configurations of the Ih0001 ice/water interface of the same system as in Figure 6.15(a). The colouring of the molecules are discussed in the text. The time sequence of the configurations (a-c) are given in the box at the bottom left of each configuration. The green arrow with its enclosing bracket indicates the centre and the width of the interface as given by the energy profile functions. The horizontal green line below the bracket shows the movement of the interface in time. The yellow and red arrows show layers A and B respectively.

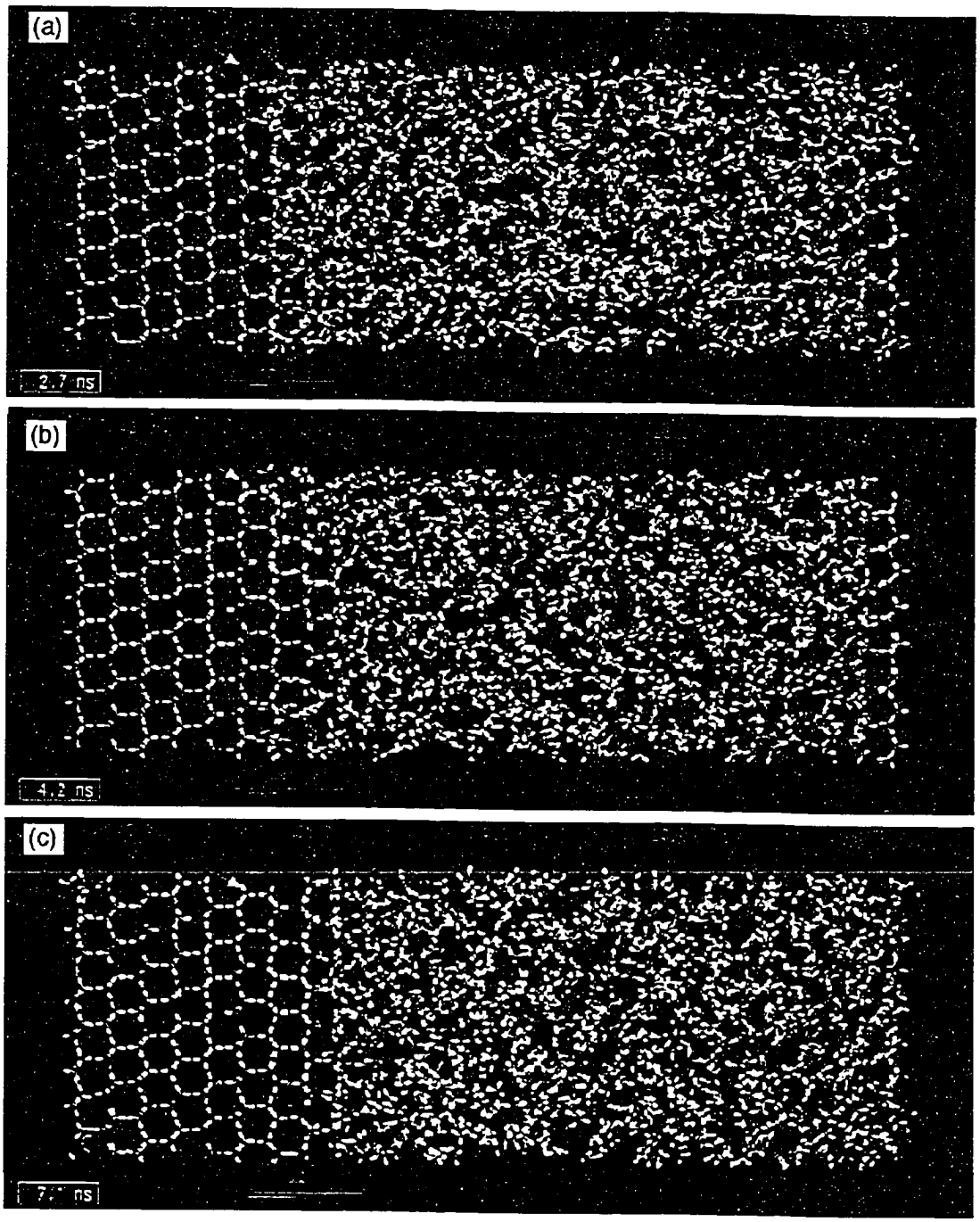

Figure 6.18 Three averaged configurations of the Ic111 ice/water of the same system as in Figure 6.16(c). The colouring of the molecules are discussed in the text. The time sequence of the configurations (a-c) are given in the box at the bottom left of each configuration. The green arrow with its enclosing bracket indicates the centre and the width of the interface as given by the energy profile functions. The horizontal green line below the bracket shows the movement of the interface in time. The yellow and red arrows show layers C and D respectively.

interfaces are provided in Figures 6.19(a-c) and 6.20, respectively. The interfaces of both Ih$10\bar{1}0$ and Ih$11\bar{2}0$ are considerably rougher than that of Ih0001. The fluctuations of Ih$11\bar{2}0$ can be better captured in the x-z plane (Figure 6.20) rather in the y-z plane (Figure 6.15(c)). Of particular interest in Figure 6.20 is the appearance of structural features that appear to be along Ih$10\bar{1}0$ micro-facets. Based on the magnitude of the observed structural fluctuations and experience with LJ systems, one would expect the interfacial tension to be higher for Ic111 and Ih0001 than for Ih$10\bar{1}0$ and Ih$11\bar{2}0$ faces. However, the values obtained in Table 6.4 do not permit any such anisotropy to be distinguished (although if present it must be relatively small).

The cubic systems Ic001 and Ic011 have measurably lower interfacial tension than the other four ice faces examined in this work. These lower values are clearly reflected in the large structural fluctuations apparent in Figures 6.21 and 6.22 for Ic001 and Ic011, respectively. Figures 6.16(b) and 6.16(a) show that there are 8 layers in the 001 (13.0 Å) and 6 layers (13.5 Å) in the 011 interfaces, respectively. The structural fluctuations are sufficiently large that their interfacial solid structure varies dramatically in depth, highlighting a pronounced non-planar three-dimensional structure. Additionally, Ic011 shows 111 micro-faceting throughout the interface. It is important to point out that, as was also observed in the LJ systems, the melting interfaces for all the ice/water systems examined in this work exhibit similar structures to those of their corresponding freezing interfaces.

While the ice/water systems have very different crystal structures (except perhaps Ic111 and Ih0001), their characteristic profile functions, such as the density or the Σ order parameter, are generally quite similar. The methodology used in this thesis, enables the

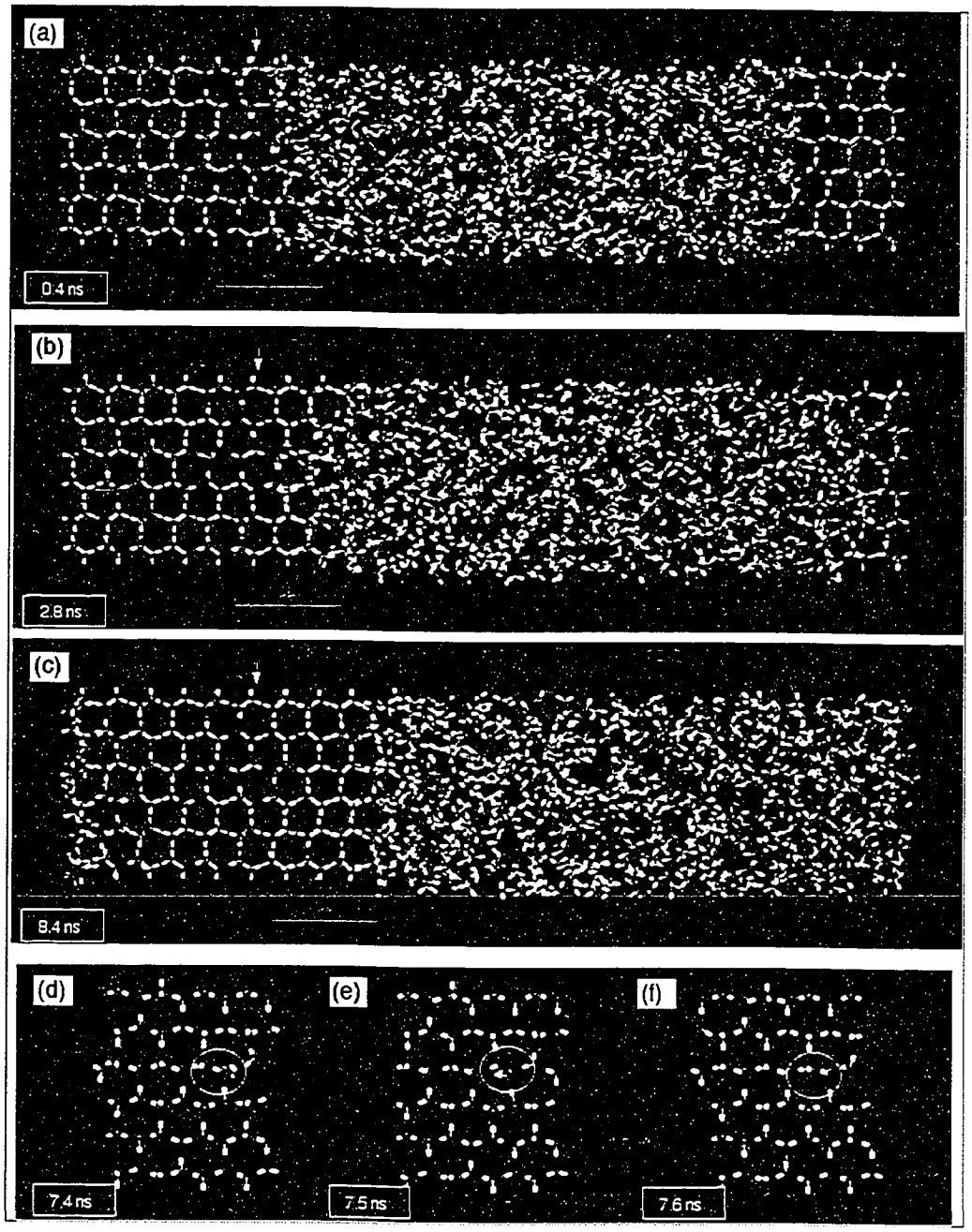

Figure 6.19 Three averaged configurations of the Ih10$\bar{1}$0 ice/water interface of the same system as in Figure 6.15(b). The colouring of the molecules are discussed in the text. The time sequence of the configurations (a-c) are given in the box at the bottom left of each configuration. The green arrow with its enclosing bracket indicates the centre and the width of the interface as given by the energy profile functions. The horizontal green line below the bracket shows the movement of the interface in time. The yellow and red arrows show layers G and H respectively. Figures d-f show a time sequence of x-y (slice) views of a defect inducing exchange as indicated by the circle of the same system as Figure 6.15(b).

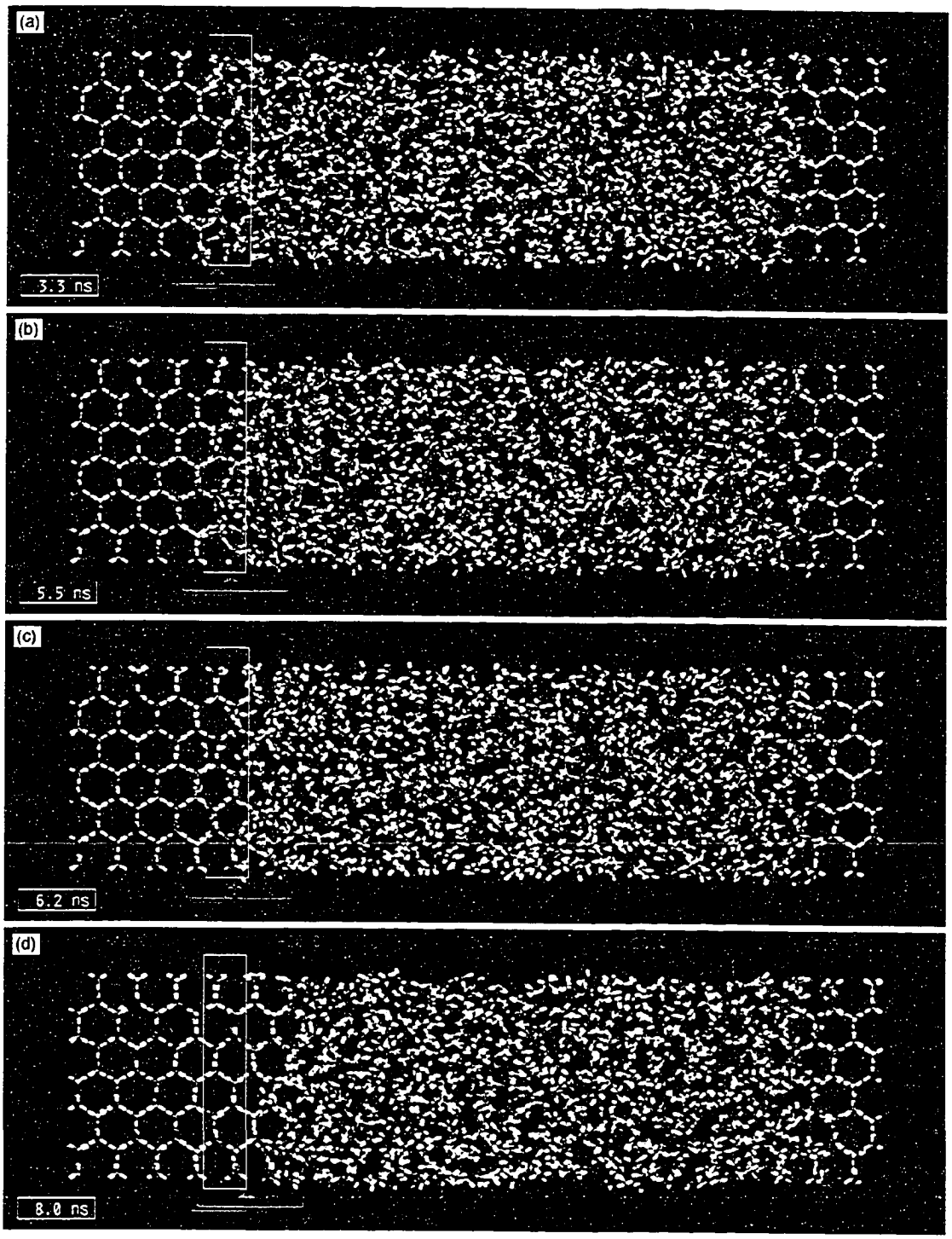

Figure 6.20 Four averaged configurations of the Ih$1\bar{1}20$ ice/water interface of the same system as in Figure 6.15(c). The colouring of the molecules are discussed in the text. The time sequence of the configurations (a-d) are given in the box at the bottom left of each configuration. The green arrow with its enclosing bracket indicates the centre and the width of the interface as given by the energy profile functions. The horizontal green line below the bracket shows the movement of the interface in time. The white box shows layer I.

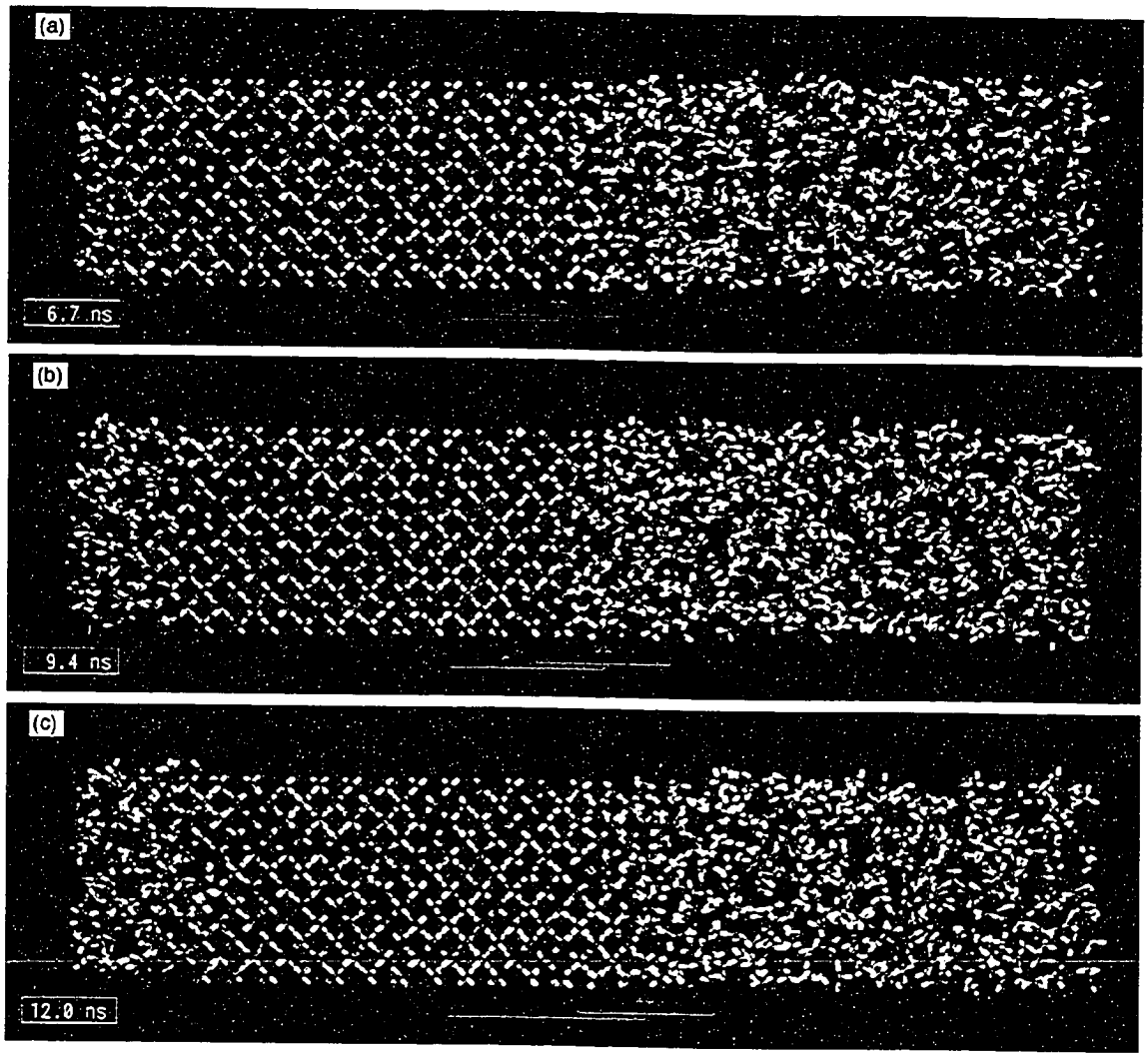

Figure 6.21 Three averaged configurations of the Ic001 ice/water interface of the same system as in Figure 6.16(b). The colouring of the molecules are discussed in the text. The time sequence of the configurations (a-c) are given in the box at the bottom left of each configuration. The green arrow with its enclosing bracket indicates the centre and the width of the interface as given by the energy profile functions. The horizontal green line below the bracket shows the movement of the interface in time.

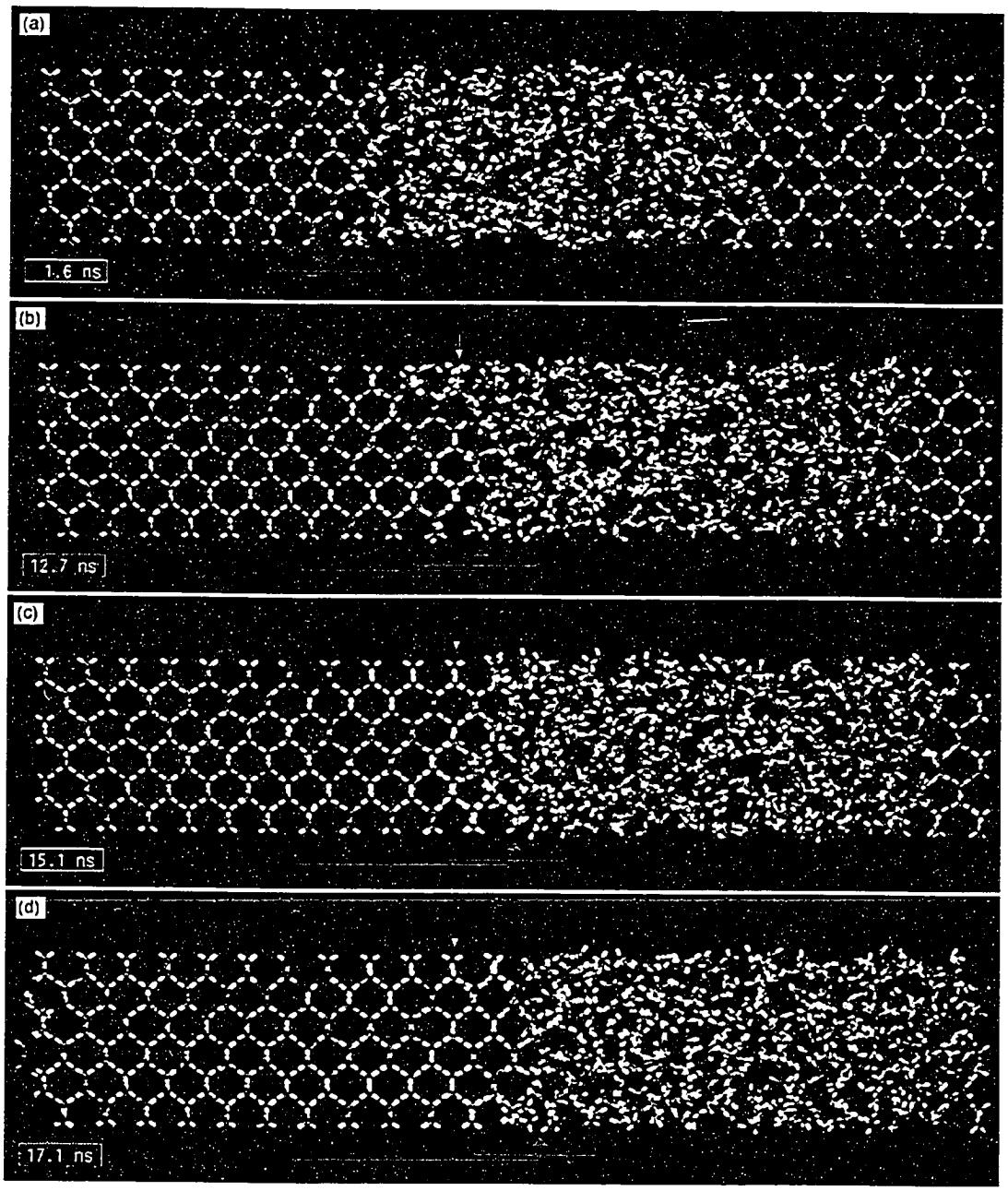

Figure 6.22 Four averaged configurations of the Ic011 ice/water interface of the same system as in Figure 6.16(a). The colouring of the molecules are discussed in the text. The time sequence of the configurations (a-d) are given in the box at the bottom left of each configuration. The green arrow with its enclosing bracket indicates the centre and the width of the interface as given by the energy profile functions. The horizontal green line below the bracket shows the movement of the interface in time. The yellow and red arrows show layers N and O respectively.

underlying molecular structure to be averaged out in the moving frame. Thus the interfacial profile functions used here represent average interfacial characteristics, that is they are averaged over the fluctuations captured within any particular simulation. Hence, although the averaged configurations used in the present discussions are useful, they furnish at best a representative glimpse into the behaviour at the interface. Their usefulness stems from aptly capturing events that can be placed in the context of the actual physical dynamics of the molecules.

6.2.3 Freezing and melting mechanisms of ice/water interfaces

The present discussions of the microscopic details of the mechanism of growth and melting can be essentially grouped into Ih0001/Ic111, Ih10$\bar{1}$0/Ih11$\bar{2}$0, and Ic001/Ic011 crystal systems. Averaged configurations will be used to investigate the underlying mechanism of crystal growth and melting. It should be noted that animations of these configurations representing trajectories as long as 24 ns were analyzed in detail. From these animations representative images were chosen as specific figures (for each crystal face) presented in this section. These images will feature entire systems (in the z-y projection) and sometimes specific slices (in the x-y projection) of various systems. Consequently, in all cases the images selected are intended to reveal some specific detail of crystal growth and melting, where the selected systems are representative of steady-state systems found for the various ice/water simulations.

Ih0001/Ic111

Investigation of growth of a crystal layer of Ih0001 can begin with an arbitrary slice next to a solid layer. The formation of such a layer, labeled B in Figure 6.23, has as a necessary condition an adjacent crystalline layer, A, which may still exchange molecules with the as yet unformed layer B. The term hopping will not be used here because the motion of molecules has been observed from averaged configurations where they appear to exchange positions rather than hop. The time sequence given in Figures 6.23 and 6.24 follows the crystallization of layer B over a period of roughly 3.5 ns. As described earlier, the molecules that eventually form the crystalline layer have blue oxygens if they are identified as a translational solid and green otherwise (translationally liquid).

Just prior to the 2.0 ns configuration shown in Figure 6.23(a), layer B (on the liquid side of the interface) shows increasing evidence of translationally solid-like molecules. The adjacent layer A (toward the solid) is partially formed, and exerts considerable influence upon layer B. At this point the structural fluctuations within B are sometimes manifest as local hexagonal rings which forms and subsequently dissolves within a 0.1 ns timescale. At 2.0 ns, layer A is now well formed and within B, solid hexagonal rings can be observed, as shown in Figure 6.23(a). Almost all the molecules within B are identified as being translationally solid-like, whereas the majority are still rotationally liquid, indicative of the fact that a stable hydrogen bonded network has not yet been formed. From the inset in Figure 6.23(b), 0.1 ns later, order appears to have extended upwards in layer B, although less order is apparent from the (x-y) slice view. Curiously, five-membered and seven membered-rings are rather conspicuous in the upper

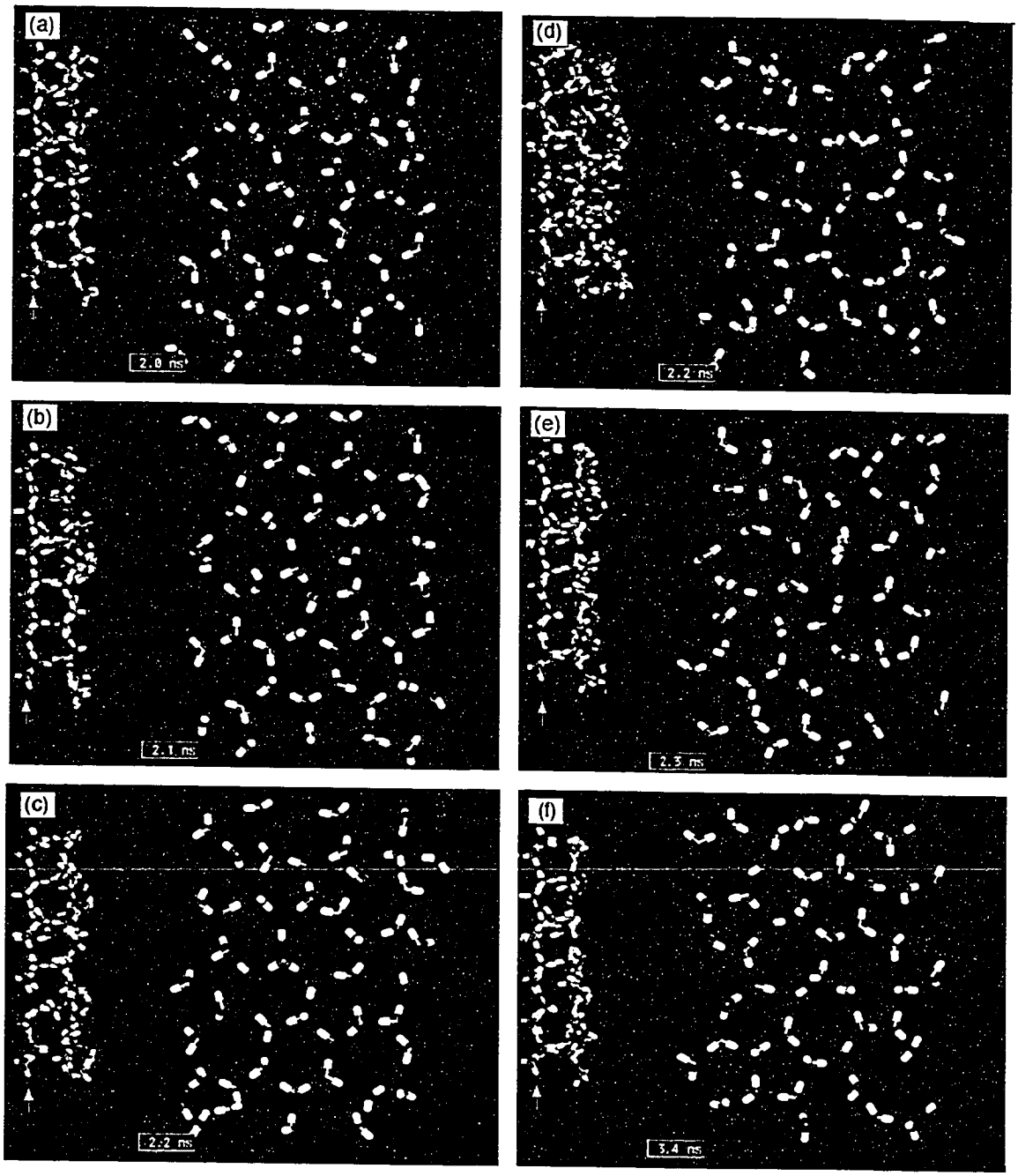

Figure 6.23 Slices of averaged configurations at different times for the Ih0001 system given in Figure 6.17. The time sequence is indicated at the bottom left of each image. The colouring of the molecules are discussed in the text. The insert in each frame shows two layers in y-z view; where the red arrow labels the slice (layer B) shown in x-y view. The yellow arrow indicates the adjacent layer, A. The labels A and B are the same as provided in Figure 6.17.

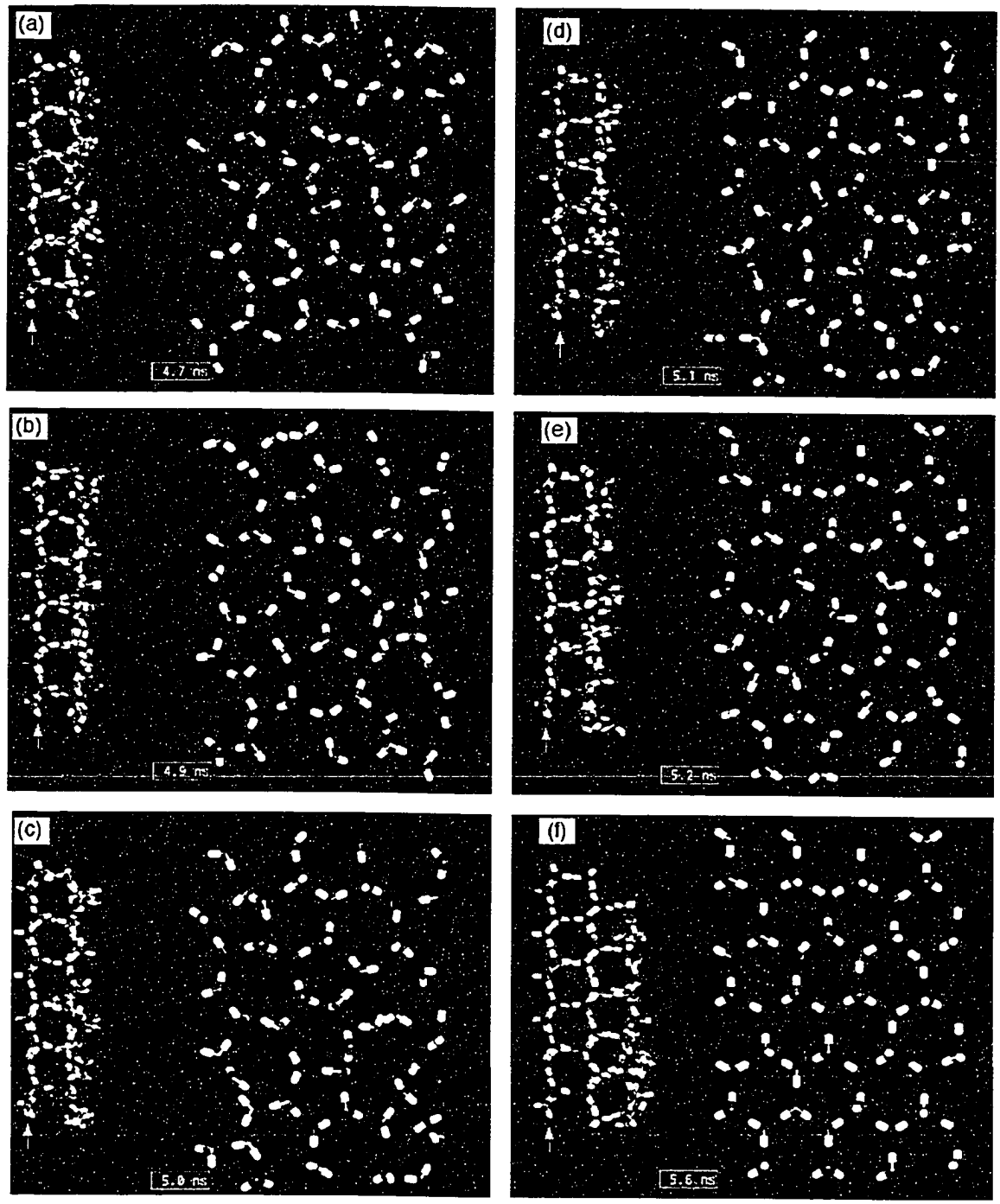

Figure 6.24 Slices of averaged configurations at different times for the Ih0001 system continued from Figure 6.23. The time sequence is continuous of that of Figure 6.23.

portion of Figure 6.23(b). Figures 6.23(c) and (d) show the order in the layer being dissolved with virtually all molecules rotationally liquid, although translationally solid-like molecules near crystalline positions are still evident. Moreover, molecular exchanges are still occurring between layers A and B. Structural fluctuations continue to occur in layer B with very few stable six-membered ring structures persisting beyond ~0.1 ns. In the time interval between 2.3 - 3.4 ns, B becomes rather diffuse and even begins disordering layer A (disordering processes appear dominant in this time window). At the end of this period, various five and seven-membered ring structures can be observed in layer B as shown in Figure 6.23(f). During this time frame, B has undergone considerable structural rearrangement without having successfully achieved crystalline order.

At 4.7 ns (see Figure 6.24(a)), hexagonal rings, as well as lateral ordering are becoming more apparent in layer B, although a majority of molecules are still orientationally liquid. In Figure 6.24(b), 0.2 ns later, a more stable hydrogen bonded network has formed as fewer orientationally liquid molecules are observed. In Figure 6.24(d), the hydrogen- bonded network that has formed contains five-, six- and seven-membered rings. These defective structures still appear to H-bond to the underlying crystalline layer (A) and thus annealing must occur to eliminate these unwanted ring structures. At 5.2 ns, many of the defective rings have either incorporated or rejected a molecule to form six-membered rings. However, this process sometimes involves propagating defects through the hydrogen-bonded network, as shown in Figure 6.24(e). At this stage, B is defective but mostly crystalline. Subsequently, in Figure 6.24(f), 0.4 ns later, layer B is essentially crystalline. One red molecule is still present, indicating that it

will still be exchanged. The cycle is now completed with the formation of layer B which is now at the center of the interface (as layer A was at 2.0 ns in this time sequence).

Structural defects can still occur deep inside the solid side of this interface, albeit as a less frequent event. This may occur if structural fluctuations cause rotationally and translationally liquid-like characteristics to develop for molecules within an adjacent interfacial layer closer to the liquid.

As noted in the foregoing discussion of the formation of a layer at the Ih0001 interface, hydrogen-bonded networks may develop in a growing layer that involve other ring structures. These distorted ring structures can cause the growing layer to be diffuse in the z-direction (perpendicular to the interface). Moreover, the hexagonal rings that do form do not usually persist and grow, instead they induce order and dissolve, exchanging molecules throughout. The occurrence of other ring structures is typically involved with the eventual formation of a stable layer. From the discussion in Chapter 5 (Section 5.3), the basal face of ice is believed to grow in layers, generally believed to start with the formation of a two-dimensional (2D) nuclei. Hence, the uniqueness of a 2D nuclei may be established if at least one hexagonal ring is identified as persisting in the formation of a complete layer from an incipient layer. Yet, it has been found that molecules in such a ring may still undergo exchanges with the surroundings. Thus, one is left with no clear idea of what a critical number of molecules would be that constitutes a stable nucleus. Observations in this thesis demonstrate that this view of layer growth in ice does not appear to be useful or relevant.

Subsequent to its formation, a seemingly stable layer can still display significant number of exchanges as captured in Figure 6.25 for another Ih0001 system. The labeling

is essentially like Figures 6.23 and 6.24 except in this case, the different planes of a hexagonal ring are labeled differently. In Figure 6.25 indexed particles have been appropriately colored, where blue/green and gold/silver oxygens correspond to solid/liquid molecules in the two different planes within the hexagonal layer. In Figure 6.25(a) there are eight red molecules (which will be exchanged eventually) with both translations and rotations all solid; the layer appears to be a stable solid. Figure 6.25(b) shows that at 7.6 ns into this trajectory two red molecules were still present in the layer. As Figures 6.25(c) and (d) demonstrate, the defects induced in the layer after the departure of the red molecules required further annealing of the solid layer. The white box in Figure 6.25(d), illustrates how a defect is annealed by lateral movement of molecules to reorganize the defective rings (Figures 6.25 (e-g)). The corresponding behaviour can be observed in the prism face in Figures 6.20(d-f).

The formation of a crystalline layer at the Ic111 interface is expected to be very similar to that of the basal system because of their related crystal structure. Figure 6.26 shows the formation of a layer for the cubic 111 ice/water system. The starting point for the analysis of crystallization of this layer follows from a point analogous to that of Figure 6.23(a). In this case, the layers are marked as C, located at the center of the interface and D, the layer of primary focus. The label colour is identical to Figure 6.25. Figure 6.26(a) shows that layer C is rather disordered with a few interesting ring structures. In the two subsequent averaged configurations (Figures 6.26 (b) and (c)), the development of some regularly ordered structures in the layer is discernable. An eight-membered ring in the upper-right of C appears stable and may possibly aid in the establishment of further order by providing a temporary (metastable) hydrogen-bonded

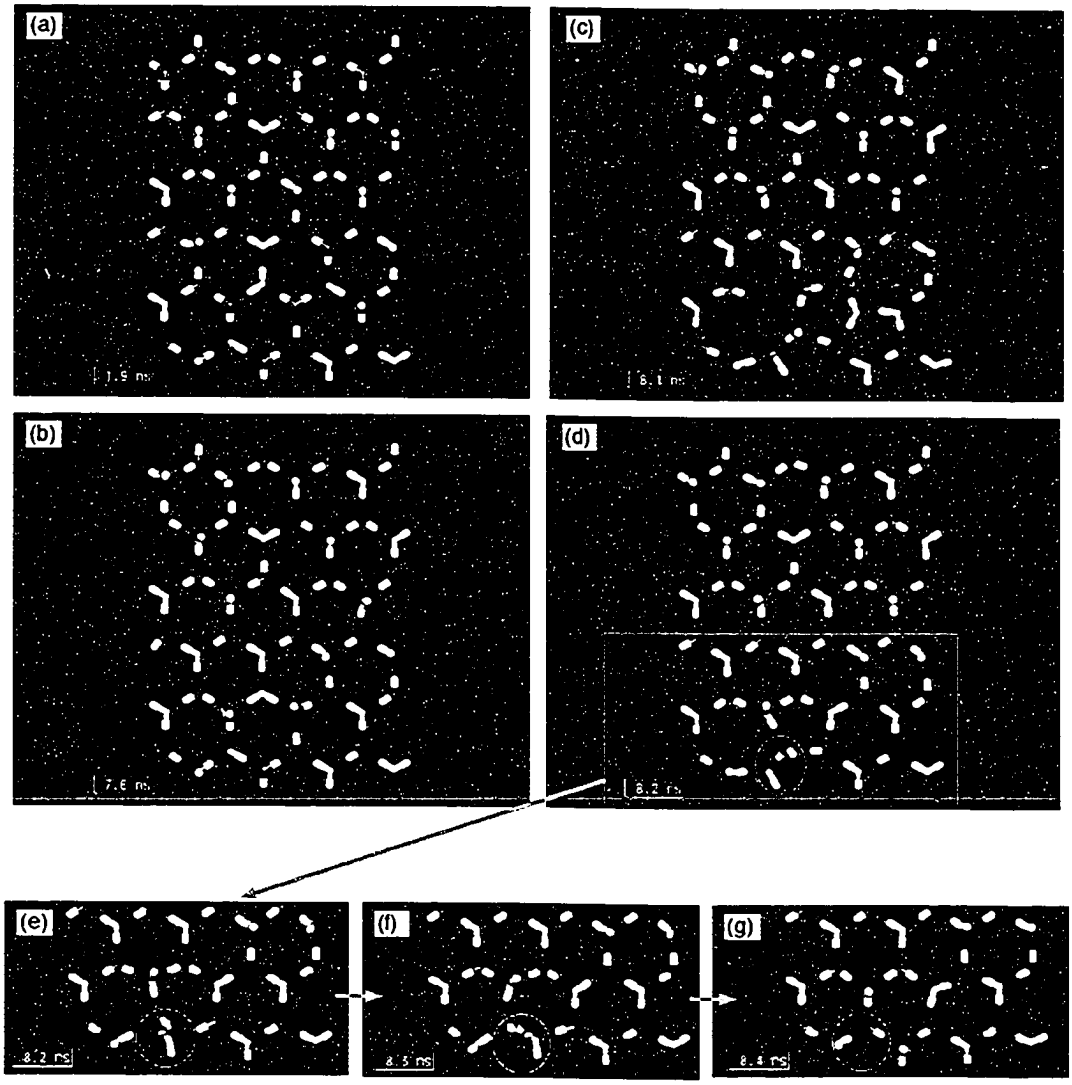

Figure 6.25 Time sequence of the exchanging of molecules within a solid layer of Ih0001 at large gradient at a growth speed of 8 cm/s. The colouring of the molecules are discussed in the text. Frames (a-c) show the propagation of ring defects through the lattice. Frames (e-f) capture the rearrangement of the local H-bond network through the movement of the circled molecules.

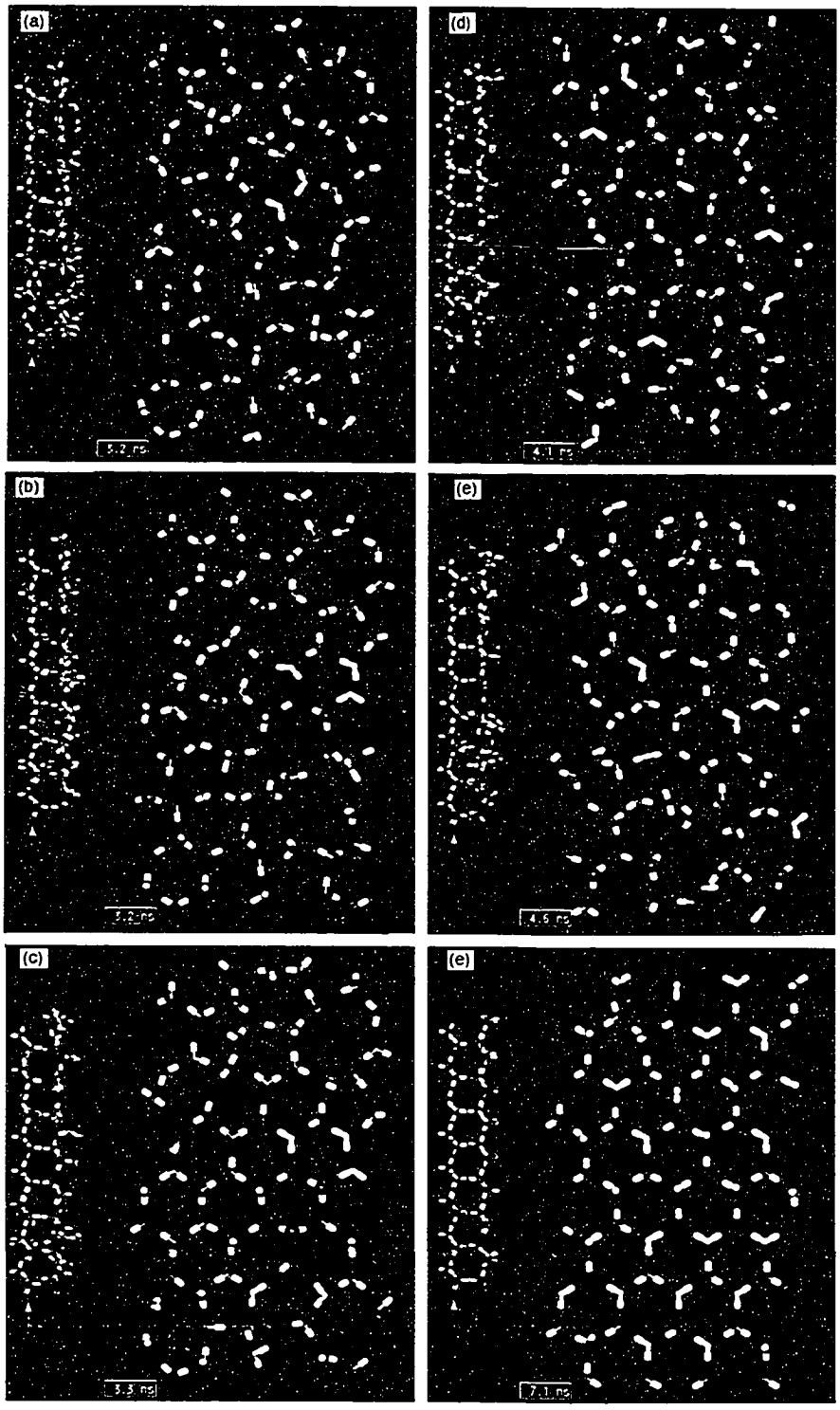

Figure 6.26 Slices of averaged configurations at different times for the Ic111 system given in Figure 6.18. The time sequence is indicated at the bottom left of each image. The colouring of the molecules are discussed in the text. The insert in each frame shows two layers in y-z view; where the red arrow labels the slice (layer D) shown in x-y view. The yellow arrow indicates the adjacent layer, C. The labels C and D are the same as provided in Figure 6.18.

network. Considerably more solid order is established in C 0.8 ns later, as can be seen in Figure 6.26 (d). From the x-y image and the y-z inset, the layer appears relatively well-formed with many solid molecules in apparently correct positions. Yet, many of the molecules in this layer must still be exchanged. At 4.6 ns (see Figure 6.26(e)), the order in the layer can be seen to be eroding as the layer experiences some disordering fluctuations. Beyond this point some order in C does always persist while it undergoes numerous exchanges and reshufflings of the hydrogen-bonded network. It eventually attains its final stable configuration at 7.1 ns (see Figure 6.26 (f)).

Although the accounts for the crystal growth of Ih0001 and Ic111 are very similar and the microscopic mechanisms seem to be the same, the (micro-faceting) fluctuations shown in Figure 6.18(b) have not been observed on any Ih0001 system. This suggests that partial crystal growth in layers and micro-faceting induced by disordering processes is normal for the 111 crystal system, even though it is a rare occurrence. This behaviour may account for its asymmetric interfacial peak (derivative of the energy).

The above descriptions of the crystallizing interfaces for the Ih0001 and Ic111 systems provide insights into how order and disorder are manifested in a crystallizing face as competing processes, similar to the LJ systems. It is appropriate at this stage to discuss these competing processes within the melting phenomenon. The melting process for Ih0001 is captured by Figures 6.27 and 6.28 with two tagged layers, E (gold/silver) and F (blue/green), where the latter is nearer the liquid and hence will melt first. Figure 6.27(a) shows two solid layers with the occasional breaking of a hydrogen bond in layer F as indicated by the yellow coloured hydrogen atoms (representing rotationally liquid behaviour). Melting is more apparent in Figure 6.27(b), where there are now more

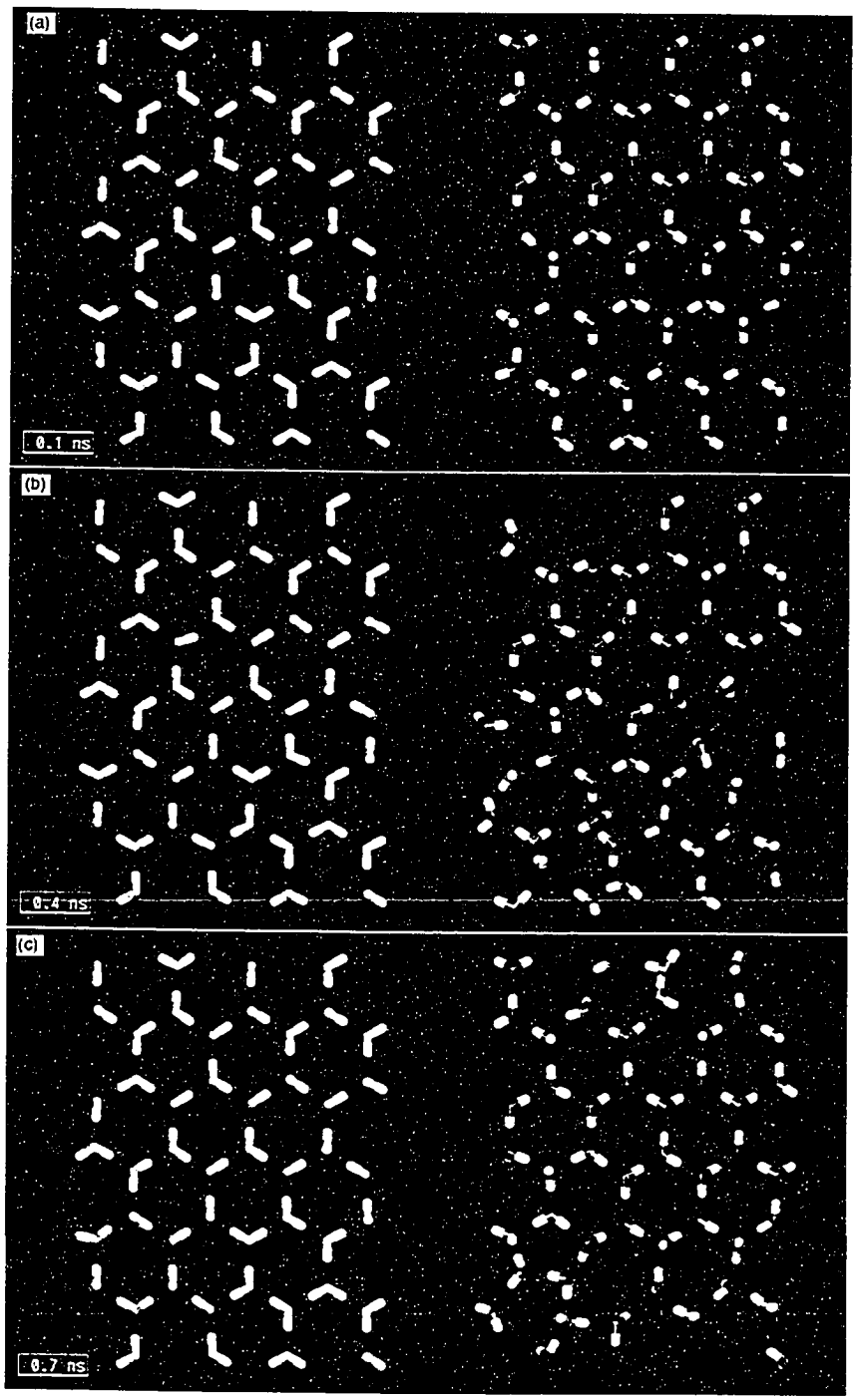

Figure 6.27 Representative averaged slice configurations of two slices at the melting interface of Ih0001 at different times of the system as given in Figure 6.17. Layer E is the gold coloured layer and layer F is the blue coloured layer. All other colours are explained in the text. The time sequence is indicated at the bottom left of each image.

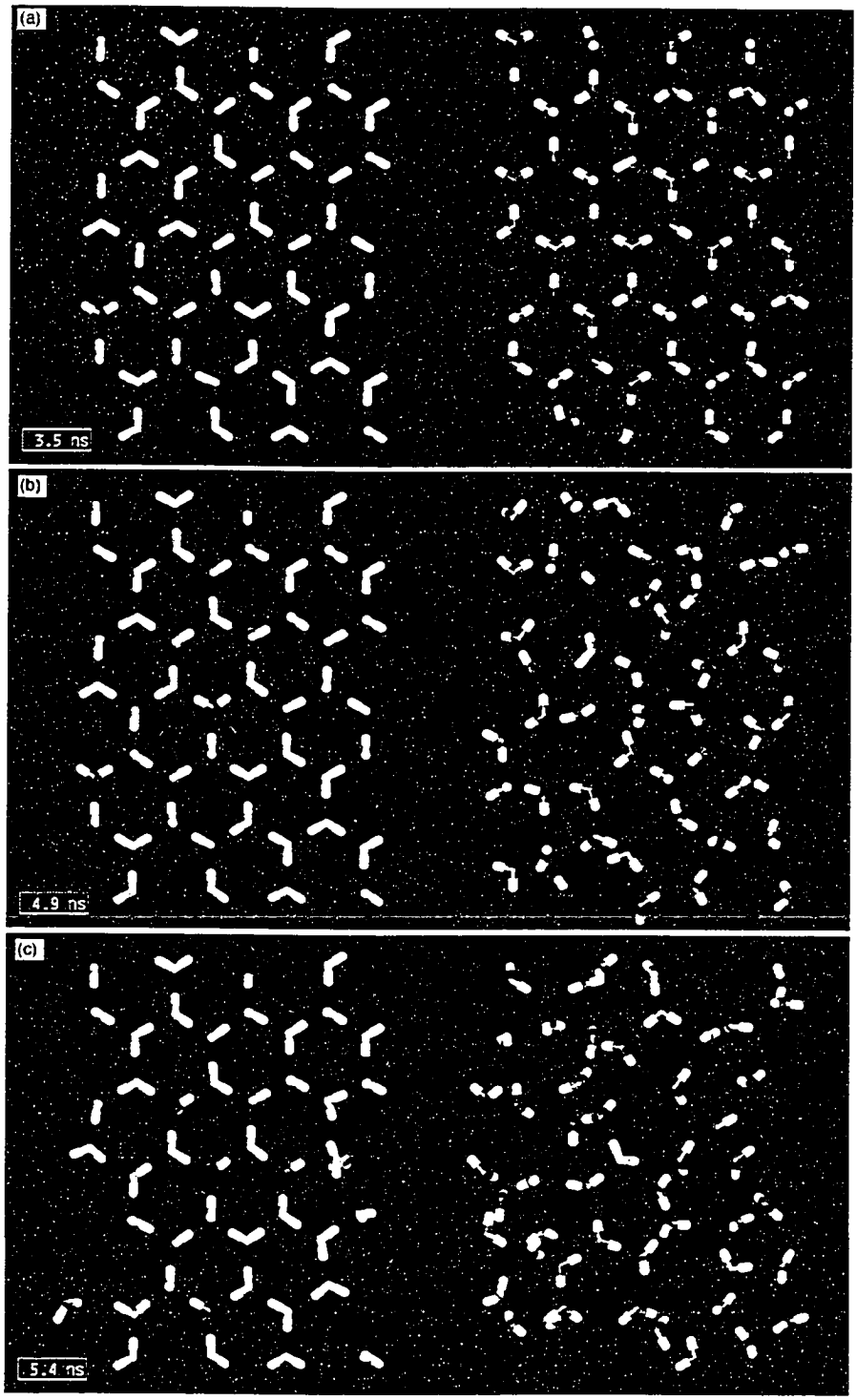

Figure 6.28 Representative averaged slice configurations of two slices at the melting interface of Ih0001 at different times continued from Figure 6.27. The time sequence is continuous of that of Figure 6.27.

rotationally liquid molecules causing a breakdown of the hydrogen-bonded network and permitting some of the molecules in F to display liquid-like translational behaviour. However, in Figure 6.27(c), ordering processes are re-introducing crystalline order back into layer F; there are molecules (not necessarily blue) in this layer that have again taken up crystalline positions. The reforming of F suggests that ordering processes dominate at this stage. In Figure 6.28(a), at 3.5 ns, layer F has incorporated many new molecules (from the liquid and layer E) but still retains its crystalline solid character. Surprisingly, at 3.5 ns F is now at the centre of the melting interface. Only in Figure 6.28(b), at 4.9 ns, does the layer in F begin to fully disorder. In Figure 6.28(c) F now appears melted and layer E is at the same stage of melting as layer F in Figure 6.27(c) (more than 4 ns earlier).

The melting phenomenon observed in Ic111 and Ih0001 is reminiscent of behaviour found in the LJ systems. In addition, it is clear that for the ice/water system rotational liquid-like behaviour occurs, first causing a weakening or breakdown in the hydrogen-bonded network, before translational disorder becomes evident. This is reflected in Figure 6.3 where it has been observed that rotational diffusive behaviour occurs before translational diffusive behaviour at the solid-side of the interface. Coupled with exchanges of molecules and introduction of defects, these features help to destabilize, and facilitate the eventual degradation of, the crystal layer.

Ih10$\bar{1}$0/Ih11$\bar{2}$0

Whereas the Ih0001/Ic111 systems seem to be governed by planar-like behaviour, the Ih10$\bar{1}$0 and Ih11$\bar{2}$0 crystal faces, both of which are perpendicular to the basal face,

can be characterized as rough, as can be seen in Figures 6.16(a) and (b). Yet, these faces also have some characteristics of growth and melting in common with the Ih0001/Ic111 systems.

The structural fluctuations experienced during growth of a Ih10$\bar{1}$0 crystal face are quite large, with the formation and destruction of essentially entire layers being reasonably common events, portrayed in Figures 6.29(a) and (b) over 0.9 ns. To capture the essential characteristics of the growth of the prism face, Figures 6.29(c-f) illustrate selected images revealing the growth mechanism of this crystal face. Figure 6.29(c) identifies layers G and H, where H is still rather disordered and exchanging molecules while G shows appreciable ordering. After 0.1 ns (see Figure 6.29(d)) crystalline order is observed to have increased in layer H. The majority of molecules in layer H are still rotationally liquid-like, with many molecules now in apparent crystalline positions, although most of these will be exchanged eventually (as evident by their oxygen colours). It is crucial to note at this point that these processes in H at this time are occurring on the liquid side of the interface. Instead of a fully formed layer, a finger of disorder permeates the lattice structure and disorder is observed in the middle of H, at 2.7 ns, as is depicted in Figure 6.29(e). In Figure 6.29(f), 1.4 ns later, layer H is now fully formed, however, more structural fluctuations still need to occur to exchange the remaining red-colored molecules. At this juncture in the time sequence, the layer is near the center of the interface, but still on the liquid side. This layer will still experience structural fluctuations that will tend to affect only local parts of the hydrogen-bonded network, until it is no longer a part of the interface. This characteristic is unlike that of Ih0001 where structural defects tend to be less localized. Thus, crystal growth, of the prism face, is characterized

by fingers of crystal order that extend into the liquid side of the interface, and these continually fluctuate until order forms.

The crystal growth of Ih$1\bar{1}20$ appears similar in many respects to that of the Ih$10\bar{1}0$. However, as was discussed in Section 6.1 this face proved to be considerably more difficult to grow. Observing the Ih$1\bar{1}20$ system in the y-z plane is less useful for examining growth; instead x-z projections were use in investigations (see Figure 6.20). Figures 6.30(a-f) capture the growth of this crystal face through a series of images of a particular layer, I (identified in Figure 6.20). The molecules of Layer I are coloured as blue and gold for the different planes of the crystal layer with the former closer to the solid. Four slices as shown in Figure 6.30 correspond to configurations displayed in Figures 6.20(a-d). The central feature of this interface is the structural fluctuations that appear to exhibit $10\bar{1}0$ micro-facets along with $11\bar{2}0$ planes (see Figure 6.20). Examining Figure 6.30(a) shows layer I as a disordered layer with translationally liquid-like and solid-like molecules with no hydrogen bonded network apparent (all orientations are liquid-like). After 3.3 ns, Figure 6.20(a) and Figure 6.30(b) both show some translational order; the top portion of Figure 6.30(b) displays more translational order than rotational order. The number of translationally solid-like molecules increases (along with the orientations labeled as rotationally solid after 4.6 ns as can be seen in Figures 6.30(c) and (d), structural fluctuations characterizing periods of continual ordering and disordering occur throughout this segment of time. After a further 0.7 ns (see Figure 6.30(e)), the layer appears ordered. The majority of blue labeled molecules and fewer gold labeled molecules are in their crystalline positions. Despite the crystalline appearance of the layer as depicted in Figures 6.20(c) and 6.30(e), more structural

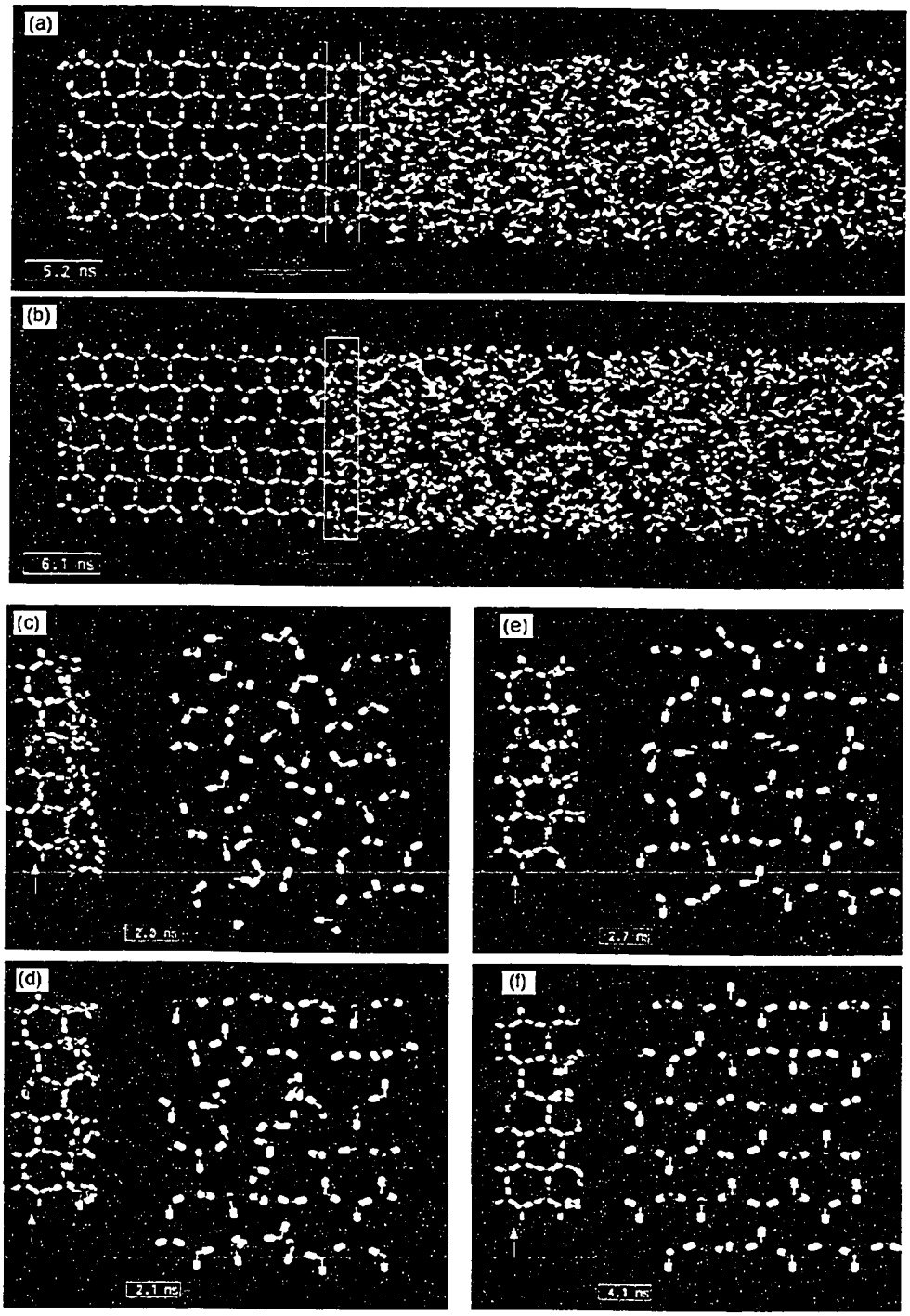

Figure 6.29 Averaged configurations of the y-z view of Ih$10\bar{1}0$ are shown in (a) and (b) along with slices x-y view showing crystallization (c-f). The white box in (a) and (b) compares the same region at different times of the interface. The time sequence is indicated at the bottom left of each image. The colouring of the molecules are discussed in the text. The insert in each frame (c-f) shows two layers in y-z view; where the red arrow labels the slice (layer F) shown in x-y view. The yellow arrow indicates the adjacent layer, E. The labels E and F are the same as provided in Figure 6.19.

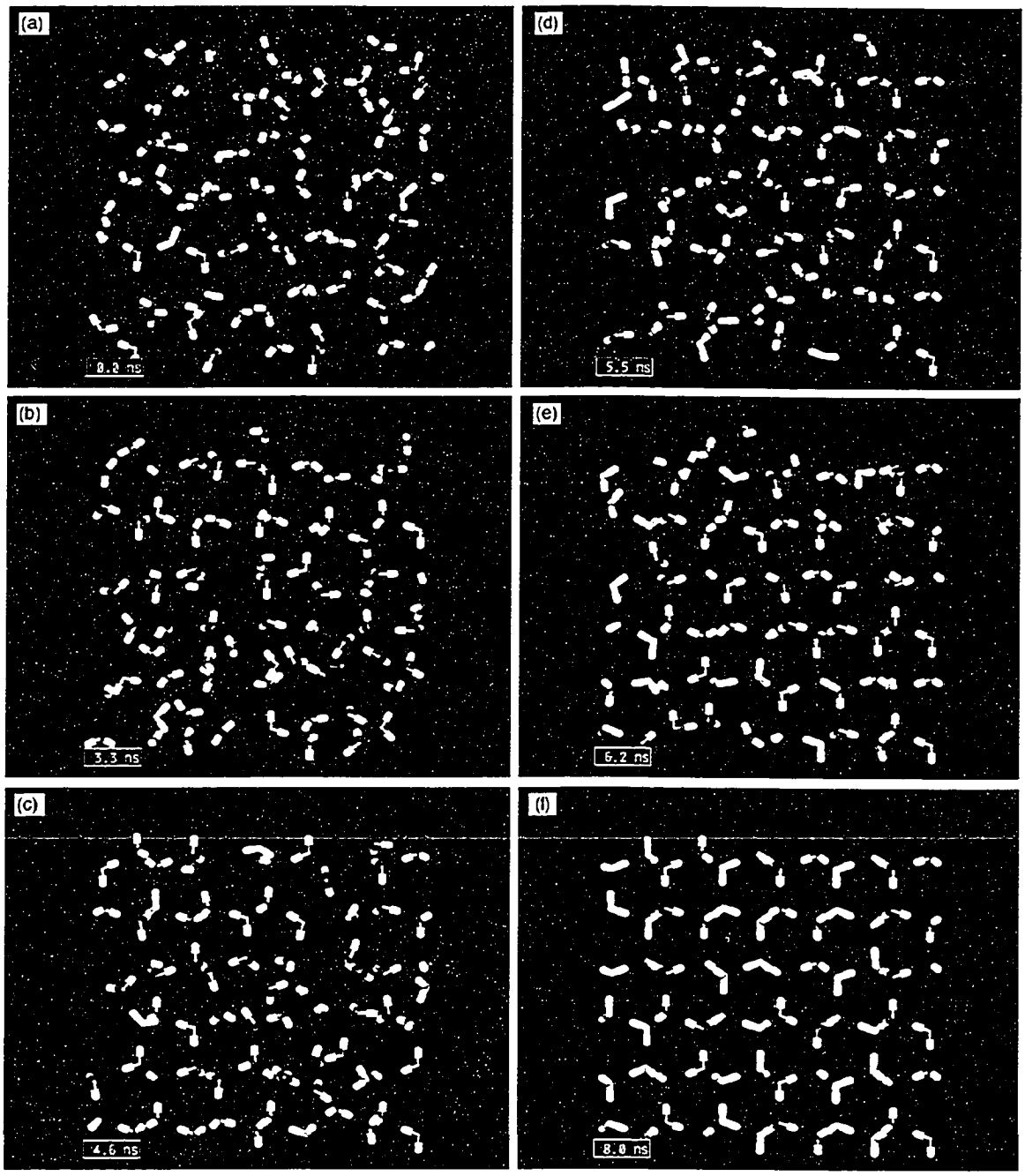

Figure 6.30 Slices of averaged configurations at different times for the Ih$1\bar{1}20$ system given in Figure 6.20. The colouring of the molecules are discussed in the text. The time sequence is indicated at the bottom left of each image. The slices in frames (b), (d), (e) and (f) correspond to slice I in Figure 6.20 (a-d), respectively.

fluctuations are necessary. The final layer is depicted in Figures 6.30(e) with the entire system shown in Figure 6.20(d). The $10\bar{1}0$ micro-facet visible in the latter figure is in the x-z plane as mentioned; the structural fluctuations responsible for this micro-facet appears to be a disordering process. There are frequent disordering (as opposed to ordering) events along $10\bar{1}0$ micro-facets. It is possible that these disordering processes retard the growth for this face.

The melting process for Ih$10\bar{1}0$ is captured in Figures 6.31 and 6.32 for layers J and K (also see Figures 6.19(a-c) and Figures 6.29(a-b)). In Figure 6.31(a) a few molecules in K, labeled as rotationally liquid-like, are disrupting the local hydrogen bonded network. As more molecules become rotationally liquid-like, further breakdown of the structure occurs (see Figures 6.31(b) and (c)) with more rotationally and a few translationally liquid-like molecules in K after 0.4 ns. Defects are concurrently developing in K as well, although some molecules can be seen taking up crystalline positions, illustrating another instance of disordering and ordering processes competing. This is a melting interface, as dictated by the imposed temperature conditions, and thus disorder will eventually triumph over the ordering process. In Figure 6.32(a), few rotationally solid-like molecules are observed in layer K, which is also losing translational crystalline order with five-, six- and seven- membered rings evident. After 1.2 ns the disorder in layer K allows the exchange of a molecule in layer J (see Figure 6.32(a)). Yet, 0.4 ns later some order returns to layer K, as seen in Figure 6.32(b). In Figure 6.32(c), at 3.8 ns, a finger of disorder can be discerned in layers J as it begins to melt in a manner similar to layer K. An essential feature in the melting phenomenon is

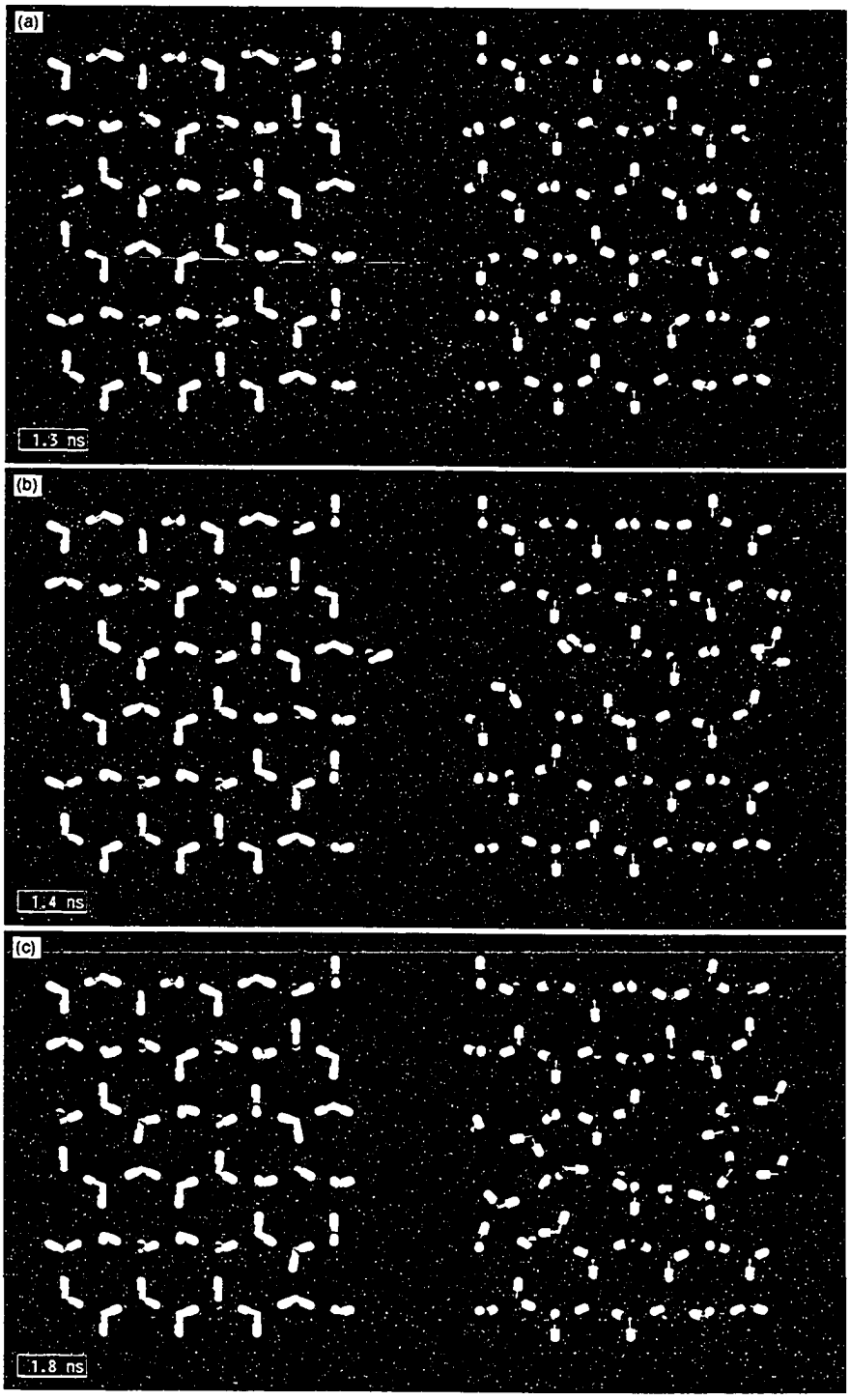

Figure 6.31 Representative averaged slice configurations of two slices at the melting interface of Ih1010 at different times of the system in Figure 6.15(b) . Layer J is the gold coloured layered and layer K is the blue coloured layer. All other colours are discussed in the text.

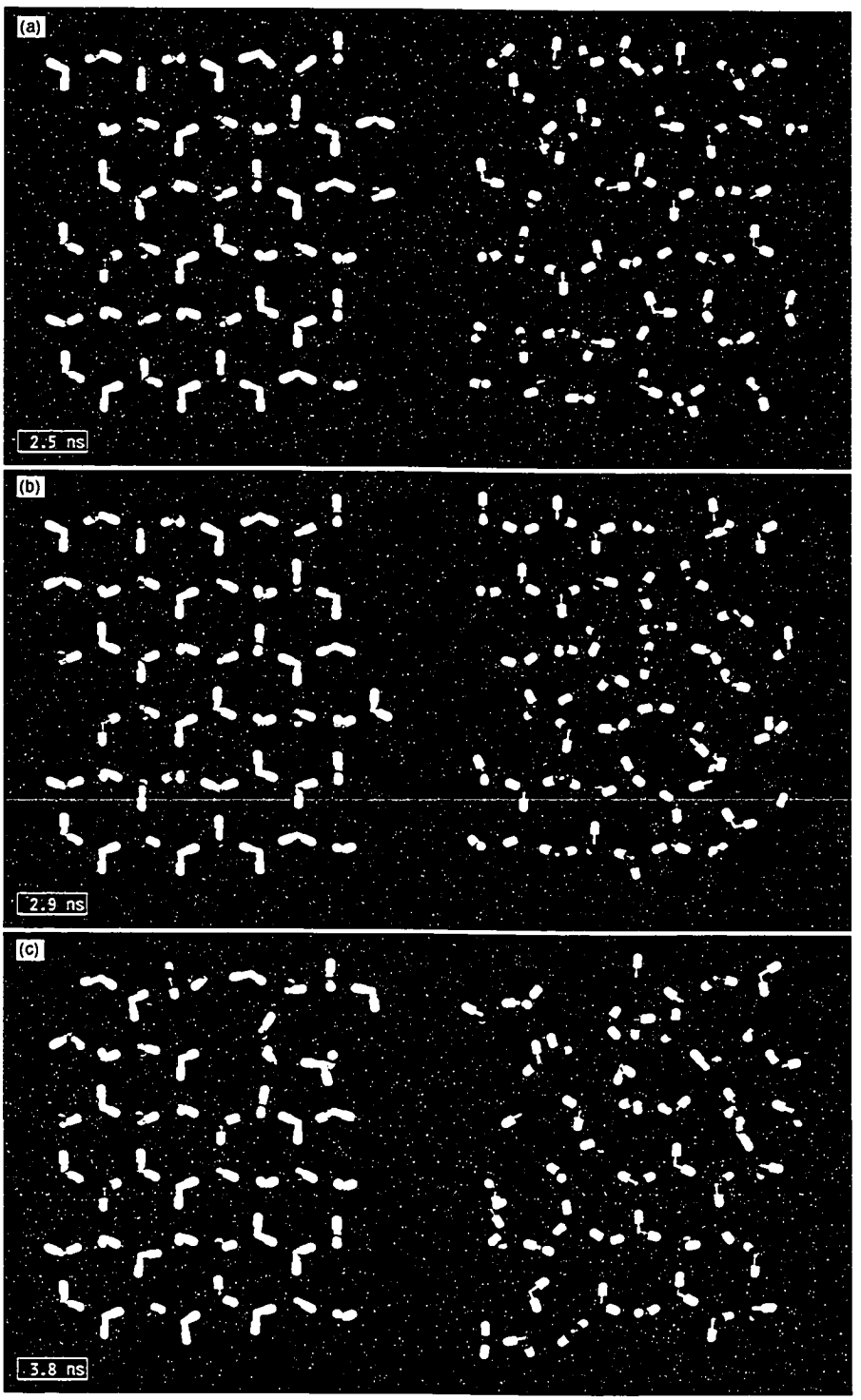

Figure 6.32 Representative averaged slice configurations of two slices at the melting interface of Ih1010 at different times continued from Figure 6.31.

the appearance of rotational defects and the occurrence of molecular exchanges. Whereas these aid the melting process, they must (usually) hinder crystallization.

Similar behaviour is demonstrated for melting of the $11\bar{2}0$ face except that micro-facets of $10\bar{1}0$ planes are visible. It is also of importance to note that the converse behaviour, where Ih$10\bar{1}0$ exhibiting $11\bar{2}0$ planes, is not observed.

Ic001/Ic011

As noted in the Ih$10\bar{1}0$ and Ih$11\bar{2}0$ systems, the Ic001 and Ic011 interfaces display large structural fluctuations and have the widest interfaces (see Figures 6.21 and 6.22 for Ic001 and Ic011, respectively). As pointed out in the preceding paragraphs, structural fluctuations may favour the formation of other crystal planes in the interfacial region. Averaged configurations of Ic001 show no preference for any particular crystal micro-facet in the interfacial region. In contrast, Ic011 exhibits 111 micro-facets during crystallization. Recall that in Figure 6.26(b) Ic111 was observed to display some evanescent 110 planes.

Crystal growth of Ic001 is illustrated by the images presented in Figures 6.33 and 6.34. Figure 6.34 shows two layers L (blue) and M (gold). No insets or arrows are used to indicate these layers in Figure 6.21 because of the difficulty in depicting growth from these images of the y-z plane. Instead, Figure 6.35, which displays only oxygen positions, will be used to highlight characteristics of growth. In Figure 6.33(a) only a few molecules can be observed to be in crystalline positions in layer L (with three molecules in crystalline positions in layer M) as indicated, with no rotationally solid-like molecules. Figure 6.35(a) shows a y-z view of the solid next to layer L (not M) where only a small

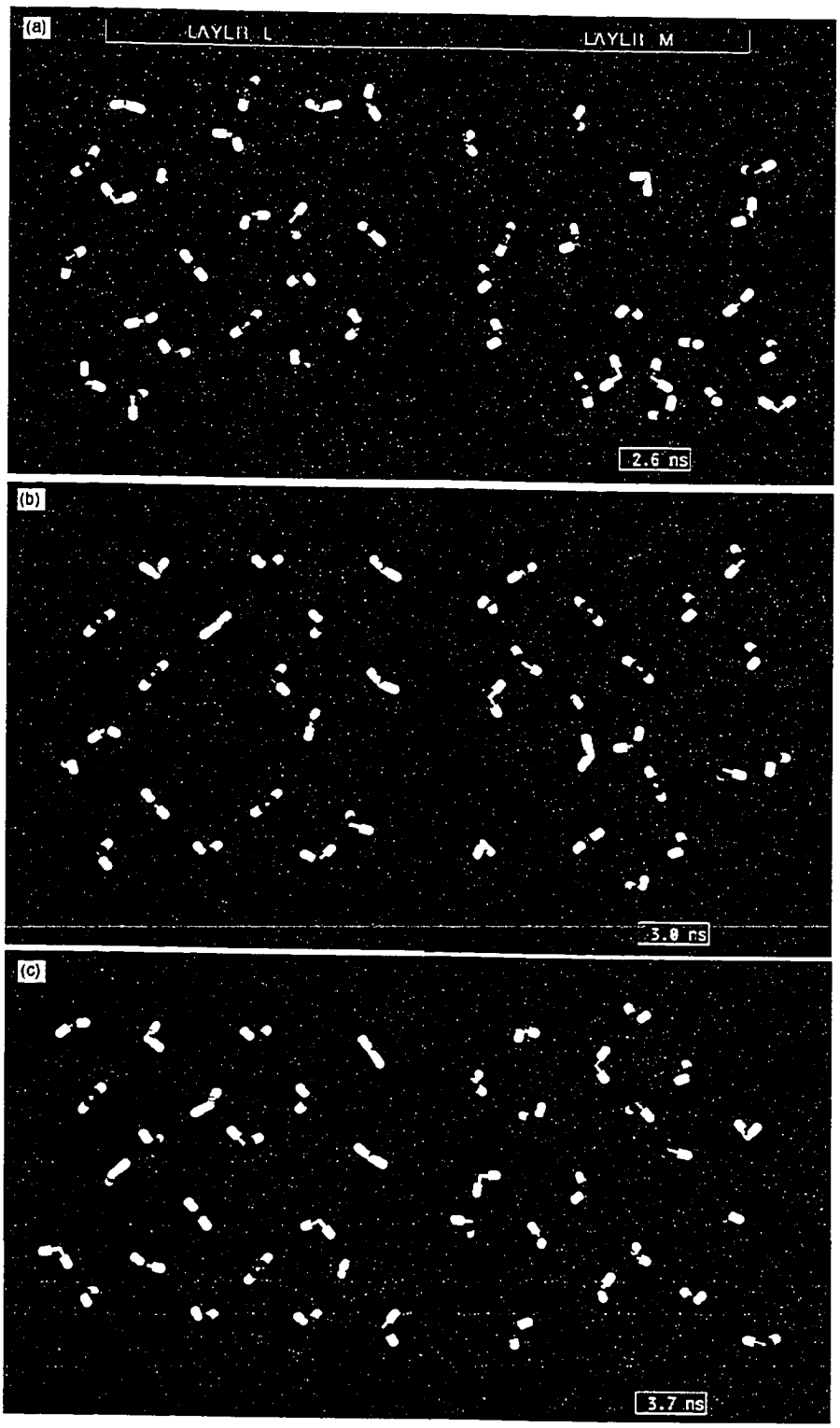

Figure 6.33 Averaged configurations of two adjacent slices, L and M of Ic001 crystallizing at different times for the system as given in Figure 6.21. The time sequence is indicated at the bottom right of each image. The colouring of the molecules are discussed in the text.

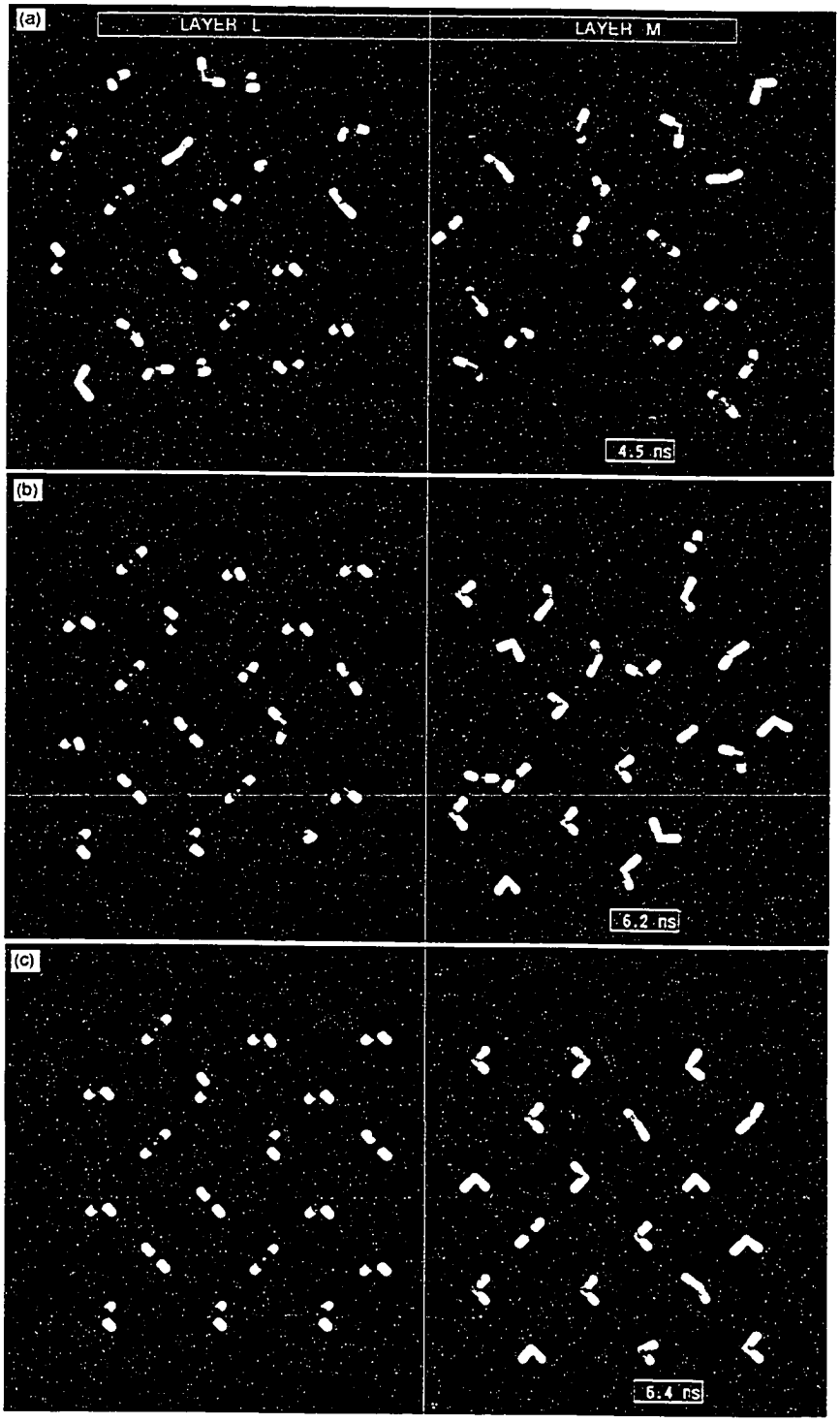

Figure 6.34 Averaged configurations of two slices of Ic001 crystallizing at different times of the system as given in Figure 6.21 continued from Figure 6.33.

portion of the oxygen positions are in crystalline positions as indicated (at 2.6 ns). Order grows in Figure 6.33(b) with a region of disorder apparent. In the y-z view of Figure 6.35(a) for the same time period (3.0 ns) as Figure 6.33(b), a distortion of the crystal layer that spans the solid layer through to layer M is visible. After 0.7 ns (see Figure 6.33(c)), the majority of molecules in L and M appear crystalline, with the overall layer structure appearing distorted (also evident at the center of the interface in Figure 6.21(c)). The vast majority of molecules are essentially translationally solid-like. In layer L most of the molecules are orientationally solid-like while in M most are orientationally liquid-like (see Figure 6.33(c)). Moreover, the majority of molecules are neither blue nor gold, meaning that significant structural fluctuations must occur before the final layers form (see Figures 6.34(a-c).

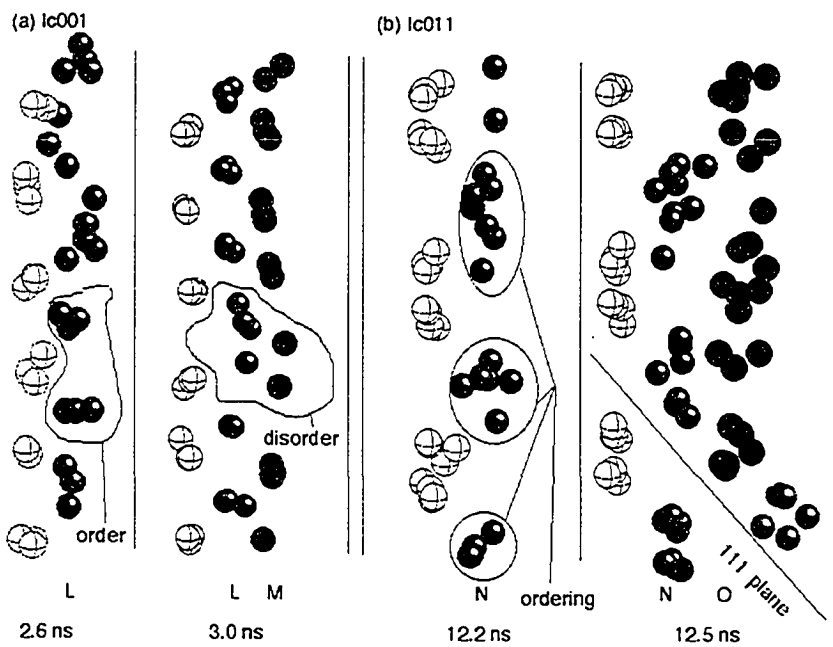

Figure 6.35 y-z views of two averaged configurations of Ic001 (a) and Ic011 (b) showing oxygen positions only. The hydrogen atoms were removed for clarity.

The growth of the 011 face is captured in the sequence of x-y images of layers N and O in Figures 6.36 and 6.37, along with Figure 6.35(b) where again only oxygen positions are shown. Layer N is closer to the solid side of the interface, and so groups of molecules appear to assemble around lattice sites, as can be seen in Figure 6.35(b) at 12.2 ns. At the lower end of this figure, this assemblage may be seen as a probable precursor to the eventual successful crystallization of these molecules (while also realizing that the continual structural fluctuations occurring at the interface play a central role in this many-bodied problem). In Figure 6.36(a) the assemblage is revealed to be loosely aligned along crystal planes. After 0.3 ns, the order in Figure 6.36(b) seems to be confined primarily in the upper and lower parts of the x-y plane. Inspection of Figure 6.35(b), at 12.5 ns, reveals that the lower part of the layer is ordered and the upper two-thirds is a distorted crystal layer. Evidently, ordering extends to layers N, O, and the layer behind O, as captured in Figure 6.35(b) at 12.5 ns; this order is along a 111 micro-facet as indicated. After a further 1.0 ns, structural fluctuations as well as exchanges continue to be present (see Figure 6.36(c)). In Figure 6.37(a) and (b) fingers of disorder can be noted within layers N and O. These fluctuations occur along planar (011) and 111 micro-facets until the layer is fully formed in Figure 6.37(c). Finally, it should be noted that melting for the Ic001 and Ic011 faces is very similar to the descriptions of melting provided for Ih10$\bar{1}$0.

Given all the above observations, it has been found that disordering processes can be roughly categorized as follows: breaking of hydrogen bonds due to rotational motion of molecules, introduction of defects (in part by exchanges) and translationally solid-like molecules reverting to liquid-like behaviour. These events are precipitated by random

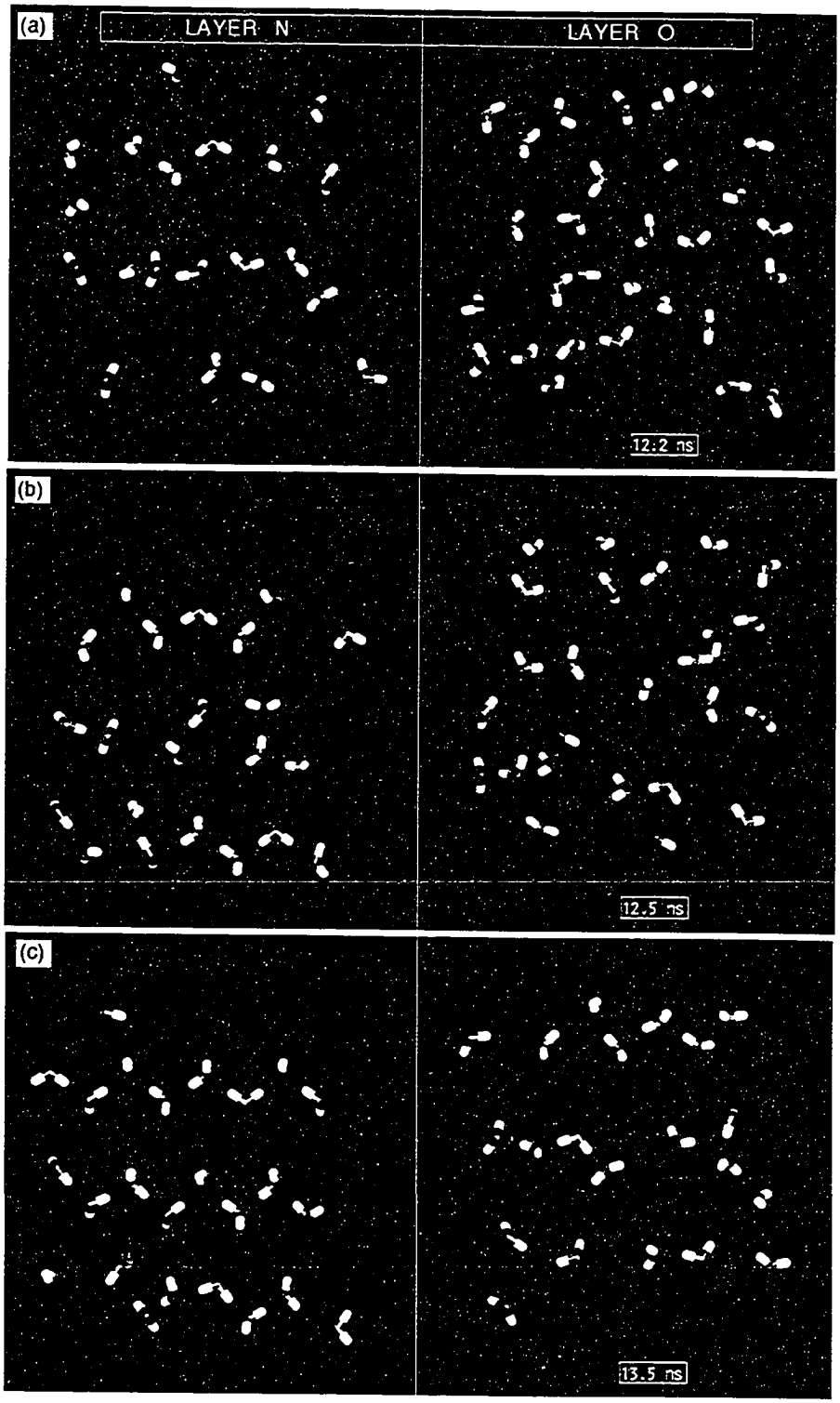

Figure 6.36 Averaged configurations of two adjacent slices, N and O of Ic011 crystallizing at different times for the system as given in Figure 6.22. The time sequence is indicated at the bottom right of each image. The colouring of the molecules are discussed in the text.

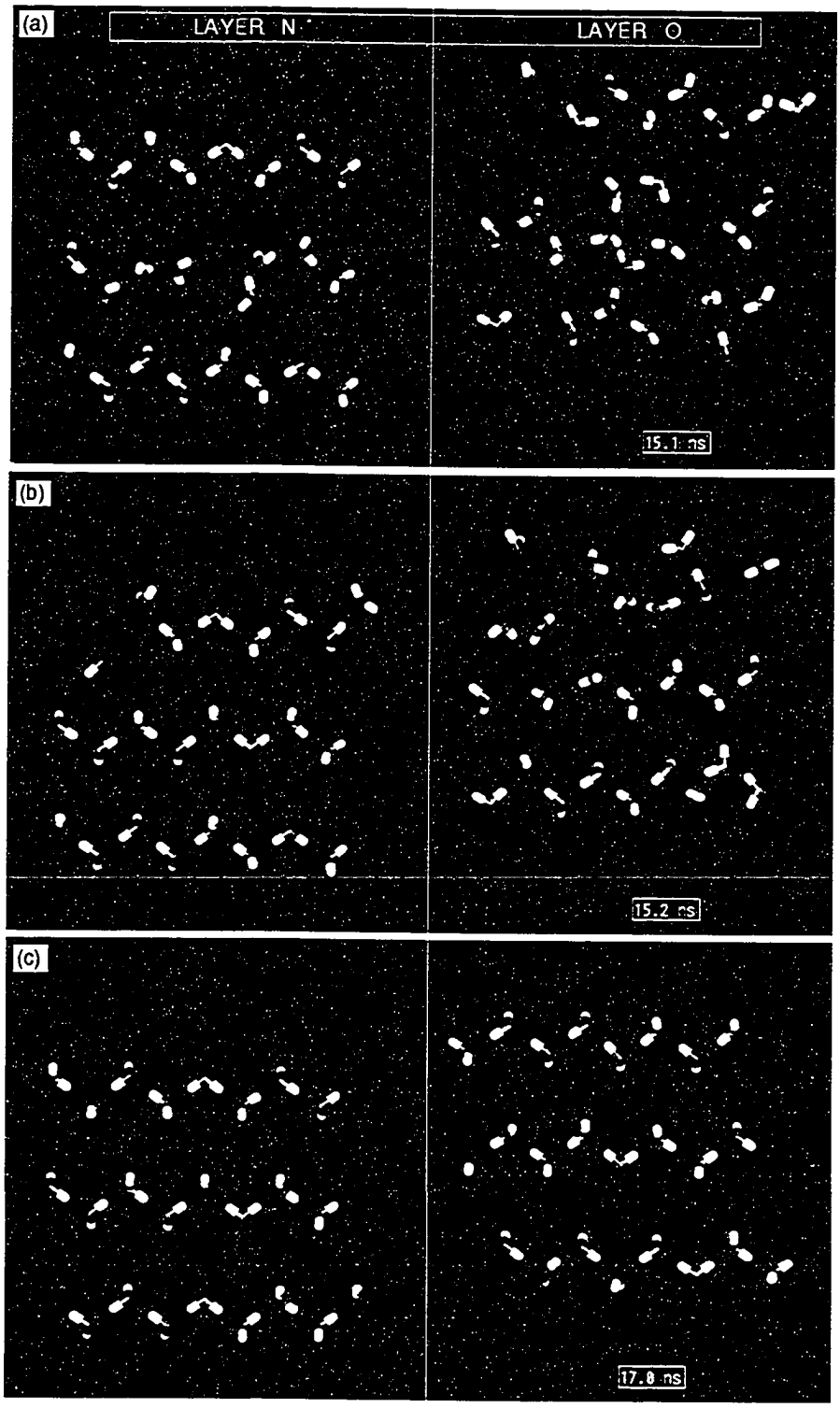

Figure 6.37 Averaged configurations of two slices of Ic011 crystallizing at different times of the system as given in Figure 6.22 continued from Figure 6.36.

thermal fluctuations occurring at both the freezing and melting interfaces, where the frequency and the magnitude of the thermal fluctuations are inherently stochastic. Ordering processes cannot be understood simply as the reverse event. In freezing, events such as annealing of defects (to form six-membered ring structures), formation of a local hydrogen-bonded network, molecules becoming translationally solid-like near crystal lattice positions can be associated with the ordering processes. In fact even at equilibrium these ordering and disordering processes are equal only in their respective rates at sufficiently large enough averaged time windows.

6.2.4 General observations from ice/water interfaces.

The various profile functions described in Section 6.1 provide a unique perspective of the interface because, in general, they each capture different aspects of the behaviour occurring in the vicinity of the interface without piecing together a consistent microscopic picture. An alternate viewpoint is that combined these profile functions are describing the changes that molecules undergo in being converted from bulk liquid to bulk solid. This latter viewpoint presupposes that there exists an *a priori* way to define the position of the interface in order to allow such a consistent description to be attempted. For such a description, a succinct overview of the profile functions is an appropriate starting point. The derivative of the energy profile demonstrated its use as a logical measure for the interfacial region along with S_g and S_k functions which have almost identical profile functions as noted earlier. The density, as already mentioned, captures the changes in the coordination moving from liquid-like to solid-like values as the local environment changes. Furthermore, the detailed averaged configurations have

revealed relatively immobile molecules with low coordination well into the liquid side of the interface. The Σ order parameter measures the change of 2D (long-range) crystalline order. Hence, any structural changes that occur at the edge of the interface, either a small fraction of a crystalline layer or any other ordered structure will be poorly detected by this function. The linear diffusion constant profile indicates that toward the middle of both the freezing and melting interfaces, the behaviour of this quantity changes abruptly as its value becomes approximately zero (see Figure 6.3). From the perspective of a molecule in bulk liquid with the approach of the advancing freezing interface, the, first obvious sign of change is a change in density. This translationally more solid-like behaviour is a manifestation of lower coordination. Within the liquid side of the interface, longer lived H-bonds with more localized translational order will occur and the molecule will change repeatedly between (translationally and rotationally) solid-like and liquid-like behaviour. Near the middle of the interface, diffusion of the molecule typically approaches zero, the molecules becoming part of localized assemblages around lattice points, whilst retaining slightly more rotational mobility. Between periods of being ordered or disordered, a molecule may eventually become part of the crystalline layer. Thus, the profile functions, when taken together, describe the above coherent microscopic picture of the interface.

The important differences of the six ice/water systems investigated here can be generally categorized into two groups: systems that show more planar-like behaviour and systems that are more rough. The Ih$10\bar{1}0$, Ih$11\bar{2}0$, Ic001 and Ic011 systems are in the latter group and Ih0001 and Ic111 the former. The systems that exhibit more planar-like interfaces grow and melt generally, layer by layer. There appears to be no distinct sites

that molecules migrate and then attach to during the crystallization process; similarly in the melting process molecules do not just leave crystal sites. In fact, ordering and disordering processes that are inherently many-bodied are operative during both freezing and melting.

The systems with rougher interfaces may exhibit different micro-facets at their interface. For example, Ic001 can show evidence of 110 and 111 micro-facets. However, on average no particular micro-facet is preferred and the interface is genuinely rough. In the case of Ih10$\bar{1}$0, no particular micro-faceting is observed and it is also generally rather rough. Nada and Furukawa [255] have coined the term *collective molecular process*[es] to describe the growth of a Ih10$\bar{1}$0 face. The present description of crystal growth of Ih10$\bar{1}$0 essentially begins with a rough interface with greater localization of molecules around lattice positions as shown in Figure 6.29(c). The existing solid structure may disorder or molecules could move into lattice positions and remain. This phenomenon shows a critical localization of molecules at the lattice positions. This assemblage may favour crystallization as these molecules may sample a smaller configurational space, thus suggesting such localization as a precursor for these molecules finding an ordered structure. Furthermore, growth of this face is not constrained to be within a specific layer. As shown in Figure 6.29(e) the top half of this layer is not commensurate with the bottom half. Additionally, these assemblages cause the formation of metastable hydrogen-bonded networks that aid in localizing molecules around possible lattice positions. Finally, crystallization of the 10$\bar{1}$0 face does not involve stacking faults or alternate crystal structures thereby aiding its growth.

Growth of Ihl$1\bar{2}0$ exhibits significant occurrences of $10\bar{1}0$ micro-facets, which would suggest that these two faces are both growing as shown in Figure 6.20. However, the formation of $10\bar{1}0$ micro-facets occurs more frequently as a disordering fluctuation than ordering. The critical structural fluctuations necessary for molecules to become crystalline appear more difficult to induce for $11\bar{2}0$ relative to the $10\bar{1}0$ face. Localized assemblages have been observed to occur on the $11\bar{2}0$ planes, with significant disordering processes occurring and forming $10\bar{1}0$ micro-facets. This may explain the observation of Ihl$0\bar{1}0$ micro-facets and the overall sluggish growth of the $11\bar{2}0$ crystal face.

In the present study, the ice/water system identified as having the fastest growth rate is the Ic011 face. In this face, the structural fluctuations are very large (as in Ic001). In addition, growth of this system seems to expose 111 micro-facets. Interestingly, this observation was also observed for the LJ 011 systems where crystallization seemed to be preferred along 111 micro-facets. Growth of such layers will always produce the correct cubic structure as 011 planes are comprised of two different layered planes. If at least one of these micro-facet forms and growth then occurs along it no ambiguity or sampling of other crystal structures will result. Further, localized assemblages of molecules is also evident in the 011 face as shown in Figure 6.35(b) with no requirement for one planar layer to have completely formed before the next layer grows. This was also observed in Ic001. Whereas in Ic111, ring defects and stacking faults result which serve to slow down the growth of this planar face.

The melting interfaces were found to be very similar in structure to their respective freezing interfaces. Careful analysis has shown that ring defects help the

melting of the layers, whereas they generally hinder the crystallizing process. These defects get introduced into a melting layer through fluctuations of the hydrogen-bond network. The formation of a metastable network destabilizes the layer and along with the other disordering processes, facilitates its eventual breakdown. Similarly in the LJ systems, the asymmetry in freezing and melting rates observed for ice/water interfaces point to the different roles defects serve in ordering and disordering processes; in the former time is required for defects to be eliminated while in the latter they simply aid the melting process. However, by far the dominant contribution for the asymmetry in the ice/water system stems from the stochastic nature of crystal growth involving some critical localization of molecular assemblages in the vicinity of lattice positions to expedite growth. Low temperatures and consequently lower mobilities increase the time required for the system to perform necessary configurational sampling.

Defects seem to be a natural part of crystal growth processes, as discussed in Section 2.2. Order is propagated if the defect can be eliminated or incorporated into the growing lattice in a way that does not hinder subsequent growth. Figure 6.38 shows a common growth defect found in one layer of a few hexagonal systems (x-z plane). This ring defect, shown here for the Ih$10\bar{1}0$ lattice, occurs by the distortion of the regular hydrogen-bonded network where the two molecules involved appear to be shifted into the hexagonal channels of the lattice structure. These are metastable structures that appear to persist in the crystal lattice over the timescale of the present simulations. The formation of these can be considered from inspecting Figures 6.20(c) and (d). These figures have captured molecules in the hexagonal channels during crystal growth for Ih$1\bar{2}10$ system. If

the molecule does not leave the channel before the lattice layer has completely formed, then such molecules become trapped, forming the defect.

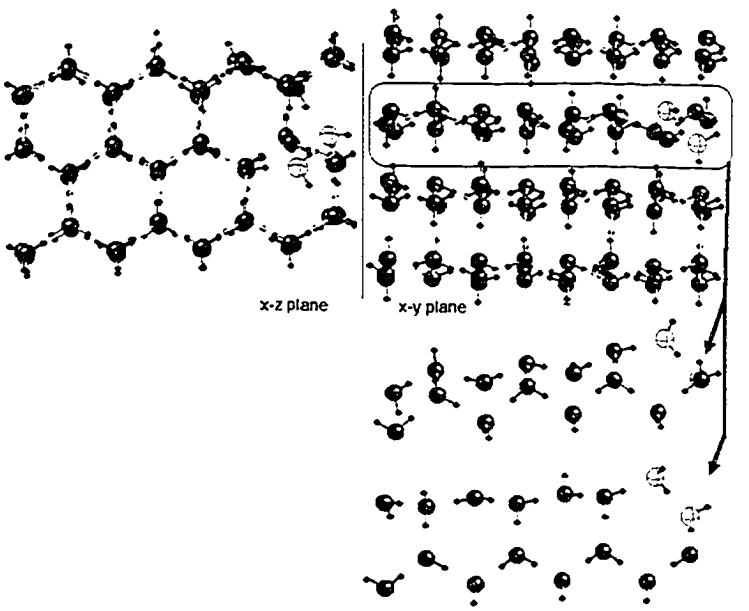

Figure 6.38 A common defect observed in hexagonal systems. The defective molecules are shown as transparent molecules in different planes of the Ih$10\bar{1}0$ crystal. The arrows show two different perspectives of the defective layer.

Within Ic111 and Ih0001 systems, another common defect is a stacking fault. A stacking fault in Ic111 takes the form of an ABA pattern of the hexagonal layers instead of its ABCA pattern. In Ih0001 the defect is the opposite, a ABC stacking instead of ABA. From totals of 29 layers grown for hexagonal as well as cubic systems, stacking faults occur ~1/3 of the time in Ic111 and ~1/2 of the time in Ih0001. These results suggest that these stacking faults are not random events and that there is something different about cubic ice. Figure 6.32(b), illustrates a (disordering) fluctuation along 011 planes of the Ic111 systems. Such a fluctuation may serve to anneal (or disfavour) a stacking fault in this face. A similar structural fluctuation can be seen in Figure 6.18(b) which subsequently destabilizes the growing layer. However, in this case the stacking

fault was not eliminated as shown in Figure 6.18(c). Such events may be the origin of the lower probability of stacking faults in the Ic111 system, although further study with better statistics is required to confirm this.

It is well known experimentally that under appropriate conditions cubic ice will convert irreversibly to hexagonal ice. A possible explanation for this transformation has been suggested by the claim that cubic ice is essentially "dirty" hexagonal ice with stacking faults that are annealed at higher temperatures. As discussed in chapter 5, Murray et al. [199] have successfully shown that droplets of water can be frozen to a structure that contains a large proportion of cubic ice. It has been reported earlier in this chapter that the interfacial tensions of the 011 and 001 faces of cubic ice are lower than those observed for the three faces examined for hexagonal ice. The values obtained of cubic ice I support the estimate of Huang and Bartell [196]. Furthermore, the misorientation of different hexagonal planes by about 70° in polycrystalline snow [190] clearly suggests that the transformation of cubic ice to hexagonal ice occurs at 111 planes, as discussed in Section 5.2.5. There is evidence in this thesis that supports the latter observation.

CHAPTER 7
CONCLUSIONS

In this thesis a new computer simulation methodology has been applied and tested for the study of heterogeneous crystal growth. This approach incorporates two local thermostats, a heat sink and heat source that create a temperature gradient within the system, allowing one to obtain with relative ease solid and liquid phases within the same simulation cell. When coupled with the movement of these thermostats at different velocities, simulations of steady-state crystal growth and melting have been achieved. The profile functions of quantities such as the density, the energy and a local crystalline order parameter are now smooth functions as a result of being measured in the moving frame. When the derivatives of these profile functions are taken, distinct peaks are obtained that provide convenient measures of the width and position of an interface.

This approach was first applied to simple atomic systems, where it was demonstrated to be a versatile method requiring relatively modest computer runtimes and system sizes. No size dependent behaviour in the simulations of steady-state growth of FCC crystal in systems of a couple of thousand Lennard-Jones particles was observed. As a test of the methodology, of the equilibrium thermodynamic melting temperature of the model systems investigated was reproduced. The apparent problems of long runtimes and big system sizes as discussed by Briels and Tepper [26] were essentially avoided because of the unique steady-state conditions achieved in these simulations.

The present approach provided a consistent means of obtaining the position and the width of the freezing and melting interfaces. The interfacial properties of FCC crystal faces were also explored. The values of the interfacial widths are in good agreement with

those of previous studies [4]. Using the derivatives of the structural order parameter and energy profiles as measures of interfacial width, it has been found that the widths for the different crystallographic faces decrease according to 001 > 011 > 111. It has been demonstrated that these different measures predict slightly different widths of the interfaces, although they provide consistent estimates for its position. In addition, the widths are observed to be only somewhat dependent on the magnitude of the applied temperature gradient and independent of the growth velocity.

The interfacial tensions were easily obtained from the derivatives of the energy profile and the results obtained generally agree with those found in the literature [20,37]. For the different crystal faces the interfacial tension decreases in the order 001 > 011 > 111. The dependence of growing/melting rates on the temperature was also examined in detail. It was discovered that near equilibrium linear behaviour for growth and melting velocities was observed and deviations from linearity are seen far from equilibrium (at high growth velocities).

To facilitate the analysis of interfacial detail for the atomic systems under investigation, averaging procedures for atomic coordinates were employed to help remove effectively all thermal motion, thereby capturing the essential translational motion associated with the steady-state freezing or melting processes. Subsequently, derivatives of the corresponding profile functions were superimposed on the resulting averaged configurations to help identify the interfacial atomic layers of the systems.

In general the interfaces of the LJ systems are not planar but rather are rough structures. For a particular crystal face the structure of the freezing and melting interfaces was found to be very similar, with the layer identified at the center of both showing 50-

80% solid structure. The interfaces were observed to be fluctuating entities, with competing ordering and disordering processes occurring at both freezing and melting interfaces; the process that dominates (determining if either net crystal growth or melting is observed) is thus dependent on the (temperature) conditions at the interface. Due to the structural fluctuations that dominate the behaviour at the interface, it is not well delimited and clearly defined sites (to which atoms can attach themselves) cannot be identified. Instead significant cooperative behaviour within clusters (or patches) of atoms was observed. Moreover, considerable atomic hopping between layers at both the freezing and melting interfaces has been found; this atomic behaviour introduces liquid-like characteristics primarily into the solid side of the interface. Based on such observations, the interface can be described as consisting of a center, a solid region with liquid-like structural fluctuations and a liquid region with solid-like structural fluctuations.

The structural fluctuations within the 001 and 011 interfaces are more pronounced than those apparent in the 111 face. These fluctuations, which help facilitate the faster growth of the 001 and 011 faces, introduce 3-dimensional crystalline "fingers" through the interface, extending as far as 3 or 4 atomic layers. In contrast, the 111 crystal interface is a narrower interface where fingers of order extend at most to two layers.

The present non-equilibrium simulation methodology has also been extended successfully to the steady-state crystal growth of cubic and hexagonal ice I. Steady-state ice crystal growth was examined for the various faces of ice I_h and I_c at different conditions of temperature and velocity. The impacts of the gradient and velocity in the ice/water systems are similar to LJ, although small velocity shifts were observed for the relatively small growth speeds achievable.

A variety of profile functions providing insights into the ice/water interface were obtained. The energy profile function, along with the S_g and S_k profiles, were used to describe the interfacial widths. The widths of the different faces obtained were found to increase in the order increasing order Ic111, Ih0001 < Ih10$\bar{1}$0 < Ih11$\bar{2}$0 < Ic001 < Ic110. The derivatives of the profile functions for the energy, Σ order parameter and density profiles exhibited notable differences, with no significant differences observed between the derivatives of the energy, S_g and S_k functions. Together with the rotational and translational diffusion profiles, these functions provided a coherent description for the average processes and environment at the interface.

The melting and freezing temperatures determined for the TIP4P systems allowed the equilibrium melting temperature of the model to be predicted; the value obtained agrees with Vega et. al [153]. However, this method could not be applied to TIP4P-Ew and SPC/E due to the lack of steady-state simulations. Yet, it proved possible to estimate the melting temperatures from simulations with the very large gradients, and the values so obtained for LJ, TIP4P, TIP4P-Ew and SPC/E were all in good agreement with other estimates. Such a method could be applied to estimate melting temperatures for new models, before more detailed studies of growth, for example, are undertaken.

The maximum growth speeds obtained in this study agree well with experimental growth rates. Growth of ice appears to be dominated by stochastic processes, and no continuous microscopic growth of ice was ever observed in any system. Crystal growth of ice was significantly slower than in the LJ systems. It is possible that in the case of LJ growth, the sampling of configurational space for local free energy minima is easier than

in water systems where simultaneous translational and orientational order was required for crystallization.

Steady state-growth was achieved at a velocity of 16 cm/s for all the ice/water interfaces except Ih$1\bar{1}20$ (which was observed to grow at 8 cm/s). Using the properties of those growing interfaces it was possible to make more specific general comparisons of the growth rates of the various ice faces. It was found that in decreasing order Ic011 > Ic001 > Ih$10\bar{1}0$ > Ih0001, Ic111 > Ih$1\bar{1}20$. It is important to note that no significant differences were found between the growth characteristics of the Ih0001 and Ic111 faces.

The interfacial tensions were also easily calculated and generally fall under two groups: (Ih0001, Ic111, Ih$10\bar{1}0$, Ih$1\bar{1}20$) and (Ic001, Ic011) with values of 30 ± 3 and 24 ± 3 mN/m, respectively. For this as well as several other key properties it appears that the Ic001 and Ic011 faces are distinctly different from the others. The implication here supports other mounting evidence to suggest that cubic ice is a precursor to hexagonal ice in nature. The faster growth faces of cubic ice, with their lower interfacial tensions, can expose Ic111 faces. There is evidence to suggest that Ic111 faces are the sites for transformation into Ih0001.

The detailed behaviour of the molecules at the interface was investigated in a manner similar for the LJ systems. Averaging procedures to remove unwanted thermal motions were applied; the resulting averaged configurations were analyzed with the aid of solid-like and liquid-like labeling of the rotations and translations of the molecules. Observations of the melting and freezing interfaces show essentially the same ordering and disordering processes present in both interfaces. The net result of these competing

processes depends on whether the applied (temperature) conditions favour melting or freezing.

Crystal layer formation within Ic111 and Ih0001 systems appears to require that a given layer essentially fully order before the next layer can begin ordering, although no distinct 2D nuclei were observed. H-bonded assemblages of molecules are observed to position themselves near lattice positions as an apparent precursor to becoming established in the lattice sites; this behaviour appears throughout the layer of Ih0001. In the other (rough) interfaces, these localized assemblages of molecules are more distinct and also appear as precursors of crystallization (as a critical ordering fluctuation).

Growth of Ih10$\bar{1}$0 and Ih11$\bar{2}$0 involves quite rough interfaces, where only the latter exhibits any significant micro-faceting (as 10$\bar{1}$0 micro-facets). These micro-facets in the Ih11$\bar{2}$0 appear predominantly as disordering processes and may contribute to the slow growth of this face. The work in this thesis indicates that the faces of hexagonal ice do have different inherent growth rates, with Ih10$\bar{1}$0 being the fastest growing face. This observation coincides with the observations of Shimada and Furukawa [203] that an anisotropy due to molecular attachment kinetics must be present for dendrite and other pattern formation for growth perpendicular to the c-axis. However, the relation between the complex macroscopic patterns formed in ice growing from its melt (e.g. see Shibov et. al [202]) to the findings presented here are difficult to rationalize.

Ih0001 shows cubic stacking faults and vice versa for the 111 face of cubic ice with significantly more such faults present in the hexagonal case. This can be rationalized when one observes that at the Ic111 interface disordering fluctuations occur along 011 microfacets. These appear to destabilize a faulty layer and may facilitate the formation of

an appropriate layer thereby reducing stacking faults. Interestingly, 111 micro-facets appear to be significant in the fluctuations of the Ic011 crystal face.

A consistent finding in this thesis, for both LJ and ice/water interfaces, is that the smoother the crystal face the higher the value of the interfacial tension, consistent with the behaviour predicted by the Jackson model (see Chapter 2). A second but less pronounced correlation was the observation that narrower interfaces tend to be slower growing.

Thus, after defining and describing the interface along with a detailed look at the interfacial structure for two model systems, an explanation will be offered on the issue of microscopic reversibility discussed in Chapter 1. Lars Onsager [14] in his famous early papers postulated that equilibrium systems undergo fluctuations from their equilibrium properties (except total mass and energy for an isolated system), and that such fluctuation decreases very sharply as one approaches the thermodynamic limit ($N \rightarrow \infty$), but become more significant over smaller timescales (seconds $\rightarrow$ picoseconds). In observing the systems presented in this thesis such fluctuations are evident within the disordering and ordering processes at a solid/liquid interface, constantly competing and involving many atoms or molecules in their asymmetric environments. At equilibrium conditions, averages over long enough time windows would indicate that the net occurrence of ordering and disordering processes are equal. Moving away from equilibrium we bias the system for melting or freezing by favouring one of these processes. The results presented in this thesis show that ordering and disordering are distinct many-bodied processes. In these condensed systems, the trajectory for any one molecule not only depends on its own coordinates and velocities, but on the environment established by the collective behaviour

of the surrounding molecules. Over times long relative to the period of molecular collisions the observed behaviour will be chaotic and stochastic (thus not reversible). Hence microscopic reversibility, at least for crystallizing and melting, will hold only on average over long enough time windows.

In this thesis, detailed microscopic descriptions of crystallization and melting were provided. Unique profile functions were used to characterize molecular and atomic interfacial properties. The methodology utilized, in this thesis, has been highly successful at overcoming difficulties faced by previous workers, it is first simulation study of its kind achieving steady-state growth and melting of LJ and ice/water systems. This methodology is now being successfully applied to methane hydrate growth studies [269] and preliminary investigations of binary LJ systems, to model growth from solution, are currently underway.

CHAPTER 8
FUTURE WORK

Although the findings in this thesis have furthered the understanding of the solid/liquid interfaces and the growth mechanisms of atomic and molecular crystals, there are many outstanding issues that could be explored further.

The width of the interface as noted in Chapter 4 is made up of two contributions, a statistical (or stochastic) term (involving the meandering of the "instantaneous centre" of the interface) and the decay of an order parameter through the interface (its inherent width). The present study accounts for both contributions. The challenge is to understand further the contribution and the nature of the fluctuations that produce the meandering. With much better data (from longer simulations) and fitting appropriate functions to a plot of width versus gradient, it may be possible to extract the extent of this contribution. The behaviour of the interface may have an impact on larger scale manifestations of cellular and dendrite formation. Moreover, more and/or better data points would enable a more accurate plot of melting and freezing temperatures versus growth speed (similar to Figure 4.9) to be constructed. This will enable empirical solid/liquid growth equations similar to the Wilson-Frenkel equation to be developed and tested, furthering progress in solid/liquid crystal growth understanding.

The present ice/water systems could benefit from significantly longer simulation times. This would allow for the differentiation of interfacial tensions of the Ih0001, Ic111, Ihl0$\bar{1}$0 and Ihl1$\bar{2}$0 crystal faces. Resolving the differences between the Ihl0$\bar{1}$0 and Ihl1$\bar{2}$0 values would be very interesting. This would clarify the growth kinetics

under a variety of conditions. Moreover, improved statistics could confirm the difference in stacking faults between Ih0001 and ic111 systems.

Another important finding that requires detailed clarification involves elucidating the detailed behaviour of the localized assemblages. The characterization of the role of these assemblages would provide more insights into crystallization. Important questions pertaining to the lifetimes of individual molecules and hydrogen bonds for these assemblages would be interesting to address.

A preliminary investigation was undertaken to clarify sintering (or regelation) in ice. It was observed that over a period of 2 ns the fluctuations in ice/water interfaces can cause a narrow liquid gap between two ice faces to freeze at the thermodynamic melting temperature of TIP4P. A systematic study of this phenomena could be undertaken to discover the timescales and distances over which it might occur.

Other interesting questions that could be addressed are the possible role of quantum effects on crystallization. There is evidence to suggest that the fastest growth rates observed in this thesis is not at the upper bound for crystal growth of water. In addition, it has been recently [270] shown that quantum effects (particular rotational tunneling) are important in the properties of liquid water. Since, in this thesis it has been demonstrated that orientational ordering (collective) is important in crystallization, the uncertainties associated with the positions of hydrogen atoms in water may provide a faster (concerted) means for molecules to find order.

APPENDIX A – Initial Ice Lattice Structures

For the generation of the appropriate ice lattices, the unit cell coordinates were obtained from Hayward and Reimers [180] and Lekner [181] for hexagonal and cubic ice I, respectively. The coordinates were transformed by trivial rotations to provide the appropriate unit cells for the various systems examined here. The ice generation algorithm then used the dimensions and coordinates of the unit cells to generate the ice lattice. An outline of the procedure will be discussed below.

A) For the creation of the desired lattice (after the unit cell information is obtained), the appropriate translation vectors in the x, y and z dimensions for a given crystallographic face is used to generate the center of mass positions in three dimensional space;

B) next, for each lattice site (for all N water molecules), the identities of all four nearest neighbours of molecules i are stored in a two-dimensional array called NB for all N water molecules;

C) initially, assign bond information for the N molecules by sequentially selecting each molecule i and assign one of six possible patterns for hydrogen bonding to occur between molecule i and its four nearest neighbours. A pattern is randomly selected only if two hydrogen bonds are donated by molecule i (assigned a value of 1) and received (assigned a value of 0) from two of its four nearest neighbors. This is described as the Bernal Fowler (BF) ice rules [177]. Only if BF rules are fulfilled will the program move onto the next molecule. This procedure may violate BF rules for the four nearest neighbour as the loop over the N molecules is completed;

D) to correct for these BF rule violations, an iterative routine is carried out which checks whether each molecule satisfies BF rules. This is also done sequentially over the N molecules; if BF rules are not satisfied, a reassignment of IBOND will be implemented, randomly changing the bonding of the molecule (breaking a H-bond and forming a new one) until BF rules are satisfied.

E) if BF rules is not fulfilled, then the hydrogen bonding pattern for a nearest neigbour (also random) is arbitrarily changed which could violate BF rules. This

procedure continues until BF rules are satisfied (at most two of the nearest neigbour bonding may have to be changed). The program then moves on to the next molecule in the sequence;

F) this reassignment procedure is repeated for all particles, spanning multiple iterations until BF rules are fulfilled for the entire lattice. This is carried out until no reassignment of IBOND occurs over 1 full loop over the N molecules;

G) the oxygen coordinates along with the nearest neighbour information (NB) and the bonding information (IBOND) is read by a companion program, that assigns hydrogen coordinates for each molecule based on the local frame of each molecule;

H) finally the total dipole moment of the crystal is calculated based on the charge position vectors of the oxygen and hydrogen. If the polarization of the system is less than 5% the configuration is accepted, if not a return to step C is required, thus repeating the cycle.

After the configuration is accepted the orientations of the molecules must be expressed in quaternion form. To accomplish this, the hydrogen position vectors (relative to the oxygen) are represented as $\mathbf{OH}_1$ and $\mathbf{OH}_2$. Adding and subtracting the two vectors provides $\mathbf{DO} = \mathbf{r}$ and $\mathbf{H}_1\mathbf{H}_2 = \mathbf{s}$, respectively. To obtain a third orthogonal vector that uniquely defines the orientation of the molecule, the cross product of the two vectors, simply given as, $\mathbf{r} \times \mathbf{s}$, provides the vector, $\mathbf{t}$, which is always perpendicular to the plane of the other two vectors as shown in Figure A-1.

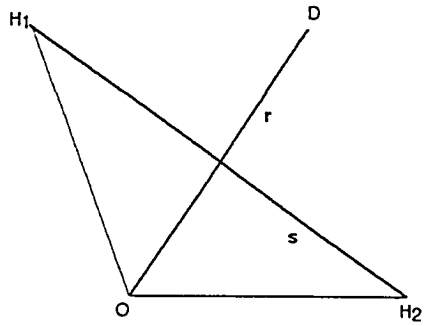

Figure A-1 Orientation of the water molecule. O, H_1 and H_2 represent the positions of the oxygen and hydrogen atoms, respectively. Vectors **r** and **s** show the two orthogonal vectors.

Before the orientation of the local frame can be expressed in quaternion form its rotation matrix, R, is first constructed,

$$R = \begin{bmatrix} \mathbf{r}_x & \mathbf{r}_y & \mathbf{r}_z \\ \mathbf{s}_x & \mathbf{s}_y & \mathbf{s}_z \\ \mathbf{t}_x & \mathbf{t}_y & \mathbf{t}_z \end{bmatrix}. \tag{A-1}$$

The relationship between the quaternion,

$$\mathbf{Q} = (q_0, q_1, q_2, q_3) \tag{A-2}$$

and the rotation matrix can be given by,

$$q_0 = \frac{1}{2}\sqrt{-\mathbf{r}_x + \mathbf{s}_y - \mathbf{t}_z + 1} * SIGN(\mathbf{r}_z - \mathbf{t}_x) \tag{A-3a}$$

$$q_1 = \frac{1}{2}\sqrt{\mathbf{r}_x - \mathbf{s}_y - \mathbf{t}_z + 1} * SIGN(\mathbf{s}_z - \mathbf{t}_y) \tag{A-3b}$$

$$q_2 = \frac{1}{2}\sqrt{-\mathbf{r}_x - \mathbf{s}_y + \mathbf{t}_z + 1} * SIGN(\mathbf{r}_y - \mathbf{s}_x) \tag{A-3c}$$

$$q_3 = \frac{1}{2}\sqrt{\mathbf{r}_x + \mathbf{s}_y + \mathbf{t}_z + 1} \tag{A-3d}$$

where the SIGN function extracts only the mathematical sign of the argument.

The resulting quaternion associated with each molecule represents its orientation. At the start of each of the simulations of ice/water systems in this thesis, the centre of mass positions and the quartenions for all molecules are read by the molecular dynamics program as a configuration file describing the system in question.

APPENDIX B – Definitions for Solid and Liquid Labeling

The labeling of a water molecule as translationally and rotationally either solid or liquid will be illustrated for a Ih0001 ice system. After 200 timesteps (0.2 ps) during a production run, a current configuration is stored. After 400 such configurations are stored (corresponding to 80 ps), an analysis procedure determines average positions and orientations while also discriminating solid and liquid characteristics for labeling procedures. Translations and rotations must be treated differently to obtain these values, as will be discussed below.

Translations

The 400 configurations stored contains information on the position vectors of the center of mass for each molecule in the system. An average of these position vectors is easily calculated, yielding averaged positions for each molecule over the 80 ps time window. Next the root mean-squared deviation from the average position vectors are calculated for each molecule from the 400 stored configurations (representing a trajectory).

Rotations

To obtain an averaging procedure for orientations (or equivalently averaged quaternions) is not a trivial task. Recently, Hernández de la Peña and Kusalik [270] have recently defined such an averaged quaternion, called the orientational centroid. This can be defined as the orientation, q_c that minimizes the function, $G(q_c)$ given by

$$G(q_c) = \sum_{k=1}^{P_q} \Gamma^2(q_c, q_t) \qquad \text{(B-1)}$$

where $\Gamma(q_c,q_t)$ is the arc length between the centroid orientation, q_c, and P (400 in this case) orientations, q_t, for each molecule. A Monte Carlo search algorithm that either accepts or rejects trial centroid moves. At each step in the algorithm, a new trial centroid is generated by a small random rotation of the previous trial centroid. Moves are accepted only if the value of $G(q_c)$ has been reduced. The minimizing of the arc length through the use of B-1 continues until the trial centroid no longer changes within some small tolerance. At this point the Monte Carlo algorithm has converged.

As in the translational case the mean-square deviations of the arc length from the orientational centroid are computed for each molecule for the 400 configurations. These deviations are stored and divided by the number of orientations to obtain the average. These averages represent the dispersion of the orientations sampled during the 80 ps time interval of the trajectory.

Labeling criteria

Representative values for the average deviations for the position vectors (translations) and arc lengths (orientations) were plotted as profile functions and compared with other profile functions. From these comparisons solid cut-off values were selected for each case. The cut off for the translations was chosen 10% higher than its mean solid value which corresponds to a cut-off value of ~ 0.7Å (~ a quarter of the oxygen-oxygen distances in ice I). The rotational cut off was chosen to coincide with the breaking of hydrogen bonds with a value of 1.5 for $G(q_c)$ which provides less direct physical interpretation. These values were confirmed with several other ice/water systems with averaged configurations ranging from 75-100 ps for their consistency in identifying solid-like behaviour.

REFERENCES

1) H. R. Shaw, *Craters, Cosmos and Chronicles: A New Theory of Earth* (Stanford University Press, Stanford, 1994).

2) G. S. H. Lock, *The Growth and Decay of Ice* (Cambridge University Press, Cambridge, 1990).

3) D. P. Woodruff, *The Solid-Liquid Interface* (Cambridge University Press, London, 1973).

4) G. S. Zhdanov, *Crystal Physics* (Oliver & Boyd, Edinburgh, 1965).

5) K. J. Laidler and M.S.Meiser,*Physical Chemistry 3th ed.*(Houghton and Mifflin.,New York,1999).

6) W. A. Tiller, *The Science of Crystallization* (Cambridge University, Cambridge, 1991).

7) N. E. Dorsey, *Properties of Ordinary Water-Substance* (Reinhold, New York, 1940).

8) F. MacRitchie, *Chemistry at Interfaces* (Academic Press, San Diego, 1990).

9) B. Yang, D. E. Sullivan and C. G. Gray, J. Phys. Conden. Matt. **6**, 4823 (1994).

10) P. S. Pershan, J. Phys. Conden. Matt. **6**, A-37 (1994); T. Somasundaram, M. I. H. Panhuus, R. M. Lynden-Bell and C. H. Patterson, J. Chem. Phys. **111**, 2190 (1999).

11) V. F. Petrenko and R. W. Whitworth, *Physics of Ice* (Oxford University, Oxford, 2002).

12a) Water - *A comprehensive treatise*, edited by F. Franks (Plenum, New York, 1982), Vol 1.

12b) Water - *A comprehensive treatise*, edited by F. Franks (Plenum, New York, 1982), Vol 2-6.

12c) *Water - A comprehensive treatise*, edited by F. Franks (Plenum, New York, 1982), Vol 7.

12d) *Water - A comprehensive treatise*, edited by F. Franks (Plenum, New York, 1982), Vol 8.

13) S. P. Das, Rev. Mod. Phys. **76**, 785 (2004).

14) *The Collected Works of Lars Onsager*, edited by P. C. Hemmer, H. Holden and S. Kjelstrup Ratkje (World Scientific, Singapore, 1996).

15) W. Greiner, L. Neise and H. Stöcker, *Thermodynamics and Statistical Mechanics* (Springer – Verlag, New York, 1995).

16) Lyklema, J., 1995 *Fundamentals of interface and colloid science: volume II solid-liquid interfaces* (London: Academic Press).

17) I. Benjamin, Annu. Rev. Phys. Chem. **48,** 407 (1997).

18) *The solid-gas interface Vol. 1*, edited by E. A. Flood (Marcel Dekker Inc., New York, 1967);*The solid-gas interface Vol. 2*, edited by E. A. Flood (Marcel Dekker Inc., New York, 1967).

19) *Handbook of surfaces and interfaces vol. I,* edited by L. Dobrzynski (New York: Garland STPM Press); *Handbook of surfaces and interfaces vol. II,* edited by L. Dobrzynski (New York: Garland STPM Press)

20) C. D. Stanners, D. Gardin and G. A. Somorjai, J. Electrochem. Soc. **141,** 3278 (1994).

21) Y. K. Tovbin, Prog. Surf. Sci. **34**, 1 (1990).

22) M. A. van Hove, Surf. Interface Anal. **28,** 36 (1999).

23) J. Stangl, V. Holy, and G. Bauer, Rev. Mod. Phys. **76**, 725 (2004)

24) P. Moriarty, Rep. Prog. Phys. **64**, 297 (2001).

25) M. Plischke and B. Bergersen, *Equilibirum statistical physics* (World Scientific, Singapore, 1999).

26) M. Asta, F. Spaepen, J. F. van der Veen, Mat. Res. Bulletin **29**, 920 (2004).

27) *Comprehensive Chemical Kinetics - Reactions at the liquid-solid interface*, edited by R. G. Compton (Elsevier, Amsterdam, 1989) Vol. 28.

28) W. L. Jorgensen, J. Chandrasekhar, J. D. Madura, R. W. Impley and M. L. Klein, J. Chem. Phys. **79**, 926 (1983).

29) H. J. C. Berendsen, J. R. Grigera and T. P. Straatsma, J. Chem. Phys. **91**, 6269 (1987).

30) H. W. Horn, W. C. Swope, J. W. Pitera, J. D. Madura, T. J. Dick, G. L. Hura and T. Head-Gordon, J. Chem. Phys. **120**, 9665 (2004).

31) T. Young, Phil. Trans. Royal Soc. **95**, 65 (1805).

32) R. Defay, I. Prigogine, A. Bellemans and D. H. Everett, *Surface tension and adsorption* (Longmans, London, 1966).

33) *Handbook of Surface and Colloid Chemistry*, edited by K. S. Birdi (CRC Press, Boca Raton, 1997).

34) W. Adamson and A. P. Gast *Physical Chemistry of Surfaces* 6th ed., edited by (John Wiley & Sons, New York, 1997).

35) B. B. Laird and A. D. J. Haymet, Chem. Rev. **92**, 1819 (1992).

36) D. Chandler, *Introduction to Modern Statistical Mechanics* (Oxford University Press, New York, 1987).

37) K. A. Jackson, J. Cryst. Growth **198/199**, 1 (1999).

38) J. Stangl, V. Holy, and G. Bauer, Rev. Mod. Phys. **76,** 725 (2004).

39) *Crystal Growth*, edited by H. S. Peiser (Pergamon Press, Oxford, 1966).

40) J. W. Mullin, *Crystallization* (Butterworths, London, 1961).

41) R. F. Strichland-Constable, *Kinetics and Mechanism of Crystallization* (Academic Press, London, 1968).

42) P. Hartman, *Crystal Growth: and Introduction* (North-Holland Publishing Co., Amsterdam, 1973).

43) J. W. Gibbs, *Collected Works* (Longman's Green, London, 1928).

44) P. Curie, Bull. Soc. Françn Mineral **8**, 145 (1885).

45) A. Pimpinelli and J. Villain, *Physics of Crystal Growth* (Cambridge University Press, Cambridge, 1998).

46) S. H. Davis, *Theory of Solidification*, (Cambridge University Press, Cambridge,

2001).

47) G. Tamman, *States of Aggregation* (Constable, London, 1926).

48) M. Volmer, Z. phys. Chem. **119**, 277 (1926).

49) H. Brandes, Z. phys. Chem. **126**, 196 (1927).

50) I. N. Stranski, Z. phys. Chem. **136**, 259 (1928).

51) W. Kossel, Ann. Phys. (Leipzig) **21**, 457 (1934).

52) B. Mutaftschiev, *The Atomistic Nature of Crystal Growth* (Springer, Berlin, 2001).

53) R. Davey and J. Garside, *From Molecules to Crystallizers: An Introduction to Crystallization* (Oxford University Press, Oxford, 2000).

54) T. G. Petrov, E. B. Treivus and A. P. Kasatlin, *Growing Crystals from Solution* (Consultants Bureau, New York, 1969).

55) F. C. Frank, *Growth and Perfection of Crystals* (John Wiley & Sons, New York, 1958).

56) W. K. Burton, N. Cabrera and F. C. Frank, Phil. Trans. Royal Soc. **243**, 299 (1951).

57) W. M. Ketcham and P. V. Hobbs, Phil. Mag. **18**, 659 (1968).

58) H. A. Wilson, Phil. Mag. **50**, 238 (1900).

59) J. Frenkel, Phys. Z. Sowjetunion. **1**, 498 (1932).

60) A. Einstein, Ann. Phys. (Leipzig) **17**, 549 (1905).

61) D. J. Evans and G. P. Morriss, *Statistical Mechanics of Nonequilibrium Liquids*, (Academic Press, London, 1990).

62) E. A. Moelwyn-Hughes, *Physical Chemistry, 2nd ed.* (Pergamon Press, Oxford,1961).

63) K. A. Jackson, *Theory of Melt Growth, in Crystal Growth and Characterization*, edited by R. Ueda and J. B. Mullin (North-Holland, Amsterdam, 1975).

64) M. H. Grabow, G. H. Gilmer and A. F. Baker, Mat. Res. Soc. Symp. Proc. **141**, 349 (1989).

65) K. A. Jackson, *Liquid Metals and Solidification*, (ASM, Ohio, 1958).

66) J. M. Ziman, *Models of Disorder*, (Cambridge University Press, Cambridge, 1979).

67) D. I. Temkin, *Growth and Imperfections of Metallic Crystals* (Consultants Bureau, New York, 1968).

68) A. D. J. Haymet and D. W. Oxtoby, J. Chem. Phys. **74**, 2559 (1981); D. W. Oxtoby and A. D. J. Haymet, J. Chem. Phys. **76**, 6262 (1982).

69) T. Klupsch, Phys. Stat. Sol. (b) **95**, K147 (1979); T. Klupsch Phys. Stat. Sol. (b) **109**, 535 (1982); T. Klupsch, Ann. Phys. (Leipzig) **39**, 179 (1982).

70) R. Evans, *Fundamentals of Inhomogeneous Fluids*, edited by D. Henderson (Marcel Dekker, New York, 1992).

71) N. Choudhury and S. K. Ghosh, Phys. Rev. E, **57**, 1939 (1998).

72) P. Tarazona, Mol. Phys. **52**, 81 (1984); P. Tarazona, Phys. Rev A **31**, 2672 (1985).

73) W. A. Curtin and N. W. Ashcroft, Phys. Rev. A **32**, 2909 (1985).

74) A. Kyrlidis and R. A. Brown, Phys. Rev. E **51**, 5832 (1995).

75) K. M. Beatty and K. A. Jackson, J. of Cryst. Growth, **174**, 28 (1997)

76) D. W. Oxtoby, Annu. Rev. Mater. Res. **32**, 39 (2002).

77) L. Gránásy and T. Pusztai, J. Chem. Phys. **117**, 6157 (2002).

78) P. R. Harrowell and D. W. Oxtoby, J. Chem. Phys. **86**, 2932 (187).

79) J. S. Langer, Rev. Mod. Phys. **52**, 1 (1980).

80) J. S. Langer, *Directions in Condensed Matter Physics, Vol. 1*, edited by G. Grinstein and G. Mazenko (World Scientific, Singapore, 1986).

81) S. H. Davis, *Theory of Solidification* (Cambridge University Press, Cambridge, 2001).

82) P. Nozières, *Solids Far From Equilibrium*, edited by C. Godrèche (Cambridge University Press, Cambridge, 1992).

83) P. A. Engelstaff, *An Introduction to the Liquid State*, 2nd ed. (Clarendon, Oxford, 1992).

84) J. P. Hansen and I. R. Macdonald, *Theory of Simple Liquids* (Academic Press, London, 1986).

85) *Solid-State NMR Spectroscopy: Principles and Applications*, edited by M. J. Duer (Blackwell Publishing, Oxford, 2002).

86) J. M. Cowley, *Diffraction Physics* (Elsener, Amsterdam, 1995).

87) M. A. Van Hove, Surf. Interf. Ana. **28**, 36 (1999).

88) D. W. L. Hukins, *X-ray Diffraction by Disordered and Ordered Systems* (Pergamon Press, Oxford, 1981).

89) E. Vlieg, Surf. Sci. **500**, 458 (2002).

90) X. Y. Liu, E. S. Boek, W. J. Briels, P. Bennema, Nature **374**, 342 (1995).

91) M. F. Toney, J. N. Howard, J. Richler, G. L. Borges, J. G. Gordon, O. R. Melroy, D. G. Wiesler, D. Yee, L. B. Sorenson, Nature **368**, 444 (1994); B. M. Ocko, Phys. Rev. Lett. **64**, 2160 (1990).

92) W. J. Huisman, J. F. Peters, M. S. Zwanenburg, S. A. de Vries, T. E. Derry, D. L. Abernathy, J. F. van der Veen, Nature **390**, 379 (1997).

93) M. F. Toney, J. G. Gordon, M. G. Samant, G. L. Borges, O. R. Melroy, L. S. Kau, D. G. Wiesler, D. Yee, L. B. Sorensen, Phys. Rev. B **42**, 5594 (1990).

94) F. Grey, R. Friedenhans'l, J. S. Pedersen, M. Nielsen, R. L. Johnson, Phys. Rev. B. **41**, 9519 (1990); S. A. de Vries, P. Goedtkindt, P. Steadman, E. Vlieg, Phys. Rev. B. **59**, 13301 (1999).

95) S. Engemann, H. Reichert, H. Dosch, J. Bilgram, V. Honkimäki and A. Snigirev, Phys. Rev. Lett. **92**, 205701 (2004).

96) H. Reichert, O. Klein, H. Dosch, M. Denk, V. Honkimäki, T. Lippmann and G. Reiter, Nature **408**, 839 (2000).

97) J. F. van der Veen and H. Reichert, MRS Bulletin **29**, 958 (2004).

98) P. E. Champness, *Electron Diffraction in the Transmission Electron Microscope* (BIOS, Oxford, 2001).

99) A. C. McLaren, *Transmission Electron Microscopy of Minerals and Rocks* (Cambridge University Press, Cambridge, 1991).

100) B. Fultz and J. M. Howe, *Transmission Electron Microscopy and Diffractometry of Materials* (Springer-Verlag, Berlin, 2001).

101) A. Hirata, T. Akane, S. Jinno, T. Kuno, Y. Xang, Y Fujiwara, A. Nakamura and Y. Takeda, Mat. Sci. Semi. Process., **6**, 473 (2003).

102) J. M. Howe and H. Saka, MRS Bulletin **29**, 951 (2004).

103) R. Wiesendanger, *Scanning Probe Microscopy and Spectroscopy: Methods and Applications* (Cambridge University Press, Cambridge, 1994).

104) M. Labayen and O. M. Magnussen, Surf. Sci., **573**, 128 (2004)

105) M. Poza, J. G. Rodrigo and S. Viera, Physica B, **218**, 265 (1996).

106) H. Shindo and M. Ohashi, App. Phys. A-Mat. Sci. Process., **66**, S487 (1998).

107) Y. R. Chen, Ann. Rev. Phys. Chem. **40**, 327 (1989).

108) Y. R. Chen, Surf. Sci. **299/300**, 551 (1994).

109) T. F. Heinz, *Nonlinear Surface Electromagnetic Phenomena*, edited by H. E. Ponath and G. I. Stegeman (North-Holland, Amsterdam, 1991).

110) Y. R. Chen, Proc. Natl. Acad. Sci. **93**, 12104 (1996).

111) A. L. Mifflin, K. A. Gerth, B. M. Weiss and F. M. Geiger, J. Phys. Chem. A. **107**, 3212 (2003); Z. Xu and Y. Dong, Surf. Sci. **445**, 65 (2000).

112) H. A. Al-Abadleh, A. L. Mifflin, P. A. Bertin, S. T. Nguyen and F. M. Geiger, J. Phys. Chem. B. **109**, 9691 (2005); X. Y. Zhang and R. A. Walker, Langmuir **17**, 4486 (2001).

113) N. Metropolis, A.W. Rosenbluth, M. N. Rosenbluth, A.H. Teller and E. Teller, J. Chem. Phys. **21**, 1087 (1953).

114) B. J. Alder and T. E. Wainwright, J. Chem. Phys. **27**, 1208 (1957).

115) J. M. Haile, *Molecular Dynamics Simulation* (John Wiley & Sons, New York, 1992).

116) M. P. Allen and D. J. Tildesley, *Computer Simulation of Liquids* (Clarendon Press, Oxford, 1989).

117) D. C. Rapaport, *The Art of Molecular Dynamics Simulation* (Cambridge University Press, Cambridge, 1995).

118) W. G. Hoover, *Studies in Modern Thermodynamics* II (Elsevier, Amsterdam, 1991).

119) W. Yourgrau, A. van der Merwe and G. Raw, *Treatise on Irreversible and Statistical Thermophysics: An Introduction to Nonclassical Thermodynamics* (The MacMillan Company, New York, 1966).

120) C. E. Hecht, *Statistical Thermodynamics and Kinetic Theory* (Dover Publications Inc., New York, 1990).

121) R. J. Sadus, *Molecular Simulation of Fluids: Theory, Algorithms and Object-Orientation* (Elsevier, Amsterdam, 1999).

122) W. G. Hoover, A. J. C. Ladd and B. Moran, Phys. Rev. Lett. **48**, 1818 (1982).

123) D. J. Evans, J. Chem. Phys. **78**, 3297 (1983).

124) L. A. Pars, *A Treatise on Analytical Dynamics* (Ox Bow, Connecticut, 1979).

125) S. Nosé, J. Chem. Phys. **81**, 511 (1985); W. G. Hoover, Phys. Rev. A., **31**, 1695 (1985).

126) H. C. Andersen, J. Chem. Phys. **72**, 2384 (1980).

127) A. K. Arora and B. V. R. Tara, Curr. Opinion Coll. Interf. Sci **78**, 49 (1998).

128) B. Kuchta and R. D. Etters, Computers Chemistry *19*,205 (1996).

129) P. A. Monson and D. A. Kofke, Adv. Chem. Phys. **115**,113 (2000).

130) F. delRio, J. E. Ramos, A. GilVillegas and I. A. McLure, J. Phys. Chem. **100**, 9104 (1996).

131) J. G. Kirkwood and E. Monroe, J. Chem. Phys. **8**, 845 (1940); J. G. Kirkwood and E. Monroe, J. Chem. Phys. **9**, 514 (1941).

132) J. G. Kirkwood, E. K. Maun and B. J. Alder, J. Chem. Phys. **18**, 1040 (1950).

133) A. Mori, R. Manabe and K. Nishioka, Phys. Rev. E. **51**, R3831 (1995).

134) R. L. Davidchack and B. B. Laird, Phys. Rev. E., **54**, R5905 (1996).

135) J. N. Cape and L. V. Woodcock, Chem. Phys. Lett. **59**, 271 (1978); J. N. Cape and L. V. Woodcock, J. Chem. Phys. **80**, 2420 (1980).

136) J. Tallon, Phys. Rev. Lett. **57**, 1328 (1986).

137) B. B. Laird and A. D. J. Haymet, Mol. Phys. **75**, 71 (1992).

138) B. B. Laird and A. D. J. Haymet, Mater. Res. Soc. Symp. Proc. **63**, 67 (1986).

139) A. J. C. Ladd and L. V. Woodcock, Chem. Phys. Lett. **51**, 155 (1977).

140) A. J. C. Ladd and L. V. J. Woodcock, Phys. Chem. **11**, 3565 (1978).

141) S. Toxvaerd and E. Praestgaard, J. Chem. Phys. **67**, 5291 (1977).

142) Hiwatari,Y., Stoll, E. and Schneider, T. J., J. Chem. Phys **68**, 3401 (1978).

143) A. Bonissent, E. Gauthier, J. L. Finney, Philos. Mag. **39**, 49 (1979).

144) G. Bushnell-Wye, J. L. Finney and A. Bonissent, Philos. Mag. **44**, 103 (1981).

145) J. Q. Broughton, A. Bonissent and F. F. Abraham, J. Chem. Phys. **74**, 4029 (1981).

146) J. Q. Broughton and F. F. Abraham, Chem. Phys. Lett. **71**, 456 (1983).

147) B. B. Laird and A. D. J. Haymet, J. Chem. Phys., **91**, 3638 (1989).

148) J. Q. Broughton and G. H. Gilmer, J. Chem. Phys. **79**, 5095 (1983).

149) J. Q. Broughton and G. H. Gilmer, J. Chem. Phys. **79**, 5105 (1983).

150) J. Q. Broughton and G. H. Gilmer, J. Chem. Phys. **79**, 5119 (1983).

151) J. Q. Broughton and G. H. Gilmer, J. Chem. Phys. **84**, 5741 (1986).

152) J. Q. Broughton and G. H. Gilmer, J. Chem. Phys. **84**, 5749 (1986).

153) J. Q. Broughton and G. H. Gilmer, J. Chem. Phys. **84**, 5759 (1986).

154) J. Q. Broughton, G. H. Gilmer and K. A. Jackson, Phys Rev. Lett. **49**, 1496 (1982).

155) E. Burke, J. Q. Broughton and G. H. Gilmer, J. Chem. Phys. **89**, 1030 (1988).

156) H. L. Tepper and W. J. Briels, Phys. Rev. Lett. **79**, 5076 (1997).

157) H, L. Tepper and W. J. Briels, J. Crystal Growth **230**, 270 (2001).

158) H. L. Tepper and W. J. Briels, J. Chem. Phys. **115**, 9434 (2001).

159) H. L. Tepper and W. J. Briels, J. Chem. Phys. **116**, 5186 (2002).

160) H. E. A. Huitema, M. J. Vlot and J. P. van der Eerden, J. Chem. Phys. **111**, 4714 (1999).

161) R. L. Davidchack and B. B. Laird, J. Chem. Phys. **118**, 7651 (2003).

162) J. R. Morris and X. Song, J. Chem. Phys. **119**, 3920 (2003).

163) A. William, R. Moss and P. Harrowell, J. Chem. Phys. **99**, 3998 (1993).

164) H. J. C. Berendsen, J. P. M. Postma, W. F. Van Gunsteren, A. Di Nola and J. R. Haak, J. Chem. Phys., **81**, 3684 (1984).

165) J. A. Hayward and A. D. J. Haymet, J. Chem. Phys., **114**, 3713 (2001).

166) M. S. Gulam Razul, E. V. Tam, M. E. Lam, P. Linden and P. G. Kusalik, Mol. Phys. **103**, 1929 (2005).

167) O. J. Lanning, S. Shellswell and P. A. Madden, Mol. Phys. **102**, 839 (2004).

168) R. J. Galej, H. J. Raveche and G. Lie, Phys. Rev. A **39**, 2574 (1989).

169) M. S. Gulam Razul, J. G. Hendry and P. G. Kusalik, submitted to J. Chem. Phys.

170) R. Moss and P. Harrowell, J. Chem. Phys. **101**, 9894 (1994).

171) F. A. Lindemann, Phys. Z. **11**, 609 (1910).

172) D. Tabor, *Gases, Liquids and Solids: and Other States of Matter* 3rd ed. (Cambridge University Press, Cambridge, 1991).

173) D. Eisenberg and W. Kauzmann, *The Structure and Properties of Water* (Oxford University, New York, 1969).

174) R. W. Bain, *National Engineering Steam Tables*, (H.M.S.O., Edinburgh, 1964).

175) N. A. Fletcher, *The Chemical Physics of Ice* (Cambridge University, Cambridge, 1970).

176) P. V. Hobbs, *Ice Physics* (Clarendon Press, Oxford, 1974).

177) J. D. Bernal, Trans. Faraday Soc. **33**, 27 (1937); J. D. Bernal, Proc. R. Soc. A **280**, 299 (1964); J. D. Bernal and R. H. Fowler, J. Chem. Phys. **1**, 515 (1933).

178) A. J. Leadbetter, R. C. Ward, J. W. Clark, P. A. Tucker, T. Matsuo and H. Suga, J. Chem. Phys. **82**, 424 (1985).

179) E. R. Davidson and K. Morokuma, J. Chem. Phys. **81**, 3741 (1984).

180) J. A. Hayward and J. R. Reimers, J. Chem. Phys. **106**, 1518 (1997).

181) J. Lekner, Phys. B **240**, 263 (1997).

182) E. Whalley, J. Chem. Phys. **87**, 4174 (1983).

183) R. C. Buchanan and T. P. Taeun, *Materials Crystal Chemistry* (Marcel Dekker, New York, 1997).

184) G. P. Johari, Philo. Mag. B. **78**, 375 (1998).

185) Y. P. Handa, D. D. Klug and E. Whalley, J. Chem. Phys. **84**, 7009 (1986).

186) D. A. Huckably, R. Pitis, R. H. Kincaid and C. Hamilton, J. Chem. Phys. **98**, 8105 (1993).

187) C. W. Lee, J. Meteorol. Soc. Jpn. **50,** 171 (1972).

188) H. Uyeda and K. Kikuchi, J. Fac. Sci. Hokkaido Univ. Ser VII **5**, 21 (1976).

189) T. Kobayashi, Y. Furukawa, T. Takahashi and H. Uyeda, J. Cryst. Growth **35**, 262 (1976).

190) H. Uyeda and K. Kikuchi, J. Meteorol. Soc. Jpn. **58**, 52 (1980).

191) H. Uyeda and K. Kikuchi, J. Meteorol. Soc. Jpn. **54**, 267(1976).

192) T. Takahashi, J. Cryst. Growth **59**, 441 (1982).

193) T. Shichiri, T. Aikami and J. Kakinoki, J. Cryst. Growth **43**, 320 (1978).

194) T. Shiojiri and C. Kaito, J. Cryst. Growth **52**, 173 (1981).

195) E. Mayer and A. Hallbrucker, Nature **325**, 601 (1987).

196) L. S. Bartell and J. Huang, J. Chem. Phys. **98**, 7455 (1994).

197) I. M. Svishchev and P. G. Kusalik, J. Am. Chem. Soc. **118**, 649 (1995).

198) I. M. Svishchev and P. G. Kusalik, Phys. Rev. Lett. **73**, 975 (1994).

199) B. J. Murray, D. A. Knopf and A. K. Betram, Nature **434**, 202 (2005).

200) *Physics of ice*, edited by N. Riehl, B. Bullemer and H. Engelhardt (Plenum, New York, 1969).

201) *Physics and Chemistry of ice*, edited by N. Maeno and T. Hondoh (Hokkaido University, Sapporo, 1992).

202) A. A. Shibkov, Y. I. Golovin, M. A. Zheltov, A. A. Korolev and A. A. Leonov, Physica A **319**, 65 (2003).

203) W. Shimada and Y. Furukawa, J. Phys. Chem. B **101**, 6171 (1997).

204) I. Braslavsky and S. G. Lipson, J. Cryst. Growth, **198/199**, 56 (1999).

205) W. B. Hillig, *Growth and Perfection of Crystals*, edited by R. H. Doremus, B. W. Roberts and D. Turnbull (Wiley, New York, 1958).

206) K. Neumann and G. Micus, Z. Physik. Chem. **2**, 25 (1954).

207) J. J. Kramer and W. A. Tiller, J. Chem. Phys. **42**, 257 (1965).

208) D. A. Rigney and J. N. Blakely, Acta Met. **14**, 1375 (1956).

209) K. A. Jackson, D. R. Uhlmann and J. D. Hunt, J. Cryst. Growth **1**, 1 (1967).

210) K. R. Jackson and J. D. Hunt, Trans. Met. Soc. **236**, 1929 (1966).

211) K. Nagashima and Y. Furukawa, Physica D **147**, 177 (2000).

212) W. Kost, Z. Elektrochem. **57**, 431 (1953).

213) J. Hallett, J. Atmos. Sci. **21**, 671 (1964).

214) E. S. Miksch, Rev. Sci. Instr. **36**, 797 (1965).

215) K. Nagashima and Y. Furukawa, J. Cryst. Growth **171**, 577 (1997).

216) M. Maruyama and T. Nishida, J. Phys. Chem B **101**, 6151 (1997).

217) P. R. Sperry, ScD Thesis, MIT, (1965).

218) P. R. Sperry, op-cit., p. 174.

219) Y. Furukawa and W. Shimada, J. Cryst. Growth **128**, 234 (1993).

220) E. Yokoyama, R. F. Sekerka and Y. Furukawa, J. Phys. Chem. B **104**, 65 (2000).

221) A. S. Michaels, P. L. T. Brian and P. R. Sperry, J. Appl. Phys. **37**, 4649 (1996).

222) Y. Teraoka, A. Saito and S. Okawa, Int. J. of Refgn. **25**, 218 (2002).

223) M. Maruyama, J. Cryst. Growth **275**, 598 (2005).

224) M. Maruyama, T. Satoi, S. Taniguchi, M. Kawamura, S. Kodera, Y. Kishimoto a nd Y. Furukawa, Jpn. J. Appl. Phys. **39**, 6696 (2000).

225) B. Pittenger, S. C. Fain, Jr., M. J. Cochran, J. M. K. Donev, B. E. Robertson, A. Szuchmacher and R. M. Overney, Phys. Rev. B. **63**, 134102-1 (2001).

226) A. Döppenschmidt, M. Kappl and H-J. Butt, J. Phys. Chem. B., 102, 7813 (1998).

227) D. S. Kliger, J. W. Lewis and C. E. Randall, *Polarized Light in Optics and Spectroscopy* (Academic press, Boston, 1990).

228) *Handbook of Optics, Devices, Measurements and Properties* 2nd ed , edited by M. Bass (Mcgraw Hill, New York, 1995), Vol II.

229) P. W. Atkins, *Physical Chemistry 6th ed.* (W. H. Freeman & Co., New York, 1998).

230) P. Böni, J. H. Bilgram and W. Känzig, Phys. Rev. A **28**, 2953 (1983).

231) D. A. Skoog and J. J. Leary, *Principles of Instrumental Analysis 4th ed.* (Saunders College, Fort Worth, 1992).

232) *Topics in Applied Physics - Light Scattering in Solids*, edited by Cardona (Springer-Verlag, New York, 1975).

233) *Light Scattering Spectra of Solids*, edited by G. B. Wright (Springer-Verlag, New York, 1969).

234) D. Beaglehole and P. Wilson, J. Chem. Phys. **97**, 11053 (1993).

235) O. A. Karim and A. D. J. Haymet, J. Chem. Phys. **89**, 6889 (1988).

236) H. Güttinger, J. H. Bilgram, and W. Känzig, J. Phys. Chem. Solids **40**, 55 (1979).

237) L. D. Landau and G. Placzek, Z. Phys. (Sowjet) **5**, 172 (1934).

238) P. U. Halter, J. H. Bilgram and W. Känzig, J. Chem. Phys. **89**, 2622 (1988).

239) J. H. Bilgram, Phys. Rep. **153**, 1 (1987).

240) H. Z. Cummins, G. Livescu, H. Chou and M. R. Srinivasan, Solid State Commun. **60**, 857 (1986).

241) O. N. Mesquita, L. O. Ladeira, I. Gontijo, A. G. Oliveira and G. A. Barbosa, Phys. Rev. B, **38**, 1550 (1988).

242) R. A. Brown, J. Keizer, U. Steiger and Y. Yeh, J. Chem. Phys. **87**, 4135 (1982).

243) M. C. Goh, J. M. Hicks, J. Kemnitz, G. R. Pinto, K. B. Eisenthal and T. F. Heinz, J. Chem. Phys. **92**, 5074 (1988).

244) F. M. Geiger, A. C. Tridico and J. M. Hicks, J. Phys. Chem. B. **103**, 8205 (1999).

245) W. P. Weglarz and H. Peemoeller, J. Magn. Reson. **124**, 484 (1997).

246) S. W. Rick, J. Chem. Phys. **114**, 2276 (2001).

247) D. -M. Duh, D. N. Perera, and A. D. J. Haymet, J. Chem. Phys., **102**, 3736 (1995).

248) H. Nada and J. P. van der Eerden, J. Chem. Phys. **118**, 7401 (2003).

249) H. Nada, J. P. van der Eerden and Y. Furukawa, J. Cryst. Growth **266**, 297 (2004)

250) O. A. Karim and A. D. J. Haymet, Chem. Phys. Lett. **138**, 531 (1987).

251) O. A. Karim, P. A. Kay and A. D. J. Haymet, J. Chem. Phys. **92**, 4634 (1990).

252) L. A. Bàez and P. Clancy, J. Chem. Phys. **103**, 9744 (1995).

253) E. Sanz, C. Vega and J. L. F. Abascal, J. Chem. Phys. **122**, 114507 (2005).

254) H. Nada and Y. Furukawa, Jpn. J. Appl. Phys., Part 1 **34**, 583 (1995).

255) H. Nada and Y. Furukawa, J. Cryst. Growth **169**, 587 (1996).

256) I. Okada, T. Nakashima, Y. Takahagi and J. Habasaki, J. Jpn. Assoc. Cryst. Growth **21**, 63 (1994).

257) J. C. Shelley and G. N. Patey, Mol. Phys. **88**, 385 (1996).

258) H. Nada and Y. Furukawa, J. Phys. Chem. B **101**, 6163 (1997).

259) J. A. Hayward and A. D. J. Haymet, Phys. Chem. Chem. Phys. **116**, 8876 (2002).

260) T. Bryk and A. D. J. Haymet, J. Chem. Phys. **117**, 10258 (2002).

261) G. –J. Kroes, Surf. Sci. **275**, 364 (1992)

262) E. Sanz, C. Vega, J. L. F. Abascal, and L. G. MacDowell, Phys. Rev. Lett. **117**, 255701 (2004).

263) E. Sanz, C. Vega, J. L. F. Abascal, and L. G. MacDowell, J. Chem. Phys. **121**, 1165 (2004).

264) M. Matsumoto, S. Saito and I. Ohmine, Nature **416**, 409 (2002)

265) E. R. Smith and P. A. Wielopolski, Mol. Phys. **61**, 1063 (1987).

266) P. L. Chau and A. J. Hardwick, Mol. Phys. **93**, 511 (1998).

267) W. B. Hillig, J. of Cryst. Growth, **183**, 463 (1998)

268) D. Turnbull, J. Appl. Phys. **21**, 1022 (1950).

269) J. Vatamanu and P. G. Kusalik, to be submitted.

270) L. Hernández de la Peña and P. G. Kusalik, Mol. Phys **102**, 927 (2004)